Year : 2021

Deciphering the tectono-metamorphic evolution of the Monte Rosa nappe: a combined petrological, structural and numerical modelling study

Vaughan-Hammon Joshua David

Faculté des géosciences et de l'environnement

Institut des sciences de la Terre

Deciphering the tectono-metamorphic evolution of the Monte Rosa nappe: a combined petrological, structural and numerical modelling study

Thèse de doctorat

présentée à la Faculté des géosciences et de l'environnement de l'Université de Lausanne par

Joshua David Vaughan-Hammon

Maîtrise ès Sciences de la Terre de l'University of Liverpool

Jury

Prof. Dr. Stefan M. Schmalholz	Université de Lausanne	Directeur de thèse
Prof. Dr. Lukas P. Baumgartner	Université de Lausanne	Co-directeur de thèse
Dr. Martin Robyr	Université de Lausanne	Expert interne
Prof. Dr. Fred Gaidies	Carleton University	Expert externe
Prof. Dr. Thomas Müller	Universität Göttingen	Expert externe
Prof. Dr. Othmar Müntener	Université de Lausanne	Président du jury

Lausanne, 2021

IMPRIMATUR

Vu le rapport présenté par le jury d'examen, composé de

Président de la séance publique :	M. le Professeur Othmar Müntener
Président du colloque :	M. le Professeur Othmar Müntener
Directeur de thèse :	M. le Professeur Stefan Schmalholz
Co-directeur de thèse :	M. le Professeur Lukas Baumgartner
Expert interne :	Docteur Martin Robyr
Expert externe :	M. le Professeur Thomas Müller
Expert externe :	M. le Professeur Fred Gaidies

Le Doyen de la Faculté des géosciences et de l'environnement autorise l'impression de la thèse de

Monsieur Joshua VAUGHAN-HAMMON

Titulaire d'un
Master en Sciences de la Terre

intitulée

DECIPHERING THE TECTONO-METAMORPHIC EVOLUTION OF THE MONTE ROSA NAPPE: A COMBINED PETROLOGICAL, STRUCTURAL AND NUMERICAL MODELLING STUDY

Lausanne, le 1er octobre 2021

Pour le Doyen de la Faculté des géosciences et de l'environnement

Professeur Othmar Müntener

And as far as I can see the world is too old for us to talk about with our new words
- We will pass just as quietly though life (passing through, passing through)
— Jack Karouac, *Big Sur*

This thesis is dedicated to my parents Karen and Paul Vaughan.

Contents

3   Peak Alpine metamorphic conditions from staurolite-bearing metapelites in the Monte Rosa nappe (Central European Alps) and geodynamic implications

Abstract

Direct evidence for deep geological processes (> 70 km) can be found in places throughout the Earth whereby plates have collided, subducted and then exhumed. Spectacular examples of this mountain building process can be seen in the European Alps. Here, changes in chemistry due to pressure (P) and temperature (T) conditions exotic to crustal rocks during subduction can be observed. One such place where we can observe such high grade rocks are within the Monte Rosa massif in the Central European Alps. However, the reported peak Alpine P and T estimates vary considerably between 1.2 and 2.7 GPa and 490 and 640°C for a variety of lithologies. More specifically, small volumes of unique whiteschist lithologies consistently record pressures up to 0.6 GPa higher than associated metapelitic and metagranitic lithologies, which yield pressures below $c.$ 1.6 GPa. These disparities pose difficulties when trying to resolve a tectono-metamorphic history for the Monte Rosa and the European Alps in general, due to the assumption that a calculated metamorphic P corresponds to a maximum burial depth (hydrostatic, or lithostatic pressure). Many explanations have been proposed for these P differences and these will be addressed throughout this thesis (e.g. tectonic mélange, kinetic effects, retrogression etc.), one such explanation suggests that lithostatic P is not always suitable to describe a three-dimensional stress state in a rock, and significant deviations from lithostatic P (tectonic, or dynamic, pressure) can occur, and could influence the metamorphic record.

Detailed fieldwork including structural and petrological analysis was undertaken in the upper portions of the Monte Rosa nappe at val d'Ayas, Italy. No evidence for tectonic mélange was observed, and the basement complex exposed represents a coherent unit. The deformation history exposed here agrees with previous observations of early Alpine top-N shear and late Alpine top-S shear and associated folding for the Monte Rosa nappe. Analysis of newly discovered outcrops of Alpine high-P rocks were undertaken on: (1) a whiteschist (calculated at 2.1 ± 0.2 GPa and 560 ± 20°C), (2) a staurolite + chloritoid bearing metapelitic rock (calculated at 1.6 ± 0.2 GPa and peak T of 585 ± 20°C), and (3) a unique chloritoid + zoisite bearing rock (calculated at 1.65 ± 0.25 GPa and 530 ± 40°C). These results continue to

highlight the consistently higher P estimates for rare, low volume whiteschists throughout the Monte Rosa nappe.

As well as detailed petrological studies within the Monte Rosa nappe, we also present a two-dimensional petrological–thermomechanical model to investigate the evolution and distribution of metamorphic facies within an orogenic wedge formed by subduction and continental collision. This model is directly applicable to the Western Alpine orogenic evolution and simulates an entire cycle of extension, with passive margin formation and mantle exhumation, followed by thermal equilibration without applied far-field deformation, convergence, with subduction initiation, basin closure and collision. The consequential metamorphic distribution is calculated using the peak P and T values of 10'000 numerical markers during their modelled P-T trajectories. Ad-hoc serpentinization of the exhumed mantle was considered. Models developing a weak subduction interface, due to 6 km serpentinite thickness, display a laterally varying peak metamorphic facies distribution, with the highest grade rocks within the core of the orogeny, agreeing with present-day distributions in the Western Alps. Whereas, models with a stronger subduction interface (3 km serpentinite thickness) develop an orogenic wedge with a vertical metamorphic gradient. These models are applicable to the Western Alps because large volumes of serpentinite are observed associated with high-P nappes, in particular the Monte Rosa nappe (Piedmont-Liguria ophiolites). Equally, the models also highlight that peak T rather than peak P is a stronger predictor of metamorphic facies distribution within the Western Alps. The models do exhibit significant deviations from lithostatic P (c. 0.4 GPa), but are typically confined to small regions within the subducted continental crust. The models also indicate, during overall convergence, local extensional tectonics between the exhuming material and overriding plate, whereby the upper-plate hanging-wall is unroofed, moving with a normal sense of shear relative to the exhuming high-pressure rocks. This exhumation style has been proposed in places throughout the Western Alps. This extrusion style of exhumation emphasises that regional scale plate divergence is not required to form extensional type shear indicators.

The multidisciplinary approach presented in this thesis, highlights that whiteschist bodies within the Monte Rosa nappe continue to show significantly higher pressures (c. 0.6 GPa)

compared to the majority, if not all other, lithologies within the nappe. Deviations from lithostatic pressure likely played a significant role in this disparity, but were most likely a mixture of compression induced, and reaction induced stresses. Equally, numerical models indicate that areas with significant tectonic pressure ($c.$ 0.4 GPa) are confined to small regions compared to the scale of the orogen. Therefore, if the calculated P of 1.6 ± 0.2 GPa represents peak Alpine conditions close to lithostatic, then the Monte Rosa nappe was exhumed from a significantly shallower depth ($c.$ 60 km) than previously assumed ($c.$ 80 km), based on peak P estimates > 2.2 GPas for whiteschist lithologies.

Résumé

Il est possible de trouver des preuves directes de processus géologiques profonds (> 70 km) dans des endroits de la Terre où des plaques sont entrées en collision, ont subi une subduction puis ont été exhumées. Des exemples spectaculaires de ce processus de formation de montagnes sont visibles dans les Alpes européennes. On peut y observer les changements chimiques dus aux conditions de pression (P) et de température (T) exotiques aux roches crustales pendant la phase de subduction. L'un des endroits où l'on peut observer ces roches de haute qualité se trouve dans le massif du Mont Rose, dans les Alpes d'Europe centrale. Cependant, les estimations de P et T alpines maximales rapportées varient considérablement entre 1.2 et 2.7 GPa et 490 et 640°C pour une variété de lithologies. Plus précisément, de petits volumes de lithologies de whiteschist uniques enregistrent systématiquement des pressions jusqu'à 0.6 GPa plus élevées que les lithologies métapélitiques et métagranitiques associées, qui donnent des pressions inférieures à environ 1.6 GPa. Ces disparités posent des difficultés lorsqu'on essaie de déterminer une histoire tectono-métamorphique du Mont Rose et des Alpes européennes en général, en raison de l'hypothèse selon laquelle une P métamorphique calculée correspond à une profondeur d'enfouissement maximale (pression hydrostatique, ou lithostatique). De nombreuses explications ont été proposées pour ces différences de P et elles seront abordées tout au long de cette thèse (par exemple, le mélange tectonique, les effets cinétiques, la rétrogression, etc.), l'une de ces explications suggère que la P lithostatique n'est pas toujours appropriée pour décrire un état de contrainte tridimensionnel dans une roche, et que des déviations significatives de la P lithostatique (pression tectonique ou dynamique) peuvent se produire, et pourraient influencer l'enregistrement métamorphique.

Un travail de terrain détaillé comprenant une analyse structurale et pétrologique a été entrepris dans les parties supérieures de la nappe du Mont Rose à Val d'Ayas, en Italie. Aucune preuve de mélange tectonique n'a été observée, et le complexe du socle exposé représente une unité cohérente. L'histoire de la déformation exposée dans ce travail est en accord avec les observations précédentes d'un cisaillement alpin top-N précoce et d'un cisaillement alpin top-S tardif, ainsi qu'avec les plissements associés pour la nappe du Mont Rose. L'analyse des

affleurements nouvellement découverts de roches alpines à haut P a été entreprise sur : (1) un whiteschist (calculé à 2.1 ± 0.2 GPa et 560 ± 20°C), (2) une roche métapélitique contenant de la staurolite et des chloritoïdes (calculée à 1.6 ± 0.2 GPa et une T maximale de 585 ± 20°C), et (3) une roche unique contenant des chloritoïdes et de la zoisite (calculée à 1.65 ± 0.25 GPa et 530 ± 40°C). Ces résultats continuent de mettre en évidence les estimations constamment plus élevées de P pour les whiteschists rares et de faible volume dans toute la nappe du Mont Rose.

En plus des études pétrologiques détaillées dans la nappe du Mont Rose, nous présentons également un modèle pétrologique-thermomécanique bidimensionnel pour étudier l'évolution et la distribution des faciès métamorphiques dans un biseau orogénique formé par la subduction et la collision continentale. Ce modèle est directement applicable à l'évolution orogénique des Alpes occidentales et simule un cycle complet d'extension, avec formation d'une marge passive et exhumation du manteau, suivi d'un équilibrage thermique sans déformation appliquée dans le champ lointain, convergence, avec initiation de la subduction, fermeture du bassin et collision. La distribution métamorphique conséquente est calculée en utilisant les valeurs maximales de P et T de 10'000 marqueurs numériques au cours de leurs trajectoires P-T modélisées. La serpentinisation ad-hoc du manteau exhumé a été considérée. Les modèles développant une interface de subduction faible, due à une épaisseur de serpentine de 6 km, montrent une distribution des pics de faciès métamorphiques variant latéralement, avec les roches de plus haute qualité dans le noyau de l'orogenèse, ce qui correspond aux distributions actuelles dans les Alpes occidentales. Cependant, les modèles avec une interface de subduction plus forte (3 km d'épaisseur de serpentine) développent un wedge orogénique avec un gradient métamorphique vertical. Ces modèles sont applicables aux Alpes occidentales car on observe de grands volumes de serpentine associés à des nappes à fort P, en particulier la nappe du Mont Rose (ophiolites du Piémont-Ligurie). De même, les modèles soulignent que le pic T, plutôt que le pic P, est un meilleur prédicteur de la distribution des faciès métamorphiques dans les Alpes occidentales. Les modèles présentent des déviations significatives par rapport au P lithostatique (environ 0.4 GPa), mais elles sont généralement limitées à de petites régions de la croûte continentale ayant subi une subduction. (Les modèles in-

diquent également, au cours de la convergence globale, une tectonique d'extension locale entre le matériel exhumé et la plaque chevauchante, par laquelle la paroi suspendue de la plaque supérieure est débarrassée de son toit, se déplaçant avec un sens normal de cisaillement par rapport aux roches de haute pression exhumées. Ce style d'exhumation a été proposé par endroits dans les Alpes occidentales. Ce style d'exhumation par extrusion souligne que la divergence des plaques à l'échelle régionale n'est pas nécessaire pour former des indicateurs de cisaillement de type extensionnel.

L'approche multidisciplinaire présentée dans cette thèse met en évidence que les corps de whiteschist de la nappe du Mont Rose continuent de présenter des pressions significativement plus élevées (environ 0.6 GPa) par rapport à la majorité, voire à toutes les autres lithologies de la nappe. Les écarts par rapport à la pression lithostatique ont probablement joué un rôle important dans cette disparité, mais il s'agit très probablement d'un mélange de contraintes induites par la compression et par la réaction. De même, les modèles numériques indiquent que les zones présentant une pression tectonique importante (environ 0.4 GPa) sont confinées à de petites régions par rapport à l'échelle de l'orogène. Par conséquent, si la P calculée de 1.6 ± 0.2 GPa représente les conditions alpines maximales proches de la lithostase, alors la nappe du Mont Rose a été exhumée à partir d'une profondeur beaucoup plus faible (environ 60 km) que ce qui avait été supposé précédemment (environ 80 km), sur la base d'estimations de P maximales > 2.2 GPa pour les lithologies de whiteschist.

CHAPTER 1

General Introduction

1.1   Objectives

The primary focus of this study is to examine further the apparent discrepancies in peak pressure incurred by the Monte Rosa nappe during peak Alpine metamorphism. The aims of this project (Kinetic versus mechanical control of petrological pressure record of the Monte Rosa nappe: a combined geomechanical and petrological approach) intends to explore the numerous theories proposed in order to explain discrepancies in pressure within the Monte Rosa nappe. In particular, the magnitude and extent of tectonic pressure (deviating from hydrostatic pressure) will be investigated.

Both a multi-disciplinary, and a multi-scale scientific approach is required to examine the interplay between metamorphism and deformation. This study aims to combine geological field-work in the Monte Rosa nappe encompassing detailed pseudo-section modelling, petrological and structural analysis, as well as two-dimensional petrological-thermomechanical numerical modelling that is directly applicable to the Monte Rosa and the Western Alps in general.

Specific aims of this study include:

- Detailed geological analysis of the Monte Rosa nappe exposed at the Véraz field area, val d'Ayas, Italy. Including exploring new areas exposed due to recent glacial retreat and snow melt.

- Structural analysis of the Monte Rosa nappe exposed at the Véraz field area to find evidence for tectonic mélange.

- Investigating new occurrences of whiteschists throughout the Monte Rosa nappe.

- Investigating the Alpine metamorphic characteristics of the polymetamorphic basement metapelites of the Monte Rosa nappe.

- Assessing the controlling parameters and evolution of high grade metamorphism exposed within the Western Alps using state of the art petrological-thermomechanical numerical models.

1.2 Geology of the Monte Rosa nappe, European Alps

The Monte Rosa massif is located within the central European Alps, and is home to the second largest peak in western Europe, the Dufourspitz (4634 m). In 1789, H.B. de Saussure devoted one of his famous Alpine journeys (1779-96) to exploring the Monte Rosa (De Saussure, 1796), and he provides us with an early geological description of the massif (looking west from Macugnaga village, Italy): *"But there I saw Mont-Rose, composed of an uninterrupted series of gigantic peaks almost equal to each other, forming a vast circus, and to enclose, within their walls, the village of Macugnaga, its hamlets, its pastures, the glaciers which border, and the steep slopes that rise to the tops of these majestic colossi. But it's not only the singularity of this form which makes it a remarkable mountain; maybe it's even more her structure. I have noticed that Mont-Blanc and all high tops of its chain are composed of layers vertical. In Monte Rosa, up to the highest peaks, everything is horizontal, or inclined at most 30 degrees."*

Geologically, the Monte Rosa belongs to the internal crystalline massifs of the Western and Central Alps, together with the Dora Maira and Gran Paradiso massifs. Primarily, these massifs consist of a pre-Variscan polymetamorphic basement, and granitic bodies that intruded during the Permian period. The present-day position of the Monte Rosa basement complex is within the collisional Austroalpine-Penninic wedge of the Eocene-aged Alpine orogeny. The dismembered continental crust of the Monte Rosa resides structurally between the overlying Zermatt-Saas and underlying Antrona ophiolite sequences (Piedmont-Liguria ocean), separated by highly tectonized regions, indicative of orogenic activity. The nappe consists of an upper portion (Oberbau) and a lower portion (Unterbau), that are separated by the strongly sheared and mylonitic Stellihorn shear zone (Dal Piaz, 2001).

Although the Monte Rosa massif consists of a suite of lithologies that attest to a rich multiphase tectono-metamorphic history (e.g. the Variscan orogeny), the most studied event is the latest orogenic event, the Alpine orogeny. The internal crystalline massifs throughout the western Alps (Monte Rosa, Dora Maira, Gran Paradiso) typically exhibit the highest grade metamorphism during the Alpine orogeny. This metamorphism reflects pressures and

temperatures typical within subduction zones, and in the Alps this is associated with sub-duction of the European passive margin below the Adriatic margin. The Monte Rosa massif is typically attributed, prior to subduction, to the southern Brianconnais domain as part of the European margin, that was separated with the Adriatic margin by the Piedmont-Liguria embryonic ocean (Trümpy, 1975; Schmid et al., 2004; Lemoine et al., 1986; De Graciansky et al., 2011; McCarthy et al., 2020; Dal Piaz, 2001; Steck et al., 2015).

Peak metamorphic conditions related to Alpine subduction incurred by the Monte Rosa nappe have been estimated from a variety of lithologies. However, large disparities exist within the literature with peak P estimates ranging between 1.2 and 2.7 GPa and peak temperature between 490 and 640 °C (Borghi et al., 1996; Chopin, 1984; Dal Piaz and Lombardo, 1986; Ferrando et al., 2002; Gasco et al., 2011; Keller et al., 2004; Lapen et al., 2007; Le Bayon et al., 2006; Luisier et al., 2019; Vaughan-Hammon et al., 2021). The highest pressure metamorphic conditions recorded for the Monte Rosa nappe primarily involve minor volumes of unique assemblages termed 'whiteschists' at $c.$ 2.4 GPa (Le Bayon et al., 2006) and $c.$ 2.2 GPa (Luisier et al., 2019), as well as mafic boudins at $c.$ 2.7 GPa (e.g. Gasco et al., 2011).

Whiteschist lithologies have been the focus of much research due to their unique metasomatic origin (Chopin, 1984; Luisier et al., 2019; Marger et al., 2019; Luisier et al., 2021; Pawlig, 2001; Pawlig and Baumgartner, 2001), as they most likely derive from a late magmatic alteration of the host granite prior to the high P Alpine event (Luisier et al., 2019; Marger et al., 2019). Notably, they exhibit relatively higher peak P estimates at 2.2 ± 0.2 GPa (Le Bayon et al., 2006; Luisier et al., 2019), compared to lower P host metagranites that do not exhibit pressures exceeding 1.6 GPa (Luisier et al., 2019), during the Alpine high P event.

Several mechanisms have been proposed to transport rocks, during subduction, from (U)HP conditions to the surface during Alpine orogenesis (Beltrando et al., 2010a,b; Burov et al., 2001; Butler et al., 2013, 2014; Campani et al., 2010; Escher and Beaumont, 1997; Froitzheim et al., 2003; Hacker and Gerya, 2013; Warren, 2013; Warren et al., 2008). However, large discrepancies in peak P within a structurally coherent nappe (e.g. between whiteschist and metagranite lithologies within the Monte Rosa) poses difficulties when attempting to resolve a

tectono-metamorphic history if it is assumed that peak P represents the lithostatic pressure, which is mainly a function of burial depth (Schenker et al., 2015; Schmalholz et al., 2014a,b).

Several explanations have been proposed for the $c.$ 0.6 ± 0.2 GPa pressure differences estimated in the Monte Rosa nappe during peak Alpine metamorphism, these include: 1) tectonic mélange, 2) differences in thermodynamic databases used in different studies, 3) lower P lithologies (e.g. metagranite) do not exhibit a high P imprint due to sluggish kinetics, 4) lower P lithologies (e.g. metagranite) did experience high P but were later retrogressed, and 5) mechanical pressure variations (tectonic, or dynamic, pressure).

1.3 Variable peak metamorphism

The 5 possible explanations for peak Alpine pressure variations recorded within the Monte Rosa nappe listed above will be expanded on in more detail in the following sections.

1.3.1 Tectonic mélange

Although the emergence of this deformation style is still debated, tectonic mixing is typically associated with deformation within an active subduction zone (Hsü, 1968, 1974; Raymond, 1975, 1984). A mélange is characterized by a chaotic block-and-matrix structure (Cowan, 1985), whereby exotic blocks are incorporated into the matrix during deformation. Famous examples of this style of deformation can be observed in the Franciscan Complex, where a highly deformed low grade mudstone matrix hosts blueschists and eclogites blocks with metamorphic pressures up to $c.$ 1.5 GPa (e.g. Wakabayashi, 2015).

Tectonic melanges are documented throughout the Western Alps (Balestro et al., 2015; Roda et al., 2018, 2020). Tectonic mixing could be a viable mechanism to explain high P whiteschist bodies emplaced within low P metagranites, especially considering some outcrops are highly deformed with the metagranite (e.g. Pawlig and Baumgartner, 2001). However, this deformation typically postdates high P metamorphism and is mainly confined to greenschist facies conditions (e.g. Pawlig and Baumgartner, 2001), and former magmatic fabrics can still be ob-

served (e.g. magmatic tourmaline phenocrysts or altered aplitic dykes) (Luisier et al., 2019, 2021; Marger et al., 2019). Equally, detailed geochemical analysis suggests that whiteschist bodies within the Monte Rosa nappe have a late magmatic, hydrothermal metasomatic (Mg-enriched), chlorite-sericite schist protolith, and are not exotic to the host metagranite (Luisier et al., 2019, 2021; Marger et al., 2019; Pawlig and Baumgartner, 2001).

1.3.2 Thermodynamic database

Differences in thermodynamic databases, solid-solution models and model assumptions (e.g. Fe^{3+} content or water activity) could produce artificial ΔP when attempting to compile calculate metamorphic conditions from various lithologies within various studies within the Monte Rosa nappe. However, Luisier et al. (2019) used consistent thermodynamic assumptions as well as the same thermodynamic database (Berman, 1988, 92 update), and still estimated significant differences in pressure of 0.6 ± 0.2 GPa between whiteschist and metagranite lithologies.

1.3.3 Kinetics and metamorphic equilibrium

Metamorphic rocks typically involve solid solution phases with complex crystal chemistry as well as fluids (e.g. H_2O-CO_2 mixtures) (Spear and Pattison, 2017). Advancements in geothermobarometry has enabled more precise inferences of pressure and temperature changes recorded in the history of metamorphic rocks (e.g. de Capitani and Brown, 1987; Holland and Powell, 1998; Spear, 1989). Advancements in analytical techniques, coupled with advancements in thermodynamic programs and internally consistent databases, enables a higher resolution of equilibrium subdomains to be distinguished and thus a more clearer metamorphic history of a rock to be revealed. In doing so, many of the assumptions that are cornerstones in quantitive metamorphic petrology have been questioned. Assumptions such as isochemical systems and local equilibria provide a good basis when estimating metamorphic conditions, used within the metamorphic facies principle and when using metamorphic assemblage diagrams. However, these assumptions are not sufficient when attempting to describe an evolv-

ing system where rates of processes are considered, e.g. introduction/removal of elements via metasomatism, nucleation, dissolution, crystal growth, inter/intra crystalline transport etc. These processes fall under the umbrella term of kinetics. A simple example of this would be a rock that is unable to transport elements to and from newly stable phases fast enough with the rate at which P and T are evolving.

Such kinetic factors have been proposed to explain the lack of high P metamorphic assemblages within metagranite lithologies of the Monte Rosa nappe. Water is a key transport mechanism for intercrystalline movement of elements needed when nucleating and growing new metamorphic phases. The assumption that the metagranites within the Monte Rosa nappe had insufficient water content needed to nucleate high P phases (e.g. jadeite), seems a logical explanation, especially considering the estimated short residence times at high P conditions (eclogite conditions dates at 42.6 ± 0.6 Ma (Lapen et al., 2007) and retrogression to greenschist facies dated between 40-37 Ma for both the Monte Rosa (Chopin, 1984) and the overlying Zermatt-Saas units (Skora et al., 2015)). However, the lack of water within the metagranite is not supported (Luisier et al., 2019). This is due to the presence of albite and zoisite pseudomorphs after igneous plagioclase (Luisier et al., 2019), and analysis of OH^- fractions of hydroxyl sites in phengites from Monte Rosa metagranites, that suggest high water activities during the high-pressure Alpine metamorphic event (Luisier et al., 2019).

1.3.4 Retrogression

Common throughout high grade metamorphic terranes are heavily retrogressed areas, recorded during exhumation from deep subduction. Within the Alps these can be observed in some regions as large domains of greenschist facies rocks, and typically coincide with later stages of an evolving orogenic system (Skora et al., 2015).

Metagranites throughout the Monte Rosa nappe typically exhibit post peak greenschist facies shear zones. However, similarly to the lack of evidence for dry conditions during peak metamorphism in metagranite lithologies, no evidence has been found for pseudomorphic textures after high P minerals (e.g. jadeite) (Luisier et al., 2019). Albite and zoisite pseudomorphs

after igneous plagioclase not only indicate that water was available, but they also indicate that no former high P minerals were retrogressed during exhumation of the Monte Rosa metagranites. To this date, no evidence for jadeite within metagranites has been observed (Luisier et al., 2019; Chopin, 1984).

1.3.5 Tectonic pressure

The last few years have seen a wealth of theoretical, petrological, experimental, and numerical modelling studies focusing on non-lithostatic pressure (Gerya, 2015; Hacker and Gerya, 2013; Jamtveit et al., 2018; Luisier et al., 2019; Moulas et al., 2014, 2013, 2019a,b; Reuber et al., 2016; Schenker et al., 2015; Schmalholz et al., 2014b; Schmalholz and Podladchikov, 2013; Schmalholz and Schenker, 2016; Tajčmanová et al., 2014). I will provide here a brief history of overpressure within the context of metamorphic geology.

The evolution of pressure recorded in metamorphic rocks has been vital in reconstructing the burial and exhumation of earth materials, particularly within dynamic areas of the Earth e.g. subduction zones. This is based on the central notion that pressure (P) and depth (z) are directly proportional using Archimedes' formula and the hydrostatic model for estimating a depth from a geo-barometrically derived pressure

$$P = \rho g z \tag{1.1}$$

Where ρ is the density of the overlying rock, g is the gravitational acceleration, and z is the height of the overlying rock. This formulation requires that P is a scalar parameter, which is also needed in the constituent equation of free energy of a chemical component (e.g. Gibbs, 1948), vital for geothermobarometry

$$G = U \ + \ PV \ - \ TS \tag{1.2}$$

Where G is the Gibbs free energy (per mole), U is the partial molar internal energy, P is the pressure, V is the partial molar volume, T is temperature, and S is the partial molar

entropy. It therefore follows that for any quasistatic process, with an unchanging particle number (N_1,..., N_i) and a constant entropy (S), a thermodynamic pressure can be defined as

$$P_{meta} = -\left(\frac{\partial U}{\partial V}\right)_{S,N_1,...,N_i} \tag{1.3}$$

Where ∂U is the change in internal energy and ∂V is the change in volume of a system. In mechanics, P is defined by the average of the three principle stresses (σ_1, σ_2 and σ_3)

$$P_{mech} = \frac{(\sigma_1 + \sigma_2 + \sigma_3)}{3} \tag{1.4}$$

The relative magnitudes of P defined by *hydrostatic* 1.1, *metamorphic* 1.3 and *mechanic* 1.4, as well as the impact on metamorphic reactions is not fully understood (Li et al., 2010; Luisier et al., 2019; Reuber et al., 2016; Moulas et al., 2019a; Wheeler, 2018). Deviations in P_{mech} from $P_{lithostatic}$ are termed non-hydrostatic, tectonic, or dynamic pressure.

Prior to the Earth Science communities acceptance of plate tectonics (Isacks et al., 1968; Le Pichon, 1968; Morgan, 1968), the first postulations of non-hydrostatic pressure appeared (Ernst, 1963, 1965). The possible pressure recorded by non-hydrostatic conditions in rocks was prompted by the experimental work of Ernst on HP-LT glaucophane, observed in blueschists of the Franciscan Complex, California. This experimental work prompted many hypotheses related to the formation of glaucophane at great depths but low temperatures, and the subsequent exhumation to the surface without chlorite replacement (Green, 2005). High horizontal stresses imposed on rocks, would lower the depth of burial required to form blueschist assemblages ($P_{lithostatic} = 0.7 - 0.9$ GPa $= 35 - 45$ km), which was a depth unfeasible solely by burial via sediments and exhumation via erosion, in an era prior to the plate tectonic revolution of the late 1960s.

The main reasons for the rejection of pressure variations being the reason for apparent rapid burial and exhumation needed to preserve blueschist lithologies was twofold: 1) acceptance of plate tectonics and thus a mechanisms fast enough to bury and exhume the rocks, and 2)

experimental rock deformation suggesting that rocks do not have sufficient strength in order to generate significant overpressure.

However, what is clear is that the pressure, or mean stress, in a rock cannot be exactly lithostatic during an orogeny due to differential stresses, required to drive rock deformation (Gerya, 2015; Mancktelow, 1993; Schmalholz et al., 2014b) or to balance lateral variations in gravitational potential energy (Molnar and Lyon-Caen, 1988; Schmalholz et al., 2019, 2014b).

Tectonic pressure has been proposed to be the cause for the apparent disparities in P (0.6 $\pm$ 0.2 GPa) between whiteschist ($\sim$ 2.2 GPa)) and metagranite ($\sim$ 1.4 GPa) lithologies within the Monte Rosa nappe (Luisier et al., 2019). More specifically, two end-member dynamic processes have been proposed that involved pressure that deviates from hydrostatic: (i) tectonic-induced compressive stresses during shearing-off of the Monte Rosa nappe from the subducting European plate, whereby viscosity differences between the strong metagranite host and weak whiteschist body would generate (required by force balance) significantly higher mean stresses within whiteschist lithologies depending on the magnitude and direction of applied differential stresses and the aspect ratio of weak whiteschist body (Luisier et al., 2019; Moulas et al., 2014), and (ii) reaction-induced stresses due to volumetric strains during dehydration reactions assuming a fixed volume during whiteschist formation (Luisier et al., 2019).

This hypothesis has implications for the geodynamic evolution of the Monte Rosa nappe. The existence of metamorphically recorded tectonic pressure would imply that the burial depth of the Monte Rosa unit was likely significantly less than 80 km, which is a depth estimate based on the lithostatic pressure assumption and local occurrences of low volume whiteschists exhibiting peak pressure > 2.2 GPa. Rather, the maximum burial depth of the Monte Rosa unit would be less than 60 km, based on values that more closely resemble lithostatic pressure throughout the nappe at > 1.6 GPa.

1.4 Synopsis

Four chapters are presented in this thesis that are accepted, under review, or are prepared for submission within peer-reviewed journals, these include:

- *Chapter 2:* **Alpine peak pressure and tectono-metamorphic history of the Monte Rosa nappe: cirque du Véraz, upper Ayas valley, Italy**. This chapter has been accepted in the *Swiss Journal of Geosciences.*

- *Chapter 3:* **Peak Alpine metamorphic conditions from staurolite-bearing metapelites in the monte Rosa nappe (Central European Alps) and geodynamic implications**. This chapter has been published in the *Journal of Metamorphic Geology*

- *Chapter 4:* **In search of Peter Bearth's whiteschist: Jägerhorn peak, Piedmont, Italy**. This chapter is in preparation to be submitted as a short communication to the *Swiss Journal of Geosciences.*

- *Chapter 5:* **Metamorphic facies evolution and distribution in the Western Alps predicted by petrological-thermomechanical models**. This chapter has been revised in the AGU journal *G-Cubed*, and is currently under the second round of reviews.

In addition to these papers, I have also co-authored two papers that have been accepted, or are prepared for submission within peer-reviewed journals:

- Evangelos Moulas, Mark T Brandon, Joshua D Vaughan Hammon, Stefan M Schmalholz, **On backflow associated with oceanic and continental subduction**, Geophysical Journal International, 2021; <https://doi.org/10.1093/gji/ggab246>

- **Mechanical instabilities control subduction—exhumation cycle of (ultra)high-pressure rocks.** Lorenzo G. Candioti, Joshua D. Vaughan-Hammon, Thibault Duretz and Stefan M. Schmalholz (in preparation)

Bibliography

Balestro, G., Festa, A., Tartarotti, P., 2015. Tectonic significance of different block-in-matrix structures in exhumed convergent plate margins: examples from oceanic and continental hp rocks in inner western alps (northwest italy). International Geology Review 57 (5-8), 581–605.

Beltrando, M., Compagnoni, R., Lombardo, B., 2010a. (ultra-) high-pressure metamorphism and orogenesis: an alpine perspective. Gondwana Research 18 (1), 147–166.

Beltrando, M., Lister, G. S., Rosenbaum, G., Richards, S., Forster, M. A., 2010b. Recognizing episodic lithospheric thinning along a convergent plate margin: The example of the early oligocene alps. Earth-Science Reviews 103 (3-4), 81–98.

Berman, R. G., 1988. Internally-consistent thermodynamic data for minerals in the system Na_2O-K_2O-CaO-MgO-FeO-Fe_2O_3-Al_2O_3-SiO_2-TiO_2-H_2O-CO_2. Journal of petrology 29 (2), 445–522.

Borghi, A., Compagnoni, R., Sandrone, R., 1996. Composite pt paths in the internal penninic massifs of the western alps: Petrological constraints to their thermo-mecanical evolution.

Burov, E., Jolivet, L., Le Pourhiet, L., Poliakov, A., 2001. A thermomechanical model of exhumation of high pressure (hp) and ultra-high pressure (uhp) metamorphic rocks in alpine-type collision belts. Tectonophysics 342 (1-2), 113–136.

Butler, J. P., Beaumont, C., Jamieson, R. A., 2013. The Alps 1: A working geodynamic model for burial and exhumation of (ultra) high-pressure rocks in alpine-type orogens. Earth and Planetary Science Letters 377, 114–131.

Butler, J. P., Beaumont, C., Jamieson, R. A., 2014. The Alps 2: Controls on crustal subduction and (ultra) high-pressure rock exhumation in alpine-type orogens. Journal of Geophysical Research: Solid Earth 119 (7), 5987–6022.

Campani, M., Herman, F., Mancktelow, N., 2010. Two-and three-dimensional thermal modeling of a low-angle detachment: Exhumation history of the simplon fault zone, central alps. Journal of Geophysical Research: Solid Earth 115 (B10).

Chopin, C., 1984. Coesite and pure pyrope in high-grade blueschists of the western alps: a first record and some consequences. Contributions to Mineralogy and Petrology 86 (2), 107–118.

Cowan, D. S., 1985. Structural styles in mesozoic and cenozoic mélanges in the western cordillera of north america. Geological Society of America Bulletin 96 (4), 451–462.

Dal Piaz, G. V., 2001. Geology of the monte rosa massif: historical review and personal comments. Schweizerische Mineralogische und Petrographische Mitteilungen 81 (3), 275–303.

Dal Piaz, G. V., Lombardo, B., 1986. Early alpine eclogite metamorphism in the penninic monte rosa-gran paradiso basement nappes of the northwestern alps. Geol. Soc. Am. Mem 164, 249–265.

de Capitani, C., Brown, T. H., 1987. The computation of chemical equilibrium in complex systems containing non-ideal solutions. Geochimica et Cosmochimica Acta 51 (10), 2639–2652.

De Graciansky, P.-C., Roberts, D. G., Tricart, P., 2011. The Birth of the Western and Central Alps: Subduction, Obduction, Collision. Vol. 14. Elsevier, pp. 289–315.

De Saussure, H. B., 1796. Voyages dans les Alpes. Vol. 3.

Ernst, W., 1963. Petrogenesis of glaucophane schists. Journal of Petrology 4 (1), 1–30.

Ernst, W., 1965. Mineral parageneses in franciscan metamorphic rocks, panoche pass, california. Geological Society of America Bulletin 76 (8), 879–914.

Escher, A., Beaumont, C., 1997. Formation, burial and exhumation of basement nappes at crustal scale: a geometric model based on the western swiss-italian alps. Journal of Structural Geology 19 (7), 955–974.

Ferrando, J., Scambelluri, M., Dal Piaz, G., Piccardo, G., 2002. The mafic boudins of the southern furgg-zone, monte rosa nappe, nw-italy: from tholeiitic continental basalts to alpine eclogites and retrogressed products. 81 riunione estiva soc. Geol. It., Torino, 10–12.

Froitzheim, N., Pleuger, J., Roller, S., Nagel, T., 2003. Exhumation of high-and ultrahigh-pressure metamorphic rocks by slab extraction. Geology 31 (10), 925–928.

Gasco, I., Borghi, A., Gattiglio, M., 2011. P–T alpine metamorphic evolution of the monte rosa nappe along the piedmont zone boundary (gressoney valley, nw italy). Lithos 127 (1-2), 336–353.

Gerya, T., 2015. Tectonic overpressure and underpressure in lithospheric tectonics and metamorphism. Journal of Metamorphic Geology 33 (8), 785–800.

Gibbs, J. W., 1948. The collected works of J. Willard Gibbs. Report, Yale Univ. Press.

Green, H. W., 2005. Psychology of a changing paradigm: 40+ years of high-pressure metamorphism. International Geology Review 47 (5), 439–456.

Hacker, B. R., Gerya, T. V., 2013. Paradigms, new and old, for ultrahigh-pressure tectonism. Tectonophysics 603, 79–88.

Holland, T., Powell, R., 1998. An internally consistent thermodynamic data set for phases of petrological interest. Journal of metamorphic Geology 16 (3), 309–343.

Hsü, K., 1974. Melanges and their distinction from olistostromes.

Hsü, K. J., 1968. Principles of melanges and their bearing on the franciscan-knoxville paradox. Geological Society of America Bulletin 79 (8), 1063–1074.

Isacks, B., Oliver, J., Sykes, L. R., 1968. Seismology and the new global tectonics. Journal of Geophysical Research 73 (18), 5855–5899.

Jamtveit, B., Moulas, E., Andersen, T. B., Austrheim, H., Corfu, F., Petley-Ragan, A., Schmalholz, S. M., 2018. High pressure metamorphism caused by fluid induced weakening of deep continental crust. Scientific reports 8 (1), 1–8.

Keller, L., Abart, R., Stünitz, H., De Capitani, C., 2004. Deformation, mass transfer and mineral reactions in an eclogite facies shear zone in a polymetamorphic metapelite (monte rosa nappe, western alps). Journal of Metamorphic Geology 22 (2), 97–118.

Lapen, T. J., Johnson, C. M., Baumgartner, L. P., Dal Piaz, G. V., Skora, S., Beard, B. L., 2007. Coupling of oceanic and continental crust during eocene eclogite-facies metamorphism: evidence from the monte rosa nappe, western alps. Contributions to Mineralogy and Petrology 153 (2), 139–157.

Le Bayon, R., de Capitani, C., Frey, M., 2006. Modelling phase–assemblage diagrams for magnesian metapelites in the system K_2O–FeO–MgO–Al_2O_3–SiO_2–H_2O: geodynamic consequences for the monte rosa nappe, western alps. Contributions to Mineralogy and Petrology 151 (4), 395.

Le Pichon, X., 1968. Sea-floor spreading and continental drift. Journal of Geophysical Research 73 (12), 3661–3697.

Lemoine, M., Bas, T., Arnaud-Vanneau, A., Arnaud, H., Dumont, T., Gidon, M., Bourbon, M., de Graciansky, P.-C., Rudkiewicz, J.-L., Megard-Galli, J., 1986. The continental margin of the mesozoic tethys in the western alps. Marine and petroleum geology 3 (3), 179–199.

Li, Z. H., Gerya, T. V., Burg, J.-P., 2010. Influence of tectonic overpressure on P-T paths of hp-uhp rocks in continental collision zones: thermomechanical modelling. Journal of Metamorphic Geology 28 (3), 227–247.
URL http://dx.doi.org/10.1111/j.1525-1314.2009.00864.x

Luisier, C., Baumgartner, L., Schmalholz, S. M., Siron, G., Vennemann, T., 2019. Metamorphic pressure variation in a coherent alpine nappe challenges lithostatic pressure paradigm. Nature communications 10 (1), 1–11.

Luisier, C., Baumgartner, L. P., Putlitz, B., Vennemann, T., 2021. Whiteschist genesis through metasomatism and metamorphism in the monte rosa nappe (western alps). Contributions to Mineralogy and Petrology 176 (1), 1–24.

Mancktelow, N., 1993. Tectonic overpressure in competent mafic layers and the development of isolated eclogites. Journal of Metamorphic Geology 11 (6), 801–812.

Marger, K., Luisier, C., Baumgartner, L. P., Putlitz, B., Dutrow, B. L., Bouvier, A.-S., Dini, A., 2019. Origin of monte rosa whiteschist from in-situ tourmaline and quartz oxygen isotope analysis by SIMS using new tourmaline reference materials. American Mineralogist: Journal of Earth and Planetary Materials 104 (10), 1503–1520.

McCarthy, A., Tugend, J., Mohn, G., Candioti, L., Chelle-Michou, C., Arculus, R., Schmalholz, S. M., Müntener, O., 2020. A case of ampferer-type subduction and consequences for the alps and the pyrenees. American Journal of Science 320 (4), 313–372.

Molnar, P., Lyon-Caen, H., 1988. Some simple physical aspects of the support, structure, and evolution of mountain belts. Processes in continental lithospheric deformation 218, 179–207.

Morgan, W. J., 1968. Rises, trenches, great faults, and crustal blocks. Journal of Geophysical Research 73 (6), 1959–1982.

Moulas, E., Burg, J.-P., Podladchikov, Y., 2014. Stress field associated with elliptical inclusions in a deforming matrix: Mathematical model and implications for tectonic overpressure in the lithosphere. Tectonophysics 631, 37–49.

Moulas, E., Podladchikov, Y. Y., Aranovich, L. Y., Kostopoulos, D., 2013. The problem of depth in geology: When pressure does not translate into depth. Petrology 21 (6), 527–538.

Moulas, E., Schmalholz, S. M., Podladchikov, Y., Tajčmanová, L., Kostopoulos, D., Baumgartner, L., 2019a. Relation between mean stress, thermodynamic, and lithostatic pressure. Journal of metamorphic geology 37 (1), 1–14.

Moulas, E., Sokoutis, D., Willingshofer, E., 2019b. Pressure build-up and stress variations within the earth's crust in the light of analogue models. Scientific reports 9 (1), 1–8.

Pawlig, S., 2001. Geological evolution of the monte rosa: constraints from geochronology and geochemistry of a talc kyanite chloritoid shear zone within the monte rosa granite (monte rosa nappe, italian western alps). Thesis.

Pawlig, S., Baumgartner, L., 2001. Geochemistry of a talc-kyanite-chloritoid shear zone within the monte rosa granite, val d'ayas, italy. Schweizerische mineralogische und petrographische Mitteilungen 81, 329–346.

Raymond, L. A., 1975. Tectonite and mélange—a distinction. Geology 3 (1), 7–9.

Raymond, L. A., 1984. Classification of melanges. Melanges: their nature, origin, and significance: Geological Society of America Special Paper 198, 7–20.

Reuber, G., Kaus, B. J., Schmalholz, S. M., White, R. W., 2016. Nonlithostatic pressure during subduction and collision and the formation of (ultra) high-pressure rocks. Geology 44 (5), 343–346.

Roda, M., De Salvo, F., Zucali, M., Spalla, M. I., 2018. Structural and metamorphic evolution during tectonic mixing: is the rocca canavese thrust sheet (italian western alps) a subduction-related mélange? Italian Journal of Geosciences 137 (2), 311–329.

Roda, M., Zucali, M., Regorda, A., Spalla, M. I., 2020. Formation and evolution of a subduction-related mélange: The example of the rocca canavese thrust sheets (western alps). GSA Bulletin 132 (3-4), 884–896.

Schenker, F. L., Schmalholz, S. M., Moulas, E., Pleuger, J., Baumgartner, L. P., Podladchikov, Y., Vrijmoed, J., Buchs, N., Müntener, O., 2015. Current challenges for explaining (ultra) high-pressure tectonism in the pennine domain of the central and western alps. Journal of Metamorphic Geology 33 (8), 869–886.

Schmalholz, S. M., Duretz, T., Hetényi, G., Medvedev, S., 2019. Distribution and magnitude of stress due to lateral variation of gravitational potential energy between indian lowland and tibetan plateau. Geophysical Journal International 216 (2), 1313–1333.

Schmalholz, S. M., Duretz, T., Schenker, F. L., Podladchikov, Y. Y., 2014a. Kinematics and dynamics of tectonic nappes: 2-d numerical modelling and implications for high and ultra-high pressure tectonism in the western alps. Tectonophysics 631, 160–175.

Schmalholz, S. M., Medvedev, S., Lechmann, S. M., Podladchikov, Y., 2014b. Relationship between tectonic overpressure, deviatoric stress, driving force, isostasy and gravitational potential energy. Geophysical Journal International 197 (2), 680–696.

Schmalholz, S. M., Podladchikov, Y. Y., 2013. Tectonic overpressure in weak crustal-scale shear zones and implications for the exhumation of high-pressure rocks. Geophysical Research Letters 40 (10), 1984–1988.

Schmalholz, S. M., Schenker, F. L., 2016. Exhumation of the dora maira ultrahigh-pressure unit by buoyant uprise within a low-viscosity mantle oblique-slip shear zone. Terra Nova 28 (5), 348–355.

Schmid, S. M., Fügenschuh, B., Kissling, E., Schuster, R., 2004. Tectonic map and overall architecture of the alpine orogen. Eclogae Geologicae Helvetiae 97 (1), 93–117.

Skora, S., Mahlen, N., Johnson, C. M., Baumgartner, L. P., Lapen, T., Beard, B. L., Szilvagyi, E., 2015. Evidence for protracted prograde metamorphism followed by rapid exhumation of the zermatt-saas fee ophiolite. Journal of Metamorphic Geology 33 (7), 711–734.

Spear, F. S., 1989. Petrologic determination of metamorphic pressure-temperature-time paths. Metamorphic Pressure-Temperature-Time Paths 7, 1–55.

Spear, F. S., Pattison, D. R., 2017. The implications of overstepping for metamorphic assemblage diagrams (MADs). Chemical Geology 457, 38–46.

Steck, A., Masson, H., Robyr, M., 2015. Tectonics of the monte rosa and surrounding nappes (switzerland and italy): Tertiary phases of subduction, thrusting and folding in the pennine alps. Swiss Journal of Geosciences 108 (1), 3–34.

Tajčmanová, L., Podladchikov, Y., Powell, R., Moulas, E., Vrijmoed, J., Connolly, J., 2014. Grain-scale pressure variations and chemical equilibrium in high-grade metamorphic rocks. Journal of Metamorphic Geology 32 (2), 195–207.

Trümpy, R., 1975. Penninic-austroalpine boundary in the swiss alps: a presumed former continental margin and its problems. American Journal of Science 275 (A), 209–238.

Vaughan-Hammon, J. D., Luisier, C., Baumgartner, L. P., Schmalholz, S. M., 2021. Peak alpine metamorphic conditions from staurolite bearing metapelites in the monte rosa nappe (central european alps) and geodynamic implications. Journal of Metamorphic Geology n/a (n/a).

URL https://onlinelibrary.wiley.com/doi/abs/10.1111/jmg.12595

Wakabayashi, J., 2015. Anatomy of a subduction complex: Architecture of the franciscan complex, california, at multiple length and time scales. International Geology Review 57 (5-8), 669–746.

Warren, C., 2013. Exhumation of (ultra-) high-pressure terranes: concepts and mechanisms. Solid Earth 4 (1), 75–92.

Warren, C., Beaumont, C., Jamieson, R. A., 2008. Modelling tectonic styles and ultra-high pressure (uhp) rock exhumation during the transition from oceanic subduction to continental collision. Earth and Planetary Science Letters 267 (1-2), 129–145.

Wheeler, J., 2018. The effects of stress on reactions in the earth: sometimes rather mean, usually normal, always important. Journal of Metamorphic Geology 36 (4), 439–461.

CHAPTER 2

Alpine peak pressure and tectono-metamorphic history of the Monte Rosa nappe: evidence from the cirque du Véraz, upper Ayas valley, Italy

Joshua D. Vaughan-Hammon[1], Cindy Luisier[2], Lukas P. Baumgartner[1], Stefan M. Schmalholz[1]

[1]Institut des Sciences de la Terre, University of Lausanne, Lausanne, Switzerland.

[2]Univ Rennes, CNRS, Géosciences Rennes UMR 6118, Rennes, France.

Abstract

The Monte Rosa nappe consists of a wide range of lithologies that record conditions associated with peak Alpine metamorphism. While peak temperature conditions inferred from previous studies largely agree, variable peak pressures have been estimated for the Alpine high-pressure metamorphic event. Small volumes of whiteschist lithologies with the assemblage chloritoid + phengite + talc + quartz record peak pressures up to 0.6 GPa compared to associated metapelitic and metagranitic lithologies, which yield a peak pressure of *c.* 1.6 GPa. The reason for this pressure difference is disputed, and proposed explanations include tectonic mixing of rocks from different burial depths (mélange) or local deviations of the pressure from the lithostatic value caused by heterogenous stress conditions between rocks of contrasting mechanical properties.

We present results of detailed field mapping, structural analysis and a new geological map for a part of the Monte Rosa nappe exposed at the cirque du Véraz field area (head of the Ayas valley, Italy). Results of the geological mapping and structural analysis shows the structural coherency within the western portions of the Monte Rosa nappe. This structural coherency falsifies the hypothesis of a tectonic mélange as reason for peak pressure variations. Structural analysis indicates two major Alpine deformation events, in agreement with earlier studies: (1) north-directed nappe emplacement, and (2) south-directed backfolding.

We also analyze a newly discovered whiteschist, which is located at the intrusive contact between the Monte Rosa metagranite and surrounding metapelites. This location is different to previous whiteschist occurences, which were entirely embedded within metagranite. Thermodynamic calculations using metamorphic assemblage diagrams (MAD) resulted in 2.1 ± 0.2 GPa and 560 ± 20°C for peak Alpine metamorphic conditions. These results agree with metamorphic conditions inferred for previously investigated nearby whiteschist outcrops embedded in metagranite. The new results, hence, confirms the peak pressure differences between whiteschists and the metagranite and metapelite. To better constrain the prograde pressure-temperature history of the whiteschist, we compare Mg zoning in chloritoid with Mg zoning predicted by fractional crystallization pseudo-section modelling for several

hypothetical pressure-temperature paths. In order to reach a *c.* 0.6 GPa higher peak pressure, our results suggest that the whiteschist likely deviated from the prograde burial path recorded in metapelite and metagranite lithologies. However, the exact conditions at which the whiteschist pressure deviated are still contentious due to the strong temperature dependency of Mg partitioning in whiteschist assemblages. Our pseudo-section results suggest at least that there was no dramatic isothermal pressure increase recorded in the whiteschist.

2.1   Introduction

The complex history of Alpine tectonic activity can be observed in the Monte Rosa region of the Central Alps (Figure 2.1). Here, the former Piedmont oceanic domain separates the continental units of the former Europe-derived southern Briançonnais margin (Monte Rosa nappe) from the Sesia-Dent Blanche units derived fromthe Adriatic margin (Figure 2.1) (Dal Piaz, 2001; Dal Piaz et al., 2001; De Graciansky et al., 2011; Steck et al., 2015). A spectacular region to view the present-day juxtaposition of these geological domains is found at the grand cirque du Véraz at the head of the Ayas valley, Aosta region, Italy (Figure 2.1b and 2.2). The area exposes portions of the Penninic nappe stack involving the crustal rocks of the former Briançonnais domain: the Monte Rosa nappe, consisting of Variscan and older paragneisses intruded by Permian-aged granite (269 ± 4 Ma, Pawlig and Baumgartner, 2001). Structurally above the Monte Rosa nappe, to the north, is the former Piedmont oceanic domain (Zermatt Saas and Combin units), comprising remnants of an oceanic domain of predominantly serpentinites (e.g. Angiboust et al., 2009; Lapen et al., 2007; McCarthy et al., 2020) as well as eclogitized metagabbros and metabasalts with locally well-preserved pillow structures, making up most of the Breithorn plateau including the Pollux, Rocca Nera and Klein Matterhorn peaks (Figure 2.1b). The former Piedmont oceanic domain was bounded by hyper-extended magma-poor passive margins (e.g. Decandia, 1972; Manatschal and Müntener, 2009), but the size and geodynamic characteristics of the former Piedmont oceanic domain are disputed. Interpretations range from a wider ocean ($> c.$ 500 km) with mature oceanic crust having typically a thickness of ca. 6 km (e.g. Stampfli et al., 1998) to a narrower oceanic domain ($<$ $c.$ 300 km) with only "embryonic" oceanic crust having a thickness of only a few kilometers due to ultra-slow spreading (e.g. McCarthy et al., 2020). Finally, continuing northwards and structurally up the sequence, the Zermatt-Saas unit is thrust by the Adria-derived continental unit of the Dent-Blanche nappe (Bucher et al., 2003a; Compagnoni, 1977; Dal Piaz, 1999; Manzotti et al., 2017), that comprises the spectacular Matterhorn peak.

Here, we present a detailed geological map and cross-section of the upper portions of the Monte Rosa nappe exposed at the grand cirque du Véraz at the head of the Ayas valley, Italy

(Figure 2.2). The overall scope of this study aims to outline the key lithologies and structural features found here, not only through our investigations but also from work undertaken in the last century in the area (Bearth, 1952, 1953; Chopin, 1984; Dal Piaz et al., 2004, 2001; Darbellay, 2005; Dessimoz, 2005; Giacomazzi, 2017; Kramer, 2002; Luisier et al., 2019, 2021; Marger et al., 2019; Pawlig, 2001; Pawlig and Baumgartner, 2001; Vaughan-Hammon et al., 2021). The structural evolution of the Monte Rosa nappe exposed at the grand cirque du Véraz is also compared with other studies throughout the nappe (e.g. Keller et al., 2004; Keller and Schmid, 2001; Kramer, 2002; Steck et al., 2015). Furthermore, due to the variety of lithologies and structures found here, as well as the complex poly-metamorphic history recorded, encompassing both Variscan and Alpine orogenesis, we outline a comprehensive geological history for the Monte Rosa nappe. Specific attention is given to the tectono-metamorphic history during Alpine orogenesis.

The Monte Rosa basement exposed at the cirque du Véraz also exhibits variable metamorphic conditions, specifically during peak Alpine high-pressure metamorphism. These variable metamorphic conditions were highlighted by the discussions on peak pressure (P) estimates (Luisier et al., 2019; Vaughan-Hammon et al., 2021), but also published temperature (T) estimates are highly variable. A wide range of calculated peak metamorphic conditions has prompted the discussion concerning variations in estimated peak metamorphic pressures in the Monte Rosa nappe. Published P estimates range between 1.2 and 2.7 GPa and T estimates between 490 and 640°C (Borghi et al., 1996; Chopin, 1984; Dal Piaz and Lombardo, 1986; Ferrando et al., 2002; Gasco et al., 2011; Keller et al., 2004; Lapen et al., 2007; Le Bayon et al., 2006). The maximum metamorphic P conditions recorded for the Monte Rosa nappe primarily involve minor volumes of talc, chloritoid, phengite and quartz lithologies termed 'whiteschists' at 2.4 GPa (Le Bayon et al., 2006) and $c.$ 2.2 GPa (Luisier et al., 2019), as well as mafic boudins indicating $c.$ 2.7 GPa (e.g. Gasco et al., 2011). In the cirque du Véraz, recent work has highlighted large disparities in peak Alpine P between whiteschist (2.2 GPa) and metagranite (1.4 to 1.6 GPa) (Luisier et al., 2019) as well as metapelitic (1.6 ± 0.2 GPa) assemblages (Vaughan-Hammon et al., 2021), resulting in a potential P difference, ΔP, of 0.6 ± 0.2 GPa for the same peak Alpine metamorphic event.
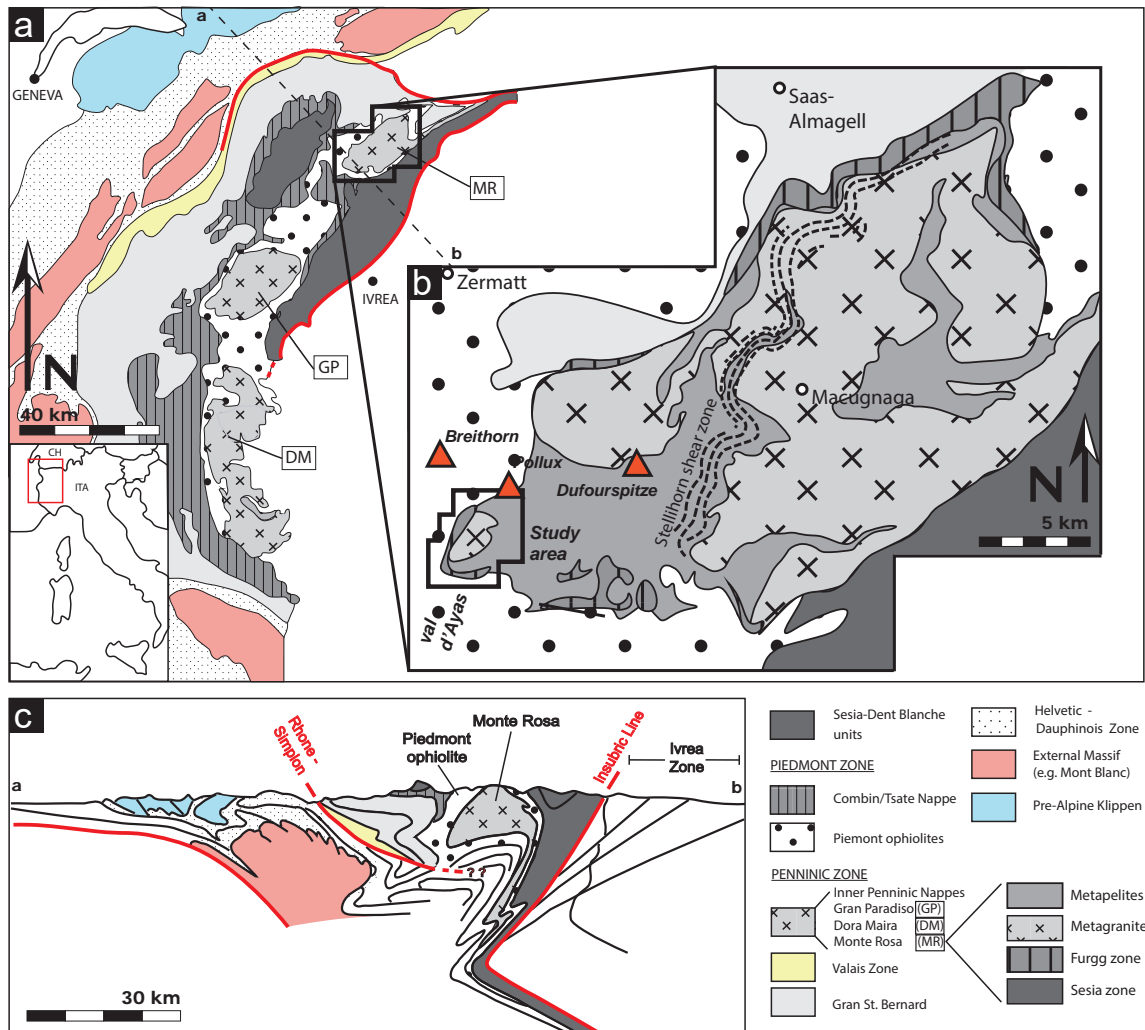
Figure 2.1: (a) Simplified geological tectonic map of the Western Alpine chain; adapted from Beltrando et al. (2010). (b) Simplified geological map of the Monte Rosa nappe; modified after Steck et al. (2015). (c) Simplified tectonic cross-section of the Western Alpine chain; modified after Steck et al. (2015).

Five possible hypotheses have been proposed to explain such P differences: (a) assemblages recording lower P were unable to equilibrate at high P conditions due to sluggish kinetics, (b) high P indicators were lost during to retrogression, (c) differences in thermodynamic databases, solid-solution model and model assumptions (e.g. Fe^{3+} content or H_2O water activity) between studies result in artificial ΔP, (d) tectonic mixing of rocks from different maximal Alpine burial depths, i.e. tectonic mélange (proposed for the Internal Penninic units

of the western Alps e.g. Dora Maira (Dobretsov, 1991)), and (e) the presence of local P deviations from the lithostatic value caused by differential stresses.

Recent studies by Luisier et al. (2019) and Vaughan-Hammon et al. (2021) suggest to exclude (a) sluggish kinetics (e.g., because of measurements of high H_2O content in phengite and presence of prograde hydrous minerals, such as phengite and zoisite in plagioclase pseudomorphs in the metagranite), (b) retrogression of high P minerals (e.g., because of observations of the preservation of the original lamellar twinning in igneous plagioclase by albite pseudomorphing igneous plagioclase in metagranites) and (c) differences in thermodynamic databases (e.g., because metagranite and metapelite provide the same, within error, peak P estimates of $c.$ 1.6 GPa using the same database) as reasons for the observed metamorphic P variations between whiteschist ($c.$ 2.2 GPa) and metapelite as well as metagranite (both $c.$ 1.6 GPa). These studies also suggest, based on local field observations, that (d) tectonic mélange is unlikely the reason for the P variations. One aim of our study is to thoroughly test hypothesis (d) with detailed geological mapping and to clarify whether the Monte Rosa nappe in the cirque du Véraz is a tectonic mélange or not. The suggested exclusion of explanations (a), (b) and (c) highlights the possibility that the reported peak P variations could have been caused by (e) local P deviations from the lithostatic P. Another aim of this study is to provide more estimates of Alpine peak P by analyzing a newly discovered whiteschist and to test whether the reported peak P variations between whiteschist and metagranite/metapelite persist.

For clarity, we briefly provide here some definitions and fundamental characteristics of stress and P in the context of geodynamics. For a lithostatic state of stress, all three principal stresses are identical and are controlled only by the gravitational acceleration, density and thickness of the overlying rock (e.g. Turcotte and Schubert, 2002). The mean stress of these identical principal stresses is, hence, equal to these principal stresses and is commonly termed lithostatic P (e.g. Turcotte and Schubert, 2002). It is well established that the state of stress cannot be lithostatic everywhere in the crust, because otherwise (i) discrete continental plates, (ii) continental plateaus or (iii) mountains would not exist over geological time scales (e.g. Jeffreys, 1937; Molnar and Lyon-Caen, 1988; Schmalholz et al., 2014; Turcotte and Schubert, 2002). To maintain lateral topographic variations of the Earth surface, for example between

continents and oceans or between mountains and neighboring lowlands, differential stresses
(up to $c.$ 100 MPa in average vertically across the lithosphere, (Schmalholz et al., 2019))
are required, which means that the three principal stresses are not identical (e.g. Molnar and
Lyon-Caen, 1988; Schmalholz et al., 2019, 2014; Turcotte and Schubert, 2002). Differential
stresses are also intrinsically linked to plate driving forces, e.g. ridge push and slab pull, and
are, hence, essential to drive continental collision and mountain building. For a differential
state of stress, the P, or mean stress, is typically not the lithostatic P since usually the
vertical principal stress is close to the lithostatic P, but one horizontal principal stress is
either significantly smaller (e.g. during extension) or larger (e.g. during compression) than the
lithostatic P (e.g. Sibson, 1974). Hence, for a differential state of stress, the P (mean stress)
is typically different to the lithostatic P. The P for a differential state of stress is sometimes
termed dynamic P (e.g. Gerya, 2015). If this dynamic P is larger than the lithostatic P,
then the P difference is commonly termed tectonic overpressure, and if this dynamic P is
smaller than the lithostatic P, the P difference is termed tectonic underpressure (e.g. Gerya,
2015; Mancktelow, 2008). In summary, a lithostatic state of stress is physically impossible
everywhere within the Earth's crust, especially during collisional mountain building. The
main questions concerning deviations from the lithostatic P are: how large are these P
deviations locally in the crust, and are these P deviations observable in the metamorphic
rock record?

Here, we aim to contribute to the ongoing discussion of peak Alpine P variations recorded be-
tween whiteschist, Monte Rosa metagranite and metapelitic lithologies, by analyzing a newly
discovered outcrop of whiteschist in the area. Detailed petrological investigations of two sam-
ples of whiteschist from this new outcrop have been undertaken, enabling a further constraint
on the peak Alpine metamorphic conditions incurred by the Monte Rosa nappe. We compare
observed zoning of Mg in chloritoid whiteschists with Mg zoning predicted by fractional crys-
tallization pseudo-section modelling for a range of prograde pathways to constrain the PT
history during peak Alpine metamorphism. We test whether the newly discovered whiteschist
confirms, or not, the estimated peak P of $c.$ 2.2 GPa for a different whiteschist outcrop Luisier
et al. (2019), which is located $c.$ 100 m away from the newly discovered outcrop.

2.2 Petrological overview

2.2.1 Geological setting

The Monte Rosa "massif" or nappe represents one amongst the three major internal crystalline massifs of the Western and Central Alpine domain, along with the Dora Maira and Gran Paradiso massifs (Figure 2.1a). The Monte Rosa nappe consists of a pre-Variscan suite, which became intruded by Permian-age granitic to granodiorite bodies (269 ± 4 Ma, Pawlig and Baumgartner, 2001) which we refer to as Monte Rosa granitoids, and was subsequently incorporated into the Alpine orogeny (Figure 2.1b). A geological map of the area is presented in Figure 2.2 showing the position and separations of the main lithological units within the western portions of the Monte Rosa nappe exposed at the grand cirque du Véraz (upper Ayas valley, Italy). A detailed map of the upper Ayas valley has also been presented in (Dal Piaz et al., 2004) with focus on Zermatt-Saas ophiolites in the western portions of the valley. The following section outlines the main field relations and petrological characteristics of lithologies belonging to the Monte Rosa nappe. The structural features of these lithologies are summarized in section 2.3.

2.2.2 Lithological descriptions

2.2.2.1 Polymetamorphic basement complex

The paragneisses of the Monte Rosa nappe exhibit a long metamorphic history. These pre-Variscan metasediments consist of complex layered gneisses of predominantly alternating garnet-biotite and quartz-plagioclase rich layers (Figure 2.3a). Areas less affected by Alpine tectonic activity, in particular the eastern Perazzispétz ridge and the area south of Rifugio Guide d'Ayas (Figure 2.2), preserve a relict assemblage of sillimanite (mostly replaced by kyanite), cordierite, biotite and garnet + quartz, K-feldspar, muscovite and plagioclase (Bearth, 1952; Dal Piaz and Lombardo, 1986). This assemblage is related to a Variscan metamorphic event in the area (Bearth, 1952, 1953; Dal Piaz and Lombardo, 1986; Engi et al., 2001; Vaughan-Hammon et al., 2021). Petrological investigations of these assemblages reveal
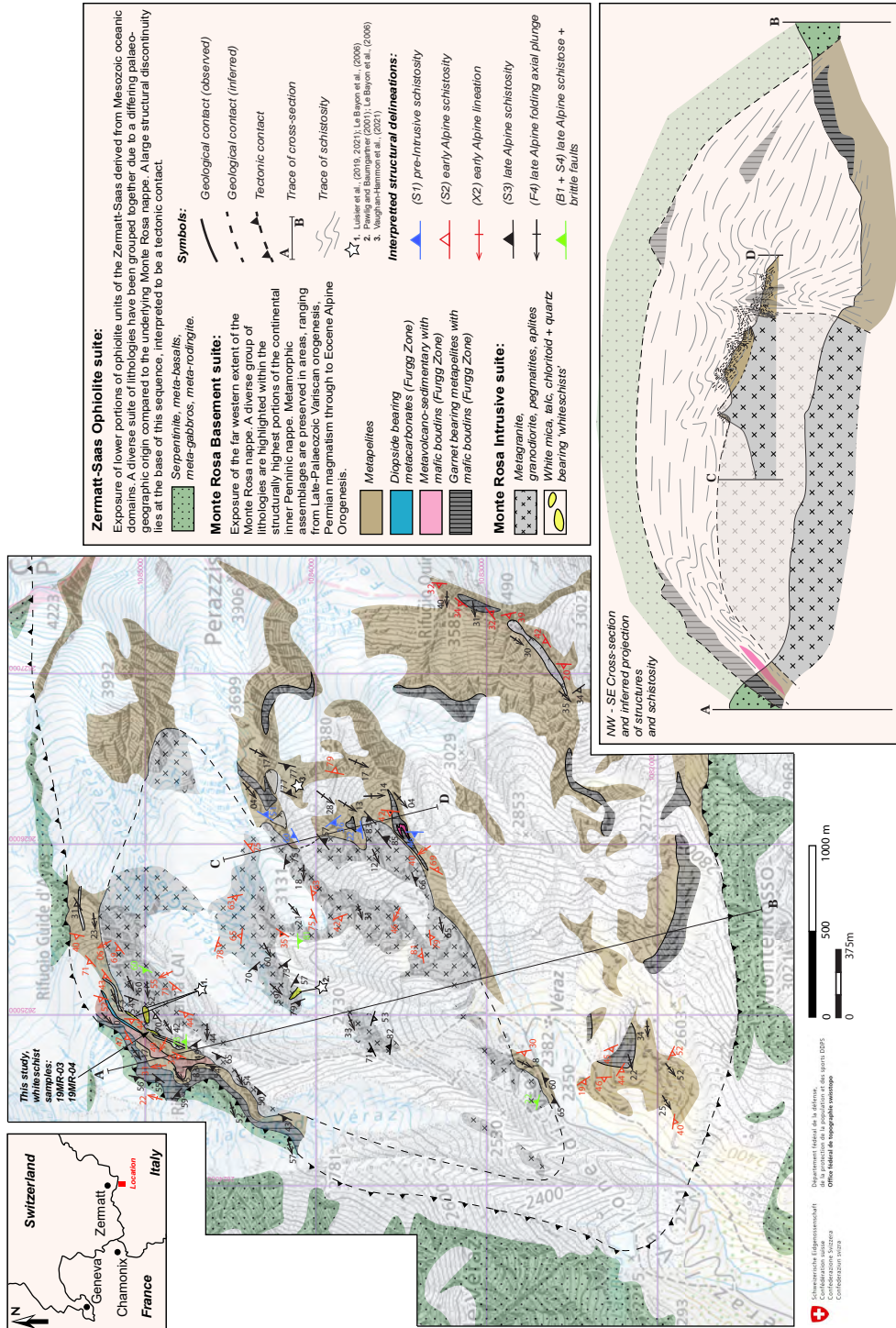
Figure 2.2: Caption on next page.

Figure 2.2: Geological map of exposure and cross-section of the Monte Rosa nappe and Zermatt-Saas nappe at the upper val d'Ayas, Italy. Location of previous studies on peak Alpine metamorphism in the area are indicated (white stars).

a high-T metamorphic event related to an upper Amphibolite facies sillimanite-K-feldspar metamorphism (*c.* 700°C/0.3-0.6 GPa) associated with Variscan metamorphism dated at *c.* 330 Ma (Engi et al., 2001). Figure 2.3b shows large relict garnets, associated with pre-intrusive high-T Variscan metamorphism.

Migmatite textures are encountered throughout the polymetamorphic Monte Rosa basement (Figure 2.3c). These migmatites occur near the post-Variscan intrusion of the Monte Rosa granite during the Permian, visible within areas that have experienced little to no Alpine overprinting deformation or metamorphism. We associate partial melting in this area of the nappe with intrusion of the Permian-age granitic body. Also associated with the thermal contact of the Monte Rosa intrusive bodies are spatially unique contact metamorphic assemblages. Areas less affected by deformation post-dating granitic intrusion (i.e. Perazzispétz ridge and the area south of Rifugio Guide d'Ayas, Figure 2.2), exhibit textures of large statically grown minerals that have later been pseudomorphosed (Figure 2.3d). Recent work by Vaughan-Hammon et al. (2021) demonstrated that these pseudomorphs contain chloritoid, white mica and staurolite. This assemblage likely represents a spatially unique high-pressure Alpine overprint of former contact metamorphic andalusite (Figure 2.3d). North of the Mezzalama Rifugio, the metasediments in contact with the Permian granite are transformed into hornfels, and in some places, coarse-grained tourmaline is observed in former hornfels.

Associated with the Monte Rosa Variscan paragneisses are structural levels that contain diverse lithologies exhibiting a complex deformation history. This is typically for the so-called Furgg zone that represents a high-strain zone following the contact of the Monte-Rosa nappe with the overlying ophiolites (Bearth, 1952, 1953; Jaboyedoff et al., 1996; Keller and Schmid, 2001; Steck et al., 2015) and typically contains mafic boudins whose geochemistry differs from that of the neighboring Piedmont ophiolites (Kramer et al., 2003) and which were formerly locally intruding Mesozoic metasediments (Jaboyedoff et al., 1996, , their Figure 5) (Figure 2.2). For clarity, we have subdivided Furgg Zone lithologies in the map into three
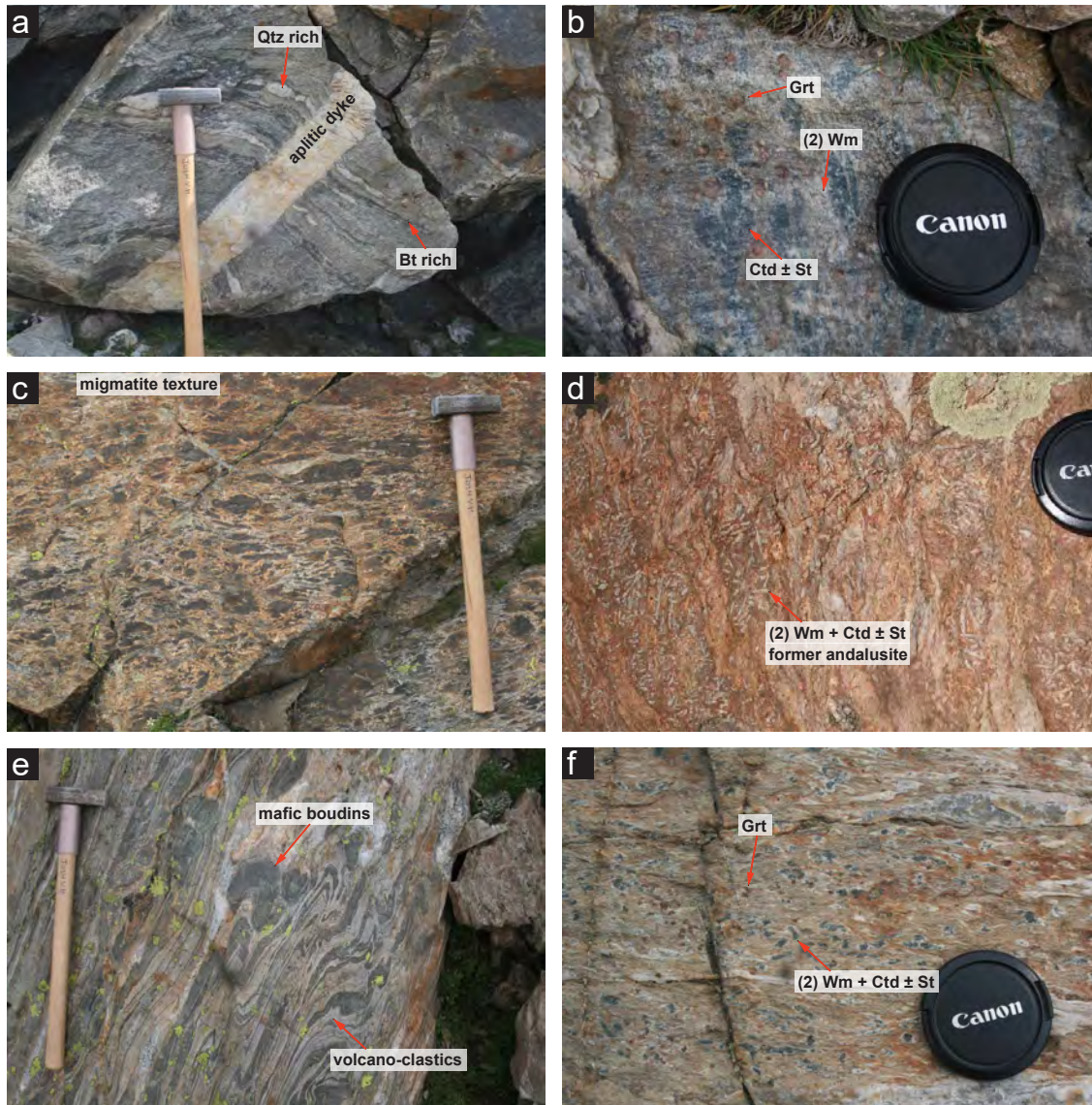
Figure 2.3: Mesoscopic aspect of some key lithologies belonging to the Monte Rosa nappe: a) layered gneiss with quartz and biotite rich bands, and younger cross-cutting aplitic dyke. b) Metamorphic assemblages: (i) large Grt formed during high temperature-low P Variscan metamorphism, and (ii) Wm + Ctd + St indicating peak conditions during the Alpine high P event. c) Migmatitic textures of basement lithologies in close proximity to granitic intrusion indicating partial melting due to the intrusion of the Monte Rosa granite. d) Wm + Ctd + St pseudomorphs after former contact metamorphic andalusite formed during the peak Alpine high P event. e) Complexly folded mafic boudins in a matrix of coarse-grained Plg + Qz volcanoclastic metasediments belonging to the Furgg zone series. f) Metamorphic assemblages: (i) large Grt formed during high temperature-low pressure Variscan metamorphism, and (ii) Wm + Ctd + St belonging to peak Alpine high P event.

sub-units: 1) garnet metapelites containing mafic boudins, 2) volcano-sedimentary layers containing mafic boudins (Figure 2.3e), and 3) metacarbonates (Figure 2.2). Particularly, north of the Mezzalama Rifugio and sporadically throughout the entire Monte Rosa nappe, outcrops of volcano-sedimentary horizons containing coarse grained plagioclase and quartz are observed. These are complexly folded with amphibolite-rich boudins (Figure 2.3e). North of the Mezzalama Rifugio, lenses and elongated bodies of metacarbonates consisting of calcite, diopside, garnet and pseudomorphs after wollastonite, as well as quartz rich meta-arkose are observed. These metacarbonates occur as extremely long and thin horizons or as boudins due to subsequent tectonic reworking (Figure 2.2). In this study, we do not elaborate further on the Furgg zone. We separate the Monte Rosa paragneisses from the Furgg zone based on outcrop investigation and the above mentioned lithological criteria (garnet metapelites with mafic boudins, volcano-sedimentary deposits with mafic boudins, and metacarbonates), and our interpreted geological history is based on that proposed in previous studies (e.g. Dal Piaz and Ernst, 1978; Dal Piaz, 2001; Dessimoz, 2005; Giacomazzi, 2017; Jaboyedoff et al., 1996; Keller and Schmid, 2001; Kramer, 2002; Steck et al., 2015).

Indicators of high-pressure metamorphism exist related to Alpine orogenesis are found throughout the Monte Rosa nappe. These consist of assemblages of phengite + paragonite + chloritoid + staurolite + garnet + kyanite + quartz in metapelites (1.6 ± 0.2 GPa and 585 ± 20°C; (Vaughan-Hammon et al., 2021)) (Figure 2.3f), and omphacite, glaucophane, garnet, phengite, lawsonite, rutile, and quartz in metabasic boudins of the Furgg zone that have not been retrogressed at amphibolite grade (1.3-2.7 GPa and 535-620°C) (Ferrando et al., 2002; Gasco et al., 2011) (Figure 2.3e). However, preserved eclogitic metabasic boudins are extremely uncommon in the mapped area..

Chlorite bearing domains are also common within the paragneiss basement, and are predominantly confined to post-peak, late Alpine shear zones (more descriptions within section 2.3). Late Alpine brittle fractures are typically infilled with albite and/or quartz.

2.2.2.2   Permian metagranite intrusive suite

In areas of low strain, the original intrusive porphyritic granite as well as leucocratic regions can be observed, consisting of coarse grained ($>$ 10 cm) K-feldspar phenocrysts, quartz, biotite, plagioclase and muscovite (Figure 2.4a). Remnants of basement metapelites can be observed as xenoliths within the granite, structures within these xenoliths indicate a younger complex deformation history prior to Permian intrusion (Figure 2.4b). Granodioritic enclaves are also observed throughout the granitic complex. Associated with the granite intrusion are a series of younger leucocratic dykes, cross-cutting both the granite and basement metapelites (Figure 2.4a and c). Aplitic dykes are most commonly consist of medium grained quartz, feldspar $\pm$ tourmaline. Coarse grained pegmatitic dykes are less common and consists of K-feldspar, white mica, quartz, tourmaline $\pm$ plagioclase $\pm$ garnet (Figure 2.4a and c).

Alpine high-pressure relicts can be observed in metagranite lithologies, consisting of a fine-grained assemblage of zoisite + albite $\pm$ phengite, pseudomorphosing igneous plagioclase at *c.* 1.4 GPa and 540-600°C (Luisier et al., 2019). Unique assemblages of chloritoid, talc, phengite and quartz $\pm$ garnet related to Alpine high P metamorphism are observed in whiteschists (Chopin, 1984; Luisier et al., 2019; Pawlig and Baumgartner, 2001). These unique assemblages are exposed towards the north and south-east of the Mezzalama Rifugio, and it is here, in the grand cirque du Véraz, where we find the largest concentrations of these whiteschists in the Monte Rosa nappe (Figure 2.2 and 2.4d). The whiteschists are either fully embedded in the metagranite (Figure 2.4d), or appear as lenses at the contact between the Monte Rosa metagranite and basement paragneisses. These whiteschists have been the focus of many studies characterizing their provenance, age and extent of metamorphic alteration (Chopin, 1984; Le Bayon et al., 2006; Marger et al., 2019; Pawlig, 2001; Pawlig and Baumgartner, 2001). Extensive textural and chemical analysis of these whiteschist bodies and analysis of alteration through a shear zone reveal a late magmatic, hydrothermal metasomatic (Mg-enriched), chlorite-sericite schist protolith (Luisier et al., 2019, 2021; Marger et al., 2019; Pawlig and Baumgartner, 2001). Whiteschist lithologies show zoning patterns related to initial metasomatic alteration and subsequent retrogression after peak Alpine conditions; the
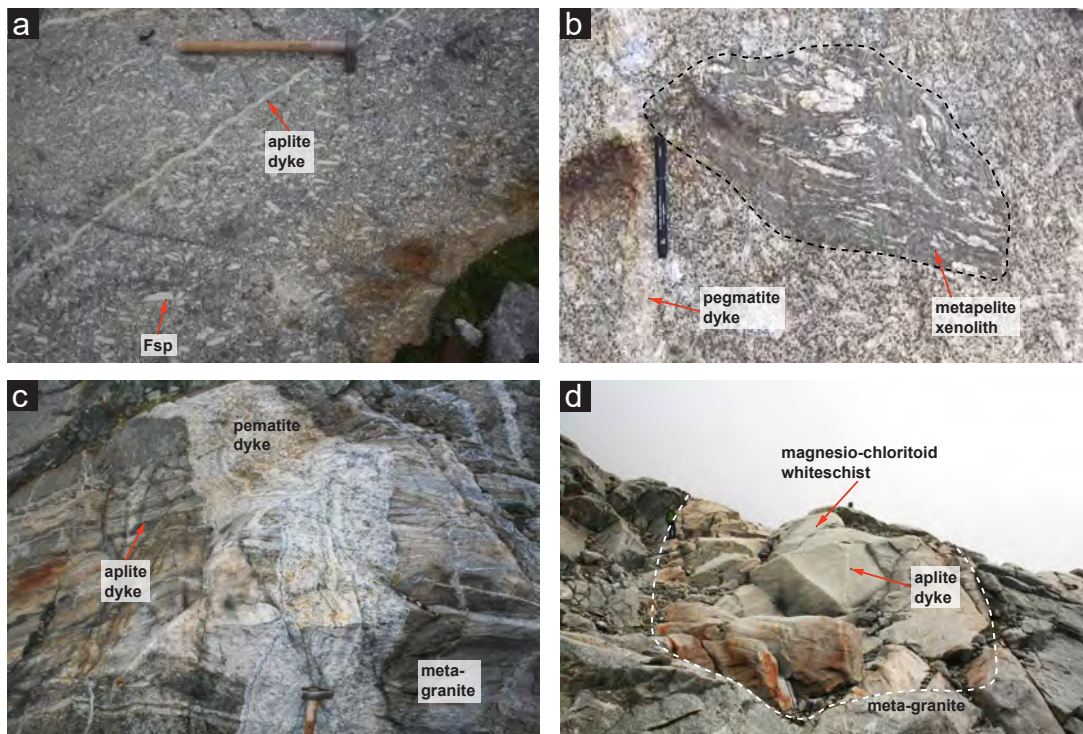
Figure 2.4: Mesoscopic aspect of key examples regarding intrusive contacts and structures belonging to the Monte Rosa nappe: a) undeformed metagranite exhibiting magmatic textures with large K-feldspar phenocrysts, as well as a younger cross-cutting aplitic dyke. b) Xenolith of Monte Rosa metapelitic Variscan basement exhibiting complex folding, enclosed within the metagranite. c) Cross-cutting relationships of late magmatic dykes within Monte Rosa metagranite and metapelite lithologies (pegmatites are usually the youngest intrusive bodies). d) Whiteschist indicating peak Alpine metamorphism enclosed within Monte Rosa metagranite lithologies (note aplitic dykes cross-cutting body- attesting to a granitic protolith).

studies of Luisier et al., (2021 and 2018 PhD thesis) and Pawlig and Baumgartner (2001) expand more upon this. The peak metamorphic conditions obtained from these whiteschist bodies during Alpine orogenesis has been recently estimated at 2.2 ± 0.2 GPa at 540-600°C (Luisier et al., 2019).

2.3 Structural observations

The Monte Rosa nappe records a complex structural history. Here we discuss 4 main deformation phases observed at the cirque du Véraz. Here we discuss 4 main deformation phases

observed at the cirque du Véraz (S1 + F1, S2 + F2 + X2, S3 + F4 + X3, and S4 + B1), whereby S(n) corresponds to the resulting planar fabric such as schistosity, X(n) corresponds to a lineation, and F(n) corresponds to a folding phase, and B1 is a brittle planar fabric. All deformation phases except D1 (pre-intrusion of Permian granites) are related to Alpine orogenesis. Representative orientations and distributions of these structures are presented in the geological map of Figure 2.2. We will discuss and compare these structures with previous studies and regional observations in section 2.5.2. (Keller et al., 2004; Keller and Schmid, 2001; Kramer, 2002; Pawlig and Baumgartner, 2001; Steck et al., 2015).

A wide range of deformation intensities can be observed within the Monte Rosa metagranite and Variscan basement of the Monte Rosa nappe. These are best observed within the metagranite due to a spatially homogenous lithology and a presumably similar rheology, compared to the lithologically diverse and thus rheologically complex paragneiss basement. Figure 2.5 demonstrates the progressive increase in strain within the metagranites from: (a) weakly deformed porphyritic texture (original feldspar observed) to (b) augen gneiss to (c) banded gneiss, and to (d) proto- and mylonite textures.
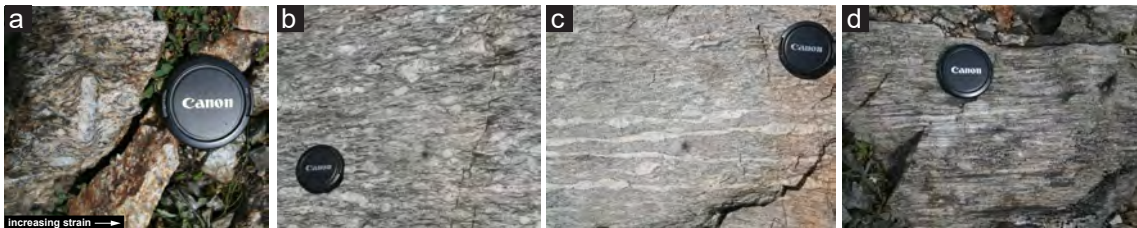
Figure 2.5: Compilation of field images illustrating the strain gradients in metagranitic lithologies of the Monte Rosa nappe: a) weakly deformed porphyritic Monte Rosa metagranite showing biotite wrapping around a large partially recrystallized K-feldspar phenocryst. b) Augen gneissic texture of K-feldspar phenocrysts and weakly interconnected biotite schistosity. c) Formation of banded gneissic texture with highly strained and connected K-feldspar phenocrysts. d) Proto-mylonitic texture with highly strained K-feldspar horizons, presumably former phenocrysts.

2.3.1 Pre-intrusive ductile deformation: D1

The most ideal areas within the metapelitic basement to observe the oldest structures are areas that preserve an intact igneous contact, with minimal post-intrusion deformation (northeast of Mezzalama Rifugio and Perazzispétz, Figure 2.2). These areas enable constraints on the relative ages of deformation, in order to distinguish pre-intrusive basement structures. Figure 2.6a shows a well preserved original igneous contact marked with a late aplitic dyke, demonstrating the complex deformation already present prior to the Permian-aged granitic intrusion. Superposition of several complex phases of folding can be observed in refolded isoclinal quartz veins (Figure 2.6a). S1 and F1 define phases of schistosity development and folding events that coincide with pre-intrusive tectonic activity. We do not elaborate further on these early pre-intrusions structures of pre-Alpine age since this is not the focus of this study.

The Furgg zone (metacarbonates, metamafics and metavolcanoclastics) displays a complex high strain complex history (Figure 2.3e and 2.6c). Earlier studies indicate that the Furgg zone represents a sedimentary cover of the Monte Rosa nappe.

2.3.2 Ductile deformation: D2

The first phase of post-intrusion deformation is predominantly seen as ductile S2 shear zones and affects both the basement complex and the metagranite (including whiteschists) (Figures 2.10a, 2.6b and c). This deformation is typically associated with a ductile foliation indicating a top-N sense of shear and northward directed lineation X2 (Figures 2.6b, c, 2.8a and 2.9a). North of the Mezzalama Rifugio, we can observe top-N shearing of aplitic dykes that remained undeformed in the metagranite and become progressively sheared within the metapelite corresponding to drag into shear zones (Figure 2.6d). Equally, increasing strain can produce isoclinal F2 folding of dykes, which is associated and parallel to S2 features (Figure 2.6c and 2.7e).

The metamorphic characteristics of this deformation event typically post-date high P phases (deformed high P garnet + white mica in metapelites and metagranites, as well as whiteschists
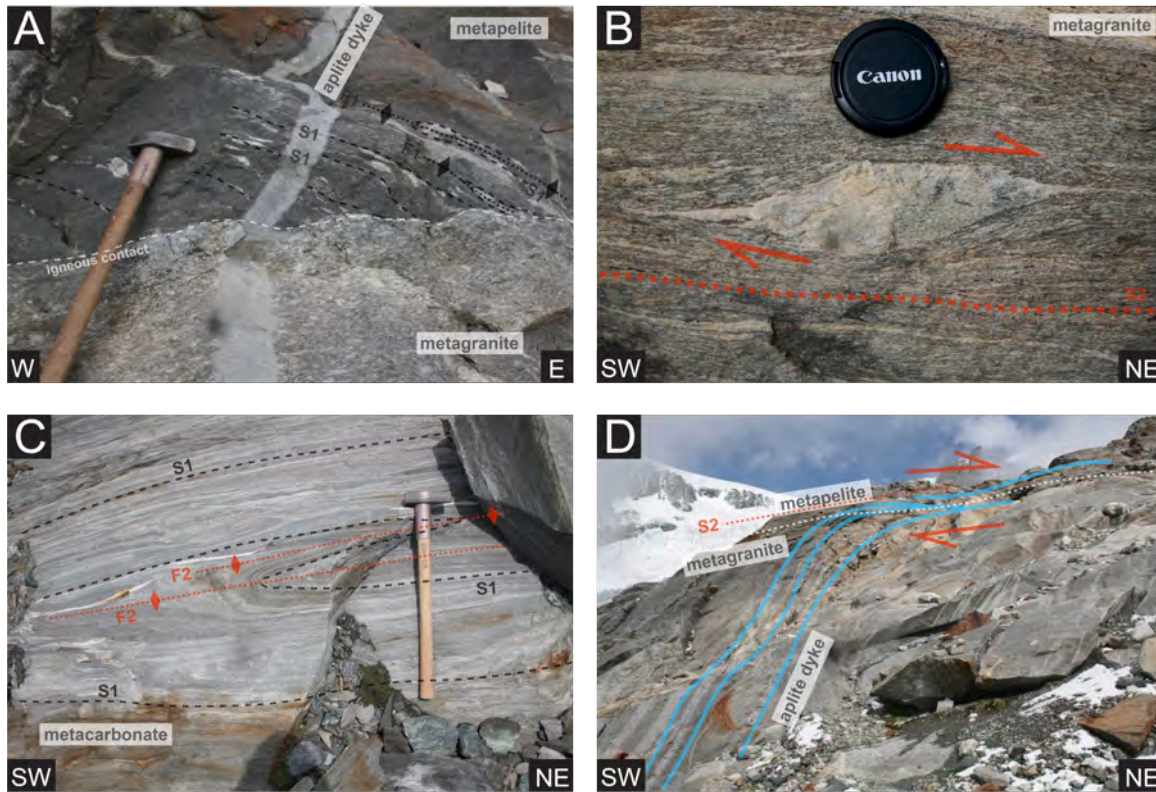
Figure 2.6: Representative field images of structural features in the Monte Rosa nappe: a) magmatic contact between metagranitic and metapelitic lithologies preserving pre-intrusive Variscan structures such as schistosity (S1) and refolded isoclinal folding (F1). b) Deformed aplitic dyke within Monte Rosa metagranite lithologies preserving S2 schistosity and dextral, top-N shear sense. c) Isoclinally folded S1 schistosity of metacarbonate lithologies within the Monte Rosa basement with a dextral, top-N shear sense. d) Large scale parallelization of aplitic dykes from undeformed Monte Rosa metagranite into rheologically weaker metapelites with a dextral, top-N shear related to F2 folding.

from this study). A greenschist overprint is present also, which is manifested as chlorite + epidote shear zones within the metagranite.

2.3.3 Ductile deformation: D3

S3 schistosity within both metapelites and metagranites is associated with a top-S sense of shear (X3 lineations) and can be observed to re-activate former top-N, S2 fabrics, but with an opposite shear sense (Figure 2.7a and b). F3 folding associated with S3 is not observed. However, by far the most pervasive and clear deformation event observed to overprint S3 is widespread folding F4 (Figure 2.7c). F4 folding is ubiquitous and typically corresponds
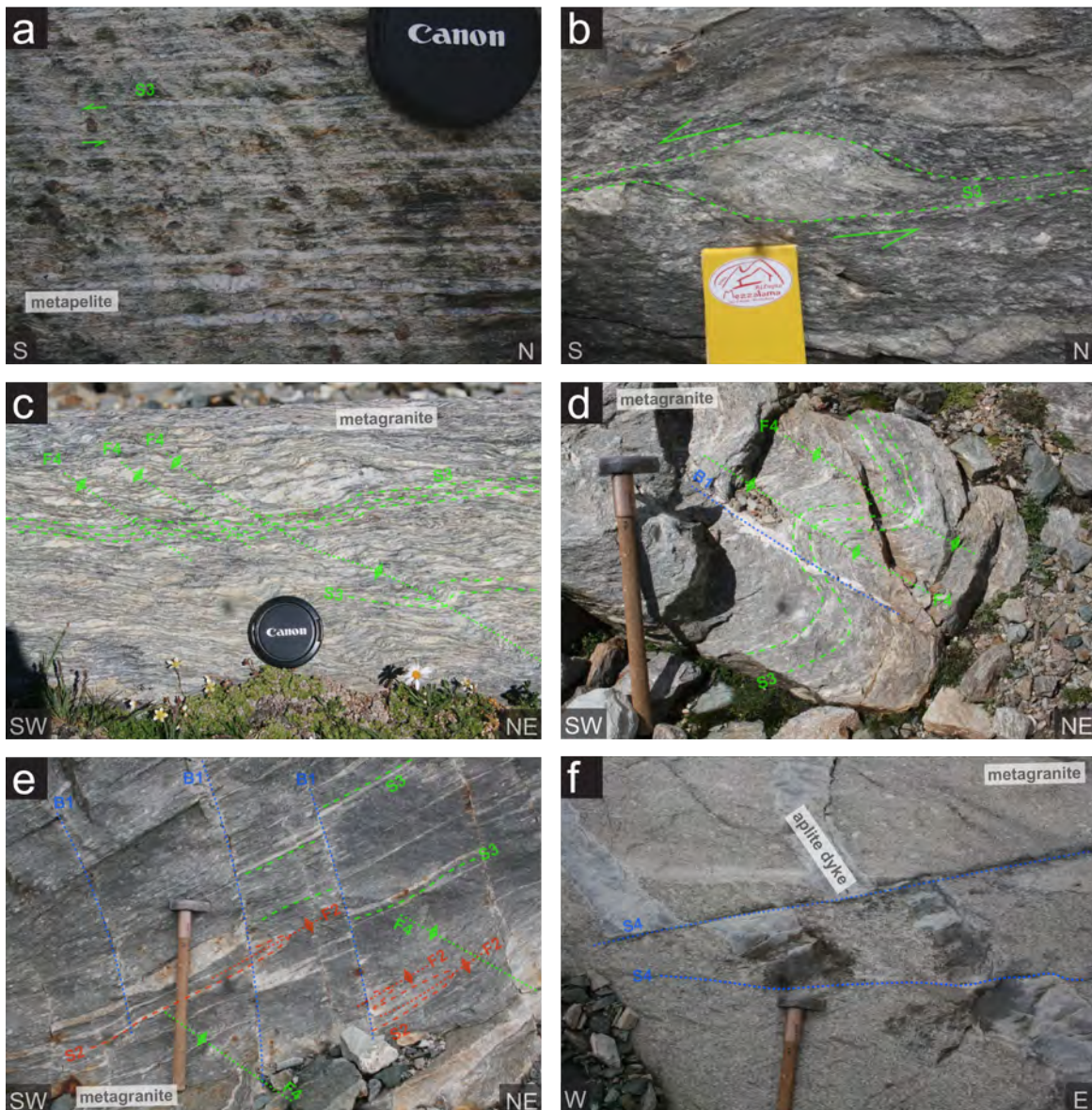
Figure 2.7: Representative field images of structural features belonging to the Monte Rosa nappe: a) Highly strained schistosity (S3) of deformed garnet-chlorite bearing metapelites, preserving sinistral, top-SW shear sense. b) Deformed aplitic dyke within Monte Rosa metagranite lithologies preserving S3 schistosity and sinistral, top-SW shear sense. c) S3 schistosity in metagranite and weak asymmetrical crenulation related to F4 folding with a sinistral, top-SW shear sense. d) F4 folding of S3 schistosity in metagranite with cross-cutting S4 brittle fracture that is subsequently filled with albite. e) highly deformed metagranite with 3 generations of cross-cutting deformation structures. f) Example of brittle S4 features offsetting aplitic dykes within the metagranite.

to a fold axial plunge dipping SW and postdates previous schistosities (S1, S2 and S3) as most schistosities hinge around the pole of a SW dipping F4 axis (Figure 2.8c). F4 is

characterized by an asymmetrical folding style with a top-S sense of shear (Figure 2.7c), therefore we consider this deformation D3 closely associated and post-dating S2. This folding can be observed as minor to tight asymmetrical crenulations, drag folds and km-scale open folds (Figure 2.2 cross-section). Figure 2.8c shows the extent of F4 folding whereby both S2 and S3 (Figure 2.8a) are observed to rotate around the pole of the F4 axial plunge (Figure 2.8c). Moreover, S2 has been influenced much more by this folding compared to S3 attesting to its relatively younger age. The large scale folding evident from the cross-section in Figure 2.2 is seen in stereographic projections for S2 and S3 fabrics north and south of the hinge point (Figure 2.8). North of the hinge point, S2 and S3 schistosity dips to the northwest whereas south of the hinge point schistosity dips to the southeast (Figure 2.8a).

The metamorphic characteristics of this deformation event is a common greenschist overprint, manifested as chlorite + epidote shear zones throughout.

2.3.4   Orogen-parallel ductile and brittle deformation: D4

A transition from ductile to brittle deformation marks one of the last phases of deformation in the area, S4 and B1 (Figure 2.7d, e and f). Ductile features S4 are thin (1-5 cm) discreet shear zones with 1-5 m offset (Figure 2.7f). Brittle features B1 are typically manifest as 1-5 cm wide fractures within the metagranite with minimal offset (Figure 2.7d) and is associated with infillings of albite or quartz veins. Planar fabrics of S4 and B1 both typically have an E – W orogen-parallel strike (Figure 2.8a).

2.4   Additional outcrop of whiteschist

A new outcrop of a whiteschist has been discovered due to recent snow melt, uncovering fresh exposure north of the Mezzalama Rifugio (E: 2624890 N: 1084985; see location of samples 19MR-03 and 19MR-03 in Figure 2.2). This whiteschist body is in close proximity to previous whiteschists investigated by Luisier et al. (2019) (Figure 2.2). Figure 2.9 shows a schematic section of the Monte Rosa basement complex, Furgg zone and Zermatt-Saas ophi-
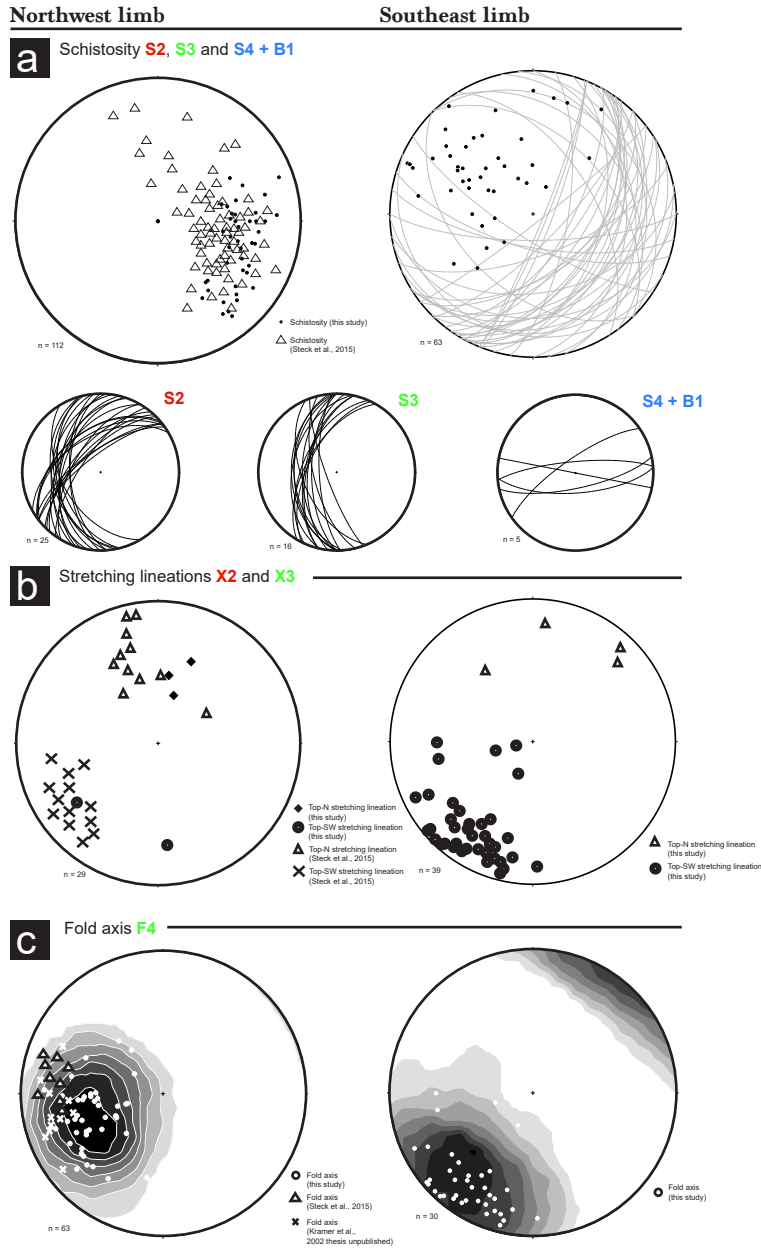
Figure 2.8: Lower hemisphere stereographic projections of major structural features of the Monte Rosa nappe (including former studies in cirque du Véraz area (Kramer, 2002; Steck et al., 2015)), taken from the northern and southern limb of the larger F4 fold (Figure 2.2 cross-section).

olites, indicating the position of the new whiteschist outcrop relative to the already described whiteschist outcrops (Luisier et al., 2019; Marger et al., 2019; Le Bayon et al., 2006; Pawlig and Baumgartner, 2001). In contrast to the whiteschist investigated by Luisier et al. (2019), the newly discovered whiteschist body is located at the contact between the Monte Rosa metagranite and basement metapelites. It comprises predominantly phengite, talc, quartz, chloritoid $\pm$ chlorite (Figure 2.10). In some areas of the whiteschist, chloritoid reaches over 1 cm in size (Figure 2.10a). We have sampled both coarse-grained (19MR-03, Figure 2.10b) and fine-grained areas (19MR-04, Figure 2.10c) for petrological analysis.

Particularly in sample 19MR-04, a schistosity is defined by deformed phengite, talc, quartz and chloritoid (048/58 NW) that is parallel to the metagranite and metapelite contact and lacks a chlorite overprint (sample 19MR-04, Figure 2.10a, c and e). This schistosity is likely S2, is similar to deformation structures in surrounding lithologies, and shows a minor later kink fold (Figure 2.10a). Since whiteschist lithologies reflect peak Alpine metamorphic conditions in the Monte Rosa nappe according to previous authors, this outcrop will enable us to constrain the nature of deformation after the peak Alpine high P metamorphism and before subsequent greenschist overprinting typical of S2 and S3 structures.

Metapelites from an outcrop in close proximity to these whiteschists exhibit a potential high-P Alpine metamorphic assemblage (garnet, phengite, biotite, quartz), and a schistosity parallel to S2 that post-dates the peak Alpine paragenesis. Microstructural evidence (section 2.4.2) suggests that this assemblage is then retrogressed and replaced with chlorite without significant deformation. See Vaughan-Hammon et al. (2021) for more detailed investigations into high P Alpine metamorphism in Monte Rosa metapelites.

2.4.1   Methodology

Electron probe microanalysis (EPMA) of major and minor element compositions of white mica, chloritoid and chlorite were conducted using a JEOL JXA-8350F HyperProbe at the University of Lausanne, Switzerland. The operating conditions were 15.0 kV acceleration voltage and 1.5 - 2.0 x 10^{-8} A, with a beam diameter of 5.0 μm. Natural minerals were used
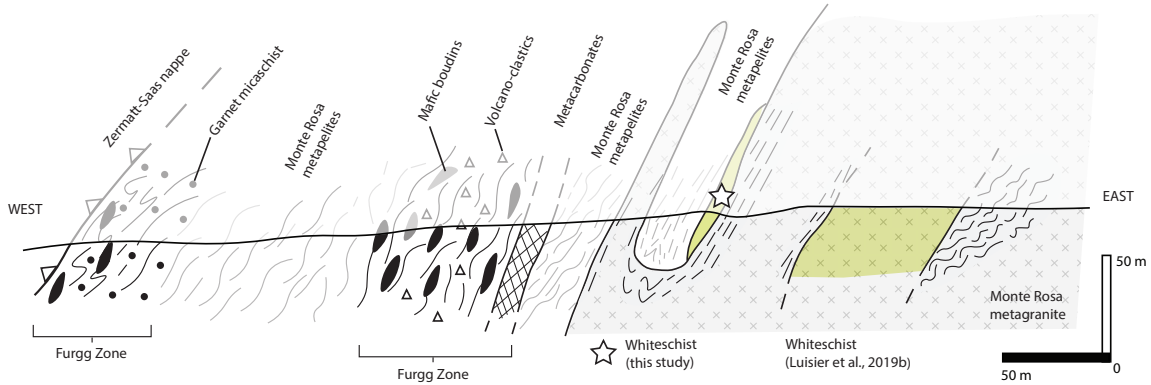
Figure 2.9: Schematic E - W lithological section from the Monte Rosa metagranite intrusive suite, Monte Rosa basement complex, and finally the over-thrusted Zermatt-Saas nappe. Structural position of whiteschist analyzed in Luisier et al. (2019) and the whiteschist of this study are indicated.

as reference materials: orthopyroxene (SiO_2), andalusite (Al_2O_3), albite (Na_2O), fayalite (FeO), forsterite (MgO), orthoclase (K_2O), nephrite (MnO), wollastonite (CaO), sphalerite (ZnO), rutile (TiO_2). Structural formulae were calculated on the basis of 11 oxygens for white mica and talc, 8 cations for chloritoid and 13 oxygens for chlorite.

Phase diagrams were calculated using the DOMINO software suite (de Capitani and Brown, 1987) in combination with the Berman database (Berman, 1988, 92 update). This database was chosen in order to: 1) have an internally consistent database, and 2) to accurately compare thermodynamically calculated P and T with the study of (Luisier et al., 2019), who also utilized this database to calculate metamorphic conditions for whiteschist assemblages. Bulk compositions were calculated based on quantitative image analysis of whole thin section domains in each sample, using EPMA derived mineral compositions, along with the MATLAB$^©$ based image processing software XMapTools (Lanari et al., 2014), in the chemical system KF-MASH. Solution models used are from the 92 update of Berman (1988) data base chloritoid and chlorite) and further included the white mica model after Massonne and Szpurka (1997). Mineral abbreviations are after Whitney and Evans (2010).

Talc is a major constituent of the whiteschist mineralogy. However, due to the only existing end-member solution data for talc being Mg (Berman, 1988, 92 update), it is necessary to account for the presence of other non-negligible talc end-members (e.g. Fe-talc) when

calculating pseudo-sections. We have employed an entropy correction (S^{corr}), defined here by $S^{corr} = S^o$ - Rlna, where S^o is the entropy for the pure phase. A full explanation and derivation of this correction is outlined in Appendix 1 of (Vaughan-Hammon et al., 2021). For a pure phase, a = 1 and $S^{corr} = S^o$, thus the entropy within the JUN92B database by Berman (1988) is unaffected. The existing solution model for talc is for Mg-rich end-members. Here we adjust the activity a_{tlc}^{Mg} of the existing Mg-talc in the database employing a site mixing model: a = $a_{tlc}^{Mg} = X_{Mg}{}^3$, where X_{Mg} = Mg/(Mg+Fe).

2.4.2   Petrography

Sample 19MR-03 displays a coarse-grained texture of 0.5-1 cm sized chloritoid in a finer grained matrix (< 1 mm) of predominantly weakly orientated phengite, as well as talc and quartz (Figure 2.10b). The large chloritoids display fracture networks that form subgrains in some places and are associated with late chlorite precipitation (Figure 2.10d and f). Areas rich in talc within the matrix seldom form interconnected textures, rather isolated regions. Estimates of modal volumes of minerals include: 33% phengite, 36% chloritoid, 7% quartz, 14% chlorite, and 9% talc.

Sample 19MR-04 displays a finer grained texture compared to 19MR-03, consisting of 2 mm sized chloritoids (Figure 2.10c and e). This sample has a much more developed schistosity defined by fine grained phengite and talc as well as having a larger volume of quartz, defined as regions of elongated recrystallized quartz aggregates (Figure 2.10e). Phengite and talc are observed to wrap around rigid chloritoid grains, with quartz (and minor amounts of talc and phengite) precipitating within strain shadows (Figure 2.10e). No syn-kinematic growth of minerals is observed. Kink bands and foliation of white mica, deformation of all mineral phases, lack of preserved foliations within chloritoid and the general lack of syn-kinematic growth indicators of chloritoid suggests pre-tectonic (pre-deformation) growth of the eclogitic whiteschists. No chlorite is observed in sample 19MR-04. Estimates of modal volumes of minerals include: 27% phengite, 16% chloritoid, 47% quartz, and 10% talc.

Table 2.1: Representative microprobe analysis (19MR-03 and 19MR-04).

	19MR-03					19MR-04		
Analysis	Phengite	Talc	Chloritoid		Chlorite	Phengite	Talc	Chloritoid
			Core	Rim				
SiO_2	52.60	62.59	24.33	25.14	26.46	52.37	62.76	25.68
Al_2O_3	27.42	0.22	43.14	44.73	23.27	27.87	0.19	43.93
TiO_2	0.26	0.01	0.00	0.01	0.07	0.23	0.01	0.00
MnO	0.01	0.00	0.34	0.11	0.06	0.00	0.00	0.09
ZnO	0.01	0.00	0.00	0.01	0.03	0.00	0.01	0.04
FeO	0.76	3.06	20.66	13.38	12.96	0.93	3.28	13.86
MgO	4.27	30.17	5.43	9.87	24.70	4.15	29.52	9.15
Na_2O	0.31	0.02	0.01	0.00	0.01	0.35	0.02	0.00
CaO	0.00	0.00	0.01	0.00	0.02	0.00	0.03	0.01
K_2O	11.10	0.00	0.01	0.00	0.03	10.83	0.01	0.00
Total	96.70	96.09	93.70	93.25	87.63	96.73	95.82	92.76
Normalized*	11 (a)	11 (a)	8 (c)	8 (c)	13 (a)	11 (a)	11 (a)	8 (c)
Si^{4+}	3.435	3.976	1.930	1.937	2.494	3.417	3.998	1.999
Al^{3+}	2.111	0.017	4.032	4.060	2.491	2.143	0.014	4.029
Ti^{4+}	0.013	0.001	0.001	0.000	0.005	0.011	0.000	0.000
Mn^{2+}	0.001	0.000	0.023	0.007	0.004	0.000	0.000	0.006
Zn^{2+}	0.001	0.000	0.000	0.001	0.002	0.000	0.001	0.002
Fe^{2+}	0.042	0.163	1.370	0.862	0.910	0.051	0.175	0.902
Mg^{2+}	0.416	2.857	0.642	1.133	3.344	0.404	2.804	1.062
Na^+	0.040	0.002	0.002	0.000	0.002	0.045	0.002	0.001
Ca^{2+}	0.000	0.000	0.001	0.000	0.002	0.000	0.002	0.001
K^+	0.921	0.000	0.001	0.000	0.004	0.902	0.001	0.000
Total	6.980	7.016	8.002	7.999	9.258	6.973	6.997	8.002

* normalization using anions (a) and cations (c)
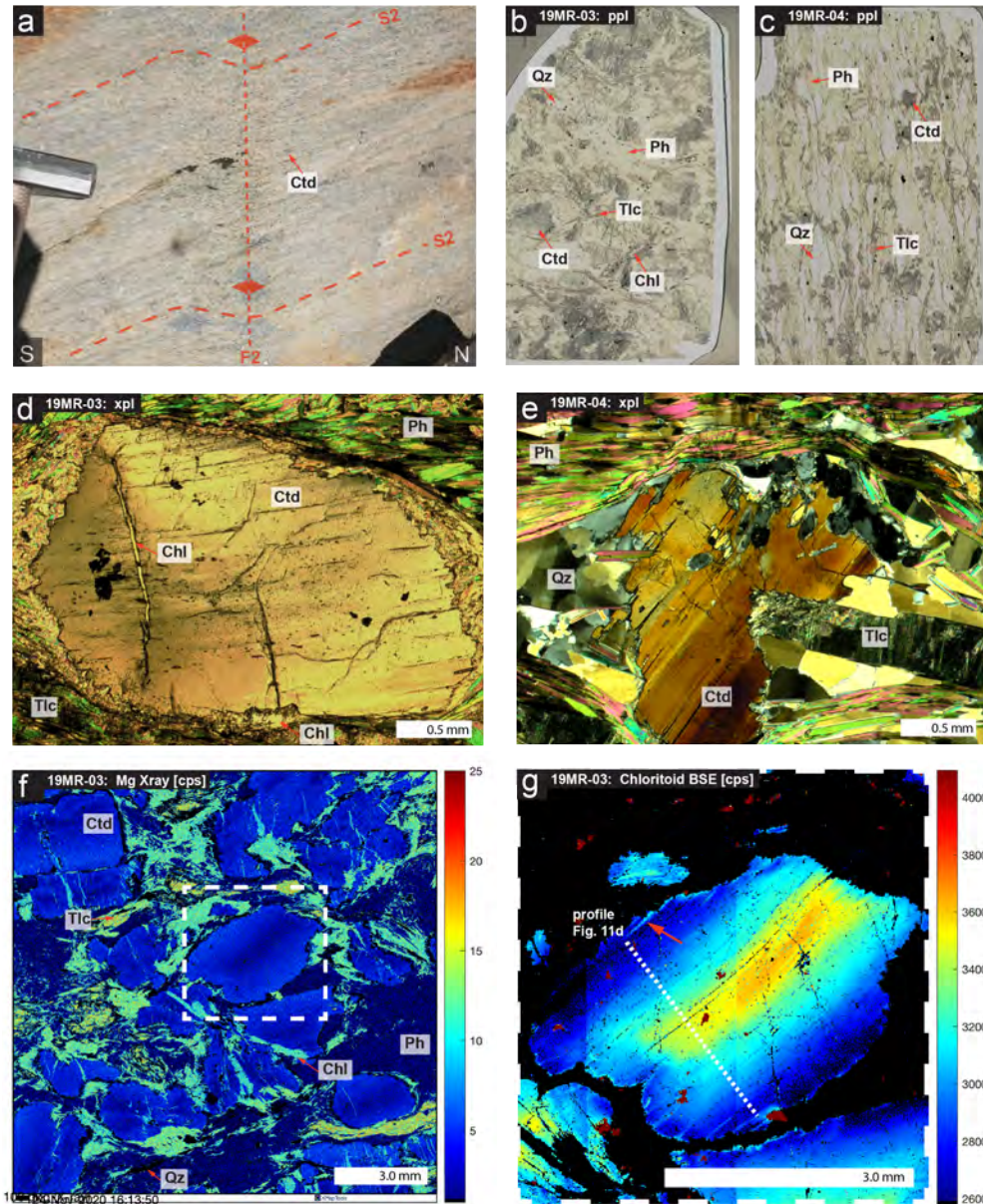
Figure 2.10: Petrological features of whiteschist samples 19MR-03 and 19MR-04: (a) field image of S2 schistosity and subsequent F2 dextral, top-N minor crenulation. (b) whole thin-section plane polarized light image of coarse-grained chloritoid whiteschist sample 19MR-03. (c) whole thin-section plane polarized light image of fine-grained whiteschist sample 19MR-04. (d) photomicrograph in cross-polarized light of late chlorite growth within coarse grained chloritoid fractures. (e) photomicrograph in cross-polarized light of typical textures observed in fine grained whiteschist samples 19MR-04. (f) X-ray map of Mg in sample 19MR-03, note high Mg talc and visible zoning in large chloritoid grains. (g) major zoning observed in BSE image for chloritoid grains, profile represented for microprobe analysis (Figure 2.11d) (XMapTools Lanari et al., 2014).

2.4.3 Mineral chemistry and pseudo-section results

Representative microprobe results for whiteschist samples 19MR-03 and 19MR-04 are presented in Table 2.1. The peak paragenesis for both samples consists of chloritoid (Ctd), phengite (Ph), talc (Tlc) and quartz (Qz).

Within 19MR-03, coarse grained chloritoid shows significant zoning (Figures 2.10f, g and 2.11d). X_{Fe} (Fe/(Fe+Mg)) is largest within the core of chloritoid grains at 0.68, compared to X_{Mg} (Mg/(Mg+Fe)) at 0.32. Towards the rims of chloritoid, X_{Fe} decreases to 0.43 and X_{Mg} increases to 0.57. Equally so, minor zoning of Mn can be observed from core to rim, at 0.008 to 0.025 atoms per formula unit (a.p.f.u) (Figure 2.11d). Phengites show a broad range of Si content ranging between 3.23 and 3.43 a.p.f.u from several different generations of white mica, which correlates with an increase of the Tschermak component between 0.26 and 0.44 (Figure 2.11a). Phengites exhibit a moderate range of XNa ((Na+Na)/K) between 0.10 and 0.21. Talc shows a rather narrow range of Si content ranging between 3.96 and 4.0 a.p.f.u, which correlates with a weak (if not absent) Tschermak component between 1.48 and 1.5 (Figure 2.11b). Talc is enriched in Mg (Table 2.1) with a narrow range of X_{Mg} between 0.93 and 0.95. Late stage chlorite is chemically nearly homogenous throughout the sample with an X_{Mg} of 0.80.

To gain insight into the phase petrology of these samples, we first calculated pseudo-section or metamorphic assemblage diagrams (MAD, Spear and Pattison, 2017). Figure 2.12a shows the calculated pseudo-section results for 19MR-03. For the peak assemblage of Ph + Ctd + Tlc + Qz, a large stability field is calculated. Employing the activity correction outlined in the methods section, the resulting stability field is enlarged towards lower pressures, indicated in the pseudo-section of Figure 2.12a. Due to the presence of late chlorite (Chl) chemistry, the retrograde path is indicated by the chlorite-in reaction of Ph + Chl + Ctd + Tlc + Qz (Figure 2.12a). This stability field agrees with bulk chemistry isopleths of chloritoid X_{Mg}, Si in phengite, and chlorite X_{Mg} (Figure 2.12a). The resulting metamorphic conditions for Ph + Chl + Ctd + Tlc + Qz taking into account errors is 1.95 ± 0.05 GPa and 555 ± 35°C.
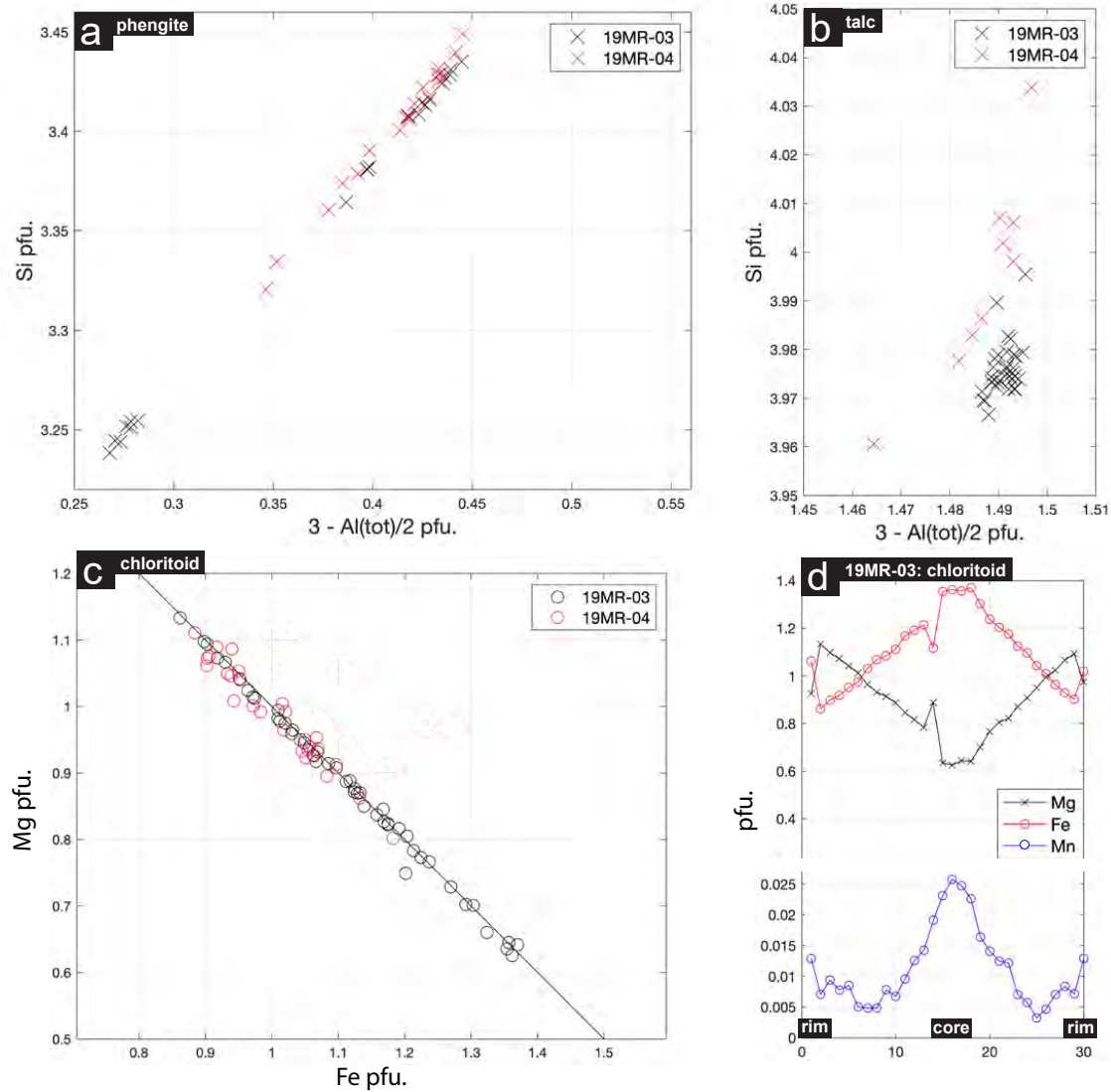
Figure 2.11: Normalized mineral chemical data for whiteschist assemblages in samples 19MR-03 and 19MR-04: (a) Si in phengites against Al tetrahedral sites. (b) Si in talc against Al tetrahedral sites. (c) Mg vs Fe-total in chloritoid. (d) Representative zoning of Mg, Fe and Mn in coarse-grained chloritoid of sample 19MR-03.

Sample 19MR-04 has minimal zoning in finer grained chloritoids with X_{Mg} of 0.49 and X_{Fe} of 0.51 (Table 2.1). Phengites show a narrow range of Si content ranging between 3.32 and 3.45 a.p.f.u, which correlates with a weak of the Tschermak component between 0.34 and 0.44 (Figure 2.11a). Phengites exhibit a moderate range of XNa between 0.10 and 0.16 which are relatively lower values compared to 19MR-03. Talc show a range of Si content between 3.96 and 4.04 a.p.f.u, which correlates with a weak (if not absent) Tschermak component between

1.46 and 1.5 (Figure 2.11b). Talc is enriched in Mg (Table 2.1) with a narrow range of X_{Mg} between 0.89 and 0.91.

Figure 2.12b shows the calculated pseudo-section results for 19MR-04. The peak assemblage of Ph + Ctd + Tlc + Qz is represented with and without the Mg-talc entropy correction. Isopleths for measured chloritoid X_{Mg} and Si in phengite are represented for the Mg-talc entropy correction stability field (Figure 2.12b). The isopleths cluster towards higher temperatures and lower pressures within the enlarged stability field. The resulting metamorphic conditions for Ph + Ctd + Tlc + Qz taking into account errors is $c.$ 2.1 ± 0.2 GPa and $560 \pm 20°$C.
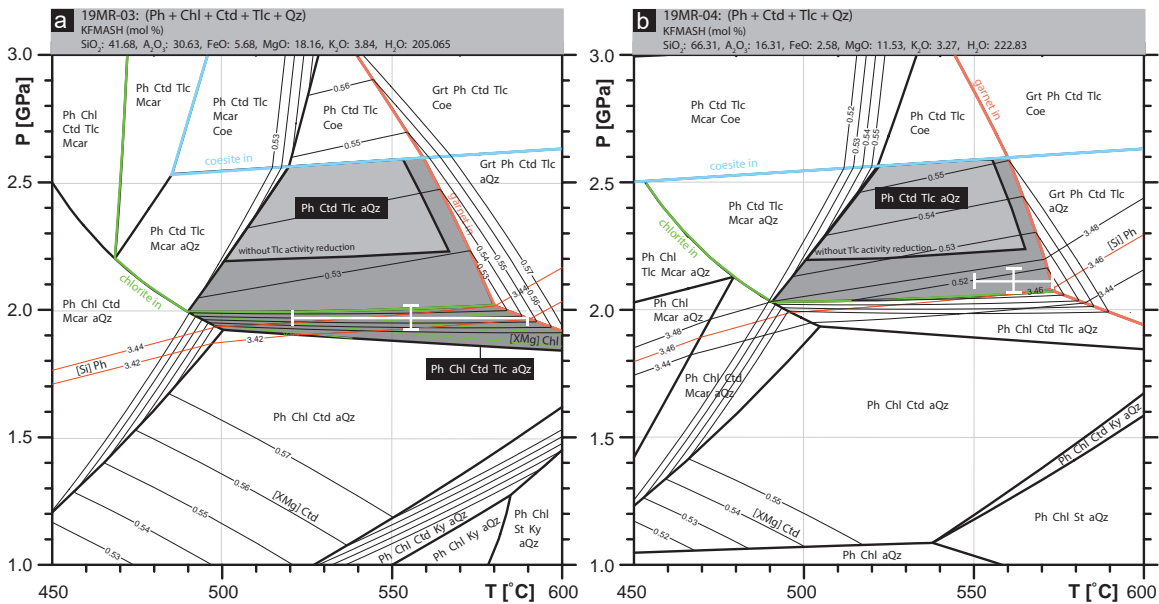
Figure 2.12: Thermodynamic pseudo-section modelling for sample 19MR-03 and 19MR-04. a) KFMASH pseudo-section calculated for sample 19MR-03, inferred peak assemblage indicated as Ph + Ctd + Tlc + Qz as well as retrogressional assemblage stability field of Ph + Ctd + Tlc + Qz + Chl. Enlarged stability field of peak assemblage resulting from the talc activity reduction due to Mg- and Fe-talc end-members. Si in phengite isopleths, X_{Mg} in chloritoid (Mg/(Mg + Fe)) isopleths, and X_{Mg} in chlorite isopleths. b) KFMASH pseudo-section calculated for sample 19MR-04, peak assemblage indicated as Ph + Ctd + Tlc + Qz as well as the enlarged stability field resulting from the talc activity reduction due to Mg- and Fe-talc end-members. Si in phengite isopleths and X_{Mg} in chloritoid are present.

2.5   Discussion

2.5.1   Whiteschist results

2.5.1.1   Comparison with previous studies

The results for peak Alpine metamorphic conditions incurred by whiteschist lithologies in this study have been calculated at 2.1 $\pm$ 0.2 GPa and 560 $\pm$ 20°C (Figure 2.12b). This result agrees with the estimated peak conditions of *c.* 2.2 $\pm$ 0.2 GPa at 540-600°C for whiteschist assemblages analyzed by Luisier et al. (2019), taken from a nearby outcrop (Figure 2.2). Le Bayon et al. (2006) also sampled a whiteschist from the nearby main whiteschist outcrop and calculated peak conditions at 2.4 GPa and 500°C. Le Bayon et al. (2006) use an averaged bulk composition in their study and a H_2O activity between 0.59 and 0.66. They do not elaborate on the interpretation of the reduced activity; some initial calculations by us suggest that if the fluid activity was reduced due to the presence of CO_2, then this would lead to the stability of magnesite under the proposed conditions, which is, however, not observed. Several decades ago, Chopin and Monié (1984) also analyzed whiteschist samples taken from a location close to the outcrop of this study (western side of the Véraz glacier, Figure 2.2). However, its provenance was unknown as it originated from a loose moraine block. A comparison of our mineral chemistry with that of Chopin and Monié (1984), as well as the position and altitude their sample was taken from, suggest that both their and our whiteschists originate from the recently uncovered outcrop (Figure 2.2). However, our peak metamorphic conditions at 2.1 $\pm$ 0.2 GPa and 560 $\pm$ 20°C do not agree with that of Chopin and Monié (1984) at *c.* 1.6 GPa and 500°C. This is likely due to older thermodynamic databases, as well as the lowered H_2O activity of 0.6 used in Chopin and Monié (1984), based on the presence of fluid inclusions with a gas bubble, which was not further studied. This lowered H_2O activity was also used in order for the temperatures to not exceed 500-550°C (Chopin and Monié, 1984), suggested by the absence of Alpine staurolite in the Monte Rosa basement metapelites. A T below 550°C suited with mid-Cretaceous ages (which is an age now known to be far too old) estimated by Ar-Ar dating for peak conditions. Chopin and Monié (1984) argue that a

higher T would have resulted in a resetting of the ages during cooling. However, more recent geochemical analysis by Luisier et al. (2019) provides estimates of H_2O activity being close to 1. Furthermore, a more recent study based on the discovery of Alpine staurolite-bearing metapelites in the Monte Rosa basement indicates a higher peak Alpine T for the Monte Rosa nappe of $< 600°C$ (Vaughan-Hammon et al., 2021). Therefore, our results confirm that the peak P of 2.1 GPa for the whiteschist is significantly higher than the peak P of $c.$ 1.4 GPa that has been estimated for metagranite lithologies (Dal Piaz and Lombardo, 1986; Luisier et al., 2019) and of 1.6 ± 0.2 GPa for metapelitic lithologies (Vaughan-Hammon et al., 2021).

Pressure conditions of > 2.2 GPa for the whiteschist do not agree with numerous studies undertaken in other portions of the western Monte Rosa nappe for different lithologies including: metagranitic assemblages < 1.6 GPa (Luisier et al., 2019), metapelitic assemblages showing peak P of 1.6 ± 0.2 GPa and $585 \pm 20°C$ (Vaughan-Hammon et al., 2021), and 1.35 GPa and 670°C (Keller et al., 2004), and metapelitic and metabasic assemblages showing 1.3 GPa and 546°C (Borghi et al., 1996) and 1.4 GPa and 546°C (Dal Piaz and Lombardo, 1986). A study on metabasic assemblages reports peak conditions of $c.$ 2.7 GPa and 570°C (Gasco et al., 2011). However, P estimates obtained by Gasco et al. (2011) are debated due to insufficient mineral solid solution models (Lardeaux, 2014). Equally, these metabasic boudins likely derive from the Furgg zone. One suggestion for this disparity is the presence of a tectonic mélange.

The majority of whiteschist bodies studied in the cirque du Véraz area originate from outcrops that are enclosed within metagranite lithologies (Le Bayon et al., 2006; Luisier et al., 2019; Pawlig and Baumgartner, 2001). For the two whiteschist samples analyzed in this study, the situation is different, as they originate from a lensoidal body located directly at the contact between the Monte Rosa metagranite and basement complex (Figures 2.2 and 2.9). This may pose difficulties when trying to attribute a protolith to the whiteschist (either metagranitic or metapelite). However, the similarity in geochemistry and resulting pseudo-section calculations to that of Luisier et al. (2019) agrees with the concept of a late hydrothermal metasomatic alteration (Mg-enrichment) of a granitic protolith that occurred prior to Alpine deformation (Luisier et al., 2019, 2021; Marger et al., 2019; Pawlig and Baumgartner, 2001). Moreover,

no field evidence suggests tectonic mixing of whiteschist and metagranite or metapelite. Furthermore, all deformation exhibited within the whiteschist samples of the study, represents post-P strain. We do not observe any indications of syn-deformational growth of whiteschist high-pressure minerals in the whiteschist (talc, phengite, chloritoid + quartz), which would be indicative of movement from higher metamorphic facies to be subsequently juxtaposed next to lower metamorphic facies. Specifically, in 19MR-04, textural observations indicate a post-crystallization deformation event (Figure 2.10c and e), with the lack of retrogressive minerals being precipitated (i.e., kyanite or chlorite), we suggest that the deformation was either soon after peak conditions, still within the stability field of the peak assemblage and/or did not involve any major fluid influx. However, for the coarser grained 19MR-03, late retrogressive chlorite is observed to grow within brittle features of large chloritoid grains (19MR-03, Figure 2.10b, d and f). This minor overprinting with chlorite can be observed in zonation patterns within chloritoid grains that exhibit a decrease in Mg and an increase in Fe and Mn (Figure 2.11d).

2.5.1.2   Modelling prograde chloritoid zoning

Due to the variability in peak P incurred by the Monte Rosa nappe during Alpine orogenesis, the P-T path during burial and exhumation is still contentious. In order to assess the possible P-T paths during prograde metamorphism, we can compare the measured zoning of Mg in chloritoid of new natural whiteschist samples (Figure 2.11d) with a range of thermodynamically predicted zoning of Mg content in chloritoid using fractionated growth of chloritoid using the Theriak-program (de Capitani and Brown, 1987) (Figure 2.13). A similar approach applied to matrix dependent garnet growth was employed by Robyr et al. (2014), as well as in much more elaborated garnet growth zoning models (e.g. Gaidies et al., 2008). We interpret zoning patterns within coarse grained chloritoid (sample 19MR-03) to represent the onset of chloritoid growth during prograde metamorphism within cores having high X_{Fe} and low X_{Mg}, and peak metamorphism having low X_{Fe} and high X_{Mg} (Figure 2.11d and 2.13c).

Both the predicted evolving X_{Mg} content of chloritoid (Figure 2.13a) and the volume% of chloritoid (Figure 2.13b) are necessary to predict the zoning patterns in natural chloritoid (Figure 2.13c). Unique P-T paths provide unique X_{Mg} zoning patterns during prograde metamorphism (Figure 2.13 a, b and d). Comparing calculated volume% zoning patterns with profiles, however, requires converting the calculated volume% to a representative radius of a 3-dimensional volume (see Appendix 2.7 for more details). Figure 2.13e shows the thermodynamically predicted X_{Mg} zoning plotted against a representative radius, which is calculated from the thermodynamically predicted volume% assuming a rectangular geometry (Appendix 2.7). Based on the average crystal dimensions in the natural whiteschist sample we suggest that the measured Mg values are taken from the second major axis of monoclinic chloritoid (represented in Figure 2.13 as axis a).

Figures 2.13a and b demonstrate a range of possible P-T prograde path incurred by the whiteschist body during Alpine metamorphism (paths (1) to (6)). We consider here the peak Alpine metamorphic conditions (1.6 $\pm$ 0.2 GPa and 585 $\pm$ 20°C) calculated for a range of metapelitic samples analyzed in Vaughan-Hammon et al. (2021), and a P of $c.$ 1.4-1.6 GPa for metagranitic assemblages (Luisier et al., 2019) to be reliable, thus we start with a prograde path from 0°C and 0 GPa to 580°C and 1.6 GPa (path 1). This prograde pathway fits well with a geotherm of 10 °C km^{-1} (Figure 2.13b), which is reasonable for subduction geotherms (e.g. Penniston-Dorland et al., 2015). In order to then reach peak metamorphic conditions for high P whiteschist lithologies calculated in this study (2.1 GPa and 580°C), we present several end-member possibilities for the prograde P-T evolution that represent a prograde path due to tectonic overpressure (with respect to the metagranite/metapelite path) that deviates from the standard burial path (paths 1 to 5), as well as an unrealistic high P path (path 6).

The most extreme path takes an almost isothermal prograde path from 1.6 GPa to 2.1 GPa (Figure 2.13a path 1). The corresponding calculated zoning pattern during chloritoid growth does not agree with the measured zoning (Figure 2.13e, path 1), due to the decrease in X_{Mg} when passing through the Ph + Ctd + Chl + Tlc + aQz stability field (Figure 2.13a). This thermodynamically predicted decrease in X_{Mg} is due to the appearance of talc. We do not

observe a decrease in X_{Mg} towards the rim of chloritoid grains for sample 19MR-03 related to prograde metamorphism (Figure 2.13a). A retrograde decrease in X_{Mg} was observed (Figures 2.10f, g and 2.11d) locally due to chlorite growth within late brittle fractures in and surrounding chloritoid (red arrow Figure 2.10g), which texturally overprints the peak paragenesis (Ph + Ctd + Tlc + aQz) (Figure 2.10b and d). This decrease in X_{Mg} locally at the rim of chloritoid is most likely due to a decompression P-T path from the peak assemblage without chlorite (Ph + Ctd + Tlc + aQz), to an assemblage with chlorite (Ph + Ctd + Chl + Tlc + aQz) (Figure 2.13b).

The second most extreme path takes an isobaric pathway at a fixed pressure of 2.1 GPa (path 6). The corresponding calculated zoning pattern predicts several breaks in slope of X_{Mg} that are not comparable to the smooth increase in X_{Mg} observed in natural chloritoid zoning (Figure 2.13c).

Several other potential P-T paths are shown in Figure 2.13a and b that deviate from the prograde path to 1.6 GPa, which represent deviations in metamorphic conditions incurred by the whiteschist prior to reaching values that are more typical for the Monte Rosa nappe at c. 1.6 GPa (Borghi et al., 1996; Dal Piaz and Lombardo, 1986; Keller et al., 2004; Luisier et al., 2019; Vaughan-Hammon et al., 2021). Due to the T sensitivity of Mg absorption during chloritoid growth, an isothermal P increase and deviation at lower temperatures (pathway 4 and 5), will result in a minor breaks in slope of X_{Mg} values and an unrealistic X_{Mg} profile (Figure 2.13e). However, these breaks in slope are small enough to be within the error range and could either be undetected or smoothed due to late stage diffusion.

P-T paths 2 and 3 do closely resemble measured X_{Mg} chloritoid zoning, which have to avoid the Ph + Ctd + Chl + Tlc + aQz stability field and the subsequent drop in X_{Mg} values (Figure 2.13a). X_{Mg} zoning calculated for prograde paths 2 and 3 closely resemble (within error) measured X_{Mg} of chloritoid, especially when considering a 3-dimensional geometry (Appendix 2.7). Therefore, observed X_{Mg} zoning in natural samples agrees with prograde paths calculated by equilibrium pseudo-sections. It is difficult to determine accurately at

which P chloritoid started to grow, because P can range significantly by $\pm$ 0.5 GPa due to the appearance of the 0.3 X_{Mg} isopleth within the chloritoid-in field (Figure 2.13a).

Although many prograde P-T paths can be taken to peak metamorphic conditions calculated for whiteschist lithologies, our data suggests a deviation from the straight P-T path having peak P and T of 1.6 GPa and 580 °C (Figure 2.13a). Such P-T path is supported by metamorphic conditions estimated for the majority of lithologies in the Monte Rose nappe, which have been calculated at $\leq$ 1.6 GPa.

Our results further suggest that there was no dramatic isothermal P increase for the whiteschist around peak conditions (path 1; Figure 2.13), but that the whiteschist experienced a prograde P-T path with a continuous increase in both P and T (paths 2 to 5; Figure 2.13). Furthermore, the measured X_{Mg} in zoned chloritoid is compatible with predictions from pseudo-section modelling, suggesting that chloritoid grew under equilibrium conditions. Consequently, our results suggest that the whiteschist exhibits a different P-T path than the metagranite and metapelite lithologies (see discussion in section 2.5.4).

2.5.2   Alpine orogenesis: structural evolution

Numerous studies have compiled the ductile deformation history incurred by the Monte Rosa nappe, specifically within the context of the larger-scale tectonics during the Alpine orogeny (Keller et al., 2004; Keller and Schmid, 2001; Kramer, 2002; Steck et al., 2015). The earliest Alpine deformation structures reported by authors involves shearing of eclogite facies rocks and is associated with top-N nappe stacking due to underplating of Europe below Adria (e.g Steck et al., 2015). Early ductile deformation is referred to as XI by Steck et al. (2015) in the cirque du Véraz locality, and D1/D2 by Keller and Schmid (2001) and Keller et al. (2004) in the eastern, Antrona valley, region of the Monte Rosa nappe. Top-N stretching lineations, referred to as X2 in this study (Figure 2.8b), correlate well with early northward directed stretching lineations reported by the aforementioned authors (Keller and Schmid, 2001; Steck et al., 2015). However, most ductile shear zones within the Monte Rosa nappe, specifically in the cirque du Véraz, do not appear to occur under high-pressure eclogite conditions, due to
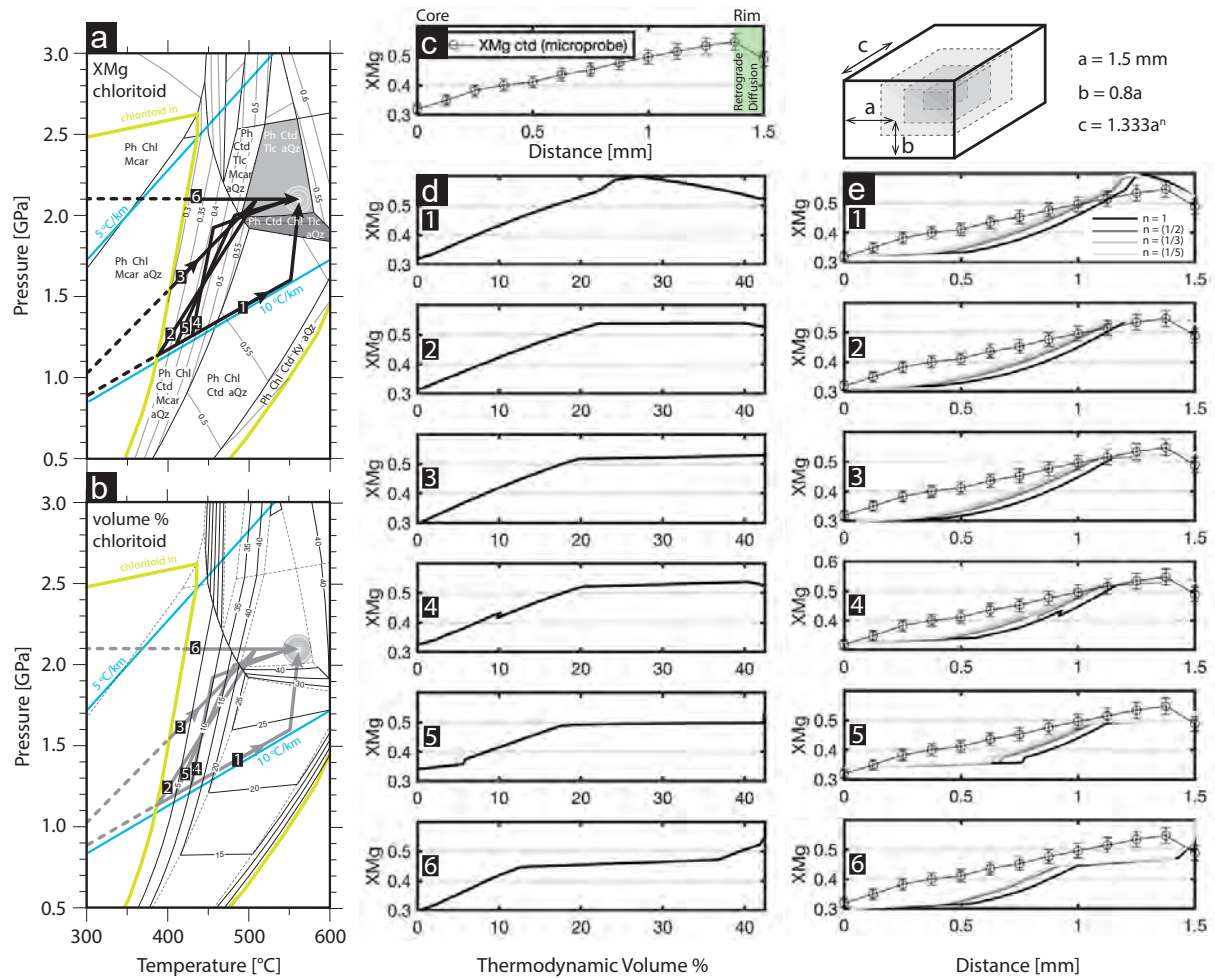
Figure 2.13: Comparison of measured X_{Mg} chloritoid zoning and thermodynamically calculated X_{Mg} chloritoid zoning: a) Thermodynamic pseudo-section, identical to pseudo-section presented in Fig. 11a including X_{Mg} values for chloritoid. Prograde pathways 1-6 marked with black arrows. Geotherms for 5 and 10 °C km^{-1} marked with blue lines. b) Thermodynamic pseud-section with volume% of chloritoid. c) Measured microprobe X_{Mg} of chloritoid from core to rim of sample 19MR-03. d) pseudo-section derived X_{Mg} of chloritoid for sample 19MR-03 for the various prograde pathways represented in a) and b), plotted against pseudo-section predicted volume% of chloritoid. e) pseudo-section derived X_{Mg} of chloritoid plotted against a radius calculated from the predicted volume% of chloritoid during prograde growth for a rectangular geometry (see Appendix 1 for details about exponential factor n).

the lack of microstructures indicating syn-kinematic growth of high-pressure minerals. Two scenarios may exist this lack: 1) insignificant deformation during high-pressure conditions, or 2) over printing of former high-P microstructures under later greenschist facies conditions. Observations of whiteschist deformation, from new samples presented in this study, do not

exhibit a syn-high-pressure fabric, rather a fabric that affects the high-pressure mineralogy, which is equally not associated with greenschist mineralogy (Figure 2.10a). Considering these observations, we interpret that top-N deformation structures (S2 and X2) (Figure 2.6, 2.8a and b), represent a deformation event closely post-dating high-pressure metamorphism during peak Alpine conditions.

Ductile deformation associated with top-S lineations, asymmetrical folding and fold hinges plunging towards the SW (S3 and X3 of this study), correlate well with top-S D3 shearing outlined in Keller and Schmid (2001) in the eastern, Antrona valley, region of the Monte Rosa nappe, stretching lineations XII and fold axis by Steck et al. (2015) in the cirque du Véraz locality, and fold axis observed by Kramer (2002) in the cirque du Véraz locality (Figure 2.8b and c). S3, top-S sense of shear, and F4 asymmetrical folding styles, agree with the backfolding style of the Western Alps, which is most evident in the distorted profile of the nappe pile southwest of the Simplon line (Figure 2.1, (e.g. Keller et al., 2005; Steck et al., 2015)). The location of the Monte Rosa nappe in the cirque du Véraz, provides a unique opportunity to observe structurally higher regions of the larger-scale backfold geometry affecting the nappe, namely a true antiformal hinge of the Western Alps (Figure 2.1c). This backfold geometry is most evident in cross section (Figure 2.2), and the observations of northward and southward dipping structures associated with schistosity development (Figure 2.8a). Exposure of the true hinge of late stage backfolding in the cirque du Véraz, is characterized by a more open fold geometry, compared to the tight, orogen parallel axial plane structures of the structurally lower portions of the nappe pile exposed to the NE, in the Vanzone region for example (Steck et al., 2015). By analyzing of the larger scale structure of late stage backfolding (our D3), we can observe a nappe refolding geometry (e.g. Bucher et al., 2003b), characterized by asymmetrical folding whereby the northern limb has a southward directed shear sense (Figure 2.7b), and the southern limb has a north directed shear sense.

2.5.3 Tectono-metamorphic history of the Monte Rosa nappe

Figure 2.14 schematically outlines the schematic tectono-metamorphic evolution of the Monte Rosa nappe exposed at the cirque du Véraz (Figure 2.2), which encompasses a range of lithologies and structures documented in this and earlier studies. This includes:

1. Varican basement complex, including paragneisses (Monte Rosa), Palaeozoic sediments, associated basic dykes, and volcano-clastic deposits (Furgg zone).

2. Permian-aged intrusion of granite bodies and associated dykes into Variscan basement complex. Contact metamorphism of Variscan basement close to the granite, leading to local migmitization. Fluids released by the crystallizing granite leads to late magmatic hydrothermal fluid-rock interaction producing the whiteschist protolith (Figure 2.14a).

3. Triassic-Jurassic extension resulting in deposition Mesozoic sediments (Furgg Zone), carbonates (Furgg Zone) and basic dykes (Furgg Zone) (Figure 2.14b).

4. Top-N shearing and nappe stacking of the overriding Zermatt-Saas ophiolitic sequence (Figure 2.14c).

5. Tertiary early Alpine continent collision resulting in an eclogitic metamorphic imprint at 1.6 ± 0.2 GPa and $585 \pm 20°C$ (affecting metapelite and metagranite lithologies), and sparse high-pressure assemblages at 2.2 ± 0.2 GPa and $560 \pm 20°C$ for whiteschist lithologies, potentially representing local deviations from lithostatic pressure.

6. Continued top-N shearing (Figure 2.14c).

7. Top-S shearing and backfolding (Figure 2.14d).

8. Tilting of western Alpine units to current position and orogen-parallel, brittle/ductile faulting (Figure 2.14e).
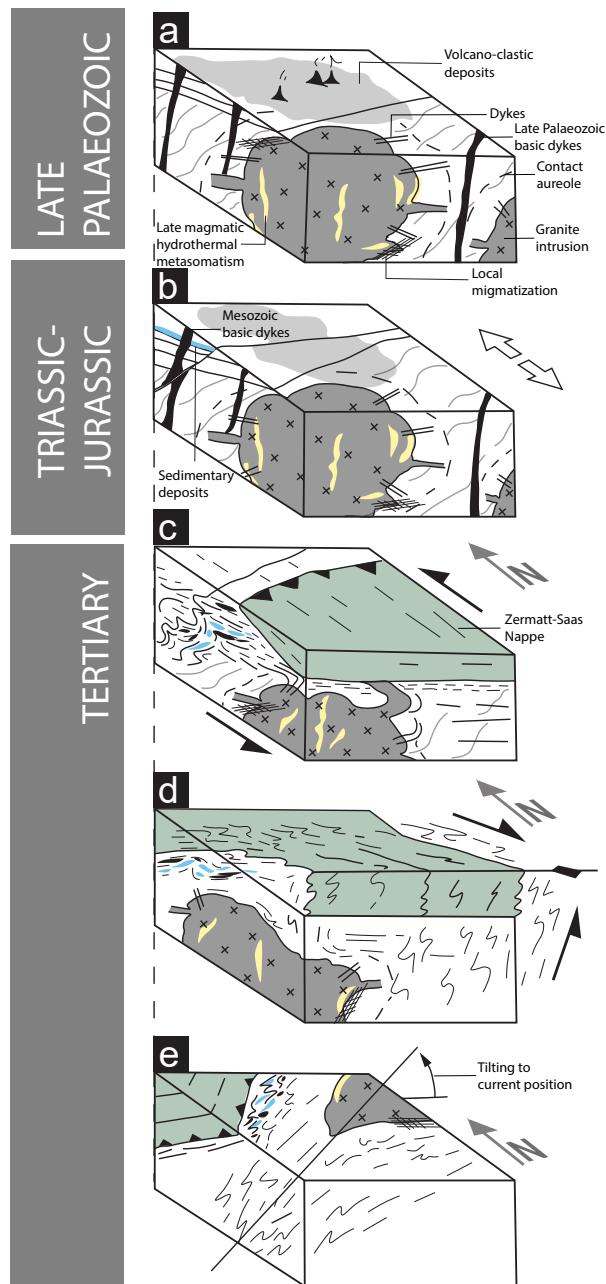
Figure 2.14: Schematic geological evolution of the Monte Rosa nappe encompassing the range of lithologies and structures exposed at the upper val d'Ayas, Italy: (a) late Paleozoic intrusion of Monte Rosa granite bodies into Variscan metapelite basement. (b) Triassic-Jurassic rifting and extension, and deposition of shallow carbonate sediments. (c) Tertiary Alpine orogenesis and over-thrusting of Zermatt-Saas ophiolite units above the Monte Rosa continental complex. (d) Late-Alpine backfolding phase. (e) Late-Alpine tilting and orogen parallel strike-slip movement, resulting in the present day position of the Monte Rosa and Zermatt-Saas nappes.

2.5.4   Possible explanations for P variations

This study confirms differences in estimated Alpine peak P between Monte Rosa metagranite and metapelite at 1.6 ± 0.2 GPa (Luisier et al., 2019; Vaughan-Hammon et al., 2021) and two whiteschist lenses at 2.2 ± 0.2 GPa, considering the whiteschist analyzed here and another one investigated by Luisier et al. (2019). There are several possible explanations, or hypotheses, for these P differences obtained in different lithologies, which are briefly discussed below.

Tectonic mixing (mélange), which is characteristic in numerical models of exhumation within a subduction channel (e.g. Gerya et al., 2008), is a possibility to juxtapose high P whiteschist bodies next to lower P metagranite and metapelite lithologies. However, field evidence from this study clearly shows that the association of metagranite intrusion and Variscan basement complex (mainly metapelites) of the Monte Rosa nappe exposed in the cirque du Véraz represents a structurally coherent body. Field observations also show that the whiteschists are part of the Monte Rosa nappe, since they are either fully embedded in metagranite or occur at the boundary between metagranite and Monte Rosa metapelite. Therefore, no evidence supporting tectonic mixing, or mélange, has been found in the field and we consider the hypothesis of tectonic mélange as falsified for the studied region (Figure 2.2, 2.3a, 2.4d and 2.6a).

It is also possible that either the peak P estimates for metagranite and metapelite or, alternatively the estimates for the whiteschists are grossly significantly inaccurate. If one or more of the peak P estimates were indeed considerably inaccurate, then all reported peak P estimates based on metagranitic, metapelitic and whiteschist lithologies have to be questioned, since at present it is not clear which of the peak P estimates would be grossly inaccurate. A possible explanation for which all P estimates would be accurate would be, for example, that P estimates for the metagranite and metapelite would both indicate a retrograde P and not peak P. Since all the peak T estimates are similar, the retrograde P-T path from high-P whiteschist to lower-P metagranite/metapelite would be close to isothermal. Another possibility would be that both metagranite and metapelite stopped recording P at $c.$ 1.6 GPa due to sluggish kinetics so that both metagranite and metapelite never recorded peak P

conditions. However, we have currently no indication that the P estimates for metagranite and metapelite were strongly affected by sluggish kinetics or reflect a retrograde overprint. Also, P estimates for metagranite and metapelite (1.4 GPa based on Si-content in phengite and $<$ 1.6 GPa based on absence of jadeite; Luisier et al. (2019)) and metapelite (1.6 $\pm$ 0.2 GPa based on pseudo-section modelling; Vaughan-Hammon et al. (2021)) agree within error, which rather suggests that both rocks recorded the same metamorphic peak event. Currently, we do not have any good reason to question any of the peak-P estimates.

Tectonic, or dynamic, P variations have been also proposed to explain the differences in peak P estimates (Luisier et al., 2019; Vaughan-Hammon et al., 2021). More specifically, two end-member dynamic processes have been proposed: (i) tectonically induced compressive stresses causing the shearing-off of the Monte Rosa nappe from the subducting European plate, and (ii) reaction-induced stresses due to volumetric strains during whiteschist formation (Luisier et al., 2019). Two arguments are frequently used against dynamic P variations in viscous rock for T $> c.$ 500°C: (1) The rocks are mechanically too weak, that means the effective viscosity is too small, and, hence, differential stresses cannot be large so that associated dynamic P variations are negligible, and (2) Tectonic overpressure cannot occur in mechanically weak rock, only in strong rock. Concerning (1): The differential stress, and hence the dynamic P, in a viscous rock is not controlled only by its viscosity, but by the product of viscosity times strain rate. Therefore, if the strain rate is temporarily and locally significantly increased, e.g., associated with the shearing-off of crustal rocks from the subducting plate, then differential stresses can be temporarily and locally much higher than expected from average tectonic strain rates. The same applies to reaction-induced stresses and to volumetric strain rates which are related to the duration of metamorphic reactions and the associated volume changes. Concerning (2): It has been shown in several studies that mechanically weak rocks that are located between stronger rocks, either as inclusion or within a shear zone, can exhibit significant tectonic overpressure (e.g. Jamtveit et al., 2018; Moulas et al., 2014; Schmalholz and Podladchikov, 2013). This tectonic overpressure in weak rocks is simply the consequence of the force balance between strong and weak rocks. Consequently, it is mechanically possible that weak viscous rocks exhibit significant tectonic overpressure.

The newly discovered whiteschist body analyzed here complicates the attribution of P variations to simple end-member processes, since the new whiteschist body is not fully embedded in metagranite but located between metagranite and metapelite, which likely exhibit different mechanical properties (Figure 2.9) (Luisier et al., 2019; Moulas et al., 2014). Although the peak P estimates for the whiteschist studied here, 2.1 ± 0.2 GPa, and the ones for the whiteschist studied by (Luisier et al., 2019), 2.2 ± 0.2 GPa, are similar, it is possible due to the error range of $\pm$ 0.2 GPa that the peak P for the two whiteschists were different by approximately 0.4 GPa. Differences in peak P between the two whiteschists would be compatible with P differences caused by differential stresses, which might have been different around the two whiteschists. If peak P was indeed different between whiteschist and metagranite/metapelite, then the minimum peak P difference, required to explain the peak P estimates within error, is 0.2 GPa (between 1.8 and 2.0 GPa). Differences in peak P ranging between 0.2 and 0.4 GPa, and related tectonic over- and underpressure up to 0.4 GPa, are already in agreement with lithospheric-scale numerical models of subduction and collision (e.g. Li et al., 2010). Peak P differences > 0.4 GPa require more specific conditions, for example transient high strain rates, local mechanical heterogeneities, and/or reaction-induced stresses, which are usually not included in standard lithosphere-scale models. A more reasonable scenario that could generate dynamic P differences between metagranite/metapelite and whiteschist, would be a combination of tectonically-induced and reaction-induced differential stresses. The coupled effect of these stress states during whiteschist formation needs to be further investigated.

2.6 Conclusions

Detailed mapping of outcrops of the Monte Rosa nappe at the cirque du Véraz reveal that the association of Monte Rosa metagranite and metapelite is a structurally coherent tectonic unit with no evidence for tectonic mixing (mélange) of these two lithologies. The studied rocks show no evidence that Alpine peak P minerals have grown during significant deformation and, hence, there is no evidence for significant deformation under peak P conditions. The structures observed during detailed mapping and the interpreted tectonic evolution of the

region around the cirque du Véraz agree with the tectonic evolution reported in previous studies; both at the local scale and for the entire Monte Rosa nappe.

We describe a newly discovered whiteschist at the contact between the Monte Rosa meta-granite and metapelite. Thermodynamic pseudo-section modelling indicates peak P of 2.1 ± 0.2 GPa and peak T of 560 ± 20°C for the whiteschist. These results agree with previously reported peak P and T estimates for another whiteschist body in the same region, which was, however, entirely embedded in the metagranite. The modelling of prograde Mg-content evolution in chloritoid suggests growth of the chloritoid during a standard burial-subduction path close to equilibrium conditions. There is no indication for a dramatic, near-isothermal P increase during prograde or peak conditions.

This study confirms peak P differences between metagranite and metapelite of 1.6 ± 0.2 GPa and two whiteschists of 2.2 ± 0.2 GPa. Furthermore, this study falsifies the hypothesis that these P differences are due to tectonic mélange, that is tectonic mixing of the whiteschists from larger burial depth into less deep metagranite and metapelite. Hence, there remain currently two basic explanations for the reported P differences: (1) whiteschists, metagranite and metapelite were exposed to the same P during Alpine orogeny but one or more of the P estimates do not indicate peak conditions or are significantly inaccurate. (2) The peak P estimates are accurate within 0.2 GPa and peak P was different between whiteschists, metagranite and metapelite. We have currently no evidence that one of the peak P estimates is significantly inaccurate or that the P estimates do not indicate peak conditions. Hence, we suggest that the variation in peak P is due to differential stresses which cause local deviations from the lithostatic P. Such differential stresses can be generated by tectonic shear deformation or by reaction-induced volumetric deformation, most likely by a combination of both.

2.7   Appendix

2.7.1   Geometrical constraints for Mg-chloritoid zoning

In order to compare the zoning of measured X_{Mg} (Figure 2.13c) values in naturally occurring chloritoid with thermodynamically predicted X_{Mg} and volume proportions (Figure 2.13d) of chloritoid during prograde metamorphism, assumptions need to be made on the distribution, geometry and zoning characteristics. For our natural sample 19MR-03 these assumptions include: (1) increase in volume proportion for bulk rock chemistry implies chloritoid growth, (2) synchronistic nucleation and growth of chloritoid during prograde metamorphism, (3) homogenous grainsize of chloritoids throughout specimen, (4) measured crystals have been cut through the center of the grain, (5) measured values in the core of the chloritoid grains are representative for the specimen and relate to the onset and initial growth of chloritoid, and (6) measured values at the rim of the chloritoid grains are representative for the specimen and relate to the final stages of chloritoid growth.

Unlike cubic minerals such as quartz or garnet, it is not appropriate to apply a spherical geometry when transforming thermodynamic volume proportions to measured radius for monoclinic chloritoid. 3-dimensional grainsize proportions for chloritoid in sample 19MR-03 can be simplified into 3 major axes a, b and c (Figure 2.13). The measured proportions of these axes with respect to the axis of the measured profile ($a = 1.5$ mm) correspond to $b = 0.8a$ and $c = 1.333a$. Therefore, solving for a rectangular geometry, the measured profile a can be calculated via

$$a = \frac{Vol\%}{b\ c}\ V^*$$

(2.1)

where Vol% is the thermodynamically predicted volume proportion of chloritoid (Figure 2.13d), and V^* is the normalization factor

$$V^* = \frac{Vm}{Vol\%}$$

(2.2)

where Vm is the measured volume using the principle axes $a = 1.5$ mm, $b = 0.8a$ and $c = 1.333a$. Rearranging equation 2.1 in order to solve for a we find

$$a = \sqrt[\frac{1}{3}]{\frac{V^*Vol\%}{1.0664}} \tag{2.3}$$

In order to better fit measured zoning along the chloritoid a axis with thermodynamically predicted zoning in 2.3, we can adjust the axes proportions of chloritoid during growth. For example, only for the c axis, we can include an exponential factor where $c = 1.333a^{1/3}$. Substituting this into 2.1 we derive

$$a = 0.82459^{\frac{1}{7}}(V^{*3}Vol\%^3)^{\frac{1}{7}} \tag{2.4}$$

2.7.2   Supplementary material

Geological field work data within the Monte Rosa massif, obtained during field seasons, has been made available via https://github.com/Josh-VH/Monte-Rosa-Field-Data-2017-to-2020. All maps, sample locations, structural measurements, and photographs are integrated into a QGIS repository. Please refer to the README file for more information on how to access specific data.

All geochemical data is available on Zenodo via https://zenodo.org/record/5519419#.YUnWddMzaLU.

Bibliography

Angiboust, S., Agard, P., Jolivet, L., Beyssac, O., 2009. The zermatt-saas ophiolite: the largest (60-km wide) and deepest (c. 70–80 km) continuous slice of oceanic lithosphere detached from a subduction zone? Terra Nova 21 (3), 171–180.

Bearth, P., 1952. Geologie und petrographie des monte rosa. Beitraege zur Geologischen Karte der Schweiz Lf. 96, 1–94.

Bearth, P., 1953. Geologischer atlas der schweiz, 1: 25000, blatt zermatt (nr. 29). Schweizerische Geologische Kommission, Bern.

Beltrando, M., Compagnoni, R., Lombardo, B., 2010. (ultra-) high-pressure metamorphism and orogenesis: an alpine perspective. Gondwana Research 18 (1), 147–166.

Berman, R. G., 1988. Internally-consistent thermodynamic data for minerals in the system Na_2O-K_2O-CaO-MgO-FeO-Fe_2O_3-Al_2O_3-SiO_2-TiO_2-H_2O-CO_2. Journal of petrology 29 (2), 445–522.

Borghi, A., Compagnoni, R., Sandrone, R., 1996. Composite pt paths in the internal penninic massifs of the western alps: Petrological constraints to their thermo-mecanical evolution.

Bucher, K., Dal Piaz, G., Oberhänsli, R., Gouffon, Y., Martinotti, G., Polino, R., 2003a. Blatt 1347 matterhorn-geologischer atlas der schweiz 1: 25 000, karte 107. Bern: Bundesamt fur Wasser und Geologie.

Bucher, S., Schmid, S. M., Bousquet, R., Fügenschuh, B., 2003b. Late-stage deformation in a collisional orogen (western alps): nappe refolding, back-thrusting or normal faulting? Terra Nova 15 (2), 109–117.

Chopin, C., 1984. Coesite and pure pyrope in high-grade blueschists of the western alps: a first record and some consequences. Contributions to Mineralogy and Petrology 86 (2), 107–118.

Chopin, C., Monié, P., 1984. A unique magnesiochloritoid-bearing, high-pressure assemblage from the monte rosa, western alps: petrologic and 40 Ar-39 Ar radiometric study. Contributions to Mineralogy and Petrology 87 (4), 388–398.

Compagnoni, R., 1977. The sesia-lanzo zone: High pressure-low temperature metamorphism in the austroalpine continental margine.

Dal Piaz, G., 1999. The austroalpine-piedmont nappe stack and the puzzle of alpine tethys. Memorie di Scienze Geologiche 51 (1), 155–176.

Dal Piaz, G., Cortiana, G., Del Moro, A., Martin, S., Pennacchioni, G., Tartarotti, P., 2001. Tertiary age and paleostructural inferences of the eclogitic imprint in the austroalpine outliers and zermatt–saas ophiolite, western alps. International Journal of Earth Sciences 90 (3), 668–684.

Dal Piaz, G., Ernst, W., 1978. Areal geology and petrology of eclogites and associated metabasites of the piemonte ophiolite nappe, breuil—st. jacques area, italian western alps. Tectonophysics 51 (1-2), 99–126.

Dal Piaz, G., Pasquarè, G., Venturini, C., 2004. From the european continental margin to the mesozoic tethyan ocean: a geological map of the upper ayas valley (western alps). Mapping Geology in Italy. APAT-Dip. Difesa del Suolo-Servizio Geol. d'Italia. SELCA, Firenze, 265–272.

Dal Piaz, G. V., 2001. Geology of the monte rosa massif: historical review and personal comments. Schweizerische Mineralogische und Petrographische Mitteilungen 81 (3), 275–303.

Dal Piaz, G. V., Lombardo, B., 1986. Early alpine eclogite metamorphism in the penninic monte rosa-gran paradiso basement nappes of the northwestern alps. Geol. Soc. Am. Mem 164, 249–265.

Darbellay, B., 2005. Histoire polymétamorphique de la nappe du mont rose et contraintes isotopiques. master thesis. univseristy of lausanne.

de Capitani, C., Brown, T. H., 1987. The computation of chemical equilibrium in complex systems containing non-ideal solutions. Geochimica et Cosmochimica Acta 51 (10), 2639–2652.

De Graciansky, P.-C., Roberts, D. G., Tricart, P., 2011. The Birth of the Western and Central Alps: Subduction, Obduction, Collision. Vol. 14. Elsevier, pp. 289–315.

Decandia, F., 1972. La zona ofiolitiferadel bracco nel settore compreso fra levanto e la val graveglia (app. ligure). Mem. Soc. Geol. It. 11, 503–530.

Dessimoz, M., 2005. Métamorphisme et déformation entre la zone de zermat-saas et la zone du combin, val d'ayas, italie. master thesis. university of lausanne.

Dobretsov, N., 1991. Blueschists and eclogites: a possible plate tectonic mechanism for their emplacement from the upper mantle. Tectonophysics 186 (3-4), 253–268.

Engi, M., Scherrer, N., Burri, T., 2001. Metamorphic evolution of pelitic rocks of the monte rosa nappe. constraints from petrology and single grain monazite age data. Schweizerische Mineralogische und Petrographische Mitteilungen 81 (3), 305–328.

Ferrando, J., Scambelluri, M., Dal Piaz, G., Piccardo, G., 2002. The mafic boudins of the southern furgg-zone, monte rosa nappe, nw-italy: from tholeiitic continental basalts to alpine eclogites and retrogressed products. 81 riunione estiva soc. Geol. It., Torino, 10–12.

Gaidies, F., De Capitani, C., Abart, R., 2008. THERIA_G: a software program to numerically model prograde garnet growth. Contributions to Mineralogy and Petrology 155 (5), 657–671.

Gasco, I., Borghi, A., Gattiglio, M., 2011. P–T alpine metamorphic evolution of the monte rosa nappe along the piedmont zone boundary (gressoney valley, nw italy). Lithos 127 (1-2), 336–353.

Gerya, T., 2015. Tectonic overpressure and underpressure in lithospheric tectonics and metamorphism. Journal of Metamorphic Geology 33 (8), 785–800.

Gerya, T., Perchuk, L., Burg, J.-P., 2008. Transient hot channels: perpetrating and regurgitating ultrahigh-pressure, high-temperature crust–mantle associations in collision belts. Lithos 103 (1-2), 236–256.

Giacomazzi, L., 2017. Age of metasediments in the furgg zone, mezzalama, italy. master thesis, university of lausanne.

Jaboyedoff, M., Béglé, P., Lobrinus, S., 1996. Stratigraphie et évolution structurale de la zone de furgg, au front de la nappe du mont-rose= stratigraphy and structural evolution of the furgg zone, in front part of the monte rosa nappe. Bulletin de la Société Vaudoise des Sciences Naturelles 84, 191–210.

Jamtveit, B., Moulas, E., Andersen, T. B., Austrheim, H., Corfu, F., Petley-Ragan, A., Schmalholz, S. M., 2018. High pressure metamorphism caused by fluid induced weakening of deep continental crust. Scientific reports 8 (1), 1–8.

Jeffreys, H., 1937. X.—note on fracture. Proceedings of the Royal Society of Edinburgh 56, 158–163.

Keller, L., Abart, R., Stünitz, H., De Capitani, C., 2004. Deformation, mass transfer and mineral reactions in an eclogite facies shear zone in a polymetamorphic metapelite (monte rosa nappe, western alps). Journal of Metamorphic Geology 22 (2), 97–118.

Keller, L. M., Hess, M., Fügenschuh, B., Schmid, S. M., 2005. Structural and metamorphic evolution of the camughera–moncucco, antrona and monte rosa units southwest of the simplon line, western alps. Eclogae Geologicae Helvetiae 98 (1), 19–49.

Keller, L. M., Schmid, S. M., 2001. On the kinematics of shearing near the top of the monte rosa nappe and the nature of the furgg zone in val loranco (antrona valley, n. italy): tectonometamorphic and paleogeographical consequences. Schweiz. Mineral. Petrogr. Mitt 81 (3), 347–367.

Kramer, J., 2002. Structural evolution of the penninic units in the monte rosa region (swiss and italian alps). phd thesis. univsersity of basel.

Kramer, J., Abart, R., Müntener, O., Schmid, S. M., Stern, W. B., 2003. Geochemistry of metabasalts from ophiolitic and adjacent distal continental margin units: Evidence from the monte rosa region (swiss and italian alps). Swiss Bulletin of Mineralogy and Petrology 83 (2), 217–240.

Lanari, P., Vidal, O., De Andrade, V., Dubacq, B., Lewin, E., Grosch, E. G., Schwartz, S., 2014. Xmaptools: A MATLAB-based program for electron microprobe X-ray image processing and geothermobarometry. Computers Geosciences 62, 227–240.

Lapen, T. J., Johnson, C. M., Baumgartner, L. P., Dal Piaz, G. V., Skora, S., Beard, B. L., 2007. Coupling of oceanic and continental crust during eocene eclogite-facies metamorphism: evidence from the monte rosa nappe, western alps. Contributions to Mineralogy and Petrology 153 (2), 139–157.

Lardeaux, J.-M., 2014. Deciphering orogeny: a metamorphic perspective. examples from european alpine and variscan belts: Part i: Alpine metamorphism in the western alps. a review. Bulletin de la Société Géologique de France 185 (2), 93–114.

Le Bayon, R., de Capitani, C., Frey, M., 2006. Modelling phase–assemblage diagrams for magnesian metapelites in the system K_2O–FeO–MgO–Al_2O_3–SiO_2–H_2O: geodynamic consequences for the monte rosa nappe, western alps. Contributions to Mineralogy and Petrology 151 (4), 395.

Li, Z. H., Gerya, T. V., Burg, J.-P., 2010. Influence of tectonic overpressure on P-T paths of hp-uhp rocks in continental collision zones: thermomechanical modelling. Journal of Metamorphic Geology 28 (3), 227–247.
URL http://dx.doi.org/10.1111/j.1525-1314.2009.00864.x

Luisier, C., Baumgartner, L., Schmalholz, S. M., Siron, G., Vennemann, T., 2019. Metamorphic pressure variation in a coherent alpine nappe challenges lithostatic pressure paradigm. Nature communications 10 (1), 1–11.

Luisier, C., Baumgartner, L. P., Putlitz, B., Vennemann, T., 2021. Whiteschist genesis through metasomatism and metamorphism in the monte rosa nappe (western alps). Contributions to Mineralogy and Petrology 176 (1), 1–24.

Manatschal, G., Müntener, O., 2009. A type sequence across an ancient magma-poor ocean–continent transition: the example of the western alpine tethys ophiolites. Tectonophysics 473 (1-2), 4–19.

Mancktelow, N. S., 2008. Tectonic pressure: Theoretical concepts and modelled examples. Lithos 103 (1-2), 149–177.

Manzotti, P., Ballèvre, M., Dal Piaz, G. V., 2017. Continental gabbros in the dent blanche tectonic system (western alps): from the pre-alpine crustal structure of the adriatic palaeo-margin to the geometry of an alleged subduction interface. Journal of the Geological Society 174 (3), 541–556.

Marger, K., Luisier, C., Baumgartner, L. P., Putlitz, B., Dutrow, B. L., Bouvier, A.-S., Dini, A., 2019. Origin of monte rosa whiteschist from in-situ tourmaline and quartz oxygen isotope analysis by SIMS using new tourmaline reference materials. American Mineralogist: Journal of Earth and Planetary Materials 104 (10), 1503–1520.

Massonne, H.-J., Szpurka, Z., 1997. Thermodynamic properties of white micas on the basis of high-pressure experiments in the systems $K_2O - MgO - Al_2O_3 - SiO_2 - H_2O and K - 2O - FeO - Al_3O_3 - SiO_2 - H_3O. Lithos 41 (1-3), 229 - -250.$

McCarthy, A., Tugend, J., Mohn, G., Candioti, L., Chelle-Michou, C., Arculus, R., Schmalholz, S. M., Müntener, O., 2020. A case of ampferer-type subduction and consequences for the alps and the pyrenees. American Journal of Science 320 (4), 313–372.

Molnar, P., Lyon-Caen, H., 1988. Some simple physical aspects of the support, structure, and evolution of mountain belts. Processes in continental lithospheric deformation 218, 179–207.

Moulas, E., Burg, J.-P., Podladchikov, Y., 2014. Stress field associated with elliptical inclusions in a deforming matrix: Mathematical model and implications for tectonic overpressure in the lithosphere. Tectonophysics 631, 37–49.

Pawlig, S., 2001. Geological evolution of the monte rosa: constraints from geochronology and geochemistry of a talc kyanite chloritoid shear zone within the monte rosa granite (monte rosa nappe, italian western alps). Thesis.

Pawlig, S., Baumgartner, L., 2001. Geochemistry of a talc-kyanite-chloritoid shear zone within the monte rosa granite, val d'ayas, italy. Schweizerische mineralogische und petrographische Mitteilungen 81, 329–346.

Penniston-Dorland, S. C., Kohn, M. J., Manning, C. E., 2015. The global range of subduction zone thermal structures from exhumed blueschists and eclogites: Rocks are hotter than models. Earth and Planetary Science Letters 428, 243–254.

Robyr, M., Darbellay, B., Baumgartner, L., 2014. Matrix-dependent garnet growth in polymetamorphic rocks of the sesia zone, italian alps. Journal of metamorphic geology 32 (1), 3–24.

Schmalholz, S. M., Duretz, T., Hetényi, G., Medvedev, S., 2019. Distribution and magnitude of stress due to lateral variation of gravitational potential energy between indian lowland and tibetan plateau. Geophysical Journal International 216 (2), 1313–1333.

Schmalholz, S. M., Medvedev, S., Lechmann, S. M., Podladchikov, Y., 2014. Relationship between tectonic overpressure, deviatoric stress, driving force, isostasy and gravitational potential energy. Geophysical Journal International 197 (2), 680–696.

Schmalholz, S. M., Podladchikov, Y. Y., 2013. Tectonic overpressure in weak crustal-scale shear zones and implications for the exhumation of high-pressure rocks. Geophysical Research Letters 40 (10), 1984–1988.

Sibson, R. H., 1974. Frictional constraints on thrust, wrench and normal faults. Nature 249 (5457), 542–544.

Spear, F. S., Pattison, D. R., 2017. The implications of overstepping for metamorphic assemblage diagrams (MADs). Chemical Geology 457, 38–46.

Stampfli, G., Mosar, J., Marquer, D., Marchant, R., Baudin, T., Borel, G., 1998. Subduction and obduction processes in the swiss alps. Tectonophysics 296 (1-2), 159–204.

Steck, A., Masson, H., Robyr, M., 2015. Tectonics of the monte rosa and surrounding nappes (switzerland and italy): Tertiary phases of subduction, thrusting and folding in the pennine alps. Swiss Journal of Geosciences 108 (1), 3–34.

Turcotte, D. L., Schubert, G., 2002. Geodynamics. Cambridge university press.

Vaughan-Hammon, J. D., Luisier, C., Baumgartner, L. P., Schmalholz, S. M., 2021. Peak alpine metamorphic conditions from staurolite bearing metapelites in the monte rosa nappe (central european alps) and geodynamic implications. Journal of Metamorphic Geology n/a (n/a).
URL https://onlinelibrary.wiley.com/doi/abs/10.1111/jmg.12595

Whitney, D. L., Evans, B. W., 2010. Abbreviations for names of rock-forming minerals. American mineralogist 95 (1), 185–187.

Peak Alpine metamorphic conditions from staurolite-bearing metapelites in the Monte Rosa nappe (Central European Alps) and geodynamic implications

Joshua D. Vaughan-Hammon[1]**, Cindy Luisier**[2]**, Lukas P. Baumgartner**[1]**, Stefan M. Schmalholz**[1]

[1]Institut des Sciences de la Terre, University of Lausanne, Lausanne, Switzerland.

[2]Univ Rennes, CNRS, Géosciences Rennes UMR 6118, Rennes, France.

Journal of
METAMORPHIC
GEOLOGY

1 mm
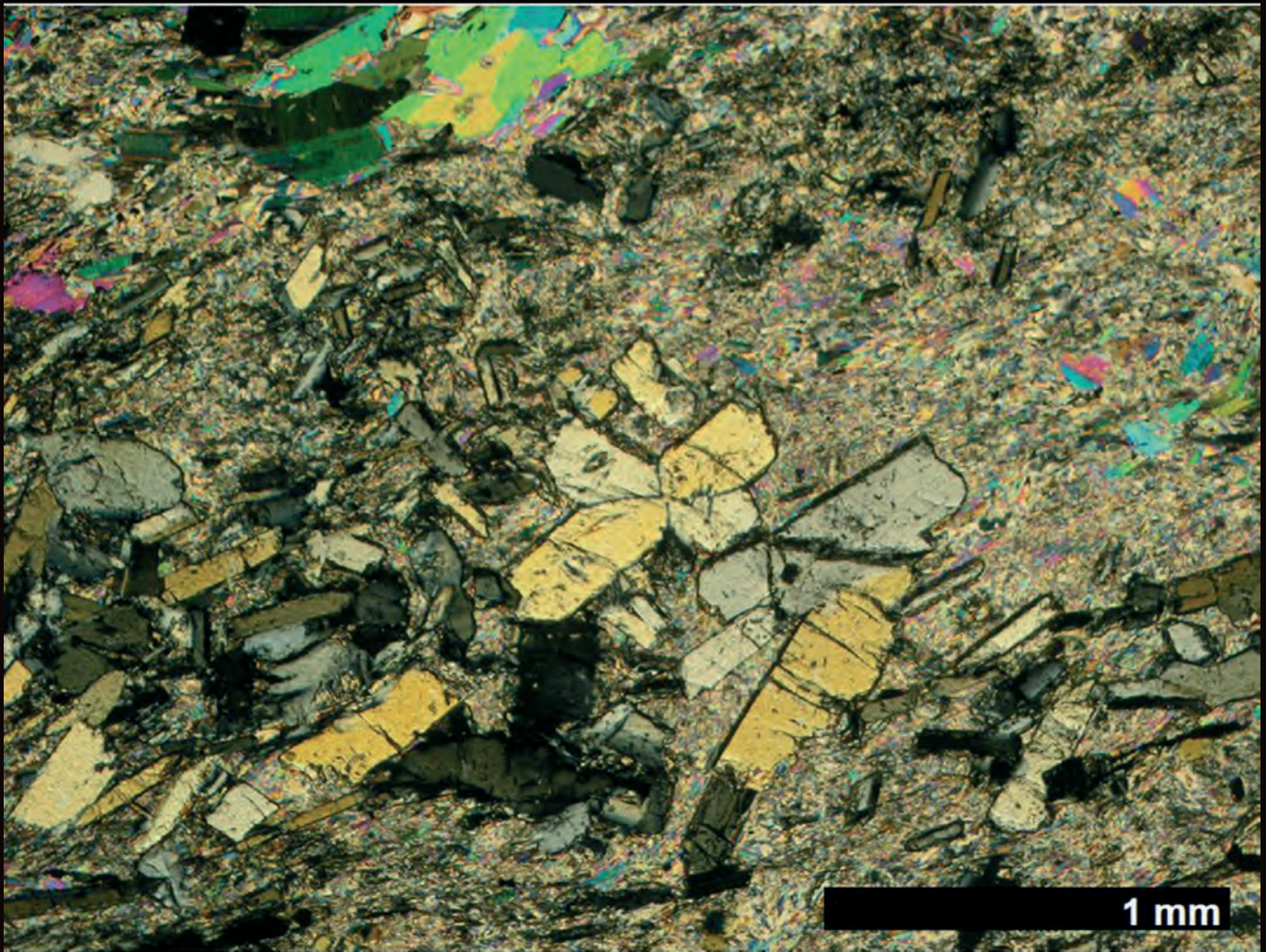
WILEY

Abstract

The tectono-metamorphic evolution of the European Alps is still contentious. The Monte Rosa tectonic unit is a prominent nappe in the Central European Alps and estimates of its peak Alpine pressure (P) and temperature (T) conditions are essential for reconstructing its tectono-metamorphic evolution. However, the reported peak Alpine P and T estimates vary considerably between 1.2 and 2.7 GPa and 490 and 640°C for a variety of lithologies.

Here, we show petrology and pseudo-section modelling of metapelitic assemblages from the western portions of the Monte Rosa nappe (upper Ayas valley, Italy). We present newly discovered staurolite-chloritoid bearing metapelitic assemblages. These assemblages exhibit an Alpine high-P metamorphic overprint of a former contact-metamorphic mineral assemblage generated by post-Variscan granitic intrusions. Staurolite contains major amounts of Zn (up to 1.0 atoms per formula units), which is currently, in contrast to Fe- and Mg-staurolite end-members, not considered in any thermodynamic database. We employ two end-member mixing models for Zn in staurolite, site mixing and molecular mixing. Both models enlarge the P and T stability range for the observed assemblage, where site mixing has the largest influence of $\pm$ 0.2 GPa and $\pm$ 20°C. Our results for three metapelite assemblages, with and without staurolite, indicate peak Alpine P of 1.6 ± 0.2 GPa and peak T of 585 ± 20°C. These peak P estimates agree with previously published estimates for metagranites in the nappe, and are in stark contrast with peak P obtained from talc, chloritoid, phengite and quartz bearing lithologies termed 'whiteschists' (> 2.2 GPa). Our results confirm a variation of peak Alpine P of 0.6 ± 0.2 GPa between metagranite/metapelite lithologies and a nearby whiteschist lens (> 2.2 GPa) within the metagranite. Field observations indicate that the studied region is structurally coherent and that the whiteschist is not a tectonic slice formed by tectonic mélange. We suggest that the consistent peak P for metapelite and metagranite assemblages represents the regional peak P and that the higher pressure recorded in the whiteschist lens is likely due to dynamic pressure, possibly resulting from tectonic and/or reaction-induced stresses. If the calculated P of 1.6 ± 0.2 GPa represents regional peak Alpine conditions,

then the Monte Rosa nappe was exhumed from a significantly shallower depth than previously assumed, based on peak P estimates > 2.2 GPa for whiteschist lithologies.

3.1 Introduction

The Western and Central European Alps (Figure 3.1) played a significant role in the pioneering discoveries of high- and ultra high-pressure, (U)HP, metamorphic rocks (Chopin, 1987; Chopin et al., 1991; Chopin, 1984; Goffe and Chopin, 1986; Reinecke, 1991). These rocks contain evidence of the geodynamic environment of orogens and provide insight into pressures, temperatures and chemical systems unobservable to humans. Geographically, the Monte Rosa nappe is located in the Central European Alps. It is a continental unit belonging to the Middle Penninic domain generated during the western Alpine orogeny (Figure 3.1; e.g. Handy et al. (2010)), that underwent HP conditions associated with its burial below the Adriatic continent during the orogenesis. Petrological investigations into rare magnesiochloritoid-bearing lithologies (named 'whiteschists') revealed Alpine eclogite facies metamorphic conditions (Chopin, 1984). These discoveries prompted numerous studies assessing suitable mechanisms by which (U)HP crustal rocks can be transported during orogenesis to and from significant depth; sometimes more than 100 km if lithostatic pressure is assumed (Hacker and Gerya, 2013; Kurz and Froitzheim, 2002). However, published estimates of peak Alpine metamorphic conditions for the Monte Rosa nappe highlight large disparities; with peak P estimates ranging between 1.2 and 2.7 GPa and temperature (T) estimates between 490 and 640°C (Figure 3.2a) (Borghi et al., 1996; Chopin, 1984; Dal Piaz and Lombardo, 1986; Ferrando et al., 2002; Gasco et al., 2011; Keller et al., 2004; Lapen et al., 2007; Le Bayon et al., 2006; Luisier et al., 2019).

The assessment of suitable mechanisms by which rocks can be transported through an orogen from (U)HP conditions to the surface requires an estimate of the maximal burial depth at which they equilibrated (e.g. Petrini and Podladchikov, 2000). Large disparities in peak P within a structurally coherent nappe poses difficulties when attempting to resolve the tectonometamorphic history if it is assumed that peak P represents the lithostatic pressure, which is mainly a function of burial depth (Schenker et al., 2015; Schmalholz et al., 2014b). However, the pressure, or mean stress, in a rock cannot be exactly lithostatic during an orogeny due to differential stresses, required to drive rock deformation (Gerya, 2015; Mancktelow, 1993; Schmalholz et al., 2014b) or to balance lateral variations in gravitational potential energy

(Molnar and Lyon-Caen, 1988; Schmalholz et al., 2019, 2014a). The deviation from lithostatic pressure is commonly termed tectonic pressure and both its magnitude (Li et al., 2010; Luisier et al., 2019; Reuber et al., 2016) and impact on metamorphic reactions is disputed (Moulas et al., 2019; Wheeler, 2018).
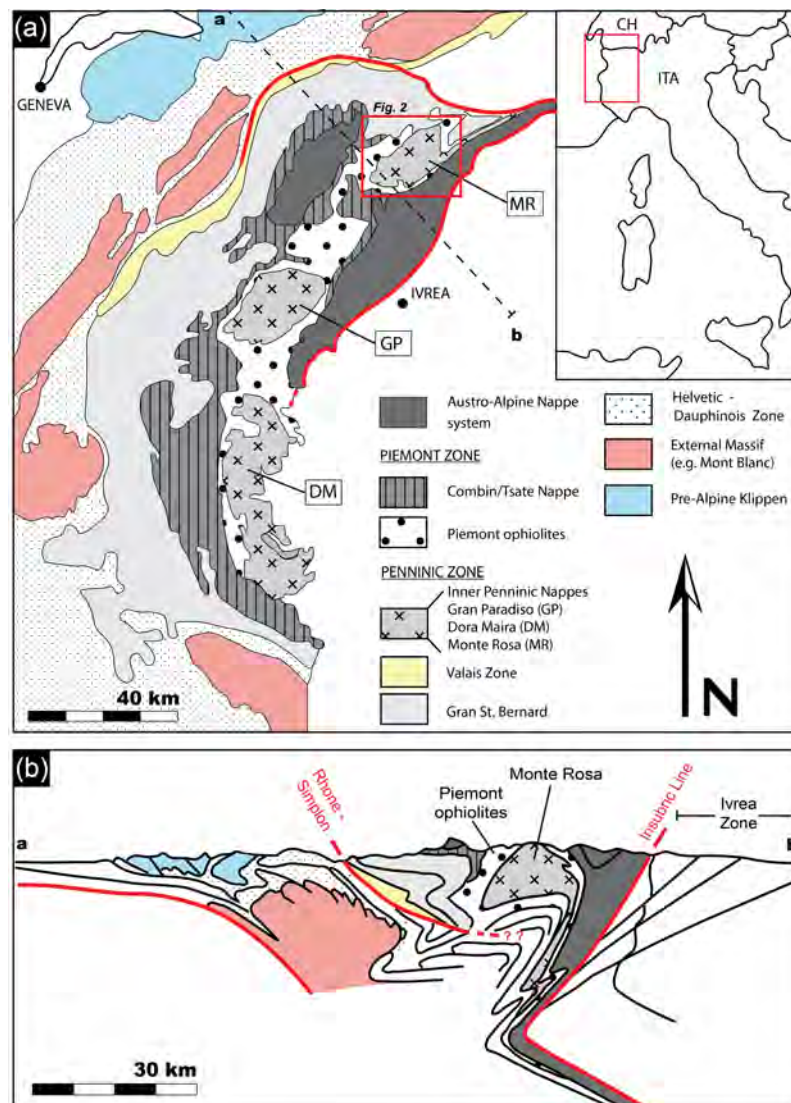
Figure 3.1: (a) Simplified tectonic map of the western Alps showing the major tectonic units; adapted from Beltrando et al. (2010). The Monte Rosa area is in the red box. (b) Simplified cross-section through the western Alps highlighting the Penninic + Piemont units and major structural discontinuities; modified from figure. 23 of Steck et al. (2015). For better visibility and to provide a first-order geometry, we have combined several tectonic units, for example, the Pre-Alpine Klippen include the Niesen nappe or the Helvetic-Dauphinois Zone includes the Ultrahelvetics. For a detailed tectonic map and section the reader is referred to Steck et al. (2015)).

For the Monte Rosa nappe, specifically within the western portions of the nappe at the head of the Ayas valley, Italy (Figure 3.2a), recent work by Luisier et al. (2019) reported peak Alpine P variations (0.8 ± 0.3 GPa) between a whiteschist (~ 2.2 GPa) and the host metagranite (~ 1.4 GPa) (Figure 3.2b). Based on field and microstructural observations, as well as geochemical analyses, Luisier et al. (2019) proposed that the pressure variations cannot be explained by tectonic mixing (mélange), as the whiteschist and metagranite are structurally coherent (documented by cross-cutting post-Variscan dikes). They also excluded complete retrogression of the jadeite-free metagranite and sluggish kinetics due to low water activity. Luisier et al. (2019) suggests that these peak P variations could represent tectonic pressure variations.

Here, we test whether the whiteschist HP imprint of 2.2 to 2.5 GPa represents regional, 'whole-nappe', metamorphic conditions or local deviations, within the upper Ayas valley region (Figure 3.2a). We have investigated numerous metapelitic samples from the Monte Rosa basement metasediments, and identified three independent mineral assemblages that are from outcrops structurally continuous with the localities of previous studies (Chopin and Monié, 1984; Luisier et al., 2019; Marger et al., 2019; Pawlig and Baumgartner, 2001). The samples are unique mineral assemblages representing peak Alpine conditions within pseudomorphs of former contact metamorphic minerals, suitable therefore, to understand further the nature and existence of peak P variations. The main assemblages we have investigated are staurolite-chloritoid bearing that are, to the best of our knowledge, the first described occurrences in the Monte Rosa nappe. Staurolite bearing assemblages can pose difficulties in thermodynamic modelling, due to the apparent compositional variability (e.g. Hawthorne et al., 1993). This variability is primarily the result of unknown site occupations involving Al, Mg, Fe^{2+}, Fe^{3+}, Ti, Cr, Zn, Co and Li, as well as H content (Dutrow et al., 1986; Griffen, 1981; Hawthorne et al., 1993; Holdaway et al., 1986; Tuisku et al., 1987). These variabilities, combined with the lack of thermodynamic data for staurolite, require consideration when calculating metamorphic conditions of formation, specifically when applying the appropriate mixing model (e.g. Berman, 1990; Powell and Holland, 1993). For the analyzed rocks, we investigate different mixing models and the subsequent effects on pseudo-section derived peak P and T.
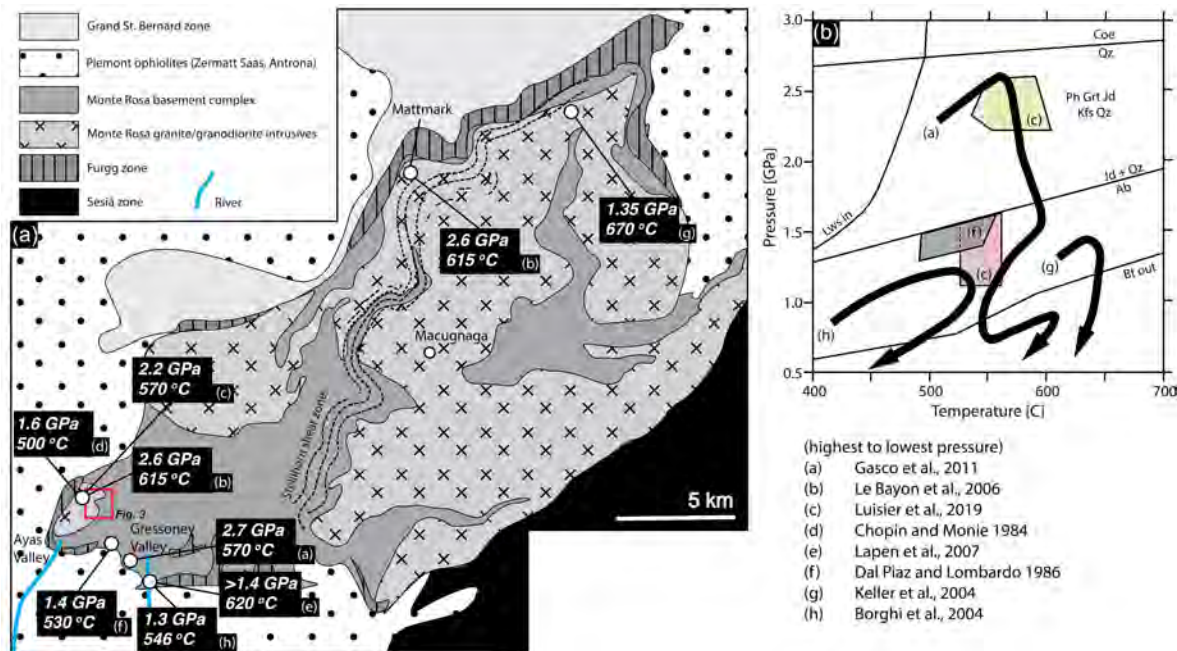
Figure 3.2: ((a) Simplified geological map of the Monte Rosa nappe modified after Steck et al. (2015) with estimates of peak Alpine metamorphism from multiple studies (represented from high to low pressure); study area in red box. (b) Pressure-temperature plot of Alpine metamorphism, outlining the peak Alpine pressure disparities, modified after Luisier et al. (2019).

3.2   Geological setting

3.2.1   General overview

The Monte Rosa massif, christened the "Queen of the Alps" (King, 1858), is one of the geologically most studied tectonic units in the Alpine orogenic chain (Dal Piaz, 2001)). It belongs to the internal crystalline massifs of the Western and Central Alps, along with the Dora Maira and Gran Paradiso massifs (Figure 3.1a). These massifs represent dismembered continental crust incorporated into the Eocene-aged Alpine orogeny (Steck et al., 2015). The Monte Rosa massif consists of a pre-Variscan basement, which was intruded by Permian-age granitic bodies (Figure 3.2a). The current position of the basement complex resides within the collisional Austroalpine-Penninic wedge and lies structurally between the overlying Zermatt-Saas and underlying Antrona ophiolitic sequences (Figure 3.1b).

The palaeogeographic location of the Monte Rosa unit has been attributed in many earlier studies to the southern Briançonnais domain as part of the European margin (Dal Piaz, 2001; Steck et al., 2015). This domain was separated from the European margin by the Valais basin to the north and bordered by the Piemont basin to the south prior to their subsequent collision during Alpine orogeny.

The Monte Rosa massif consists of lithologies that record a multiphase metamorphic history. This massif was described as a complex poly-metamorphic basement by Bearth (1952), consisting of high grade deformed paragneisses and a younger granitic complex, consisting of granitic to granodioritic intrusions and associated dykes. The pre-granitic polymetamorphic basement complex contains metapelites locally preserving a high grade relict assemblage composed of garnet, biotite, sillimanite, quartz, K-feldspar, cordierite, muscovite and plagioclase (Bearth, 1952; Dal Piaz and Lombardo, 1986). Subsequent petrological investigations of these assemblages revealed a high-temperature, pre-Alpine assemblage related to an upper Amphibolite facies sillimanite-K-feldspar metamorphism, $\sim 700°C/0.3$-0.6 GPa (Ferrando et al., 2002), associated with Variscan metamorphism and dated at $c.$ 330 Ma (e.g. Engi et al., 2001). This basement complex was folded and deformed prior to the post-Variscan granitic intrusions dated at 269 ± 4 Ma (Pawlig, 2001). A contact aureole in the metasediments of the basement complex resulted from the thermal perturbation related to the granitic intrusions, leading locally to partial melting (Dal Piaz, 2001) (S3.10 supplementary material, herein referred to as SM-S(n)). Hydrothermal alteration locally overprinting the granite has been documented (Luisier et al., 2019; Marger et al., 2019; Pawlig and Baumgartner, 2001). Th e Alpine HP eclogite facies metamorphism (1.2-2.7 GPa/490-640°C (Borghi et al., 1996; Chopin, 1984; Dal Piaz and Lombardo, 1986; Ferrando et al., 2002; Gasco et al., 2011; Keller et al., 2004; Lapen et al., 2007; Le Bayon et al., 2006)) has been dated at 42.6 ± 0.6 Ma (Lapen et al., 2007) and retrogression to greenschist facies was dated between 40-37 Ma for both the Monte Rosa (Chopin, 1984) and the overlying Zermatt-Saas units (Skora et al., 2015). Lastly, the Monte Rosa nappe exhibits an albite-oligoclase metamorphic isograd first described by (Bearth, 1953). This Barrovian-style isograd is similar to other units of the Central Alps (e.g. Lepontine Dome), and suggests a post-peak Alpine regional thermal metamorphic event

(Niggli, 1960). Fission track zircon ages indicate that the western region of the Monte Rosa nappe cooled below $\sim 225°C$ at $c.$ 33 Ma (Hurford et al., 1991). Hence, the massif was exhumed to a depth less than ~ 10 km already at $c.$ 33 Ma, assuming a geothermal gradient of 22.5 $°C\,km^{-1}$.

3.2.2   Previous estimates of peak Alpine PT

We review shortly previous estimates for peak Alpine conditions incurred by basement lithologies of the Monte Rosa nappe, focusing on its western portions, namely the upper Ayas and Gressoney valleys in the southwest portions of the nappe and the Mattmark and Loranco localities (Figure 3.2a). The western portion of the Monte Rosa nappe is separated from the eastern portion by a structural discontinuity, termed the Stellihorn shear zone (Figure 3.2a, Steck et al. (2015)).

Dal Piaz and Lombardo (1986) described micaschist and metabasalt samples from the upper Gressoney valley (Figure 3.2a). Micaschist peak HP paragenesis consists of Ph, Cld, Grt, Ky $\pm$ Gln (mineral abbreviations after Whitney and Evans (2010)). Metabasaltic peak paragenesis consists of Grt, Omp, Gln, Rt, Pg $\pm$ Qz $\pm$ Zo. Peak P was constrained at 1.4 GPa due to the absence of jadeite within the metagranite via the reaction Ab = Jd + Qz (Dal Piaz and Lombardo, 1986; Holland, 1979). The minimum P was estimated at 0.8-1.0 GPa, using jadeite and omphacite molar contents of pyroxene within metabasalt samples (Holland, 1979). Minimum temperature (T) estimates were defined by the paragonite-in reaction in metabasalts: Lws + Ab = Pg + Qz + H2O (Holland, 1979). Maximum T is constrained via the chloritoid-out reaction in micaschists: Cld + Qz = St + Grt + H2O (Rao and Johannes, 1979). Peak T ranges were refined using the garnet-clinopyroxene thermometer from Ellis and Green (1979) between 440-530°C.

Borghi et al. (1996) sampled metapelitic and metabasic lithologies from the upper Gressoney valley. High pressure minerals consist of Qtz, Ab, Ph, Pg, Chl, Grt, Ky, Cld, Gln, Rt and Ep. Peak P from silica content of phengite (Massonne and Schreyer, 1987) and peak T from garnet-phengite reveal a minimum pressure of 1.3 GPa and a temperature of 546 $\pm$ 21°C.

Keller et al. (2004) examined two metapelitic samples from a continuous structural layer involved within a shear zone from the Loranco locality (Figure 3.2). The shear zone is interpreted to represent peak Alpine HP conditions, partially preserving pre-Alpine mineral assemblages. The HP paragenesis consists of Ph, Pg, Qz, Grt, Pl, Ky, Ilm, Rt and Tur. The resulting stability field is between 620-670°C and 1.20-1.35 GPa, via thermodynamic modelling using Berman (1988), update 92 database, constrained also by the lack of granite anatexis (Huang and Wyllie, 1974).

Gasco et al. (2011) investigated metapelitic samples and metabasic samples from a mafic boudin within the Monte Rosa basement micaschists in the upper Gressoney valley, close to the tectonic contact with the structurally higher Zermatt-Saas unit (Figure 3.2). Eclogite metabasic boudins represent a mineral assemblage of Omp, Gln, Grt, Ph, Lws, Rt, and Qz, presumably equilibrated at peak conditions at 2.4-2.7 GPa and 550-570°C (Holland and Powell (1998), update 2004). Metapelite assemblages of Ph, Pg, Grt, Chl, Ab/Olig, Hbl, Qz, Rt, Ilm ± Bt, are interpreted to represent re-equilibration during decompression at 0.7-0.9 GPa and 550-600°C.

Peak Alpine HP conditions have also been calculated from assemblages within the Monte Rosa metagranites known as "whiteschists", consisting of chloritoid, talc, phengite and quartz ± garnet or kyanite (Chopin, 1984; Le Bayon et al., 2006; Marger et al., 2019). A refinement of these estimates has recently been made by Luisier et al. (2019) (Figure 3.2b). This unique assemblage has a protolith chemistry deriving from the late magmatic metasomatic alteration of the host granite (Pawlig and Baumgartner, 2001). The peak P paragenesis indicates approximately 2.2 ± 0.2 GPa at 540-600°C (Luisier et al., 2019). Peak Alpine conditions were also estimated for the host/protolith metagranite. Peak metamorphic assemblages consist of phengite + titanite pseudomorphs replacing biotite, as well as fine-grained pseudomorphs after plagioclase, consisting of albite + zoisite ± phengite ± garnet. These parageneses, as well as additional pressure estimates based on Si-content in phengite, combined with water activity estimates, and the lack of jadeite within the metagranite, prompted the interpretation that the metagranite never experienced pressures over 1.6 GPa (at T 540-600°C).

3.2.3   Study area

We have investigated metapelitic samples in the western extent of the Monte Rosa basement in a region termed the "Cirque du Véraz" (personal communication with G. Dal Piaz) within the upper Ayas valley, Italy (Figures 3.2 and 3.3). Due to recent glacial retreat, a newly exposed area has become accessible for detailed geological mapping and sampling (Figure 3.3). The field area provides an exposed section through the Monte Rosa basement complex up to the overlying Zermatt-Saas Unit. Geometrically, the study area has a domal structure with Monte Rosa metagranites residing within the core of the dome, overlain sequentially by Monte Rosa polymetamorphic basement metapelites, locally overlain by a thin layer of Furgg zone metasediments, and eventually the tectonic contact with the overlying Zermatt-Saas units. The locality is situated directly on the antiformal trace of the backfold, which pervasively affects the nappe (Steck et al., 2015) (Figures 3.1a and 3.3). High strain domains typically display late-Alpine metamorphism and deformation, equilibrated to greenschist facies during decompression (Figures 3.3 and 3.4c). The basement complex locally preserves pre-Alpine structures in low strain domains (Figure 3.3), whose mineral assemblages were re-equilibrated during peak Alpine metamorphism (Figures 3.4c and d).

Samples were obtained east of the Perazzispétz ridge (Swiss coordinates E: 2626459 N: 84117 alt: 3302 m and E: 2626048 N: 83526 alt: 2920 m, Figures 3.3 and 3.4). The samples consist of layered metapelites (Figures 3.4b and c) recording a pre-Alpine foliation. Locally, granitic dikes crosscut the foliation (Figure 3.4b), attesting to the pre-Alpine age of the main deformation seen in these outcrops. We report few samples of former aluminosilicate bearing contact metamorphic metapelites that were subsequently equilibrated at HP conditions (Figures 3.4d and SM-S3.11). The peak Alpine metamorphic minerals are observed within pseudomorphs replacing former larger pre-Alpine minerals (Figures 3.4d and SM-S3.12). The presence of pre-Alpine dykes crosscutting metapelite lithologies (Figures 3.4a and b), and migmatite textures associated with pre-Alpine granitic intrusion (SM-S3.10) indicate that this area represents a structurally coherent tectonic body, and not a tectonic mélange.
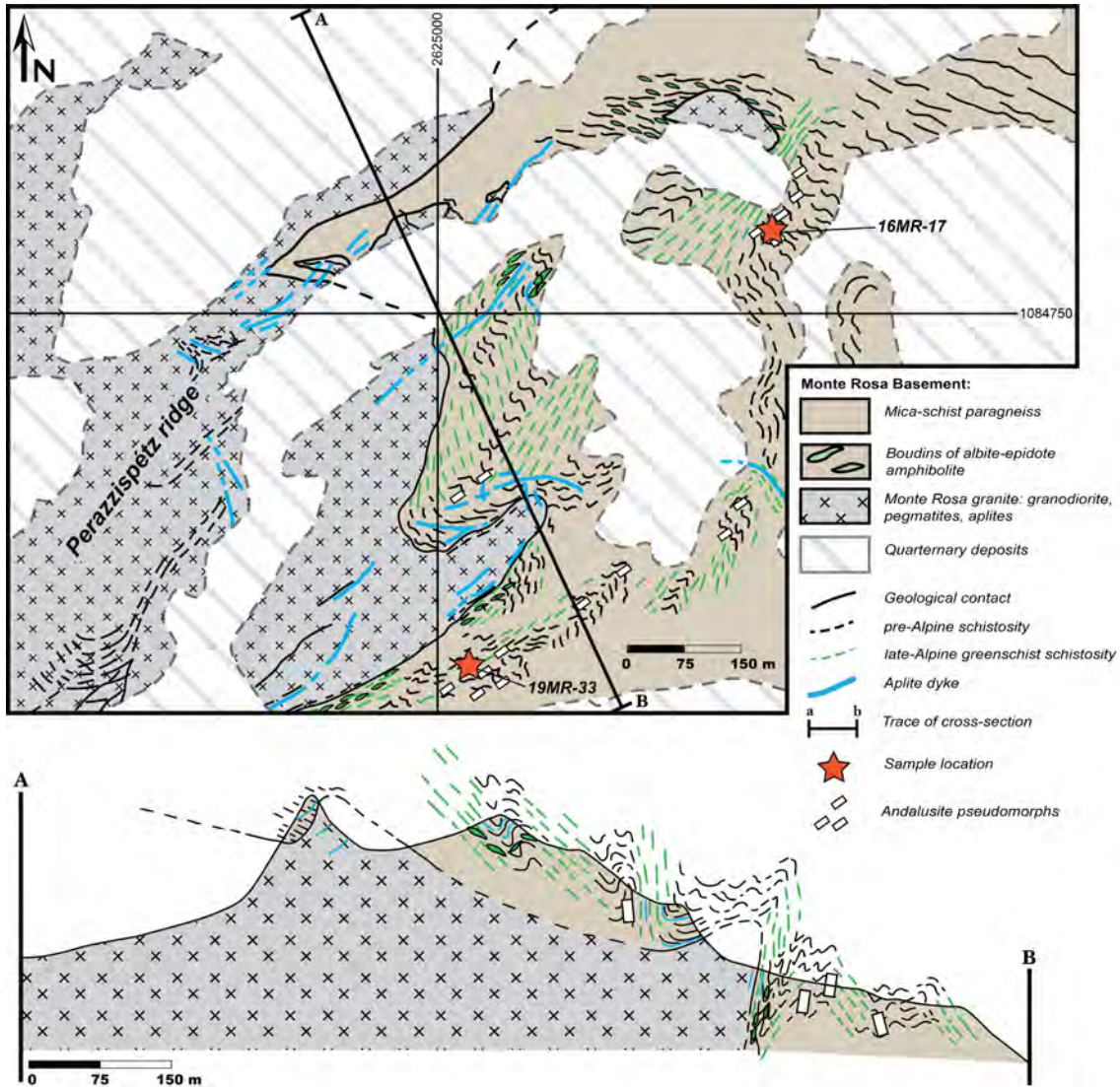
Figure 3.3: Geological map and cross-section of the "Peraz" study area in the western Monte Rosa basement and metagranite, including the location of metapelite samples taken for this study (Red stars). Note the separation of pre-Alpine and late-Alpine schistosity.

3.3 Methodology

3.3.1 Analytical methods

Electron probe microanalysis (EPMA) of major and minor element compositions of white mica, chloritoid, staurolite, garnet and chlorite were conducted using a JEOL JXA-8350F HyperProbe at the University of Lausanne, Switzerland. In total, quantitative analysis of 46 white mica grains (197 points), 11 chloritoid grains (149 points), 12 stauro-

lite grains (68 points), 8 garnet grains (72 points), and 5 chlorite grains (30 points) was undertaken. The operating conditions were 15.0 kV acceleration voltage and 1.5-2.0 x 10^{-8} A, with a beam diameter of 5.0 μm. Natural minerals were used as reference materials: orthoclase (K_2O, SiO_2), andalusite (Al_2O_3), albite (Na_2O), fayalite (FeO), forsterite (MgO), tephrite (MnO), wollastonite (CaO), sphalerite (ZnO), and rutile (TiO_2). Structural formulae from Howie et al. (1992) were used for stoichiometric calculations on the basis of 11 oxygens for white mica, 8 cations for chloritoid, 12 oxygens for garnet and 13 oxygens for chlorite (($Mg,Fe)_5Al[AlSi_3O_{10}](OH)_8$). For staurolite (($Fe^{+2},Mg,Zn)_{3-4}(Al,Fe^{+3},Ti)_{17-18}O_{16}[(Si,Al)O_4]_8H_{3-4}$ (Deer et al., 2013)), normalization assuming $Si + Al - \frac{1}{3} Li + \frac{2}{3} Ti + Fe^{3+} = 25.55$ cations as proposed in Holdaway et al. (1991) was used, due to uncertainties in H and Fe^{3+} content.

3.3.2   Thermodynamic modelling

Phase diagrams were calculated using the THERIAK-DOMINO software suite (de Capitani and Brown, 1987) in combination with the Berman database (Berman, 1988, 92 update). This database was chosen in order to: 1) have an internally consistent database, and 2) to accurately compare thermodynamically calculated P and T with results of the study of Luisier et al. (2019). Bulk compositions were calculated based on quantitative image analysis of equilibrium subdomains in each sample, using EPMA derived mineral compositions, along with the MATLAB$^{©}$ based image processing software XMapTools (Lanari et al., 2014), in the chemical system NCKFMASH (SM-S3.16 and S3.20). Solution models used are after the 92 update of Berman (1988) which include: H_2O after the HAAR equation of state (Haar, 1984), white mica after Massonne and Szpurka (1997), chloritoid, garnet and chlorite after the 92 update of Berman (1988), and staurolite after Nagel et al. (2002).

The current solution model data for staurolite considers only Fe and Mg-endmembers (Nagel et al., 2002). However, a wealth of literature highlights a wider range of possible staurolite endmembers (e.g. Zn (e.g. Holdaway et al., 1991)). In order to account for the lack of variability in experimentally derived endmember thermodynamic data, e.g. Zn in staurolite,

we have employed a method to adjust the activity of available solid solution endmember data (Nagel et al., 2002). To do so, the activity (a_i^{reduced}) for Mg and Fe staurolite endmembers were reduced to account for the Zn endmember (see appendix 3.9). The thermodynamic data of the endmember staurolites were adjusted, using two mixing models to account for the Zn-concentrations analyzed, within the JUN92B database by Berman (1988) utilized by THERIAK-DOMINO. Both models assume ideal mixing: model 1 assumes molecular mixing, while model 2 assumes site mixing. We adjust the thermodynamic properties of Fe and Mg staurolite endmembers using an entropy correction, $S_{\text{eff}}^{(\text{T0,P0})} = S_{\text{MgSt}}^{(\text{T0,P0})} - \text{R}\ln a_i^{\text{reduced}}$ (see appendix 3.9 for full derivation). PT errors are estimated from the resulting stability fields calculated with and without the entropy correction for staurolite bearing assemblages.
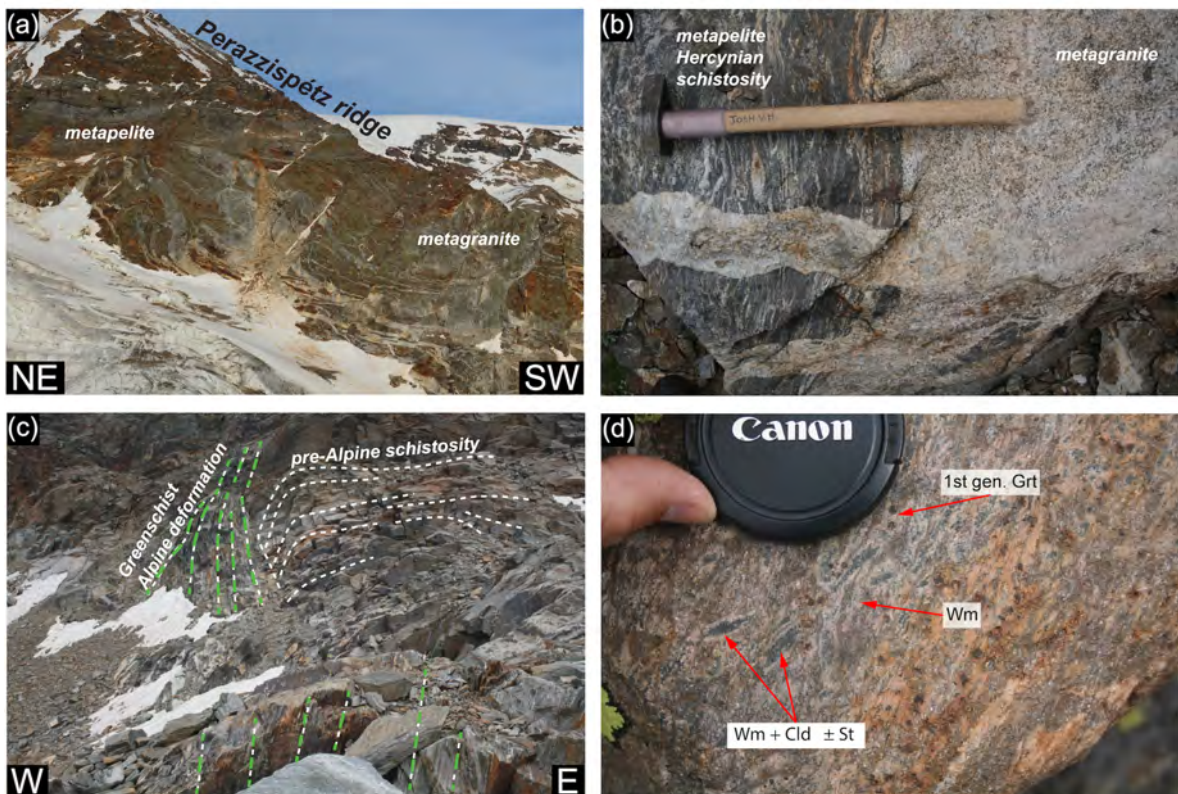
Figure 3.4: Representative field images for the study area and metapelitic samples: (a) outcrop of basement metapelites intruded by metagranites (note aplitic dykes), (b) aplitic dyke of the Permian Monte Rosa metagranite cross-cutting gneisses of the Monte Rosa basement, (c) deformed metapelitic basement showing horizontal pre-Alpine deformation sheared and deformed by vertical late Alpine greenschist facies shear zones, (d) domains of preserved peak Alpine assemblages (mineral abbreviations after Whitney and Evans (2010)).

3.4   Petrographic descriptions

In order to capture peak Alpine conditions, samples were taken from within the Monte Rosa polymetamorphic basement that has experienced little to no late Alpine metamorphic and deformational overprint (Figures 3.3 and 3.4c). The two samples analyzed (16MR-17 & 19MR-33) were taken from close proximity to each other (Figure 3.3). These samples are metapelites, which show different mineral paragenesis due to variable protolith chemistry.

3.4.1   Sample 16MR-17

Sample 16MR-17 displays a weakly inherited foliation defined by an assemblage of fine-grained quartz + white mica + garnet + chlorite, wrapping around large garnet porphyroblasts, as well as domains consisting of a fine-grained assemblage of staurolite, chloritoid, phengite and paragonite (Figures 3.5a, b and c, and SM-S3.13). These fine-grained domains have a pseudomorph texture, presumably after a larger mineral, due to their sharp boundaries and regular form (Figures 3.5a and SM-S3.13). Accessory minerals are apatite, rutile, tourmaline, ilmenite, zircon and monazite. Late matrix phases consist of biotite, replacing garnet, and chlorite, partially replacing garnet and biotite (Figure 3.5e). Two generations of garnet exist (Figure 3.5b). Larger garnet porphyroblasts represent an older 1st generation Grt. A second generation of smaller garnets (2nd generation Grt) are embedded in a fine-grained matrix of white mica (phengite + paragonite, Figure 3.5b) and minor amounts of quartz and chlorite (Figure 3.5e). First generation garnets show dark dissolution-precipitation rims marked by fine inclusions of an unknown mineral (Figure 3.5b). These dark precipitation growth rims coincide with the smaller 2nd generation garnets, which have inclusion rich cores (Figure 3.5b). The schistosity defined by white mica envelops 1st generation garnets suggesting the garnet grew pre- or syn-tectonically (Figure 3.5b). However, 2nd generation garnets grow statically and post-tectonically with undeformed white mica (Figure 3.5e). 2nd generation garnet is observed to grow statically over former pressure shadows associated with 1st generation garnets (Figure 3.5b).

Based on textural domains, two equilibrium assemblages were defined that are interpreted to have captured peak Alpine metamorphic conditions. Assemblage 1 consists of domains of staurolite, chloritoid, phengite and paragonite, pseudomorphing former andalusite, as high-lighted in Figures 3.5a and SM-S3.12. The whole pseudomorph domains after andalusite have grown statically, with un-oriented mica and staurolite twins (Figure 3.5c). Assemblage 2 consists of 2nd generation garnets, phengite, paragonite, chlorite and quartz (Figures 3.5b and e). Assemblage 1 and 2 are statically grown and therefore post-kinematic.

3.4.2 Sample 16MR-33

Sample 19MR-33 is texturally and petrologically similar to 16MR-17. However, no staurolite is observed in the fine-grained pseudomorph domains that characterize assemblage 1, only chloritoid is present in a matrix of phengite and paragonite (Figure 3.5d).

3.5 Mineral chemistry

Representative compositional results for phengite, paragonite, chloritoid and staurolite in assemblage 1, as well as phengite, paragonite, garnet and chlorite in assemblage 2 of sample 16MR-17 and phengite, paragonite, chloritoid in assemblage 3 of sample 19MR-33 are displayed in Table 3.1. In assemblage 1, two white micas are distinguished. Phengite has Si content ranging between 3.18 to 3.25 a.p.f.u, which is correlated with an increase of the Tschermak component between 0.18 to 0.25 (Figure 3.6a). Phengites have a K content ranging between 0.85 and 0.91 a.p.f.u. (Figure 3.6c). Phengite coexists with paragonite with a Na content between 0.83 to 0.87 a.p.f.u. (Figure 3.6c). Chloritoid compositions are relatively richer in Fe compared to Mg, with an X_{Mg} (Mg/(Mg+Fe)) between 0.26 – 0.33. Similarly, staurolite is Fe rich, with a X_{Fe} (Fe/(Mg+Fe)) of 0.68 – 0.74 (Figure 3.6b). The high content of zinc is remarkable in staurolite, reaching 1.0 a.p.f.u. in some samples (Figure 3.6d and Table 3.1). No Zn was found by EPMA analysis in any other mineral.
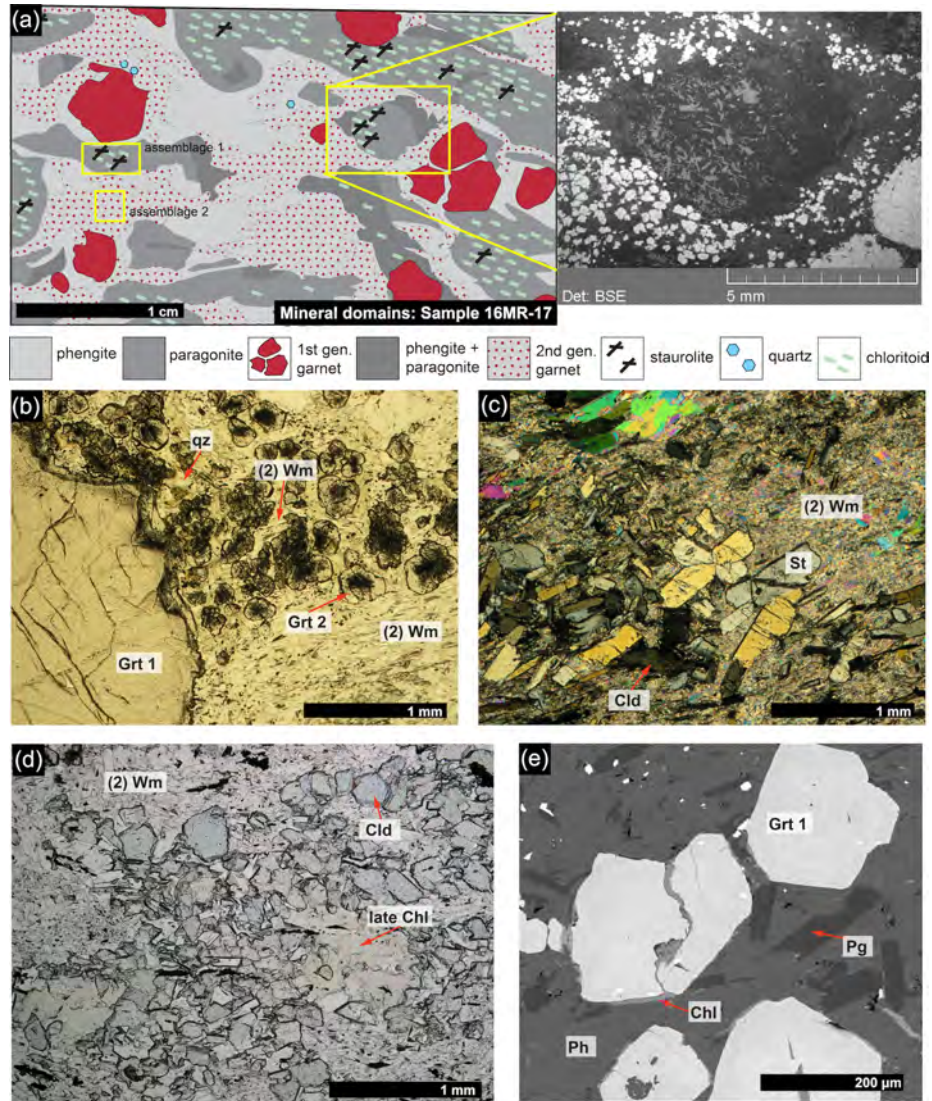
Figure 3.5: Representative petrological images for the study area and metapelitic samples: (a) textural and compositional domains for sample 16MR-17 including SEM image of typical assemblage 1 and 3 pseudomorph form, (b) plane polarized light image of sample 16MR17 showing the two generations of garnet (assemblage 2), (c) cross polarized light image of sample 16MR17 showing staurolite-chloritoid bearing assemblage (assemblage 1), (d) plain polarized image of sample 19MR-33 showing chloritoid, white mica and late chlorite (assemblage 3), and (e) SEM image of typical assemblage 2 textures. Mineral abbreviations after Whitney and Evans (2010).

For assemblage 2 of sample 16MR-17, two white micas are also present. Phengite has Si content ranging between 3.20 to 3.37 a.f.p.u, which correlates with an increase of the Tschermak component between 0.20 to 0.37 (Figure 3.6a). Notably, the highest Si contents are typically within the core of phengite and the lowest at the rim (Table 3.1). Compared to assemblage 1

Table 3.1: Representative microprobe analysis (16MR-17 and 19MR-33).

| Analysis | Assemblage 1 | | | | Assemblage 2 | | | | | | Assemblage 3 | | |
	Phengite	Paragonite	Chloritoid	Staurolite	Phengite Core	Rim	Paragonite	Garnet Core	Rim	Chlorite	Phengite	Paragonite	Chloritoid
SiO_2	48.65	47.11	24.96	28.19	50.05	48.02	46.28	37.51	37.11	25.86	47.52	47.59	24.12
Al_2O_3	32.44	40.01	42.10	52.91	28.50	31.84	40.01	20.83	20.86	21.59	34.63	40.85	42.69
TiO_2	0.25	0.08	0.11	0.33	0.18	0.25	0.05	0.41	0.02	0.08	0.57	0.04	0.01
MnO	0.03	0.00	0.00	0.03	0.00	0.00	0.01	1.50	0.59	0.05	0.01	0.00	0.10
ZnO	0.03	0.00	0.00	4.74	0.00	0.02	0.00	0.00	0.02	0.11	0.02	0.00	0.08
FeO	1.35	0.26	20.40	9.59	1.70	1.27	0.33	30.54	36.49	20.10	1.59	0.61	22.94
MgO	2.05	0.10	5.32	1.81	3.21	2.18	0.08	2.72	3.50	18.27	1.20	0.08	3.90
Na_2O	0.96	7.14	0.01	0.09	0.48	0.86	7.07	0.00	0.011	0.01	1.32	7.08	0.00
CaO	0.00	0.13	0.00	0.01	0.00	0.00	0.42	6.74	1.41	0.01	0.02	0.06	0.01
K_2O	9.70	1.11	0.10	0.01	10.43	10.08	0.69	0.01	0.01	0.06	9.58	0.70	0.01
F	0.25	0.04	-	-	-	-	-	-	-	-	-	-	-
Cl	0.01	0.00	-	-	-	-	-	-	-	-	-	-	-
Total	95.71	95.97	93.00	97.71	94.55	94.52	94.56	100.29	100.04	86.13	96.45	97.01	93.86
Normalized*	11 (a)	11 (a)	8 (a)	25.55 (c)**	11 (a)	11 (a)	11 (a)	12 (a)	12 (a)	13 (a)	11 (a)	11 (a)	8 (a)
Si^{4+}	3.22	2.99	2.00	7.95	3.36	3.21	2.98	2.99	2.99	2.51	3.12	2.98	1.94
Al^{3+}	2.53	2.99	3.98	17.58	2.25	2.51	3.03	1.96	1.98	2.47	2.68	3.02	4.04
Ti^{4+}	0.01	0.00	0.00	0.07	0.01	0.02	0.00	0.03	0.00	0.01	0.03	0.00	0.00
Mn^{2+}	0.00	0.00	0.01	0.01	0.00	0.00	0.00	0.10	0.04	0.00	0.00	0.00	0.01
Zn^{2+}	0.00	0.00	0.01	0.99	0.00	0.00	0.00	0.00	0.00	0.01	0.00	0.00	0.01
Fe^{2+}	0.08	0.01	1.37	2.26	0.10	0.08	0.02	2.04	2.46	1.63	0.09	0.03	1.54
Mg^{2+}	0.20	0.01	0.64	0.76	0.32	0.23	0.01	0.32	0.42	2.64	0.12	0.01	0.47
Na^+	0.12	0.88	0.00	0.00	0.06	0.11	0.88	0.01	0.00	0.00	0.17	0.86	0.00
Ca^{2+}	0.00	0.01	0.00	0.00	0.00	0.00	0.00	0.58	0.12	0.00	0.00	0.00	0.00
K^+	0.82	0.09	0.00	0.00	0.89	0.86	0.06	0.00	0.00	0.01	0.80	0.06	0.00
F	0.00	0.00	-	-	-	-	-	-	-	-	-	-	-
Cl	0.00	0.00	-	-	-	-	-	-	-	-	-	-	-
Total	6.98	6.98	8.01	29.62	6.99	7.02	6.98	8.01	8.01	9.28	7.01	6.96	8.01

* normalization using anions (a) and cations (c)

** normalization after Holdaway et al. (1991)

and 3, Si content of phengite are highest in this quartz bearing assemblage. Phengites have a K content ranging between 0.85 and 0.96 a.p.f.u. (Figure 3.6c). Phengite coexists with paragonite with a Na content between 0.85 to 0.89 a.p.f.u. (Figure 3.6c). Garnet compositions are almandine rich (Figure 3.6d) with Fe ranging between 1.41 and 1.55 a.p.f.u. and minimal zoning is observed (SM-S3.19).

For assemblage 3 of sample 19MR-33, two white micas are also distinguished. Phengite has Si content ranging between 3.10 to 3.21 a.f.p.u, which correlates with an increase of the Tschermak component between 0.10 to 0.21 (Figure 3.6a). Phengites have a K content ranging between 0.81 and 0.88 a.p.f.u. (Figure 3.6c). Phengite coexist with paragonite with a Na content between 0.85 to 0.95 a.p.f.u. (Figure 3.6c). Chloritoid compositions are enriched in Fe (1.41 and 1.55 a.p.f.u.) compared to Mg ranging between 0.50 and 0.59 a.p.f.u. (Figure 3.6b).
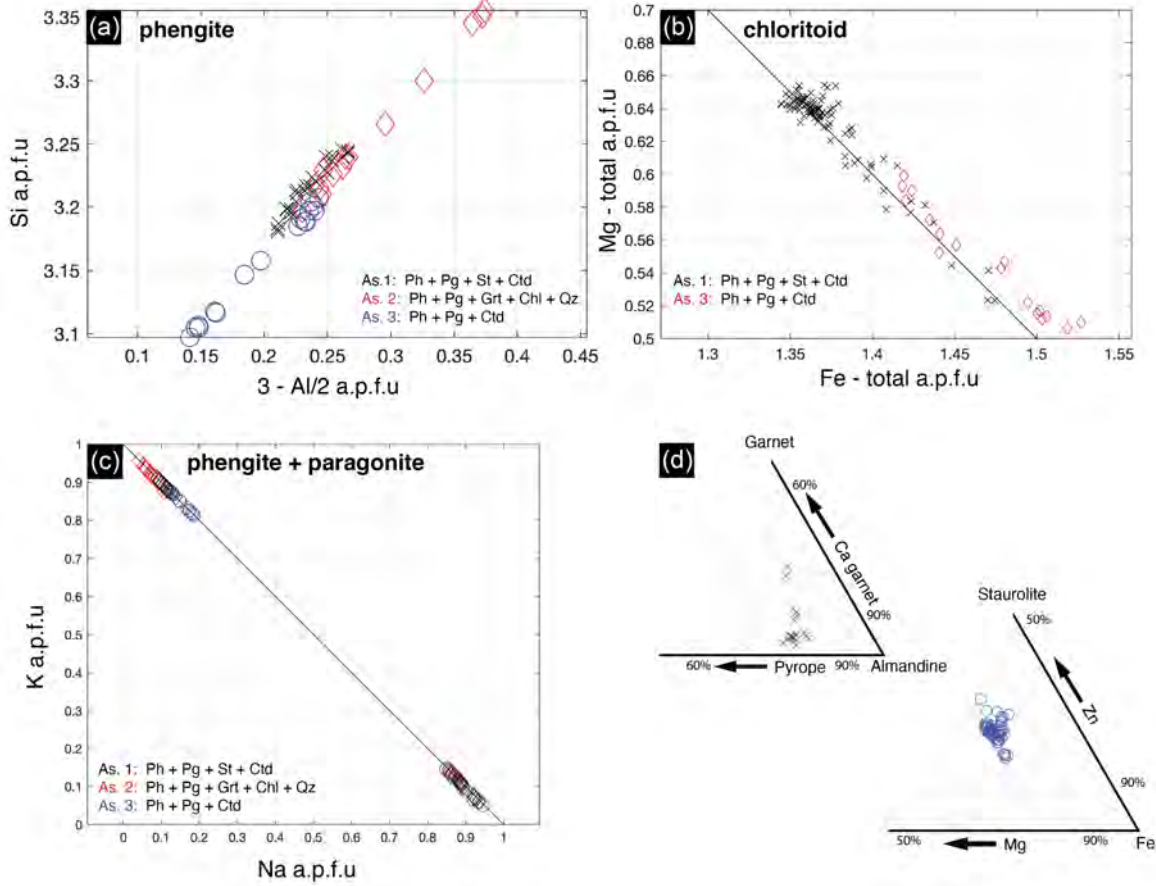
Figure 3.6: Normalized mineral chemical data for assemblages 1, 2 and 3 (sample 16MR-17 and 19MR-33): (a) Si in phengites against Al tetrahedral site, (b) chloritoid Mg and Fe-total, (c) Na in paragonite and K in phengite mixing gap of white micas, and (d) ternary plot for garnet compositions in assemblage 2, and ternary plot for staurolite compositions in assemblage 1 (note non-negligible Zn).

3.6   Phase petrology

Due to the minimal compositional zoning of all minerals, a pseudo-section approach was used in order to calculate PT conditions at fixed bulk-rock composition. Figures 3.7a and b show the pseudo-section results in the NKFMASH system (SiO_2-Al_2O_3-FeO-MgO-K_2O-Na_2O-H_2O) with the bulk compositions displayed for assemblage 1 (phengite + paragonite + staurolite + chloritoid). The stability field of assemblage 1 was well constrained at 1.6 ± 0.05 GPa and 605 ± 2°C. The results for the entropy correction, due to Zn, based on a 'molecular mixing' model are presented along with Si in phengite isopleths (Figure 3.7a). The new stability field

for this assemblage is comparatively larger, expanding towards lower temperatures and higher pressures, resulting in 1.6 ± 0.1 GPa at 600 ± 5°C. The new stability field resulting from the 'site mixing' correction is larger than the 'molecular mixing' model and results in 1.6 ± 0.2 GPa at 585 ± 15°C (Figure 3.7b). The appearance of staurolite is shifted towards lower temperatures in comparison with the results using the molecular mixing model in Figure 3.7a and the classical solution model. Equally, the pseudo-section calculations for this assemblage predicts quartz (< 1%). However, we have not observed quartz in these staurolite – chloritoid bearing assemblages.

Representative compositional microprobe results for assemblage 2 from sample 16MR-17 are displayed in Table 3.1 (garnet + phengite + paragonite + chlorite). Minor zoning is observed in phengite, namely high Si-content in the core of phengites, up to 3.37 a.p.f.u (Figure 3.6a). Similarly, minor zoning of Ca and Mn can be observed in garnet (Table 3.1). Therefore, we took average compositions of Si, Ca and Mn of phengite and garnet respectively, as input for bulk rock compositions. Figure 3.7c shows pseudo-section results in the NCKFMASH system (SiO_2-Al_2O_3-FeO-MgO-K_2O-Na_2O-CaO-H_2O). Using isopleths for the modal volume of chlorite (vol%), Xparagonite and Si in phengite (a.p.f.u.), the stability field for the observed mineral assemblage ranges from 1.3 – 1.4 GPa at ∼ 575°C (Figure 3.7c).

Representative composition microprobe results for assemblage 3 from sample 19MR-33 are displayed in Table 3.1 (phengite + paragonite + chloritoid). We observe minimal zoning in this assemblage with similar values as assemblage 1 (Ph + Pg + St + Ctd). Bulk compositions are similar to assemblage 1 with the exception of lower Zn values. The stability field for the peak paragenesis is large, spanning a wider field of pressures and temperatures (Figure 3.7d). At temperatures of 575°C, inferred from assemblage 1 and 2, pressure ranges between 1.1 and 1.6 GPa.
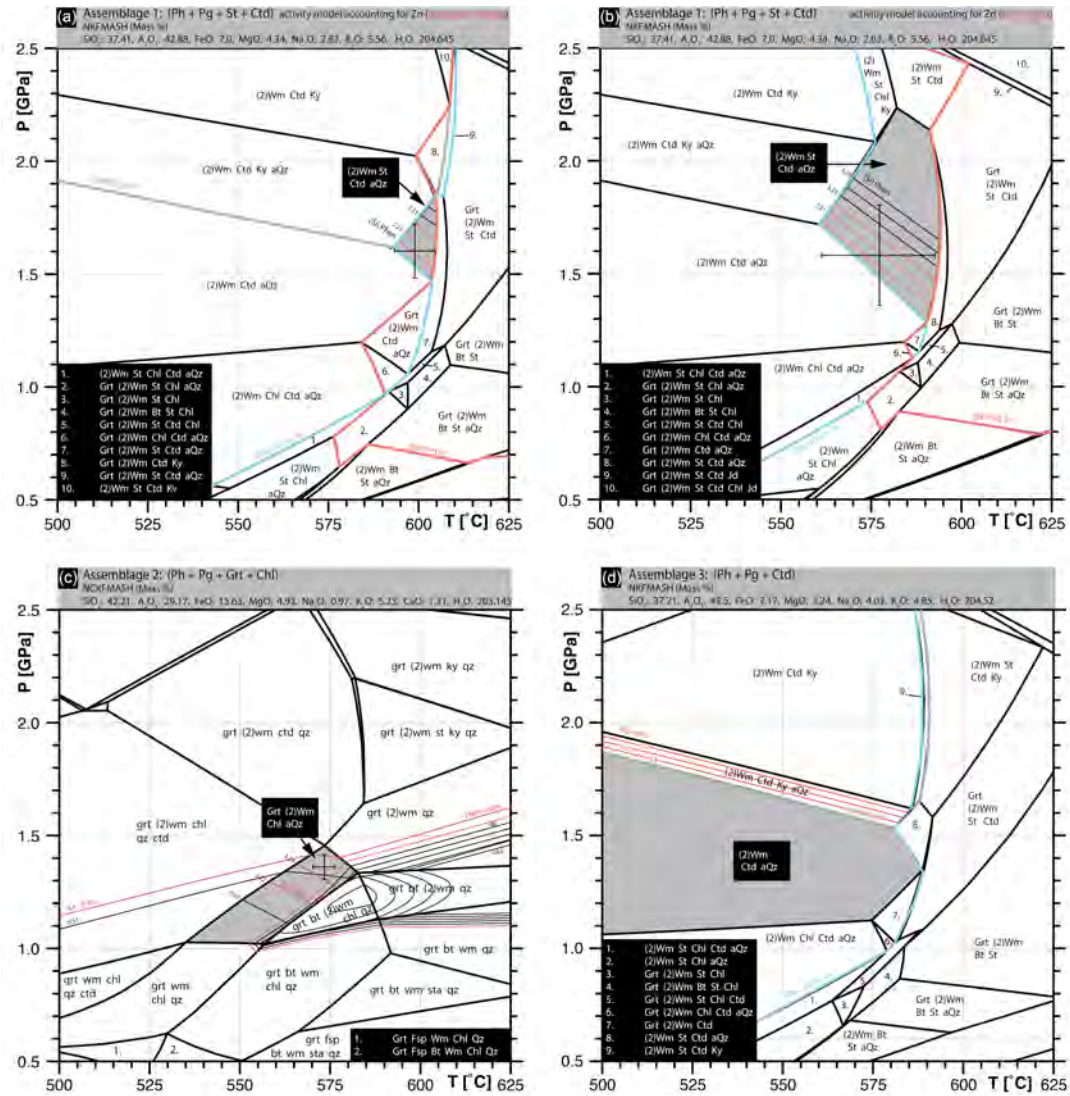
Figure 3.7: Thermodynamic pseudo-section modelling for assemblages 1, 2 and 3 (sample 16MR17 and 19MR33) using the Theriak/Domino software and JUN92 Berman database (Berman, 1988): (a) assemblage 1 results in NKFMASH with reduced activity for Mg-Fe endmember solutions based on molecular mixing assumption (a.p.f.u isopleths for Si in phengite), (b) assemblage 1 results in NKFMASH with reduced activity for Mg-Fe endmember solutions based on site mixing assumption (a.p.f.u isopleths for Si in phengite), (c) assemblage 2 results in NCKFMASH (a.p.f.u isopleths for Si in phengite, X paragonite and phengite vol%), and (d) assemblage 3 results in NKFMASH system (a.p.f.u. isopleths for kyanite vol%).

3.7 Discussion

3.7.1 Estimating peak Alpine conditions

Due to the complexity of the polymetamorphic Monte Rosa basement, three periods of geological activity may be responsible for the formation of assemblages 1, 2 and 3, that we interpret to have formed during peak Alpine conditions. These events include (from oldest to youngest): (1) HT-LP Variscan orogenesis, (2) peak high-P Alpine orogenesis, and (3) a late Alpine thermal pulse. However, field occurrences, textural relationships and petrological investigations from this study, enable us to attribute the investigated assemblages to equilibration during peak Alpine conditions (Figure 3.7).

Typically, the studied assemblages occur within centimeter-sized pseudomorphs in low-strain domains (Figures 3.3, 3.4c and d, and SM-S3.12). These pseudomorphs occur close to the late Palaeozoic metagranite intrusion and associated basement migmatites (Figure 3.4b). We interpret these pseudomorphs to represent relics of former contact metamorphic andalusite that formed during granite emplacement (SM-S3.12). Therefore, the staurolite + chloritoid bearing assemblages post-date granite emplacement and thus post-date Variscan orogenesis. Equally, the calculated P-T results for the assemblages analyzed in this study do not agree with the older high-T and low-P metamorphism, characteristics of the Variscan orogeny. Our results of 1.6 ± 0.2 GPa and 585 ± 20°C indicate too high pressures and too low temperatures compared with estimates of 0.3-0.6 GPa and 700°C for Variscan metamorphism (Bearth, 1952; Dal Piaz et al., 2001; Dal Piaz and Lombardo, 1986; Engi et al., 2001).

Another argument for the Alpine formation of the assemblages investigated, is the apparent enrichment of Na (Table 3.1). This enrichment resulted in the occurrence of large volume proportions of paragonite observed (up to 30%). Similar enrichment in Na of metapelites in close proximity to intrusive bodies has been reported (e.g. Eugster, 1985). These occurrences have been attributed to host-rock interaction with late magmatic hydrothermal fluids. Evidence for post-intrusion hydrothermal activity is also observed in close proximity to our locality, namely the formation of Mg-rich sericite-chlorite schists, that are the precursory equivalent to

HP 'whiteschists' within the metagranite (Luisier et al., 2019; Marger et al., 2019; Pawlig and Baumgartner, 2001). Associated with hydrothermally induced Mg-enrichment of the granite protolith, depletion of Na has be observed (Pawlig and Baumgartner, 2001). The ensuing fluid migration may have contributed to the enrichment of Na in the basement metapelites.

Previous observations of staurolite within the Monte Rosa nappe have been interpreted to be associated with the post-peak Alpine Barrovian metamorphism in the Lepontine dome, far to the East of our finding (Engi et al., 2001; Niggli, 1960; Niggli and Niggli, 1965; Niggli, 1970). This isograd exists in the far eastern extent below the Monte Rosa nappe pile in the Camugera Moncucco unit (CM), which is structurally one of the deepest unit in the Western Alps (Keller et al., 2004). Observations of relic staurolite have been reported further west from the CM and are linked possibly to a HP Alpine phase, however, no thermodynamic calculations of P and T have been made (Engi et al., 2001; Niggli, 1960; Niggli and Niggli, 1965). Until now, no observations of staurolite, to the best of our knowledge, in the Monte Rosa nappe have been made west of the Stellihorn shear zone (Figure 3.2a).

To place the staurolite investigated within the timeframe of the late thermal pulse may pose some difficulties. Firstly, due to the location in the far western portion of the nappe, as Frey et al. (1999) places the western portions of the Monte Rosa nappe at greenschist facies during this time. Secondly, the calculated P and T within this study have too high pressures at 1.6 ± 0.2 GPa, and even at the lowest structural levels (i.e. within the CM) these pressures would be too high, as Engi et al. (2001) calculated re-equilibration during decompression at conditions of 1.1 ± 0.12 GPa and $652 \pm 41°$C.

Mineral textures and calculated metamorphic conditions in this study exclude the possibility of equilibration during: (1) Variscan orogenesis, and (3) late Alpine thermal decompression, therefore, equilibration during (2) peak Alpine conditions remains. The observed assemblages most likely equilibrated in a pressure-temperature maximum during Alpine burial. This is observed both texturally and geochemically with garnet growth, as isopleths for garnet growth increase with prograding P-T conditions. Thus, the assemblages investigated here formed during peak Alpine conditions, rather than superimposing them onto a retrogressive pathway

during decompression. If these assemblages represent retrogression however, the question remains: from what assemblages did they retrogress? The only pseudomorphic textures we can observe are likely after former andalusite related to Permian-aged contact metamorphism (Figure 3.4d and SM-S3.11). However, when comparing calculated P-T equilibrium domains for both assemblage 1 and 2, there does exists a small disparity (Figure 3.7). Assemblage 1 has ~ 0.2 GPa higher pressures and ~ 50°C higher temperatures. This is likely due to chlorite replacing garnet (Figure 3.5e) during retrogression from peak conditions recorded in the staurolite-chloritoid bearing assemblages along with the influx of H_2O rich fluids. The presented field relations, textural observations and thermodynamic calculations suggest equilibration during peak Alpine conditions.

3.7.2   Sensitivity of thermodynamic mixing models: Zn in staurolite

In order to constrain a reliable Alpine peak P and T incurred by the Monte Rosa basement, the calculated thermodynamic stability fields must replicate the observed mineral textures, chemistry and modal abundances. Here we will address two caveats in our calculated pseudo-sections: (i) the presence of Zn in staurolite in assemblage 1, and (ii) the calculated presence of quartz in assemblages 1 and 3.

Concerning caveat (i), we must consider the non-negligible quantities of ZnO measured in staurolite (Table 3.1). Assessing our microprobe data, staurolite is the only Zn bearing phase, which is in agreement with other occurrences of Zn-staurolite (e.g. Fox, 1971; Griffen, 1981; Guidotti, 1970; Tuisku et al., 1987). Even with the uniqueness of assemblage 1 of this study (St, Cld, Ms, Pg $\pm$ Qz) as well as the apparent lack of zoning, the range of P and T varies somewhat considerably when adjusting the existing thermodynamic data of staurolite endmembers in the thermodynamic database for Zn (Figure 3.7a and b). Considering these adjustments, we are able to calculate the new stability fields taken as a whole at 1.6 ± 0.2 GPa and 585 ± 20°C (Figure 3.7b). Few authors have investigated the effects of ZnO within staurolite, and similarly reported its large influence on a metamorphic stability field (e.g. Fox, 1971; Holdaway et al., 1991; Tuisku et al., 1987). Considering Zn's large influence on the P and

T range of stability, treating it as an additional component in staurolite is important (Tuisku et al., 1987). The approach presented here is a suitable way of dealing with Zn-staurolite in the absence of experimentally constrained end-member thermodynamic data and where staurolite is the only Zn bearing phase. The two model calculations (ideal molecular and site mixing) give reasonable bounds on the effect of Zn on the staurolite stability. Although not correlated with Zn content, Li-bearing staurolites have also been demonstrated to expand its stability field (e.g. Dutrow et al., 1986). However, we have not analyzed Li in staurolite.

Concerning caveat (ii), one result from the calculations for assemblage 1 and 3 (Figures 3.7a, b and c) is the presence of quartz predicted in the stability field. Quartz modal abundance ranges from 1.0-0.1% with increasing P, T and Si content of phengite (Figures 3.7a and b). However, after detailed microscope investigations and microprobe analysis of several pseudomorph domains from different samples we have not observed quartz associated with chloritoid and staurolite assemblages. This could be due to the very low proportions of quartz predicted ($< 1\%$) and the statistical chances of cutting a sample in order to observe quartz. Most likely there are two explanations for the predicted quartz: (1) white mica is an abundant phase and the K-Na exchange mixing model may be unreliable, thus Si in paragonite may not be accounted for, and (2) the garnet bearing assemblages surrounding the pseudomorphs containing staurolite + chloritoid are observed to have quartz (Figure 3.5a and b), hence staurolite + chloritoid assemblages are most likely quartz saturated (or approaching quartz saturation).

3.7.3   Tectono-metamorphic history of the metapelite

Figure 3.8 outlines the schematic geological history recorded in the metapelitic lithologies of the Monte Rosa. (a) Variscan HT-LP orogenesis, overprinting metapelitic lithologies and the formation of 1st generation garnets. (b) Intrusion of Variscan-age granite bodies, resulting in local migmatization and a contact metamorphic aureole forming andalusite. (c) Peak Alpine high-P imprint over contact metamorphic andalusite resulting in staurolite-chloritoid within

former andalusite pseudomorphs, and 2nd generation garnet bearing assemblages. (d) Late

Alpine deformation of the basement locally producing greenschist lithologies.
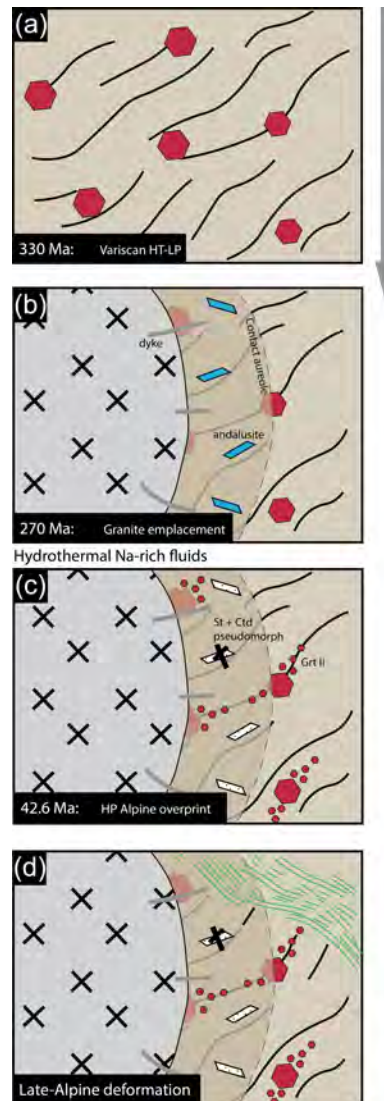
Figure 3.8: Schematic geological evolution of the polymetamorphic basement of Monte Rosa nappe: (a) Variscan high temperature-low pressure orogenic imprint, defined in this study as large 1st generation garnets at 330 Ma (Engi et al., 2001), (b) intrusion of post-Variscan aged granite bodies (Pawlig and Baumgartner, 2001), associated dykes and associated contact metamorphic aureole most likely forming andalusite grade contact metapelites and late magmatic overprint by Na-saturated hydrothermal alteration, (c) HP imprint during Alpine orogenesis pseudomorphing after andalusite, forming the assemblages investigated in this study, (d) late Alpine deformation associated with decompression to greenschist facies grade.

3.7.4   Pressure variations and geodynamic implications

Figure 3.9a shows a comparison of the results of this study with the results from Luisier et al. (2019). When comparing the peak metamorphic conditions of metapelites from this study at 1.6 ± 0.2 GPa, with the peak metamorphic conditions of the whiteschist at 2.2 ± 0.2 GPa and the host metagranite at 1.4 ± 0.2 GPa, the metapelite and metagranite show a consistent peak P, within error, while the whiteschist shows a considerably higher peak P. Even with a conservative estimate (including the error range introduced via Zn-staurolite reduced activity), differences in peak P between metapelite and whiteschist are $\sim$ 0.6 ± 0.2 GPa. Peak T of approximately 550-600°C for the metagranite was estimated by Luisier et al. (2019) from the whiteschist pseudo-section results. Assuming that the staurolite is a reliable thermometer (see staurolite-in line of Figure 3.5a), we are able to adjust the metagranite peak T estimates of Luisier et al. (2019) to our calculated temperatures of 585 ± 20°C. Consequently, the data indicates that metagranite, metapelite and whiteschist assemblages exhibit the same peak T, within error (Luisier et al., 2019).

There are two end-member interpretations for the geodynamic evolution of the Monte Rosa nappe, namely an interpretation based on lithostatic pressure (Figure 3.9b) and one based on tectonic pressure variations (Figure 3.9c). For the lithostatic interpretation, the peak P of the whiteschist indicates a burial depth of the Monte Rosa nappe of $\sim$ 80 km (using 2.35 GPa as peak P and assuming an overburden with an average density of 3000 $\mathrm{kg\,m^{-3}}$). Consequently, all peak P estimates for the metagranite and metapelite must be considered as totally unreliable, because all lithologies were at approximately the same burial depth (no tectonic mélange; see section 3.2.3). In this scenario, the Monte Rosa nappe would have been most likely exhumed exclusively due to buoyancy forces (e.g. Butler et al., 2013, 2014).

We do not favor the lithostatic interpretation, because peak P estimates for metagranite and metapelite are consistent, within error, although the mineral assemblages are considerably different (Figure 3.9a). Also, the peak T estimates coincide with estimates for the whiteschist. Moreover, a characteristic structural feature of rocks exhumed by buoyancy in a subduction channel, under approximately lithostatic conditions, should be the formation of a tectonic
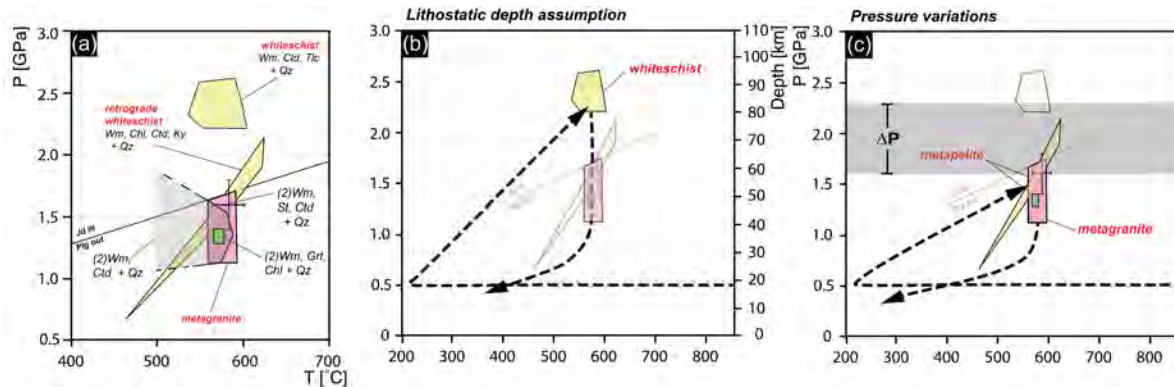
Figure 3.9: (a) Final PT results of metapelite samples and comparison of results with whiteschist assemblages and metagranite of Luisier et al. (2019): (b) hypothetical clockwise *P-T*-depth loop for the Monte Rosa nappe, peak pressure equating to deepest burial of unit using the lithostatic depth assumption, (c) hypothetical clockwise *P-T* loop for the Monte Rosa nappe where the metagranite and metapelites represent the regional peak pressure in the nappe and the whiteschist represents a local and volumetrically minor area of relatively higher pressure ΔP, potentially caused by mechanical- or reaction-induced stress.

mélange whereby rocks from different depths, having different peak *P* and T, are mixed inside the same tectonic units (Gerya and Stöckhert, 2006; Roda et al., 2012); but the studied region is not a mélange. For the tectonic pressure interpretation, peak *P* of the metagranite and metapelite indicate regional peak *P* of the Monte Rosa nappe whereas the peak *P* of the whiteschist indicates local pressure variations with pressures higher than the corresponding lithostatic value. Mechanically, such locally higher pressures could be due to compressional stress during the continental collision of the Alpine orogeny, or due to reaction-induced stresses due to volume changes during whiteschist formation (e.g. Luisier et al., 2019). We suggest that the higher pressure in the whiteschist was due to a combination of compressional and reaction-induced stresses. The ∼ 1.6 GPa peak *P* of the entire Monte Rosa nappe is compatible with the orogenic wedge model in which nappe stacking is due to a combination of buoyancy and compressive forces involving accretion, or underplating, during progressive subduction of mainly the European lower crust and mantle (e.g. Escher and Beaumont, 1997; Platt, 1986). Furthermore, Manzotti et al. (2018) recently estimated peak metamorphic conditions for the two main sub-units of the neighboring Gran Paradiso massif (Figure 3.1), the Gran Paradiso and Money units, and dated the peak metamorphism. They obtained 1.8-2.0 GPa and 500-520°C for the Gran Paradiso unit, and 1.7-1.8 GPa and ∼ 550°C for the Money unit;

dated both at the same age of c. 42 Ma. The peak metamorphic conditions and age of the Gran Paradiso tectonic units are, hence, close to the peak metamorphic conditions of 1.6 ± 0.2 GPa and 585 ± 20°C (and their age of 42.6 ± 0.6 Ma; (Lapen et al., 2007)), which are representative for the Monte Rosa nappe. We consider this similarity in peak metamorphic conditions of the two neighboring internal crystalline massifs (Figure 3.1a) as further support for the feasibility of our proposed peak values.

3.8   Conclusions

For the western portions of the Monte Rosa nappe, we have further constrained the metamorphic conditions associated with peak Alpine activity within the Western Alps from metapelitic lithologies. A unique staurolite-chloritoid bearing assemblage was petrologically and thermodynamically investigated resulting in an Alpine peak pressure of 1.6 ± 0.2 GPa and a peak temperature of 585 ± 20°C. Comparing these results with the peak pressure variations of 0.8 ± 0.3 GPa previously reported in metagranite lithologies, between whiteschist and metagranite, large peak pressure disparities of 0.6 ± 0.2 GPa persist (Figure 3.9). We rule out explanations for an apparent variability in pressure, such as sluggish kinetics in the metapelites or tectonic mixing, and further highlight the possible existence of mechanically- and/or reaction-induced pressure differences.

Based on our new data and previously published results, we propose that the maximum burial depth of the Monte Rosa unit was likely significantly less than 80 km, which is a depth estimate based on the lithostatic pressure assumption and the local occurrence of minor volumes of whiteschist exhibiting peak pressure > 2.2 GPa. The maximum burial depth of the Monte Rosa unit was presumably less than 60 km, which is a depth compatible with burial and exhumation within an orogenic wedge. We further suggest that special care should be taken when using maximal values from published pressure estimates to reconstruct the burial and exhumation history of the corresponding tectonic unit, particularly, when the maximum pressure estimates are limited to minor volumes within the unit.

3.9 Appendix

All data relevant to this publication is available on Zenodo via https://zenodo.org/record/5519374#.YUnSL9MzaLU.

3.9.1 Fe and Mg end-member corrections for Zn in staurolite

Due to the absence of thermodynamic data for Zn-staurolite end-members (Fox, 1971; Holdaway et al., 1986, 1991), the experimentally derived thermodynamic activity of available endmembers (i.e. Fe- or Mg-staurolite) must be adjusted. In order to adjust the activity for endmembers for non-negligible Zn values we begin with the general equation of the apparent Gibbs free energy (G) for a single component defined in Theriak/Domino (de Capitani and Petrakakis, 2010) as

$$G_i^{T,P} = H_i^{T0,P0} - T S_i^{T0,P0} + \int_{T0}^{T} Cp_i \, dT - T \int_{T0}^{T} \frac{Cp_i}{T} dT \; + \int_{P0}^{P} V_i^{T,P0} \, dP \qquad (3.1)$$

For a single mineral endmember the index i = 1. In the case of a multi-component ideal solution, G_{sol} would equal

$$G_{sol} = G^{mech} + G^{mix} = \sum_{i=1}^{n} x_i G_i + \sum_{i=1}^{n} x_i RT ln(a_i^{ideal}) \qquad (3.2)$$

The x_i represent the relative fraction of each component and $\sum_{i=1}^{n} x_i = 1$. The Gibbs energy for the single component of Mg-staurolite (MgSt) is

$$G_{MgSt}^{T,P} = H_{MgSt}^{T0,P0} - T S_{MgSt}^{T0,P0} + \int_{T0}^{T} Cp_{MgSt} \, dT - T \int_{T0}^{T} \frac{Cp_{MgSt}}{T} dT \; + \int_{P0}^{P} V_{MgSt}^{T,P0} \, dP \quad (3.3)$$

The endmember adjustment for a single component (e.g. MgSt & x_i=1) is performed by modifying $S_{MgSt}^{T0,P0}$ in equation 3.3. For reducing the activity of the pure ($x_i \approx 1$) end-member (e.g. MgSt) and due to the presence of Zn (Zn-MgSt) we introduce the mixing term G^{mix} in

3.2 in 3.3 and assume that the remaining thermodynamic properties of the Zn-bearing MgSt are identical

$$G_{\text{Zn-MgSt}}^{\text{T,P}} \approx H_{\text{MgSt}}^{\text{T0,P0}} - TS_{\text{MgSt}}^{\text{T0,P0}} + \int_{T0}^{T} Cp_{MgSt}\, dT - T \int_{T0}^{T} \frac{Cp_{MgSt}}{T} dT + \int_{P0}^{P} V_{\text{MgSt}}^{\text{T,P0}}\, dP + RTln(a_{\text{i}}^{\text{reduced}})$$

(3.4)

For pure St end-members (Zn free), equations 3.4 and 3.3 are equivalent because $a_{\text{i}}^{\text{reduced}} = 1$. Instead of explicitly treating the mixing term in the Gibbs energy equation 3.4 we prefer to introduce an "effective" entropy ($S_{\text{eff}}^{\text{T0,P0}}$) in the Gibbs equation, which includes the mixing term. We thus write

$$G_{\text{Zn-MgSt}}^{\text{T,P}} \approx H_{\text{MgSt}}^{\text{T0,P0}} - TS_{\text{eff}}^{\text{T0,P0}} + \int_{T0}^{T} Cp_{MgSt}\, dT - T \int_{T0}^{T} \frac{Cp_{MgSt}}{T} dT + \int_{P0}^{P} V_{\text{MgSt}}^{\text{T,P0}}\, dP \quad (3.5)$$

Equations 3.4 and 3.5 must be equivalent expressions and their difference must, hence, be zero. Subtracting equation 3.4 from 3.5 yields

$$- TS_{\text{eff}}^{\text{T0,P0}} + TS_{\text{MgSt}}^{\text{T0,P0}} - RTln(a_{\text{i}}^{\text{reduced}}) = 0$$

(3.6)

which after division by T and rearrangement provides the expression for the "effective" entropy

$$S_{\text{eff}}^{\text{T0,P0}} = S_{\text{MgSt}}^{\text{T0,P0}} - Rln(a_{\text{i}}^{\text{reduced}})$$

(3.7)

Therefore, the presence of Zn, causing $a_{\text{i}}^{\text{reduced}} < 1$, would always increase the total entropy via $S_{\text{eff}}^{\text{T0,P0}}$ and therefore reduce the $G^{T,P}$ of the mixture.

We do not adjust H^o(Fe-staurolite = -23765364 J mol^{-1} and Mg-staurolite = -25112909 J mol^{-1}) within THERIAK-DOMINO after Nagel et al. (2002). $S_{\text{eff}}^{\text{T0,P0}}$ defines an entropy

correction, where $S_{\text{MgSt}}^{\text{T0,P0}}$ is the entropy for the pure phase after Nagel et al. (2002) (Fe-staurolite $= 1005.327$ $\text{J mol}^{-1}\,\text{K}^{-1}$ and Mg-staurolite 905.396 $\text{J mol}^{-1}\,\text{K}^{-1}$). For a pure phase, $a_{\text{i}}^{\text{reduced}} = 1$, thus $S_{\text{eff}}^{\text{T0,P0}} = S_{\text{MgSt}}^{\text{T0,P0}}$. Due to the site multiplicity of staurolite being 4 (T2, M1 – M4) and the equivalent substitutions being $Fe^{2+} = Mg = Zn$ (e.g. Holdaway et al., 1991) we are able to calculate two potential "endmember" mixing models in order to correct the activity of Mg and Fe endmembers. Firstly, a 'molecular mixing' model that assumes components are equivalent to mole fractions, thus a linear mixing model via $a_{\text{i}}^{\text{reduced}} = (1 - (\frac{Zn}{4}))$. Where Zn $= 0.99$ atoms per formula unit (a.p.f.u) (Table 3.1), the resulting $S_{\text{eff}}^{\text{T0,P0}}$ for Fe-staurolite is 1007.6911 $\text{J mol}^{-1}\,\text{K}^{-1}$ and Mg-staurolite 907.7601 $\text{J mol}^{-1}\,\text{K}^{-1}$. The second, 'site mixing' model has a dependence on the site multiplicity of staurolite being 4 (Holdaway et al., 1991), thus a highly non-linear dependence via $a_{\text{i}}^{\text{reduced}} = (1 - (\frac{Zn}{4}))^4$. Where Zn $= 0.99$ a.p.f.u. (Table 3.1), the resulting $S_{\text{eff}}^{\text{T0,P0}}$ for Fe-staurolite is 1014.7834 $\text{J mol}^{-1}\,\text{K}^{-1}$ and Mg-staurolite 914.8524 $\text{J mol}^{-1}\,\text{K}^{-1}$.

3.9.2 Supplementary material

The ability to sample the metapelitic basement of the western Monte Rosa (upper val d'Ayas), has been made possible by the considerable reduction in glacial coverage. The discovery of staurolite-chloritoid bearing rocks previously located below ice, has enabled an additional constrain of peak metamorphic conditions during Alpine orogenesis. This independent PT calculation confirms the pressure disparities within the nappe, which have recently been attributed to mechanically induced variations in pressure (Luisier et al., 2019).

The unique assemblages investigated in this study typically occur in proximity to the meta-granite bodies, and associated migmatized basement metapelites (Figure 3.10). They typically occur in low strain domains unaffected by migmatization, seen in the attached image (Figure 3.11) whereby assemblages are preserved in fold hinges of late alpine greenschist deformation. These assemblages occur in pseudmorphs that are spatially unique to areas close to the metapelite-metagranite contact, interpreted to be former contact metamorphic andelusite (Figure 3.12).

Figure 3.13 outlines the main petrological domains within the metapelitic sample 16MR17. Note the large garnets, that are interpreted to grown during metamorphism associated with Variscan orogenesis (Figure 3.14 Mn cps. map). The zones under investigation include the staurolite-chloritoid and fine grained second generation garnet zone (Figure 3.13). These domains along with field evidence showing little deformation and retrogression associated with late Alpine greenschist shear zones, indicates growth during HP Alpine metamorphism (Figure 3.15). The first assemblage we investigated consists of staurolite, chloritoid, phengite, paragonite, rutile ($\pm$ quartz). Figure 3.16 shows the relative proportions and phases of minerals (using the MATLAB$^{\copyright}$ based image processing software XMapTools (Lanari et al., 2014), of X-ray data taken from a representative area within assemblage 1. These phase proportions were used to calculate vol% for the computation of equilibrium assemblage diagrams using Theriak/Domino (de Capitani and Petrakakis, 2010). In order calculate these pseudo-sections, certain assumptions have to be made. One of the major assumptions we make is the Fe^{3+} content, for our calculations we neglect Fe^{3+}. Figure 3.17 shows the a.p.f.u Mg vs. Fe for chloritoid and Figure S9 shows the Mg vs Fe^{2+} calculated for the remaining Al-octrahedral sites. Therefore, the deviation from the line represents an estimate for the possible Fe^{3+} in chloritoid.

The second assemblage investigated consists of garnet, chlorite, phengite, paragonite ($\pm$ quartz). One caveat in thermodynamic modelling of equilibrium assemblage diagrams is the existence of zoning within minerals. In particular, garnet can be a heavily zoned mineral e.g. growth during peak PT conditions would result in garnet cores having different chemistry compared to garnet rims. This therefore poses difficulties when averaging bulk compositions for a garnet phase when using the pseudo-section approach. However, for out samples we see limited elemental zoning within garnet (Figure 3.19). Figure 3.20 shows the relative proportions and phases of minerals (using the MATLAB$^{\copyright}$ based image processing software XMapTools), of X-ray data taken from a representative area within assemblage 2.

Figure 3.10: Partial melting migmatitic textures of basement lithologies in close proximity to granitic intrusion.
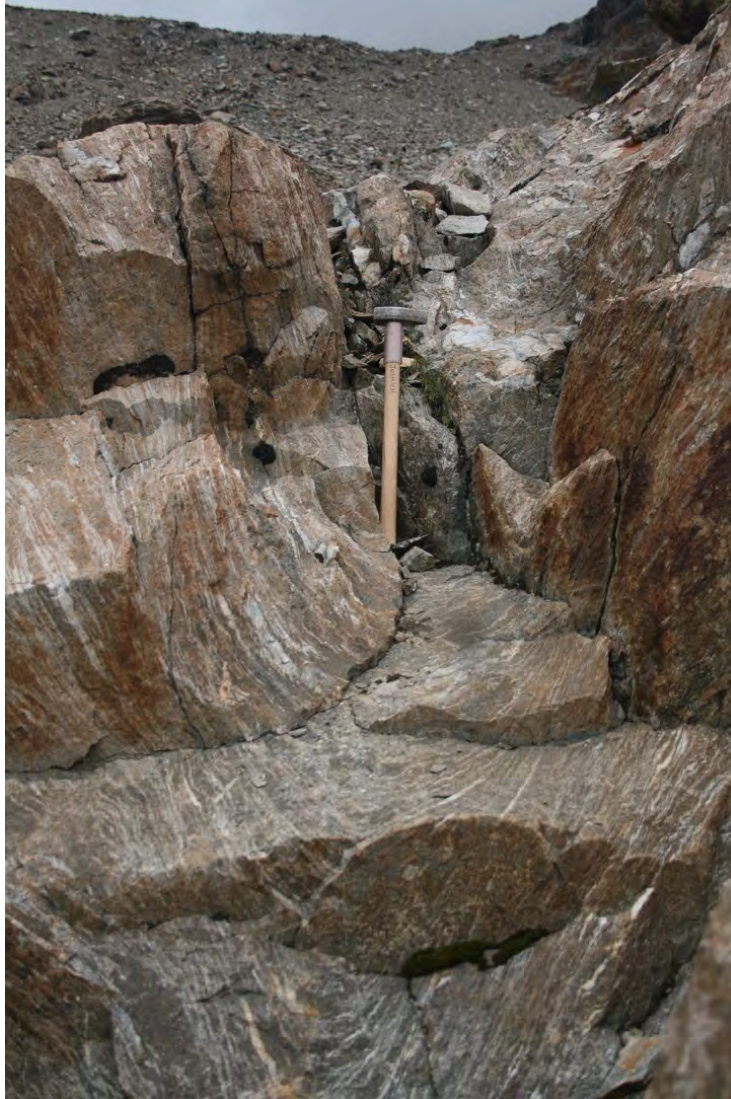
Figure 3.11: Folding in metapelitic basement with highly strained limbs and relatively low strain hinges that preserve peak Alpine metamorphic assemblages.

Figure 3.12: Contact metamorphic pseudomorphs after andalusite containing staurolite + chloritoid assemblages related to peak Alpine metamorphism.
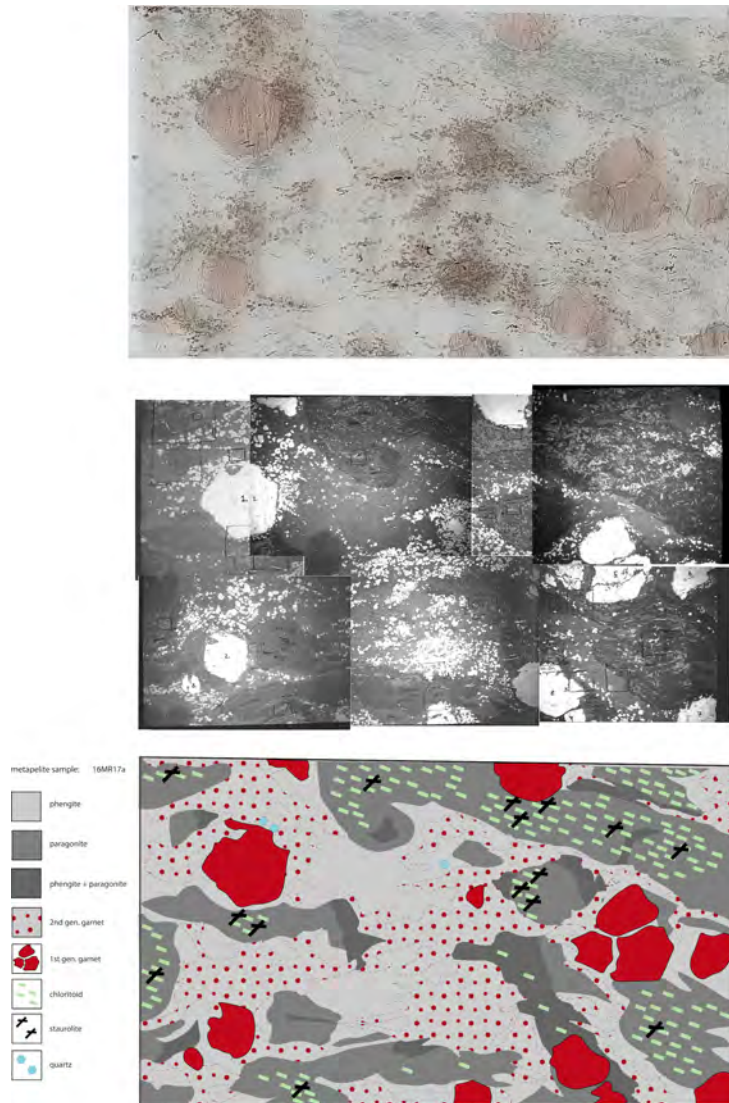
Figure 3.13: Thinsection characteristics and mineralogical domains of sample 16MR17.
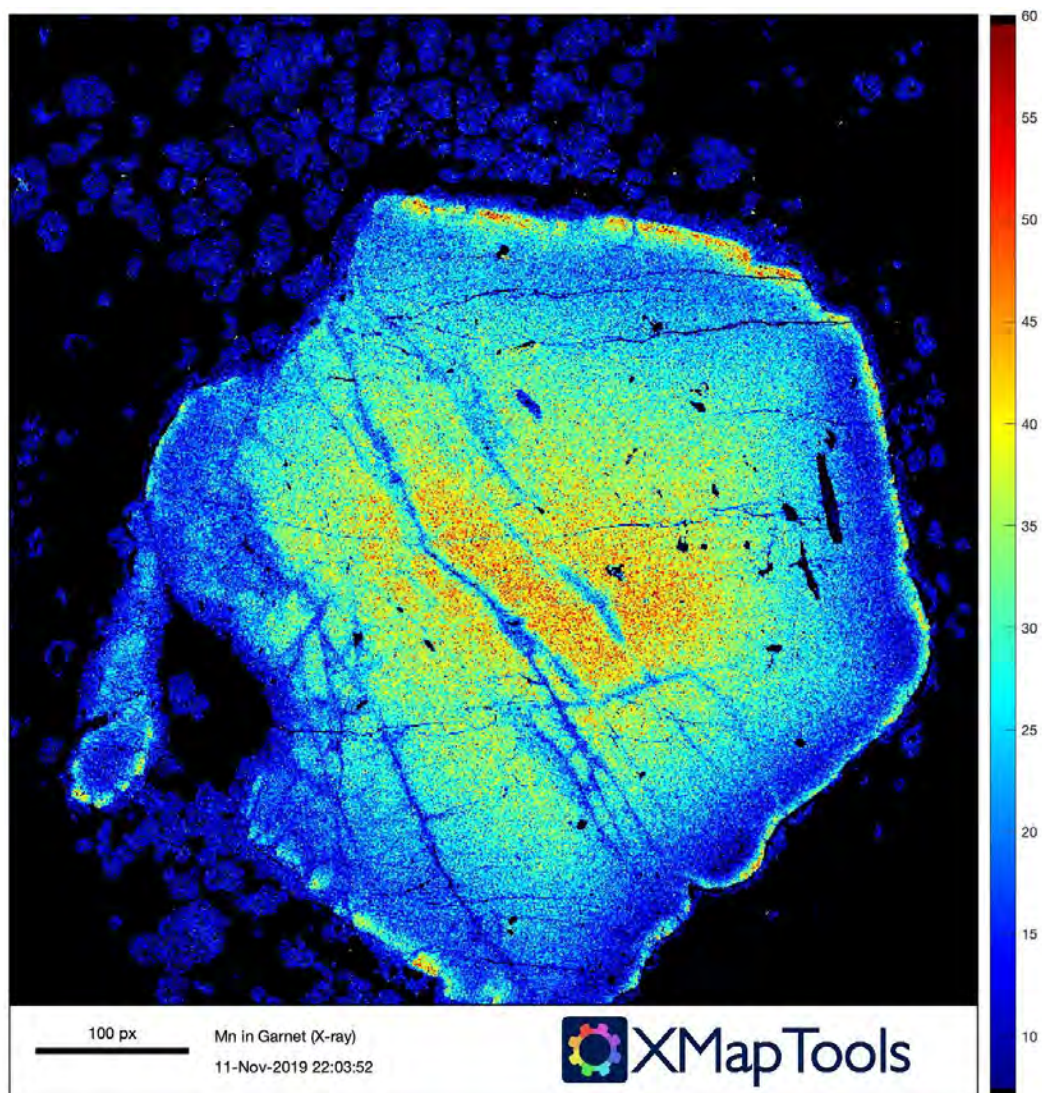
Figure 3.14: Mn zoning in pre-Alpine Variscan garnet.
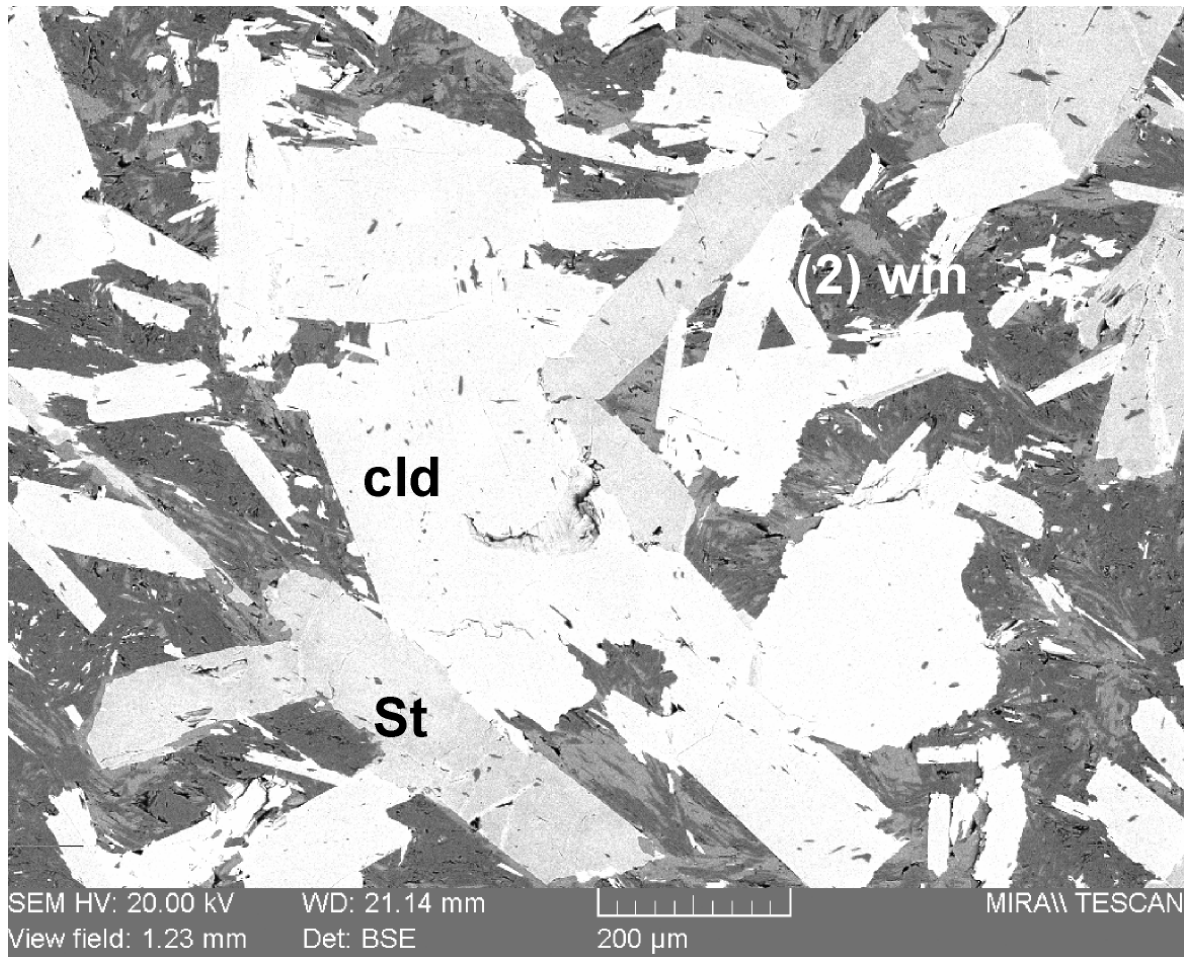
Figure 3.15: BSE image of staurolite + chloritoid textures.
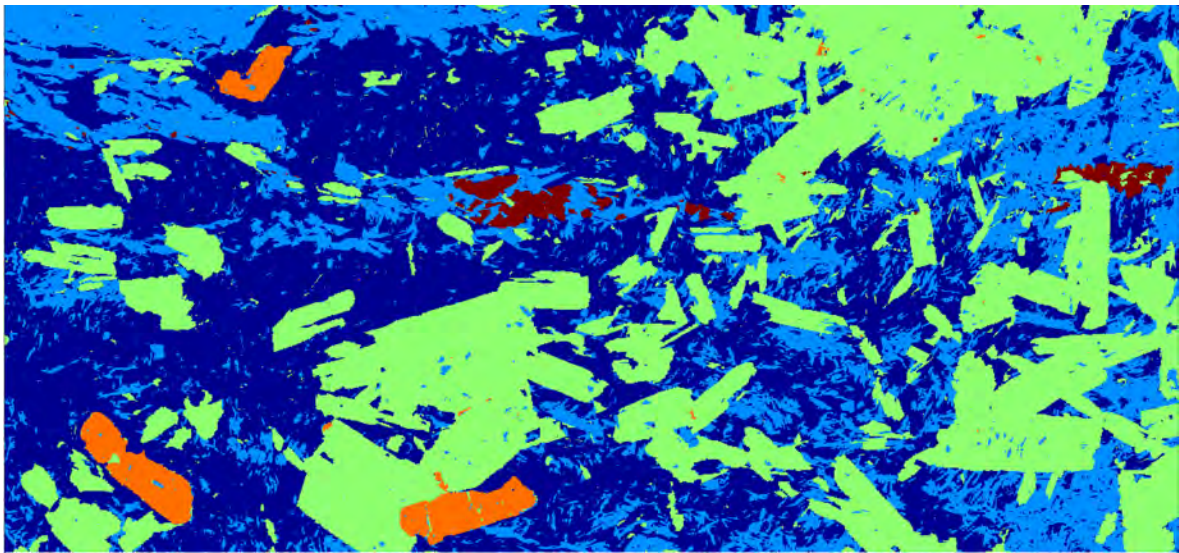
Figure 3.16: Assemblage 1 mineral phases calculated from image analysis from XMapTools (Lanari et al., 2014) (light blue = phengite, dark blue = paragonite, maroon = rutile, green = chloritoid, and orange = staurolite).
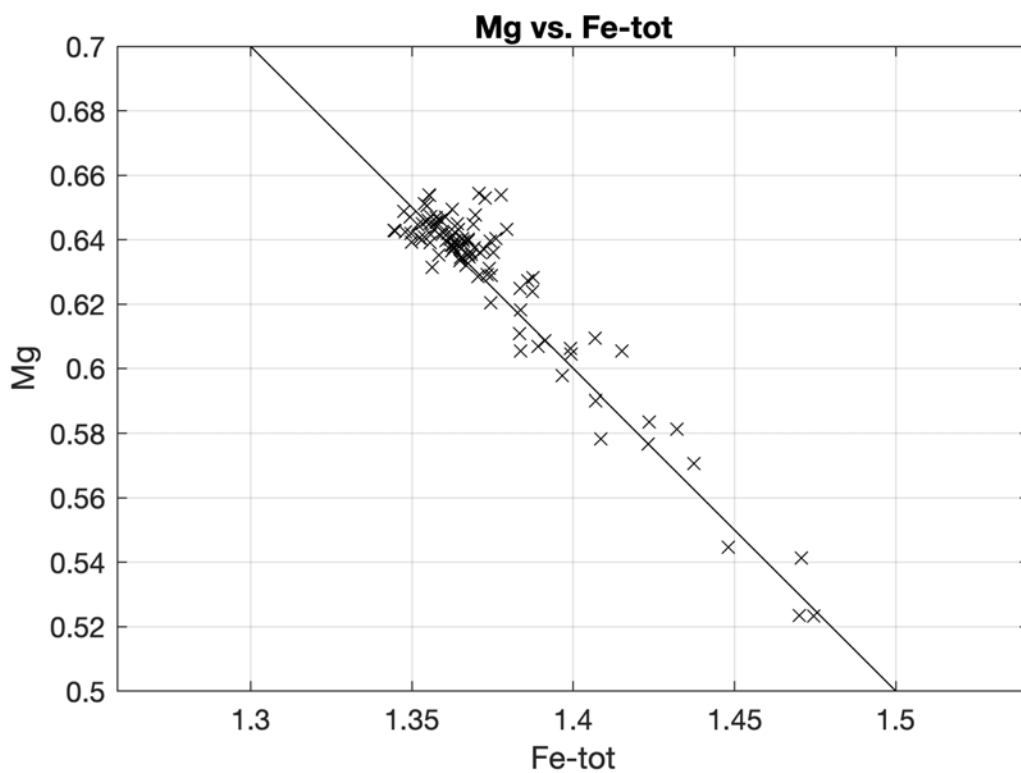
Figure 3.17: Atomic proportions of Mg and Fe-total in chloritoid.
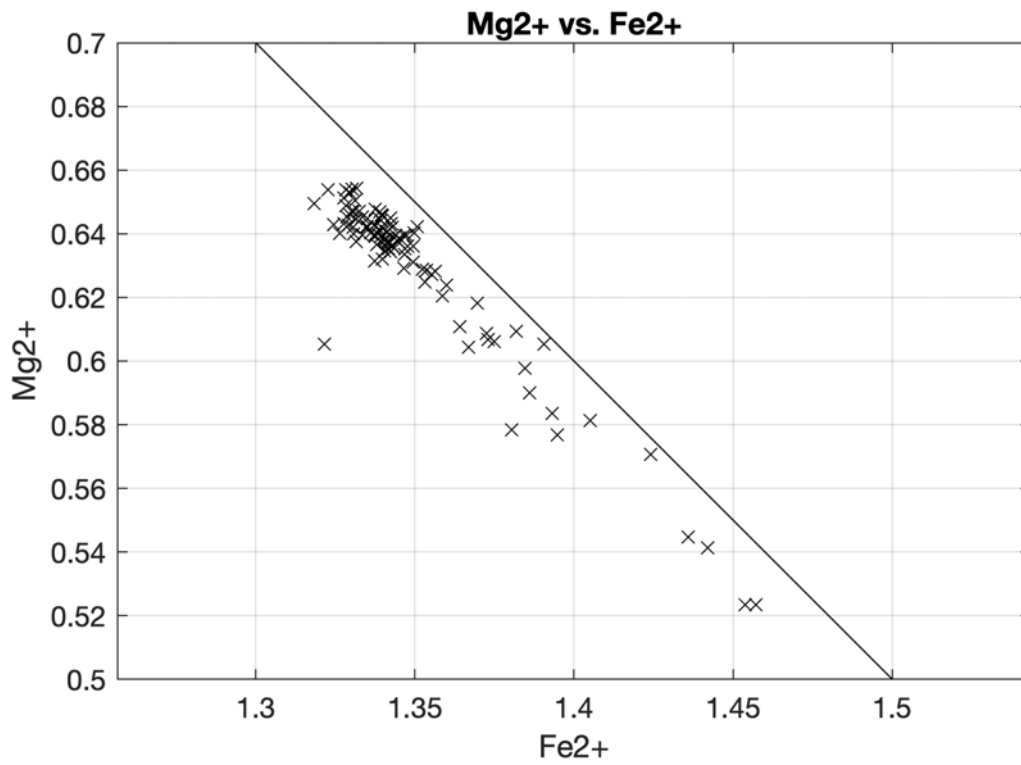
Figure 3.18: Atomic proportions of Mg and Fe^{2+} calculated for the remaining Al-octrahedral sites in chloritoid.
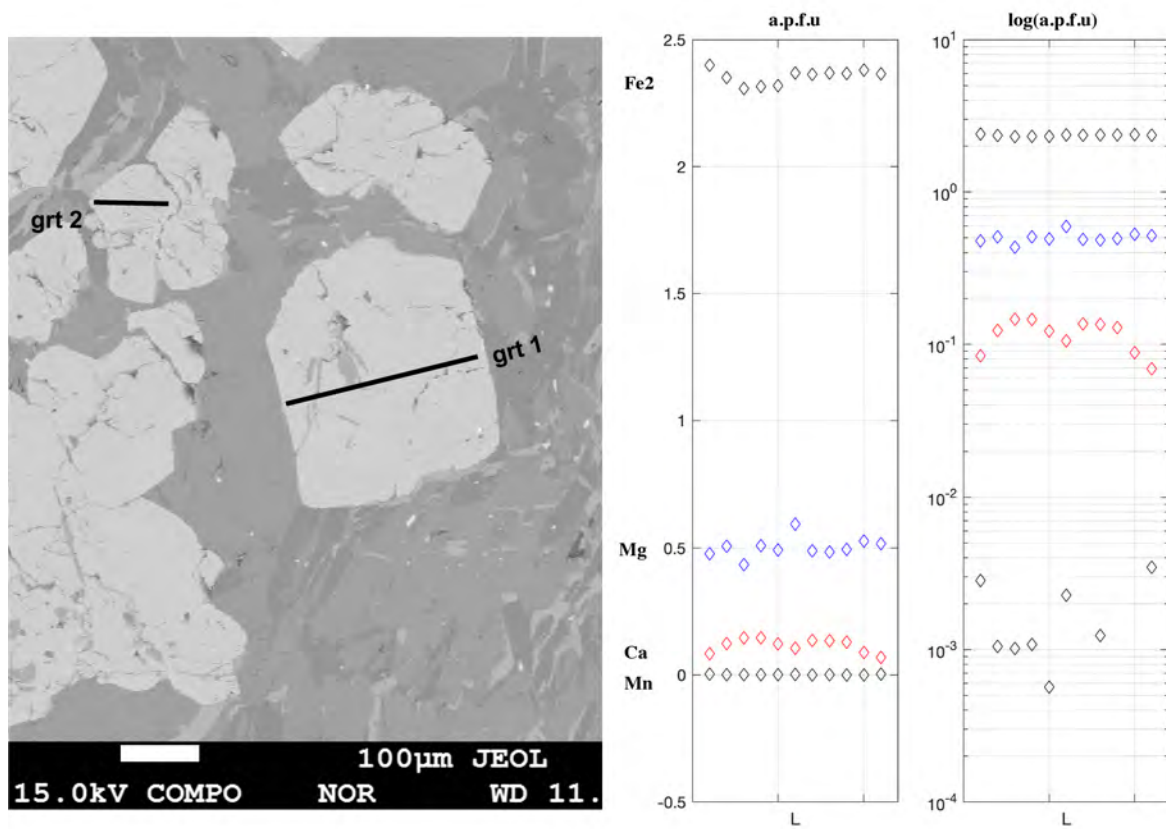
Figure 3.19: Zoning profiles in Alpine garnet bearing assemblages.
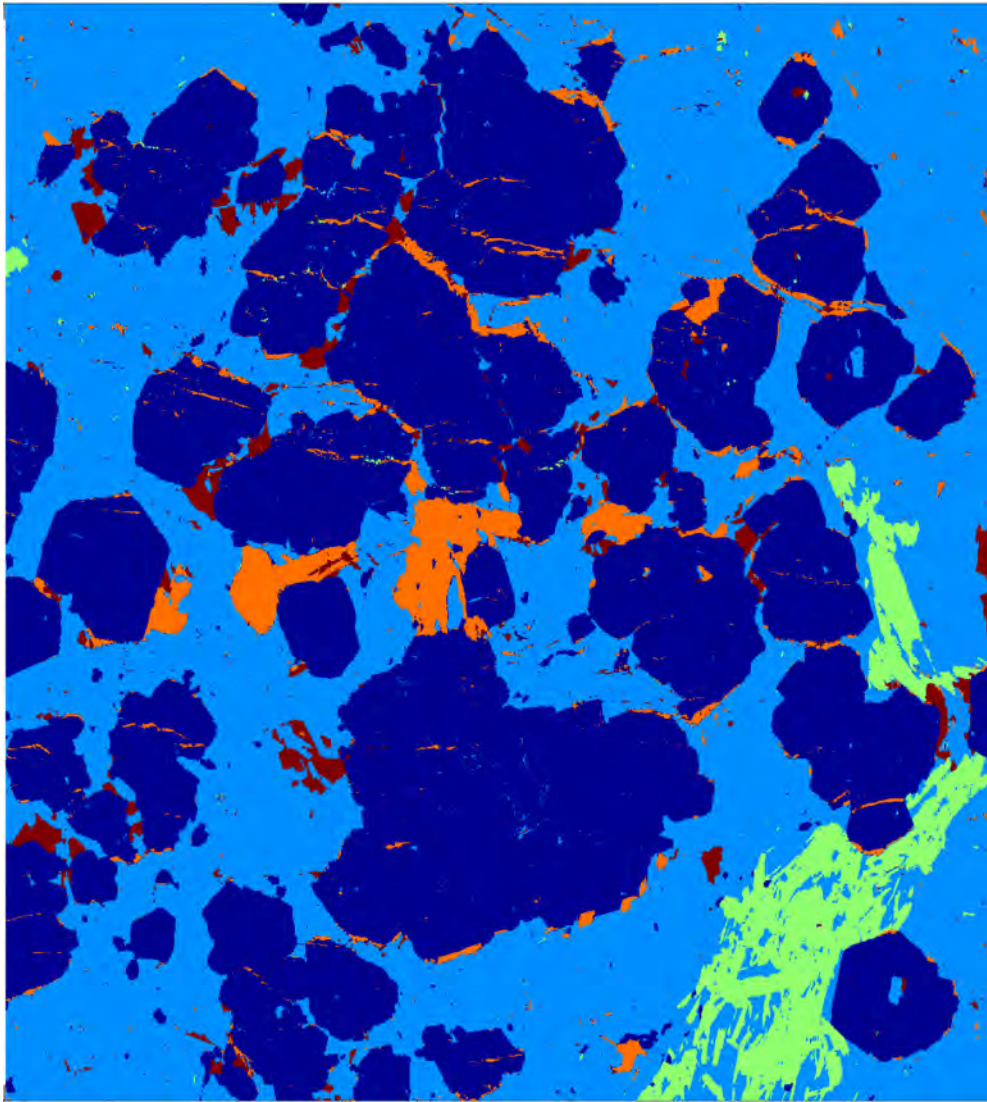
Figure 3.20: Assemblage 2 mineral phases calculated from image analysis from XMapTools (Lanari et al., 2014) (light blue = phengite, dark blue = garnet, maroon = quartz, orange = chlorite, and green = paragonite).

Bibliography

Bearth, P., 1952. Geologie und petrographie des monte rosa. Beitraege zur Geologischen Karte der Schweiz Lf. 96, 1–94.

Bearth, P., 1953. Geologischer atlas der schweiz, 1: 25000, blatt zermatt (nr. 29). Schweizerische Geologische Kommission, Bern.

Beltrando, M., Compagnoni, R., Lombardo, B., 2010. (ultra-) high-pressure metamorphism and orogenesis: an alpine perspective. Gondwana Research 18 (1), 147–166.

Berman, R., 1990. Mixing properties of Ca-Mg-Fe-Mn garnets. American Mineralogist 75 (3-4), 328–344.

Berman, R. G., 1988. Internally-consistent thermodynamic data for minerals in the system $Na_2O-K_2O-CaO-MgO-FeO-Fe_2O_3-Al_2O_3-SiO_2-TiO_2-H_2O-CO_2$. Journal of petrology 29 (2), 445–522.

Borghi, A., Compagnoni, R., Sandrone, R., 1996. Composite pt paths in the internal penninic massifs of the western alps: Petrological constraints to their thermo-mecanical evolution.

Butler, J. P., Beaumont, C., Jamieson, R. A., 2013. The Alps 1: A working geodynamic model for burial and exhumation of (ultra) high-pressure rocks in alpine-type orogens. Earth and Planetary Science Letters 377, 114–131.

Butler, J. P., Beaumont, C., Jamieson, R. A., 2014. The Alps 2: Controls on crustal subduction and (ultra) high-pressure rock exhumation in alpine-type orogens. Journal of Geophysical Research: Solid Earth 119 (7), 5987–6022.

Chopin, C., 1984. Coesite and pure pyrope in high-grade blueschists of the western alps: a first record and some consequences. Contributions to Mineralogy and Petrology 86 (2), 107–118.

Chopin, C., 1987. Very-high-pressure metamorphism in the western alps: implications for subduction of continental crust. Philosophical Transactions of the Royal Society of London. Series A, Mathematical and Physical Sciences 321 (1557), 183–197.

Chopin, C., Henry, C., Michard, A., 1991. Geology and petrology of the coesite-bearing terrain, dora maira massif, western alps. European Journal of Mineralogy 3 (2), 263–291.

Chopin, C., Monié, P., 1984. A unique magnesiochloritoid-bearing, high-pressure assemblage from the monte rosa, western alps: petrologic and 40 Ar-39 Ar radiometric study. Contributions to Mineralogy and Petrology 87 (4), 388–398.

Dal Piaz, G., Cortiana, G., Del Moro, A., Martin, S., Pennacchioni, G., Tartarotti, P., 2001. Tertiary age and paleostructural inferences of the eclogitic imprint in the austroalpine outliers and zermatt–saas ophiolite, western alps. International Journal of Earth Sciences 90 (3), 668–684.

Dal Piaz, G. V., 2001. Geology of the monte rosa massif: historical review and personal comments. Schweizerische Mineralogische und Petrographische Mitteilungen 81 (3), 275–303.

Dal Piaz, G. V., Lombardo, B., 1986. Early alpine eclogite metamorphism in the penninic monte rosa-gran paradiso basement nappes of the northwestern alps. Geol. Soc. Am. Mem 164, 249–265.

de Capitani, C., Brown, T. H., 1987. The computation of chemical equilibrium in complex systems containing non-ideal solutions. Geochimica et Cosmochimica Acta 51 (10), 2639–2652.

de Capitani, C., Petrakakis, K., 2010. The computation of equilibrium assemblage diagrams with theriak/domino software. American Mineralogist 95 (7), 1006–1016.

Dutrow, B. L., Holdaway, M., Hinton, R., 1986. Lithium in staurolite and its petrologic significance. Contributions to Mineralogy and Petrology 94 (4), 496–506.

Ellis, D., Green, D., 1979. An experimental study of the effect of Ca upon garnet-clinopyroxene Fe-Mg exchange equilibria. Contributions to Mineralogy and Petrology 71 (1), 13–22.

Engi, M., Scherrer, N., Burri, T., 2001. Metamorphic evolution of pelitic rocks of the monte rosa nappe. constraints from petrology and single grain monazite age data. Schweizerische Mineralogische und Petrographische Mitteilungen 81 (3), 305–328.

Escher, A., Beaumont, C., 1997. Formation, burial and exhumation of basement nappes at crustal scale: a geometric model based on the western swiss-italian alps. Journal of Structural Geology 19 (7), 955–974.

Eugster, H. P., 1985. Granites and hydrothermal ore deposits: a geochemical framework. Mineralogical Magazine 49 (350), 7–23.

Ferrando, J., Scambelluri, M., Dal Piaz, G., Piccardo, G., 2002. The mafic boudins of the southern furgg-zone, monte rosa nappe, nw-italy: from tholeiitic continental basalts to alpine eclogites and retrogressed products. 81 riunione estiva soc. Geol. It., Torino, 10–12.

Fox, J., 1971. Coexisting chloritoid and staurolite and the staurolite–chlorite isograd from the agnew lake area, ontario, canada. Geological Magazine 108 (3), 205–219.

Frey, M., Desmons, J., Neubauer, F., 1999. Metamorphic maps of the alps. an enclosure to. Schweiz. Mineral. Petrogr. Mitt 79 (1).

Gasco, I., Borghi, A., Gattiglio, M., 2011. P–T alpine metamorphic evolution of the monte rosa nappe along the piedmont zone boundary (gressoney valley, nw italy). Lithos 127 (1-2), 336–353.

Gerya, T., 2015. Tectonic overpressure and underpressure in lithospheric tectonics and metamorphism. Journal of Metamorphic Geology 33 (8), 785–800.

Gerya, T., Stöckhert, B., 2006. Two-dimensional numerical modeling of tectonic and metamorphic histories at active continental margins. International Journal of Earth Sciences 95 (2), 250–274.

Goffe, B., Chopin, C., 1986. High-pressure metamorphism in the western alps: zoneography of metapelites, chronology and consequences. Schweizerische mineralogische und petrographische Mitteilungen 66 (1-2), 41–52.

Griffen, D. T., 1981. Synthetic Fe/Zn staurolites and the ionic radius of IVZn2+. American Mineralogist 66 (9-10), 932–937.

Guidotti, C. V., 1970. The mineralogy and petrology of the transition from the lower to upper sillimanite zone in the oquossoc area, maine. Journal of Petrology 11 (2), 277–336.

Haar, L., 1984. NBS/NRC steam tables. CRC Press.

Hacker, B. R., Gerya, T. V., 2013. Paradigms, new and old, for ultrahigh-pressure tectonism. Tectonophysics 603, 79–88.

Handy, M. R., Schmid, S. M., Bousquet, R., Kissling, E., Bernoulli, D., 2010. Reconciling plate-tectonic reconstructions of alpine tethys with the geological–geophysical record of spreading and subduction in the alps. Earth-Science Reviews 102 (3-4), 121–158.

Hawthorne, F., Ungaretti, L., Oberti, R., Caucia, F., Callegari, A., 1993. The crystal chemistry of staurolite; i, crystal structure and site populations. The Canadian Mineralogist 31 (3), 551–532.

Holdaway, M., Dutrow, B., Shore, P., 1986. A model for the crystal chemistry of staurolite. American Mineralogist 71 (9-10), 1142–1159.

Holdaway, M., Mukhopadhyay, B., Dyar, M., Dutrow, B., Rumble, D., Grambling, J., 1991. A new perspective on staurolite crystal chemistry: Use of stoichiometric and chemical end-members for a mole fraction model. American Mineralogist 76 (11-12), 1910–1919.

Holland, T., 1979. Reversed hydrothermal determination of jadeite-diopside activities. Eos 60, 405.

Holland, T., Powell, R., 1998. An internally consistent thermodynamic data set for phases of petrological interest. Journal of metamorphic Geology 16 (3), 309–343.

Howie, R., Zussman, J., Deer, W., 1992. An introduction to the rock-forming minerals. Longman.

Huang, W., Wyllie, P., 1974. Melting relations of muscovite with quartz and sanidine in the K_2O-Al_2O_3-SiO_2-H_2O system to 30 kilobars and an outline of paragonite melting relations. American Journal of Science 274 (4), 378–395.

Hurford, A. J., Hunziker, J. C., Stöckhert, B., 1991. Constraints on the late thermotectonic evolution of the western alps: evidence for episodic rapid uplift. Tectonics 10 (4), 758–769.

Keller, L., Abart, R., Stünitz, H., De Capitani, C., 2004. Deformation, mass transfer and mineral reactions in an eclogite facies shear zone in a polymetamorphic metapelite (monte rosa nappe, western alps). Journal of Metamorphic Geology 22 (2), 97–118.

King, S. W., 1858. The Italian Valleys of the Pennine Alps: A Tour Through All the Romantic and Less-frequented" vals" of Northern Piedmont, from the Tarentaise to the Gries. J. Murray.

Kurz, W., Froitzheim, N., 2002. The exhumation of eclogite-facies metamorphic rocks—a review of models confronted with examples from the alps. International Geology Review 44 (8), 702–743.

Lanari, P., Vidal, O., De Andrade, V., Dubacq, B., Lewin, E., Grosch, E. G., Schwartz, S., 2014. Xmaptools: A MATLAB-based program for electron microprobe X-ray image processing and geothermobarometry. Computers Geosciences 62, 227–240.

Lapen, T. J., Johnson, C. M., Baumgartner, L. P., Dal Piaz, G. V., Skora, S., Beard, B. L., 2007. Coupling of oceanic and continental crust during eocene eclogite-facies metamorphism: evidence from the monte rosa nappe, western alps. Contributions to Mineralogy and Petrology 153 (2), 139–157.

Le Bayon, R., de Capitani, C., Frey, M., 2006. Modelling phase–assemblage diagrams for magnesian metapelites in the system K_2O–FeO–MgO–Al_2O_3–SiO_2–H_2O: geodynamic consequences for the monte rosa nappe, western alps. Contributions to Mineralogy and Petrology 151 (4), 395.

Li, Z. H., Gerya, T. V., Burg, J.-P., 2010. Influence of tectonic overpressure on P-T paths of hp-uhp rocks in continental collision zones: thermomechanical modelling. Journal of Metamorphic Geology 28 (3), 227–247.
URL http://dx.doi.org/10.1111/j.1525-1314.2009.00864.x

Luisier, C., Baumgartner, L., Schmalholz, S. M., Siron, G., Vennemann, T., 2019. Metamorphic pressure variation in a coherent alpine nappe challenges lithostatic pressure paradigm. Nature communications 10 (1), 1–11.

Mancktelow, N., 1993. Tectonic overpressure in competent mafic layers and the development of isolated eclogites. Journal of Metamorphic Geology 11 (6), 801–812.

Manzotti, P., Bosse, V., Pitra, P., Robyr, M., Schiavi, F., Ballevre, M., 2018. Exhumation rates in the gran paradiso massif (western alps) constrained by in situ U–Th–Pb dating of accessory phases (monazite, allanite and xenotime). Contributions to Mineralogy and Petrology 173 (3), 24.

Marger, K., Luisier, C., Baumgartner, L. P., Putlitz, B., Dutrow, B. L., Bouvier, A.-S., Dini, A., 2019. Origin of monte rosa whiteschist from in-situ tourmaline and quartz oxygen isotope analysis by SIMS using new tourmaline reference materials. American Mineralogist: Journal of Earth and Planetary Materials 104 (10), 1503–1520.

Massonne, H.-J., Schreyer, W., 1987. Phengite geobarometry based on the limiting assemblage with K-feldspar, phlogopite, and quartz. Contributions to Mineralogy and Petrology 96 (2), 212–224.

Massonne, H.-J., Szpurka, Z., 1997. Thermodynamic properties of white micas on the basis of high-pressure experiments in the systems $K_2O - MgO - Al_2O_3 - SiO_2 - H_2O$ and $K - 2O - FeO - Al_3O_3 - SiO_2 - H_3O$. $Lithos$ 41 $(1-3), 229--250$.

Molnar, P., Lyon-Caen, H., 1988. Some simple physical aspects of the support, structure, and evolution of mountain belts. Processes in continental lithospheric deformation 218, 179–207.

Moulas, E., Schmalholz, S. M., Podladchikov, Y., Tajčmanová, L., Kostopoulos, D., Baum-gartner, L., 2019. Relation between mean stress, thermodynamic, and lithostatic pressure. Journal of metamorphic geology 37 (1), 1–14.

Nagel, T., De Capitani, C., Frey, M., 2002. Isograds and P–T evolution in the eastern lepontine alps (graubünden, switzerland). Journal of Metamorphic Geology 20 (3), 309–324.

Niggli, E., 1960. Mineral-zonen der alpinen metamorphose in den schweizer alpen. Int. geol. Congr. Copenhagen, Rep. 21st Sess. Norden 13, 132–138.

Niggli, E., 1970. Alpine metamorphose und alpine gebirgsbildung. Fortschritte der Mineralogie 47 (1), 16–26.

Niggli, E., Niggli, C., 1965. Karten der verbreitung einiger mineralien der alpidischen meta-morphose in den schweizer alpen (stilpnomelan, alkali-amphibol, chloritoid, staurolith, dis-then, sillimanit). Eclogae Geologicae Helvetiae 58, 335–368.

Pawlig, S., 2001. Geological evolution of the monte rosa: constraints from geochronology and geochemistry of a talc kyanite chloritoid shear zone within the monte rosa granite (monte rosa nappe, italian western alps). Thesis.

Pawlig, S., Baumgartner, L., 2001. Geochemistry of a talc-kyanite-chloritoid shear zone within the monte rosa granite, val d'ayas, italy. Schweizerische mineralogische und petrographische Mitteilungen 81, 329–346.

Petrini, K., Podladchikov, Y., 2000. Lithospheric pressure-depth relationship in compressive regions of thickened crust. Journal of Metamorphic Geology 18, 67–77.

Platt, J., 1986. Dynamics of orogenic wedges and the uplift of high-pressure metamorphic rocks. Geological society of America bulletin 97 (9), 1037–1053.

Powell, R., Holland, T., 1993. On the formulation of simple mixing models for complex phases. American Mineralogist 78 (11-12), 1174–1180.

Rao, B., Johannes, W., 1979. Further data on the stability of staurolite, neues jahrb. Mineral. Monath 10, 437–447.

Reinecke, T., 1991. Very-high-pressure metamorphism and uplift of coesite-bearing metasediments from the zermatt-saas zone, western alps. European Journal of Mineralogy, 7–18.

Reuber, G., Kaus, B. J., Schmalholz, S. M., White, R. W., 2016. Nonlithostatic pressure during subduction and collision and the formation of (ultra) high-pressure rocks. Geology 44 (5), 343–346.

Roda, M., Spalla, M. I., Marotta, A. M., 2012. Integration of natural data within a numerical model of ablative subduction: a possible interpretation for the alpine dynamics of the austroalpine crust. Journal of Metamorphic Geology 30 (9), 973–996.

Schenker, F. L., Schmalholz, S. M., Moulas, E., Pleuger, J., Baumgartner, L. P., Podladchikov, Y., Vrijmoed, J., Buchs, N., Müntener, O., 2015. Current challenges for explaining (ultra) high-pressure tectonism in the pennine domain of the central and western alps. Journal of Metamorphic Geology 33 (8), 869–886.

Schmalholz, S. M., Duretz, T., Hetényi, G., Medvedev, S., 2019. Distribution and magnitude of stress due to lateral variation of gravitational potential energy between indian lowland and tibetan plateau. Geophysical Journal International 216 (2), 1313–1333.

Schmalholz, S. M., Duretz, T., Schenker, F. L., Podladchikov, Y. Y., 2014a. Kinematics and dynamics of tectonic nappes: 2-d numerical modelling and implications for high and ultra-high pressure tectonism in the western alps. Tectonophysics 631, 160–175.

Schmalholz, S. M., Medvedev, S., Lechmann, S. M., Podladchikov, Y., 2014b. Relationship between tectonic overpressure, deviatoric stress, driving force, isostasy and gravitational potential energy. Geophysical Journal International 197 (2), 680–696.

Skora, S., Mahlen, N., Johnson, C. M., Baumgartner, L. P., Lapen, T., Beard, B. L., Szilvagyi, E., 2015. Evidence for protracted prograde metamorphism followed by rapid exhumation of the zermatt-saas fee ophiolite. Journal of Metamorphic Geology 33 (7), 711–734.

Steck, A., Masson, H., Robyr, M., 2015. Tectonics of the monte rosa and surrounding nappes (switzerland and italy): Tertiary phases of subduction, thrusting and folding in the pennine alps. Swiss Journal of Geosciences 108 (1), 3–34.

Tuisku, P., Ruosresuo, P., Häkkinen, A.-M., 1987. The metamorphic behaviour and petrogenetic significance of zinc in amphibolite facies, staurolite-bearing mica schists, puolankajärvi formation, central finland. Geochimica et Cosmochimica Acta 51 (6), 1639–1650.

Wheeler, J., 2018. The effects of stress on reactions in the earth: sometimes rather mean, usually normal, always important. Journal of Metamorphic Geology 36 (4), 439–461.

Whitney, D. L., Evans, B. W., 2010. Abbreviations for names of rock-forming minerals. American mineralogist 95 (1), 185–187.

In search of Peter Bearth's whiteschist: Jägerhorn peak, Piedmont, Italy

Joshua D. Vaughan-Hammon[1], **Lukas P. Baumgartner**[1], **Stefan M. Schmalholz**[1]

[1]Institut des Sciences de la Terre, University of Lausanne, Lausanne, Switzerland.

Abstract

Unique rocks known as 'whiteschists' are found throughout the Monte Rosa nappe and typically consist of phengite, talc, chloritoid and quartz. These assemblages are vital in reconstructing the metamorphic history of the Monte Rosa nappe due to their high pressure eclogitic imprint during Alpine subduction, estimated at ca. 2.2 GPa. Tectonic, or dynamic, pressure has recently been proposed in order to explain the 0.6 ± 0.2 GPa higher pressure recorded in these whiteschist lithologies, compared to lower pressure metapelitic and metagranitic rocks. Peter Bearth (1902-1989) was a pioneer in the geological mapping and understanding of the Monte Rosa nappe. However, during the 1950s, the metamorphic significance of whiteschist bodies was not fully understood until later in the mid 1980s. A potential outcrop of whiteschist was described, but not sampled by Peter Bearth in his 1952 geological map of Zermatt, translated from German as "platy, shiny-silver, quartz-muscovite schist with kyanite and ?chloritoid?". This outcrop was successfully located ~ 400 m below the summit of the Jägerhorn peak in a 2020 field campaign. This short communication provides a first geochemical analysis of the outcrop originally described by Peter Bearth.

4.1   Introduction

The Monte Rosa massif is a prominent area in the Swiss Valais and Italian Piedmont region (Figure 4.1a). The highest summit of the Monte Rosa massif is the Dufourspitz (4634 m), second to the highest mountain in western Europe, the Mont Blanc (4809 m). In 1789, H.B. de Saussure devoted one of his famous Alpine journeys (1779-96) to exploring the Monte Rosa massif (De Saussure, 1796). His *Voyage autour de Mont Rose* went from the Simplon pass to Macugnaga, and he writes: *"But there I saw Mont Rose, composed of an uninterrupted series of gigantic peaks almost equal to each other, forming a vast circus, and to enclose, within their walls, the village of Macugnaga, its hamlets, its pastures, the glaciers which border, and the steep slopes that rise to the tops of these majestic colossi. But it's not only the singularity of this form which makes it a remarkable mountain; maybe it's even more her structure. I have noticed that Mont-Blanc and all high tops of its chain are composed of layers vertical. In Monte Rosa, up to the highest peaks, everything is horizontal, or inclined at most 30 degrees."*

Geologically, the Monte Rosa nappe has a rich tectono-metamorphic history that spans > 300 Ma of activity and includes two major orogenic events, three thermal events, and > 10 deformation events (e.g. Dal Piaz, 2001; Engi et al., 2001; Froitzheim, 2001; Keller et al., 2004; Lapen et al., 2007; Pawlig and Baumgartner, 2001; Steck et al., 2015). The most studied period of tectono-metamorphic history incurred by the nappe is the youngest orogenic event, the Alpine orogeny, with peak metamorphism dated at 42.6 ± 0.6 Ma (Lapen et al., 2007). The current juxtaposition of tectonic units is a direct result of this Alpine orogenic event (Steck et al., 2015). Unique rocks within the Monte Rosa nappe known as whiteschists have been the focus of many studies aimed at characterizing Alpine subduction related peak metamorphism (Chopin, 1984; Dal Piaz et al., 2004, 2001; Luisier et al., 2019, 2021; Marger et al., 2019; Pawlig, 2001; Pawlig and Baumgartner, 2001). Eclogite conditions have been calculated for these whiteschist rocks, defined as the assemblage talc, chloritoid, phengite and quartz at c. 2.2-2.5 GPa and 500-600°C (Le Bayon et al., 2006; Luisier et al., 2019). A pre-Alpine, hydrothermal metasomatic (Mg-enriched), chlorite-sericite schist protolith has been proposed for the origin of whiteschists in the Monte Rosa nappe (Luisier et al., 2019, 2021; Marger

et al., 2019; Pawlig and Baumgartner, 2001). Notably, whiteschists within the Monte Rosa nappe have been the focus of recent studies quantifying potential contributions of tectonic, or dynamic, pressure during peak Alpine metamorphism, because peak pressure estimates for whiteschist formation systematically exhibit higher pressures (*c.* 0.6 GPa) compared to a host of other lithologies within the nappe such as metapelites and metagranites (Luisier et al., 2019; Vaughan-Hammon et al., 2021).

A notable figure in geological studies throughout the Monte Rosa was Peter Bearth (1902-1989), whose fieldwork pioneered much of our understanding of the nappe (Bearth, 1952, 1953b,a, 1958; Dal Piaz, 2001). One of Bearth's enduringly relevant contributions is the 1:25,000 sheet of Zermatt in the Geologischer Atlas der Schweiz (Bearth, 1953a). During Bearth's time mapping in Zermatt, the unique mineralogy and high-pressure implications of whiteschist lithologies were not known. A small elongate body was documented in Bearth's 1:25,000 Zermatt sheet, below the Jägerhorn summit to the east, within the Valle Anzasca, that was described as "platy, shiny-silver, quartz-muscovite schist with kyanite and ?chloritoid?". This petrological description is strikingly similar to assemblages documented for whiteschist bodies throughout the Monte Rosa nappe (Chopin and Monié, 1984; Le Bayon et al., 2006; Luisier et al., 2019, 2021; Marger et al., 2019; Pawlig and Baumgartner, 2001). However, Bearth did not investigate this body further, and no known samples were taken. This short communication intends to present the geological findings made when locating this 'whiteschist' during a field campaign in September 2020.

4.2   Location of sample

The outcrop in question resides within the steep, eastern wall of the Monte Rosa massif above the village of Macugnaga in the Valle Anzasca (Figure 4.1a). A two day climb, done by the first author together with mountain guide Alexander von Ungern, was required to pass from Macugnaga, over the Jägerhorn summit at the Italian-Swiss border, finishing in Zermatt (Figure 4.1a). A detailed climb-
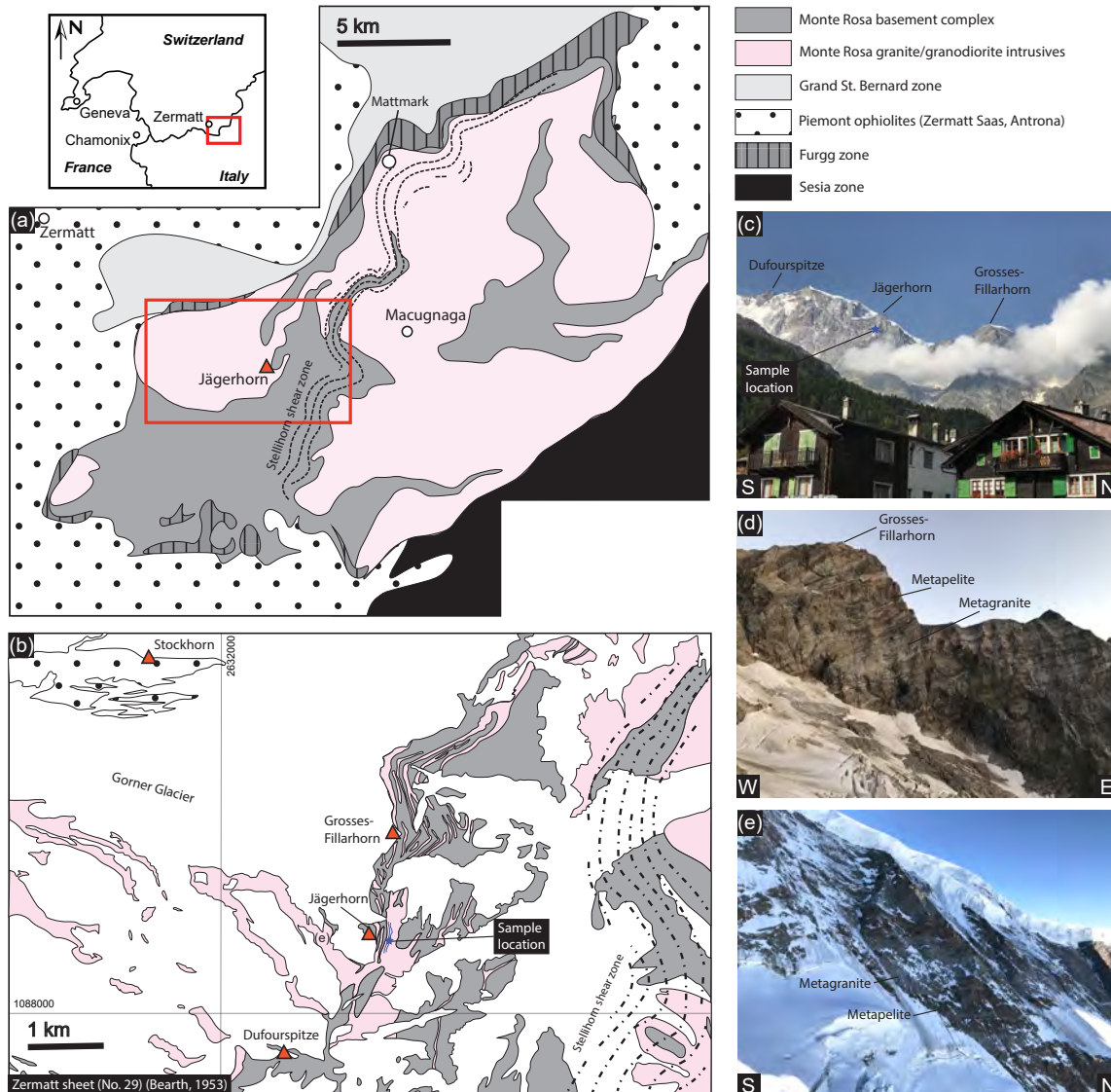
Figure 4.1: Location and photographs of field area. (a) Simplified geological map of the Monte Rosa nappe; modified after Steck et al. (2015). (b) Geological map surrounding the Jägerhorn summit (adapted from Bearth (1953a)) as well as location of samples. (c) Photograph of the Monte Rosa massif looking west from the village of Macugnaga, Italy. (d) Photograph of the main structures within the Monte Rosa nappe between metagranitic and metapelitic lithologies. d) Photograph of largescale igneous structures preserved within the Monte Rosa nappe (looking west from the summit of the Jägerhorn).

ing guide can be found online at `https://www.camptocamp.org/outings/1250102/fr/traversee-du-jagerhorn-arete-est-descente-gorner-gletscher`.

The western portions of the Valle Anzasca expose the upper portions of the Monte Rosa nappe (Oberbau), that is separated by the lower portions of the nappe (Unterbau) by the

strongly sheared and mylonitic Stellihorn shear zone exposed west of the Macugnaga village (Dal Piaz, 2001) (Figure 4.1a and b). The eastern wall of the Monte Rosa massif above Macugnaga where the Jägerhorn summit resides (Figure 4.1a, b and c), is west of this shear zone, and predominantly exposes horizontally intercalated basement metapelites and intrusive metagranites (Figure 4.1b and d). At 3000 m altitude, beginning the main wall climbing section towards the Jägerhorn summit, the first contact between the basement metapelites and metagranites are observed. Predominantly, these contacts are free from late Alpine reworking, typical of the Stellihorn shear zone, and metagranites exhibit original pre-Alpine, Permian-aged igneous fabrics. Approaching the summit of the Jägerhorn, the Monte Rosa nappe exhibits a series of intercalated basement and granite layers that are horizontally orientated, with irregular thicknesses ranging from 5 to 50 m in width (Figure 4.1d).

At an altitude of approximately 3523 m, we encountered the *c.* 20 m thick and > 100 m in length horizontal body of shiny-silver, quartz-muscovite schist indicated in Bearth's sheet of Zermatt (Bearth, 1953a) (Figure 4.1b and 4.2a). The outcrop is situated above a highly deformed section of biotite rich metapelite schists, within a section of metagranite. Two lithologies are encountered within this body, separated by a discrete transition zone. Approximately 90% of the body is made up of highly deformed, asymmetrically folded quartz-muscovite schists (schistosity = 161/63 (dip direction/dip), fold hinge lineation = 09-005 (dip-dip direction)). At the base of the quartz-muscovite schists, a 1 m layer of undeformed, medium grained, quartz + white mica + chloritoid bearing lithology is found (Figure 4.2b). No jadeite was observed within metagranite lithologies.

4.3 Sample description, mineral chemistry and phase petrology

Two samples were taken (Figure 4.1b), one from the quartz-muscovite schist 20MR-02 (Figure 4.2a) and one from the chloritoid bearing assemblage 20MR-01 (Figure 4.2b). For a description of the analytical methods and thermodynamic modelling methods, the reader is referred

to Vaughan-Hammon et al. (2021). This study primarily focuses on sample 20MR01. Two thin-sections were made from sample 20MR-01: 20MR-01.1 and 20MR-01.2.

Sections 20MR-01.1 and -01.2 display a weak foliation defined by orientated coarse-grained chloritoid + zoisite in a matrix of phengite + paragonite + quartz (Figure 4.2c). Late chlorite is observed throughout the sample replacing chloritoid, white mica and zoisite and precipitating in fractures (Figure 4.2c). Chloritoid and zoisite coexist as well as phengite + paragonite that also form dissolution precipitation rims surrounding chloritoid (Figure 4.2d). Notably, both thin-sections contain abundant quartz (c. 50%), and chloritoid contains abundant quartz inclusions that exhibit sector hour-glass zoning in three dimensions within chloritoid (Figure 4.2d and e). A stable peak paragenesis of phengite + paragonite + chloritoid + zoisite + quartz is inferred from textural observations.

Representative compositional results for phengite + paragonite + chloritoid + zoisite in thin-sections 20MR-01.1 and 20MR-01.2 are displayed in Table 4.1. Modal abundances of minerals were estimated for 20MR-01.1: phengite (15%), paragonite (14%), chloritoid (8%), zoisite (9%), and quartz (54%). Modal abundances of minerals were estimated for 20MR-01.2: phengite (9%), paragonite (18%), chloritoid (8%), zoisite (9%), and quartz (55%). Based on the modal abundances and representative compositional results in Table 4.1, bulk chemistry was calculated for thin-section 20MR-01.1 (Mass %): SiO2 = 69.97, Al_2O_3 = 19.91, FeO = 1.6, MgO = 1.85, CaO = 2.73, K_2O = 2.19, Na_2O = 1.75, H = 100, O = 227.955. Bulk chemistry was calculated for thin-section 20MR-01.2 (Mass %): SiO_2 = 70.31, Al_2O_3 = 19.93, FeO = 1.7, MgO = 1.76, CaO = 2.68, K_2O = 1.6, Na_2O = 2.03, H = 100, O = 228.47.

Figure 4.3a and b show the calculated pseudo-section results in the NCKFMASH system (SiO_2-Al_2O_3-FeO-MgO-CaO-K_2O-Na_2O-H_2O) for the bulk compositions mentioned above, for thin-sections 20MR-01.1 and 20MR-01.2 respectively (stable assemblages: Ph + Pg + Cld + Zo + Qtz) (mineral abbreviations after Whitney and Evans (2010)).

Phase calculations for thin-section 20MR-01.1 (Figure 4.3a) predict the observed mineral assemblage to be stable at 1.7 ± 0.2 GPa and 535 ± 15°C. Isopleths for volume proportions and elements in stable phases do not vary considerably within the stability field. Thermodynamic

Table 4.1: Representative microprobe analysis (20MR-01.1 and 20MR-01.2).

	20MR-01.1				20MR-01.2			
Analysis	Phengite	Paragonite	Chloritoid	Zoisite	Phengite	Paragonite	Chloritoid	Zoisite
SiO_2	47.14	47.02	25.51	40.35	49.63	47.68	25.51	40.06
Al_2O_3	36.62	40.66	42.00	33.77	31.34	41.37	42.74	33.47
TiO_2	0.01	0.06	0.01	0.04	0.23	0.05	0.00	0.06
MnO	0.00	0.00	0.16	0.01	0.00	0.00	0.13	0.04
ZnO	0.01	0.00	0.00	0.04	0.00	0.05	0.04	0.00
FeO	0.75	0.19	16.7	0.43	1.00	0.14	16.65	0.94
MgO	0.83	0.09	7.11	0.01	2.69	0.11	7.36	0.10
Na_2O	1.48	6.87	0.01	0.00	0.66	6.47	0.01	0.02
CaO	0.02	0.62	0.01	24.77	0.01	0.70	0.00	24.65
K_2O	9.81	0.79	0.00	0.00	10.59	1.55	0.01	0.00
Total	96.67	96.3	91.51	99.42	96.15	98.12	92.45	99.34
Normalized*	11 (a)	11 (a)	8 (c)	8 (c)	11 (a)	11 (a)	8 (c)	8 (c)
Si^{+4}	3.073	2.970	2.047	2.990	3.264	2.965	2.022	2.996
Al^{+3}	2.813	3.027	3.971	2.978	2.429	3.032	3.992	2.950
Ti^{+4}	0.005	0.003	0.000	0.001	0.011	0.002	0.000	0.003
Mn^{+2}	0.000	0.000	0.010	0.000	0.000	0.000	0.009	0.003
Zn^{+2}	0.000	0.000	0.000	0.001	0.000	0.002	0.003	0.000
Fe^{+2}	0.041	0.010	1.120	0.026	0.055	0.007	1.103	0.058
Mg^{+2}	0.081	0.010	0.850	0.005	0.264	0.010	0.870	0.011
Na^{+}	0.187	0.841	0.001	0.002	0.085	0.780	0.000	0.003
Ca^{+2}	0.002	0.042	0.000	1.988	0.001	0.047	0.000	1.975
K^{+}	0.816	0.064	0.000	0.000	0.889	0.123	0.000	0.000
Total	7.018	6.967	7.999	7.991	6.998	6.968	7.999	7.999

* normalization using anions (a) and cations (c)
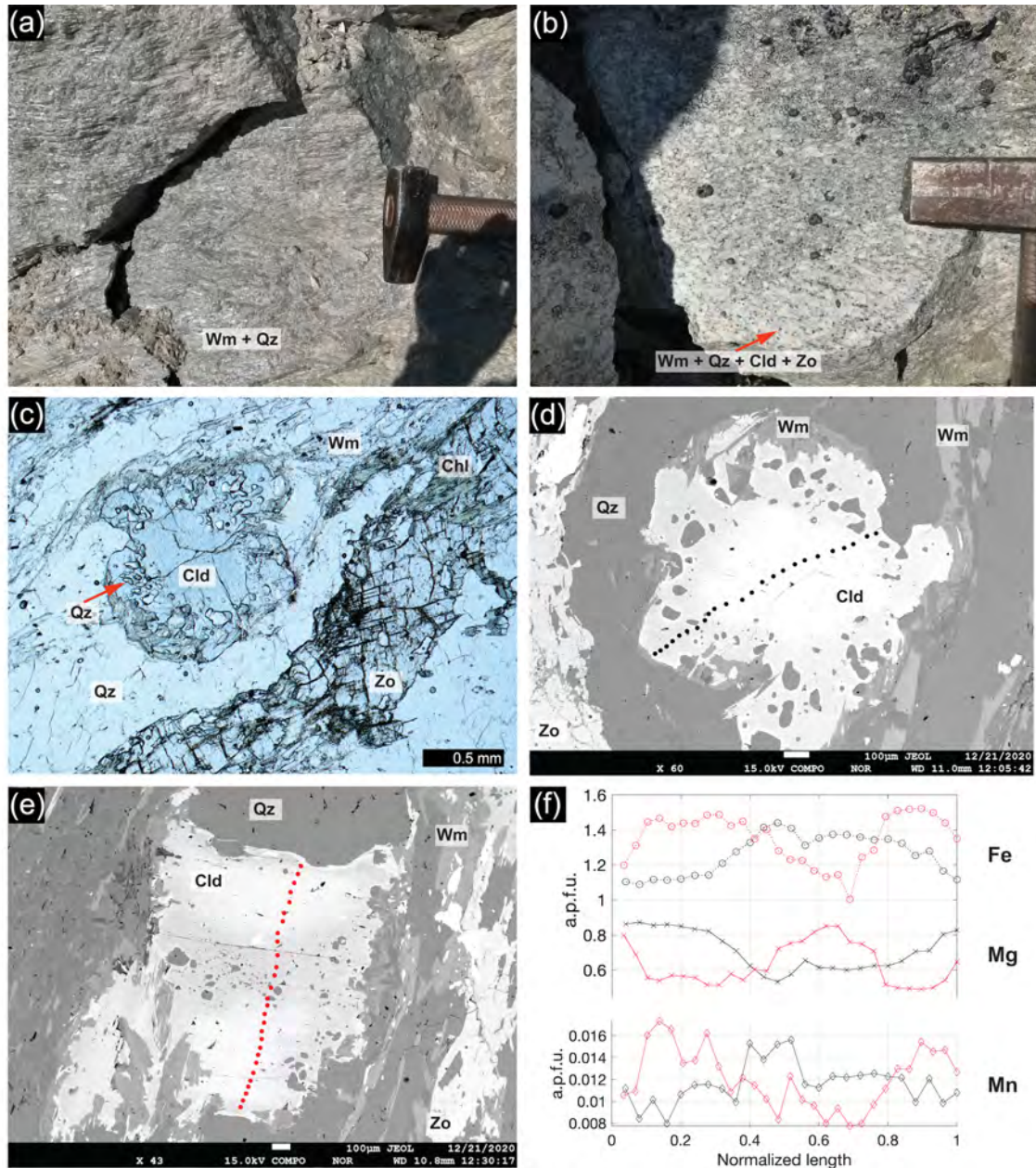
Figure 4.2: Petrology and outcrop images of samples. (a) quartz + phengite rich body, sample 20MR-02. (b) chloritoid bearing assemblages sample 20MR-01. (c) Thin-section plane polarized light image chloritoid bearing sample 20MR-01. (d) SEM image of chloritoid crystals containing abundance quartz inclusion and trace of microprobe point analysis (sample 20MR-01). (e) SEM image of chloritoid crystals containing abundance quartz inclusion and trace of microprobe point analysis (sample 20MR-01). (f) Microprobe point analysis for major elements Fe and Mg, as well as minor element Mn (sample 20MR-01).

volume proportion predictions for thin-section 20MR-01.1 (at 1.6 GPa and 540°C) are: Ph (15%), Pg (11%), Cld (9%), Zo (9%), and Qz (55%). Error percentages between measured and predicted phase proportions are calculated via $P_{error} = \frac{vol\%_{measured} - vol\%_{predicted}}{vol\%_{measured}}$: Ph$_{error}$ (-1%), Pg$_{error}$ (19%), Cld$_{error}$ (-10%), Zo$_{error}$ (-7%), and Qz$_{error}$ (-2%).

Phase calculations for thin-section 20MR-01.2 (Figure 4.3b) predicts the observed mineral assemblage to be stable at 1.65 ± 0.25 GPa and 530 ± 40°C. Isopleths for volume proportions and elements in stable phases do not vary considerably within the stability field. Thermodynamic volume proportion predictions for thin-section 20MR-01.2 (at 1.6 GPa and 540°C) are: Ph (11%), Pg (13%), Cld (10%), Zo (9%), and Qz (56%). Error percentages between measured and predicted phase proportions are: Ph$_{error}$ (-22%), Pg$_{error}$ (28%), Cld$_{error}$ (-22%), Zo$_{error}$ (-1%), and Qz$_{error}$ (-2%).

4.4   Discussion and conclusions

A sample reported by Peter Bearth as "platy, shiny-silver, quartz-muscovite schist with kyanite and ?chloritoid?" (Bearth, 1953a) was located and sampled within the Monte Rosa basement exposed below the summit of the Jägerhorn peak (Figure 4.1b). Two lithologies were identified, (1) a highly folded and schistose muscovite + quartz lithology, and (2) a relatively undeformed phengite + paragonite + chloritoid + zoisite + quartz (+ chlorite) lithology. What Peter Bearth initially observed as kyanite, was most likely zoisite (Figure 4.2).

The lack of talc (thus a low wt% of Mg) and abundance of zoisite (high wt% of Ca) within the sample does not fit the criteria for whiteschists observed throughout the Monte Rosa nappe (Chopin and Monié, 1984; Luisier et al., 2019, 2021; Marger et al., 2019; Pawlig and Baumgartner, 2001). Field observations indicate that the body occurs within the metagranitic complex of the Monte Rosa basement, close to the contact with basement metapelites. The relative abundance of Si, Al and Ca could indicate a metasomatic metagranitic protolith, however the low bulk Mg content is not in agreement with typical whiteschist metasomatic enrichment reported throughout the nappe (Chopin and Monié, 1984; Luisier et al., 2019; Pawlig and Baumgartner, 2001).
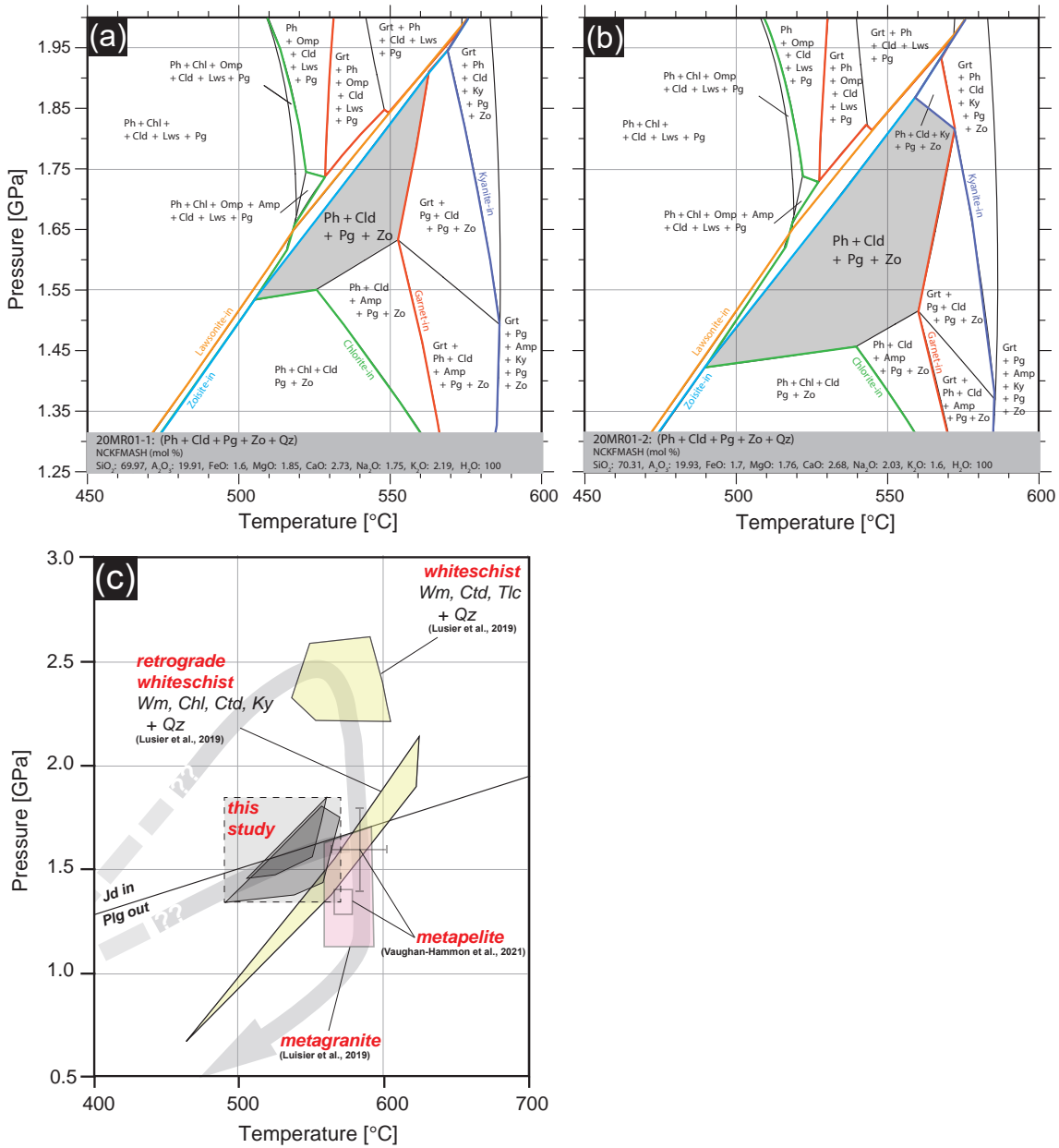
Figure 4.3: (a) and (b) Thermodynamic pseudo-section modelling for sample 20MR-01-1 and 20MR-01-2) using the Theriak/Domino software and JUN92 Berman database (Berman, 1988). (c) Compilation of peak Alpine metamorphic conditions obtained from various lithologies within the Monte Rosa nappe, as well as two scenarios highlighting the potential *P-T* pathways based on (i) lithostatic *P* and (ii) contributions of tectonic, or dynamic, pressure.

Peak metamorphic conditions are calculated at 1.65 ± 0.25 GPa and 530 ± 40°C for the unique stable assemblage of coexisting chloritoid + zoisite as well as phengite + paragonite + quartz (Figure 4.3). Assuming that this assemblage reflects peak Alpine metamorphic

conditions, the estimated peak P agrees within error with metapelite ($\sim$ 1.6 GPa (Vaughan-Hammon et al., 2021)) and metagranite ($\sim$ 1.4 GPa (Luisier et al., 2019)) estimates within the nappe (Figure 4.3c). The peak metamorphic conditions determined here continue to highlight a pressure disparity of 0.6 $\pm$ 0.2 GPa between the high pressure whiteschists ($\sim$ 2.2 GPa) (Luisier et al., 2019) and most other lithologies in the Monte Rosa nappe, such as metagranite, metapelite and the sample analyzed here, having all peak pressures within 1.65 $\pm$ 0.25 GPa. Qtz inclusions in chloritoid could provide further insights using Raman spectra to measure entrapment pressure (e.g. Angel et al., 2014), and many uncertainties are being addressed with regards to anisotropic inclusions (Mazzucchelli et al., 2019; Murri et al., 2018), e.g. rutile in garnet. However, anisotropic host minerals, such as quartz in chloritoid (this study), present many complications, and for now, our understanding is limited.

Revisiting the reported occurrences of shiny-silvery schists reported in seminal geological maps of the Monte Rosa massif by Bearth (1953a), highlights the accuracy and exhaustive work that was undertaken over half a century ago. The wealth of data available in these maps is still relevant for modern research studies today. During the 1950s, high-pressure lithologies such as whiteschists were not known until 30 years after (Chopin and Monié, 1984). However, Bearth's clear observations in the field, enable us with hindsight to benefit in understanding further the geological evolution of the Monte Rosa nappe.

4.5 Appendix

4.5.1 Supplementary material

All fieldwork and geochemical data is available on Zenodo via https://zenodo.org/record/5519475#.YUnc2dMzaLU.

Bibliography

Angel, R. J., Mazzucchelli, M. L., Alvaro, M., Nimis, P., Nestola, F., 2014. Geobarometry from host-inclusion systems: the role of elastic relaxation. American Mineralogist 99 (10), 2146–2149.

Bearth, P., 1952. Geologie und petrographie des monte rosa. Beitraege zur Geologischen Karte der Schweiz Lf. 96, 1–94.

Bearth, P., 1953a. Geologischer atlas der schweiz, 1: 25000, blatt zermatt (nr. 29). Schweizerische Geologische Kommission, Bern.

Bearth, P., 1953b. Geologischer atlas der schweiz, 1: 25000, blatt zermatt (nr. 29). Schweizerische Geologische Kommission, Bern.

Bearth, P. P., 1958. Über einen Wechsel der Mineralfazies in der Wurzelzone des Penninikums.

Berman, R. G., 1988. Internally-consistent thermodynamic data for minerals in the system Na_2O-K_2O-CaO-MgO-FeO-Fe_2O_3-Al_2O_3-SiO_2-TiO_2-H_2O-CO_2. Journal of petrology 29 (2), 445–522.

Chopin, C., 1984. Coesite and pure pyrope in high-grade blueschists of the western alps: a first record and some consequences. Contributions to Mineralogy and Petrology 86 (2), 107–118.

Chopin, C., Monié, P., 1984. A unique magnesiochloritoid-bearing, high-pressure assemblage from the monte rosa, western alps: petrologic and 40 Ar-39 Ar radiometric study. Contributions to Mineralogy and Petrology 87 (4), 388–398.

Dal Piaz, G., Cortiana, G., Del Moro, A., Martin, S., Pennacchioni, G., Tartarotti, P., 2001. Tertiary age and paleostructural inferences of the eclogitic imprint in the austroalpine outliers and zermatt–saas ophiolite, western alps. International Journal of Earth Sciences 90 (3), 668–684.

Dal Piaz, G., Pasquarè, G., Venturini, C., 2004. From the european continental margin to the mesozoic tethyan ocean: a geological map of the upper ayas valley (western alps).

Mapping Geology in Italy. APAT-Dip. Difesa del Suolo-Servizio Geol. d'Italia. SELCA, Firenze, 265–272.

Dal Piaz, G. V., 2001. Geology of the monte rosa massif: historical review and personal comments. Schweizerische Mineralogische und Petrographische Mitteilungen 81 (3), 275–303.

De Saussure, H. B., 1796. Voyages dans les Alpes. Vol. 3.

Engi, M., Scherrer, N., Burri, T., 2001. Metamorphic evolution of pelitic rocks of the monte rosa nappe. constraints from petrology and single grain monazite age data. Schweizerische Mineralogische und Petrographische Mitteilungen 81 (3), 305–328.

Froitzheim, N., 2001. Origin of the monte rosa nappe in the pennine alps—a new working hypothesis. Geological society of America bulletin 113 (5), 604–614.

Keller, L., Abart, R., Stünitz, H., De Capitani, C., 2004. Deformation, mass transfer and mineral reactions in an eclogite facies shear zone in a polymetamorphic metapelite (monte rosa nappe, western alps). Journal of Metamorphic Geology 22 (2), 97–118.

Lapen, T. J., Johnson, C. M., Baumgartner, L. P., Dal Piaz, G. V., Skora, S., Beard, B. L., 2007. Coupling of oceanic and continental crust during eocene eclogite-facies metamorphism: evidence from the monte rosa nappe, western alps. Contributions to Mineralogy and Petrology 153 (2), 139–157.

Le Bayon, R., de Capitani, C., Frey, M., 2006. Modelling phase–assemblage diagrams for magnesian metapelites in the system K_2O–FeO–MgO–Al_2O_3–SiO_2–H_2O: geodynamic consequences for the monte rosa nappe, western alps. Contributions to Mineralogy and Petrology 151 (4), 395.

Luisier, C., Baumgartner, L., Schmalholz, S. M., Siron, G., Vennemann, T., 2019. Metamorphic pressure variation in a coherent alpine nappe challenges lithostatic pressure paradigm. Nature communications 10 (1), 1–11.

Luisier, C., Baumgartner, L. P., Putlitz, B., Vennemann, T., 2021. Whiteschist genesis through metasomatism and metamorphism in the monte rosa nappe (western alps). Contributions to Mineralogy and Petrology 176 (1), 1–24.

Marger, K., Luisier, C., Baumgartner, L. P., Putlitz, B., Dutrow, B. L., Bouvier, A.-S., Dini, A., 2019. Origin of monte rosa whiteschist from in-situ tourmaline and quartz oxygen isotope analysis by SIMS using new tourmaline reference materials. American Mineralogist: Journal of Earth and Planetary Materials 104 (10), 1503–1520.

Mazzucchelli, M., Morganti, S., Reali, A., Domeneghetti, C., Angel, R., Alvaro, M., 2019. Elastic geobarometry: Relaxation of elastically anisotropic inclusions. Lithos 350, 351.

Murri, M., Mazzucchelli, M. L., Campomenosi, N., Korsakov, A. V., Prencipe, M., Mihailova, B. D., Scambelluri, M., Angel, R. J., Alvaro, M., 2018. Raman elastic geobarometry for anisotropic mineral inclusions. American Mineralogist: Journal of Earth and Planetary Materials 103 (11), 1869–1872.

Pawlig, S., 2001. Geological evolution of the monte rosa: constraints from geochronology and geochemistry of a talc kyanite chloritoid shear zone within the monte rosa granite (monte rosa nappe, italian western alps). Thesis.

Pawlig, S., Baumgartner, L., 2001. Geochemistry of a talc-kyanite-chloritoid shear zone within the monte rosa granite, val d'ayas, italy. Schweizerische mineralogische und petrographische Mitteilungen 81, 329–346.

Steck, A., Masson, H., Robyr, M., 2015. Tectonics of the monte rosa and surrounding nappes (switzerland and italy): Tertiary phases of subduction, thrusting and folding in the pennine alps. Swiss Journal of Geosciences 108 (1), 3–34.

Vaughan-Hammon, J. D., Luisier, C., Baumgartner, L. P., Schmalholz, S. M., 2021. Peak alpine metamorphic conditions from staurolite bearing metapelites in the monte rosa nappe (central european alps) and geodynamic implications. Journal of Metamorphic Geology n/a (n/a).

URL https://onlinelibrary.wiley.com/doi/abs/10.1111/jmg.12595

Whitney, D. L., Evans, B. W., 2010. Abbreviations for names of rock-forming minerals. American mineralogist 95 (1), 185–187.

CHAPTER 5

Metamorphic facies evolution and distribution in the Western Alps predicted by petrological–thermomechanical models

Joshua D. Vaughan-Hammon[1], **Lorenzo G. Candioti**[1], **Thibault Duretz**[2], **Stefan M. Schmalholz**[1]

[1]Institut des Sciences de la Terre, University of Lausanne, Lausanne, Switzerland.

[2]Univ Rennes, CNRS, Géosciences Rennes UMR 6118, Rennes, France.

Abstract

The distribution of metamorphic rocks throughout the western European Alps indicates subduction-related metamorphism. However, processes by which high-grade metamorphic rocks are formed and exhumed remain disputed. Here, we present two-dimensional petrological–thermomechanical models to investigate the metamorphic facies evolution during orogeny. The model simulates closure of an oceanic basin with exhumed mantle bounded by two passive margins. The initial model configuration is calculated with a lithosphere rifting simulation to ensure that the basin configuration is thermomechanically feasible. Initially, a serpentinite layer rests above the exhumed mantle. Both location and orientation of subduction are not prescribed and subduction initiates self-consistently during convergence. A weak subduction plate interface develops if serpentinite is initially thick enough (here 6 km) so that it becomes distributed along the interface. For a weak interface, syn-convergent exhumation occurs, enabled by local upper-plate extension and hanging-wall unroofing. We calculate the metamorphic facies evolution with peak P and T values of 10'000 numerical markers. The results show: (i) exhumed, structurally coherent regions with the same metamorphic facies, indicating absence of significant mechanical mixing (mélange) and (ii) a facies distribution corresponding to first order to the one observed in the Western Alps (from eclogite to blueschist to greenschist when going from internal to external domains). Models with a stronger subduction interface (here 3 km initial serpentinite thickness) develop an orogenic wedge with a vertical metamorphic gradient and minor exhumation. The results show that calculating metamorphic facies distribution is important to test the applicability of numerical models to natural orogens.

5.1 Introduction

Since the observation of regional-scale systematic changes in index minerals (Barrow, 1893), the subsequent conceptualization of metamorphic facies (Eskola, 1915) and the introduction and acceptance of plate tectonics (Wegener, 1915; Isacks et al., 1968; Le Pichon, 1968; Morgan, 1968), the dynamic nature of the Earth's crust has become a more clearer picture. More specifically, areas of crustal convergence, forming extensive mountain belts such as the European Alps, are observed to have unique metamorphic facies sequences linked to specific tectonic processes (Miyashiro, 2012). High-grade rocks exhumed in mountain belts, such as the European Alps, provide an ideal place to reconstruct deep tectono-metamorphic processes and subduction interface dynamics. In the European Alps, the distribution of metamorphic facies allows to identify (i) the spatial distribution of exhumed rocks that have been metamorphosed under similar pressure and temperature conditions (Bousquet et al., 2008; Frey et al., 1999; Lardeaux, 2014), (ii) the assessment of the ancient subduction direction (Ernst, 1971), and (iii) the spatial evolution of metamorphism through time (e.g. Lardeaux, 2014).

Advancements in dating metamorphism, in thermodynamic data and methods, in deterministic modelling as well as the vast number of field and geophysical studies, has improved our understanding of the tectono-metamorphic evolution of the Western Alps (Figure 5.1). Nevertheless, questions remain open regarding the transient conditions recorded in exhumed metamorphic terranes and the associated exhumation mechanisms. For example, some studies propose that rock exhumation and evolution of metamorphic facies in the Western Alps are due to exhumation during continuous plate convergence, so-called syn-convergent exhumation (e.g. Escher and Beaumont, 1997; Butler et al., 2014). In contrast, other studies argue that syn-convergent exhumation requires unrealistic erosion for the Western Alps, and propose exhumation during periods of plate divergence (e.g. Malusà et al., 2015; Liao et al., 2018). However, for these two fundamentally different exhumation mechanisms, the metamorphic facies evolution and distribution has not been studied in detail, to the best of our knowledge. Here, we investigate the metamorphic facies distribution for syn-convergent exhumation with

the aim to test whether syn-convergent exhumation can generate a metamorphic facies evolution and distribution which is comparable to the one of the Western Alps.
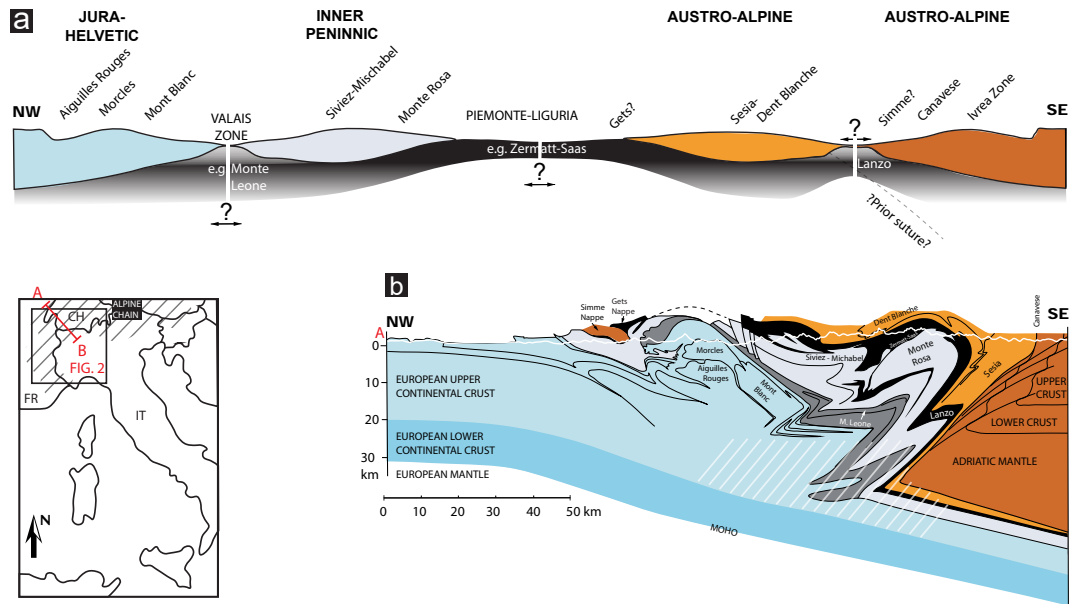
Figure 5.1: (a) Paleogeographic cross-section reconstruction of the western Alpine Tethys domain between the Adriatic and European margin prior to convergence (distorted horizontal and vertical scales), modified after Dal Piaz et al. (2001) and McCarthy et al. (2020). (b) Present-day cross-section of the Western Alps coloured with respect to paleogeographic domains in (a), modified after Escher et al. (1993), Escher et al. (1993) and Steck et al. (2015) (structure of white shaded area is not well constrained).

In addition to these questions concerning the fundamental exhumation process, more specific questions concern, for example: 1) The temperature evolution with potentially episodic heating events, such as Barrovian metamorphism in the Lepontine dome (Berger et al., 2011; Burg and Gerya, 2005; Jamieson et al., 1998; Ryan and Dewey, 2019; Stüwe, 1998), which is vital for reconstructing paleo-geotherms during orogenesis. 2) The pressure evolution with potential local deviations from lithostatic pressure (Luisier et al., 2019; Schenker et al., 2015; Vaughan-Hammon et al., 2021), which is essential for reconstructing the vertical movement of rocks during orogenesis. 3) The mechanisms by which small volumes of ultrahigh-pressure (UHP) rocks are exhumed and embedded in lower grade high-pressure (HP) units, for example the ca. 1 km thick Brosasco-Isasca UHP Unit within the HP Dora Maira massif (e.g. Chopin, 1987; Hacker and Gerya, 2013; Kurz and Froitzheim, 2002; Warren, 2013; Schmalholz and

Schenker, 2016; Groppo et al., 2019). With the aim of eventually resolving the issues mentioned above, we also (i) investigate the temporal relation between peak pressure and peak temperature for pressure-temperature-time (P-T-t) paths and (ii) study the relation between the metamorphic grade of exhumed rocks and their original paleogeographic position.

A wealth of petrologically-inspired burial and exhumation cycles of rocks within the Alps as well as their distribution through time and space exists (e.g. Bousquet et al., 2008; Lardeaux, 2014). This petrological data provides ample resources to test the validity of the tectono-metamorphic evolution predicted by deterministic numerical models. These numerical models are based on fundamental laws of physics, which are expressed by a system of partial differential equations describing conservation of mass, momentum and energy, and are constrained by mechanical properties and flow laws derived from laboratory rock deformation experiments. Many of such numerical models have been applied to characterize the mechanisms of exhumation of HP and UHP rocks within Alpine-type collisional belts (Burov et al., 2001; Butler et al., 2014; Gerya et al., 2002; Stöckhert and Gerya, 2005; Warren et al., 2008; Yamato et al., 2007, 2008; Ruh et al., 2015). Several of these studies trace individual numerical markers (Gerya and Yuen, 2003) in order to assess P-T-t trajectories of both continental and oceanic crustal material (e.g. Butler et al., 2014; Gerya et al., 2002; Stöckhert and Gerya, 2005; Warren et al., 2008; Yamato et al., 2007, 2008; Ruh et al., 2015). Several petrological studies have made considerable efforts to compile large datasets of subduction-related peak metamorphism for the entire Alps (e.g. Bousquet et al., 2008). However, no numerical modelling study, to the best of our knowledge, has attempted to reproduce in detail, and with comparable resolution, the regional-scale metamorphic architecture throughout the Western Alps (Figure 5.2). Therefore, we use here a petrological–thermomechanical numerical model for lithosphere deformation in order to calculate the associated metamorphic facies evolution and distribution during orogeny. The evolution of pressure and temperature of rocks that are subducted and exhumed are traced through space and time with numerical markers, which enables metamorphic facies to be mapped within the modelled orogen. We analyse $c.$ 10'000 numerical markers (out of $c.$ 56 million markers in total) for each simulation and use them to generate cross-sections showing the metamorphic facies evolution and distribution, which

we compare to published metamorphic facies distributions. The main aim of using so many markers is to calculate metamorphic facies fields, and not only individual *P-T* paths, in order to determine (i) whether exhumed rock units underwent significant tectonic mixing and (ii) whether the exhumed rocks form a regional trend of metamorphic facies which is comparable to the one observed in the Western Alps. As well as metamorphic facies distribution, the analysis of numerical markers enables investigating the palaeogeography and the timing of the metamorphic imprint.

Furthermore, numerical investigations highlight the importance of serpentinite during orogenic processes and particular the exhumation of UHP rocks (e.g. Agard et al., 2018; Ruh et al., 2015; Guillot and Hattori, 2013; Guillot et al., 2015; Schwartz et al., 2001; Candioti et al., 2020, 2021). The detailed rheological properties of serpentinite during subduction are still not well constrained (e.g. Hirth and Kohlstedt, 2003; Guillot and Hattori, 2013; Guillot et al., 2015; Amiguet et al., 2014; Hilairet et al., 2007). However, serpentinite is thought to contribute to the weakening of the plate-interface during active subduction (e.g. Hess, 1955; Agard et al., 2018; McCarthy et al., 2020), allowing for various segments of the subducted crust to exhume (Agard et al., 2018; Guillot and Hattori, 2013; Guillot et al., 2015). Hence, we also investigate the role of serpentinite during subduction and exhumation. We investigate the influence of serpentinite on the strength of the evolving subduction plate interface and its impact on the resulting spatio-temporal distribution of metamorphic facies comprising exhuming continental rocks.

5.2   Tectono-metamorphic evolution of the Western Alps

The present-day large-scale tectonic architecture of the Western Alps derives from the convergence and ultimate collision of the formerly hyper-extended margins of the northern Adriatic continent and southern European continent (Figure 5.1). Subduction presumably started in the distal parts of the Adriatic margin and persisted from the late-Cretaceous (85–65 Ma, Sesia-Lanzo zone: Duchêne et al., 1997; Engi et al., 2011; Inger et al., 1996; Rubatto et al., 1999; Manzotti et al., 2014a) to the late-Eocene (35–32 Ma, Dora Maira: Tilton et al., 1989;
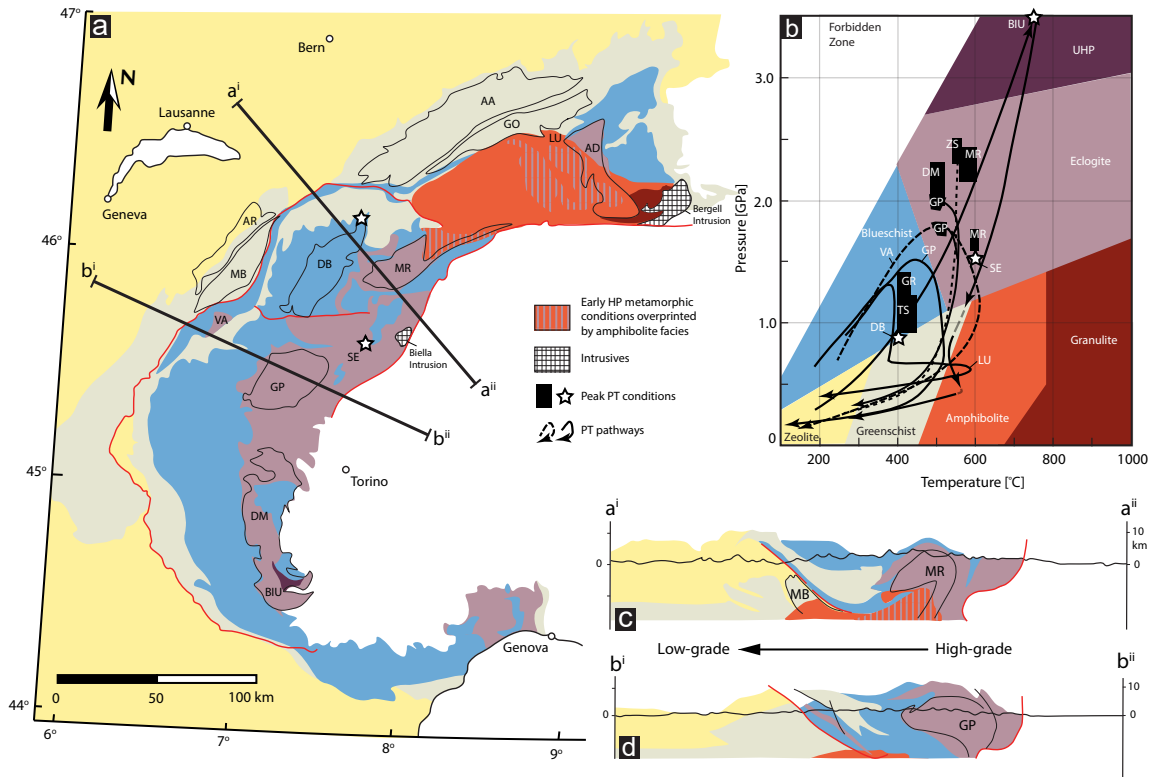
Figure 5.2: (a) Peak Alpine metamorphic facies distribution throughout the Western Alps with major units indicated, modified after Oberhänsli et al. (2004) and Bousquet et al. (2008) (AA = Aar massif, GO = Gotthard massif, LU = Lucomagno, AD = Adula, MR = Monte Rosa, DB = Dent Blanche, GP = Gran Paradiso, DM = Dora Maira, BIU = Brossasco-Isasca unit, SE = Sesia, VA = Valaisan, MB = Mont Blanc massif, AR = Aiguilles Rouge massif). (b) Approximate pressure-temperature metamorphic facies grid (modified after Philpotts and Ague, 2009) with representative *P-T* estimates for Western Alpine units (dashed and solid lines are used for clearer visualization), BIU = (Rubatto and Hermann, 2001), MR = (Luisier et al., 2019; Vaughan-Hammon et al., 2021), SE = (Lardeaux and JM, 1982; Vuichard and Ballevre, 1988), VA = (Goffé and Bousquet, 1997; Bousquet et al., 2002; Wiederkehr et al., 2007), GP = (Bousquet et al., 2008; Manzotti et al., 2018), LU = (Wiederkehr et al., 2008), DB = (Cortiana et al., 1998), DM = (Liati et al., 2009), TS = Tambo Suretta (Challandes et al., 2003), ZS = Zermatt-Saas (Angiboust et al., 2009), GR = Grisons (Bousquet et al., 2002). (c) and (d) cross-sections of peak metamorphic facies with direction of decreasing subduction related metamorphism indicated.

Duchêne et al., 1997; Gebauer et al., 1997; Di Vincenzo et al., 2006). Later-stage folding events (40–25 Ma, Mischabel folding: Keller et al., 2005; Barnicoat et al., 1995) combined with earlier subduction related nappe emplacement resulted in the current tectonic configuration (Figure 5.1b), which can be constructed in section due to the strong Alpine topography, axial plunges of exhumed units and interpretation of high resolution seismic data (Escher and

Beaumont, 1997; Escher et al., 1993; Schmid and Kissling, 2000; Schmid et al., 2017; Steck et al., 2015; Malusà et al., 2021). Paleogeographic reconstructions (e.g. Trümpy, 1975; Schmid et al., 2004; Lemoine et al., 1986; De Graciansky et al., 2011; McCarthy et al., 2020; Dal Piaz et al., 2001; Steck et al., 2015) of the Western Alps define 5 main domains (Figure 5.1a): 1) the structurally highest Adriatic margin comprising of the Ivrea Zone and Sesia–Dent Blanche continental units presumably separated by the exhumed sub-lithospheric mantle (e.g. Lanzo peridotites) from the main Adriatic margin, 2) the Piedmont oceanic domain, or upper Penninic, separating Adria and Europe (e.g. Zermatt-Saas ophiolites), 3) the middle Penninic domain (e.g. Monte Rosa and Siviez-Mischabel), 4) the Valais Zone, or lower Penninic, of sub-lithospheric mantle (e.g. Monte Leone peridotites), and 5) the external Jura-Helvetic domains comprising external crystalline basement massifs (e.g. Mont Blanc) and sedimentary cover series (e.g. Morcles nappe).

Widespread occurrences of deeply subducted oceanic domains, such as the former Piedmont ocean (e.g. Zermatt-Saas ophiolites) are comprised of significant proportions of serpentinite (c. 50 %, e.g. Angiboust et al., 2009). Continental internal crystalline massifs, such as the Monte Rosa, are almost entirely enveloped in serpentinite bearing oceanic domains (Zermatt-Saas and Antrona) (Figure 5.1b). The presence of serpentinite bearing oceanic domains is thought to be integral to an evolving collisional orogen such as the Western Alps (e.g. Hess, 1955; Forster et al., 2004; Angiboust et al., 2009; McCarthy et al., 2020).

The arcuate nature of the Western and Central Alpine mountain belt has resulted in a metamorphic zoning pattern of similar geometry (Figure 5.2a). Throughout the western Alps, metamorphic facies conditions related to subduction are observed, from UHP to greenschist facies (Figure 5.2a and b) (Oberhänsli et al., 2004; Bousquet et al., 2008). Studies from the early 1970s provide first overviews of the metamorphic facies distribution in the Alps (Ernst, 1971) and a first overview of the mineralogy and distribution of metamorphic indicators was provided in the 26th international Geol. Congress (Saliot, 1973), although UHP rocks were not identified until a few years after (e.g. Chopin, 1984). Soon after it was becoming more apparent that there exists a regional metamorphic trend, with an internal zone of high-pressure

domains and decreasing metamorphic grade towards the external, foreland basin direction (Figure 5.2a, c and d).

Figure 5.2 shows a simplified metamorphic distribution of rocks within the Western Alps, modified after Oberhänsli et al. (2004) and Bousquet et al. (2008), based on approximate pressure and temperature ranges for basic metamorphic facies (Philpotts and Ague, 2009). Petrologically-determined pressure-temperature pathways for a range of lithologies and from various locations within the Western Alpine metamorphic belt, typically exhibit clockwise direction burial and exhumation pathways (Figure 5.2b). This subduction related metamorphism is, in some places, overprinted by a thermally dominated metamorphic event, e.g. Lucomagno nappe heating during decompression (Wiederkehr et al., 2008). This thermal perturbation within the Central Alps is known as the Lepontine Dome, and is characterized by a metamorphic domal structure of concentric thermal isograds (e.g. Steck and Hunziker, 1994) that presumably cross-cut early-Alpine high-pressure, low-temperature nappe boundaries of the Penninic units (e.g. Burg and Gerya, 2005). This heating event reaches amphibolite to granulite facies conditions c. 600 ± 150 (e.g. Engi et al., 1995) dated between 40–30 Ma (e.g. Schlunegger and Willett, 1999), as well as local anatexis in the southern Central Alps and close to the late Alpine Bergell intrusion (32.8–22 Ma: von Blackenburg, 1992; Oberli et al., 2004; Gregory et al., 2009; Rubatto et al., 2009; Gianola et al., 2014). In cross-section, late-Alpine thermal overprinting is mainly confined to rocks derived from the subducting European plate, reaching the highest structural levels at the Monte Rosa and Antrona contact (Figure 5.2c) (Bousquet et al., 2008). Compared to earlier subduction related metamorphism, the mechanisms for the late thermal event are still disputed, with interpretations based on viscous heating or increased radiogenic heat production (e.g. Jamieson et al., 1998; Burg and Gerya, 2005).

5.3   Numerical model

5.3.1   Model approach and overview

We apply a numerical model to simulate the convergence of a marine basin with exhumed mantle which is bounded by two magma-poor passive margins (Figure 5.3b). We do not design this initial basin configuration ad hoc, but generate this basin configuration with a lithospheric rifting simulation using the same numerical model. The model characteristics such as the size of the basin, the rifting and convergence velocities or the duration of rifting and convergence are chosen to be applicable to the Western Alpine orogeny, which likely resulted from a Wilson Cycle involving an embryonic ocean (e.g. Wilson, 1966; Dewey and Burke, 1974; Mohn et al., 2010; Beaussier et al., 2019; Erdős et al., 2019; Chenin et al., 2019; Candioti et al., 2021). The term embryonic implies that the basin formed mainly by ultra-slow spreading without the generation of significant mature oceanic crust (e.g. McCarthy et al., 2020). Although the numerical simulation covers an entire extension–convergence cycle, we focus here only on the last stages of the convergence period involving subduction and exhumation of continental crust. Our modelling approach is different to most previous numerical models focusing on rock exhumation and, therefore, we provide here first an overview and reasoning of the entire simulation before providing more details on the model configuration and applied numerical algorithm.

We simulate the initial basin configuration with two subsequent model periods: 1) Extension for 50 Myr of a continental lithosphere with initially constant thickness (see Table S1 and Figure S1), which leads to the formation of asymmetric passive continental margins bounding a marine basin floored by exhumed mantle (Duretz et al., 2016; Petri et al., 2019) (Figure 5.3a). We apply 1.0 cm yr^{-1} absolute boundary velocity during extension, which corresponds approximately to the average extension velocities during Mesozoic rifting (Le Breton et al., 2021). 2) A 60 Myr long period without far-field extension or convergence allowing for thermal equilibration of the evolved basin–margin system (e.g. Le Breton et al., 2021) (Figure 5.3b). At the end of this cooling period, we parameterize a serpentinization front at the upper portions of the mantle exhumed in the basin (e.g. McCarthy et al., 2020). The simulated

basin configuration, involving the serpentinite, serves as initial model configuration for the convergence simulation. We simulate the initial basin configuration, instead of describing it ad hoc, because this approach guarantees that (i) the initial asymmetric passive margin geometry is thermomechanically feasible, since it results from a thermomechanical numerical simulation, (ii) the initial geometry is isostatically stable since there are no major vertical movements in the lithosphere during the final stages of the cooling period and (iii) the thermal field in the lithosphere has established a conductive equilibrium geotherm, a stable thermal lower boundary of the lithosphere and stable thermal convection cells in the upper mantle, which would not be the case if the model would be started with zero velocities in the upper mantle (see also Candioti et al., 2020).

Figure 5.3b displays the initial configuration for the convergence simulation, which is separated in two periods: 1) Convergence is applied with 1.5 cm yr^{-1} absolute boundary velocity for 30 Myr to model plate boundary formation by subduction initiation and basin closure (e.g. Dewey et al., 1989; Schmid et al., 1996; Handy et al., 2015; Manzotti et al., 2014a) (Figure 5.3c). 2) The applied boundary velocity is reduced to 1.0 cm yr^{-1} for the rest of the simulation when the continental crust of the lower plate starts subducting. Subduction and exhumation of continental crustal rocks takes place during this period with reduced convergence velocity (e.g. Schmid et al., 1996; Handy et al., 2015) (Figure 5.3d), which is the main focus of our study.

5.3.2 Numerical algorithm and model configuration

The applied petrological–thermomechanical model is a state-of-the-art model for lithosphere and upper mantle deformation (Duretz et al., 2016; Petri et al., 2019; Candioti et al., 2020, 2021). The model considers visco-elasto-plastic incompressible deformtion, gravity, heat transfer, a simple erosion model and thermodynamically constrained densities. The mathematical model, the numerical algorithm and its calibration to the lithosphere–upper mantle system are described in detail in the open access articles of Candioti et al. (2020, 2021). We therefore do not describe again these details here but, for completeness, provide the de-
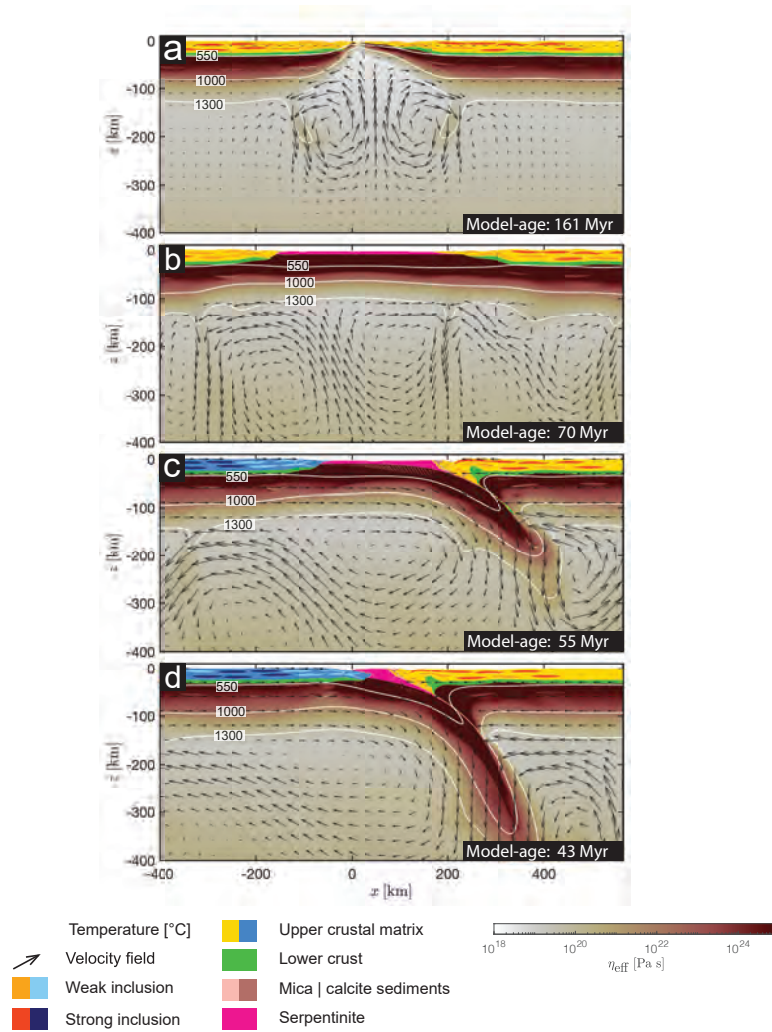
Figure 5.3: Numerical model evolution of phases and effective viscosity (η_{eff}) of the mantle prior to continental convergence. (a) Rifting of continental lithosphere and exposure of sub-lithospheric mantle. (b) Thermal relaxation of model and serpentinization of upper portions of exposed mantle. (c) Convergence of model and single-sided subduction initiated below distal portions of the hyper-extended continental margin. Continental phase colours changed to blue for subducted crust in order to delimit and imitate the European margin subducting below Adria (Figure 5.1). (d) Onset of continental collision and subduction of continental crust.

tailed description of the applied petrological–thermomechanical model in the supplementary material.

The initial model configuration for the extension model consists of a model domain with dimensions 1600×680 km (Figure S1). We employ a global resolution of 1×1 km. Modelled

units include a 25 km thick mechanically heterogeneous upper crust and an 8 km thick homogeneous lower crust (Figure S1b,c). Heterogeneities in the upper crust are modelled with elliptical regions having different mechanical properties than the surrounding, background, crust (see supplementary material, Figure S1c; see also Candioti et al. (2021)). The lithospheric mantle extends down to 120 km depth and we include the upper mantle down to a depth of 660 km. The upper regions of the mantle lithosphere contain similar elliptical regions with different mechanical properties as the surrounding mantle (see supplementary material, Figure S1c; see also Candioti et al. (2021)). These mechanical heterogeneities in the lithosphere are motivated by field observations in the exhumed Alpine passive margins (Duretz et al., 2016; Petri et al., 2019). We apply horizontal far-field tectonic forces by prescribing the material inflow/outflow velocities at the lateral boundaries (Figure S1a,d).

After the extension and cooling period (Figure 5.3a and b) the upper crust is separated by a basin with exhumed mantle lithosphere. The top of the exhumed mantle is replaced by a layer of serpentinite with different thickness, either 3, 5 or 6 km. Based on this initial configuration, we performed a systematic analysis of 18 numerical convergence simulations which test the impact of three parameters on the subduction and exhumation dynamics: 1) continental crustal strength by using a flow law for either Westerly granite or wet anorthite, 2) degree of parameterized serpentinization by applying different serpentinite thickness (3, 5 or 6 km), and 3) convergence velocity after basin closure (see supplementary material; Figures S2 and S3). The applied flow laws for the lower crust (wet anorthite), mantle lithosphere (olivine), the elliptical heterogeneities and serpentinite (antigorite) are specified in the supplementary information (Table S1). From these 18 simulations we selected two simulations: the flow law for the crust is that of Westerly granite, the convergence velocity after basin closure is 1.0 cm yr^{-1} and the serpentinite thickness is either 3 or 6 km. We chose these two simulations because they show two endmember scenarios for orogenic wedge formation applicable to the Western Alps: 1) a thrust dominated wedge (for 3 km serpentinite) and 2) a diapir dominated wedge (for 6 km serpentinite; see also Candioti et al. (2021)).

For these two convergence simulations, the effective density for all model units is calculated beforehand, with Perple_X phase equilibria models (Connolly and Petrini, 2002), based on

their corresponding pressure and temperature conditions for average bulk rock compositions (see table S2 in supplementary material).

The term "model-age (Myr)" presented in each figure, denotes the use of the numerical time being analogous to geological time used in many petrological studies, whereby the present day is regarded as 0 million years ago (Ma) and increases positively into the past. In this study, we adopt the same approach, whereby the final time-step has a model-age of 0 Myr. When applying the presented models to the Western Alps, the relative timescale of events should be considered. The absolute "model-ages" are of no significance, and 0 Myr (for the end of each simulation) has been chosen to aid comparison of timescales of orogenic activity, and therefore, should not be compared with absolute timing in the geological history of the Alps.

5.3.3   Defining numerical metamorphic facies

In order to assess the distribution of metamorphic facies within the modelled orogen, detailed P-T-t histories for numerical markers are analyzed. A Marker-in-Cell method (Gerya and Yuen, 2003) is employed to transport physical properties throughout the numerical grid. Nearly 56 million Lagrangian markers are used to transport physical properties at each time step. From the 56 million markers in total, $c.$ 10'000 representative markers are chosen for each simulation from the continental passive margin of the subducting plate prior to subduction. Following the P-T trajectory of markers during subduction, the maximum values of P and T are used to define a metamorphic facies (Figure 5.2b). This metamorphic facies identity at peak conditions is then stored for each individual marker regardless of its position during subsequent exhumation. Although a somewhat oversimplified metamorphic facies grid (Philpotts and Ague, 2009), i.e. neglecting subdivision such as upper greenschist facies and blueschist subdivisions etc., the main subdivisions are captured, e.g. eclogite–UHP transition defined by quartz–coesite. Also, a limiting geothermal gradient of 5/km for the forbidden zone conditions is implemented (Figure 5.2b). These metamorphic facies divisions are similar to

those used in studies characterising the metamorphic structure of metasediments throughout the European Alps (Figure 5.2) (e.g. Bousquet et al., 2008).

Since we are assessing subduction related metamorphism, i.e. peak metamorphic conditions, several assumptions are made. Firstly, a major assumption is that peak metamorphic conditions define an equilibrium state in a rock, and thus peak metamorphic rates are attained at peak conditions (e.g. Spear, 1989). Secondly, rocks defined by facies domains are assumed to be saturated and in equilibrium with water. Thirdly, we do not define transition zones between facies that could correspond to variations in bulk rock compositions or kinetic factors, which is a mixture of the above mentioned assumptions (Philpotts and Ague, 2009). Overall, we do not numerically model mineral assemblages that evolve during changing P-T conditions, rather, we infer the range of P-T conditions that would define an assemblage. This enables us to build a picture of the relative P-T conditions for subducted and exhumed continental rocks (Ghent, 2020).

A caveat of this numerical method is that the maximum P and maximum T of P-T pathways rarely correspond to the same point in P-T space. Therefore, we evaluate two peak metamorphic condition scenarios: 1) maximum T and corresponding P (herein referred to as max. T), and 2) maximum P and corresponding T (herein referred to as max. P). For each numerical simulation we present the results for both facies based on the max. P or max. T. A graphical representation of the difference between the max. P and max. T facies and the resulting computed metamorphic facies disparity can be found in the supplementary material (Figure S4).

5.4 Results

5.4.1 Pre-convergence situation and subduction initiation

Lithospheric extension leads to crustal break-up and the formation of two conjugate asymmetric magma-poor (see depth of 1300°C isotherm in Figure 5.3a) continental margins. After cooling at 70 Myr, a *c.* 360 km wide marine basin has formed which is floored by exhumed

mantle material (Figure 5.3b). Convection in the upper mantle has stabilised the thermal and mechanical thickness of the lithosphere to $c.$ 120-140 km (region without velocity glyphs in Figure 5.3b). At the end of the cooling period, the top 3 or 6 km of the exhumed mantle are replaced by material properties of serpentinite (Table S1 in supplementary material) to test the impact of the initial serpentinite thickness on subduction and exhumation. The extension and cooling period has generated a situation of a basin with exhumed mantle bounded by two asymmetric passive margins with the following characteristics: (i) the basin–passive margin geometry is thermomechanically feasible, (ii) the basin–passive margin system is mechanically and isostatically stable since there are no significant horizontal and vertical displacements during the cooling period, (iii) an equilibrium conductive geotherm has established across the lithosphere and stable thermal convection cells have stablished an average adiabtic thermal gradient in the upper mantle (see also results of Candioti et al., 2020) and (iv) there are no major prescribed weak zones across the lithosphere. This simulated basin–passive margin configuration serves as initial configuration for the convergence simulations.

During the early stages of convergence, subduction initiation is horizontally-forced, triggered by thermal softening (Kiss et al., 2019, 2020) and occurs below the distal portions of one continental hyper-extended margin (Figure 5.3c). The location and polarity of subduction initiation is not prescribed, but developes spontaneously in both models with a 3 and 6 km serpentinite layer thickness. Subduction initiation is, hence, a self-consistent thermomechanical feature of the converging basin–passive margin system. Furthermore, the characteristics of the emerging subduction plate interface have not been prescribed and this interface also emerges in a self-consistent manner. During basin closure and subduction, the serpentinites are strongly deformed, partly sheared off the subducting slab and eventually reorganise along the subduction interface (Figure 5.3d). In this study, we focus on the model evolution after basin closure, starting from the onset of subsequent subduction of continental crust during the final 40 Myr (Figure 5.4 and 5.5).
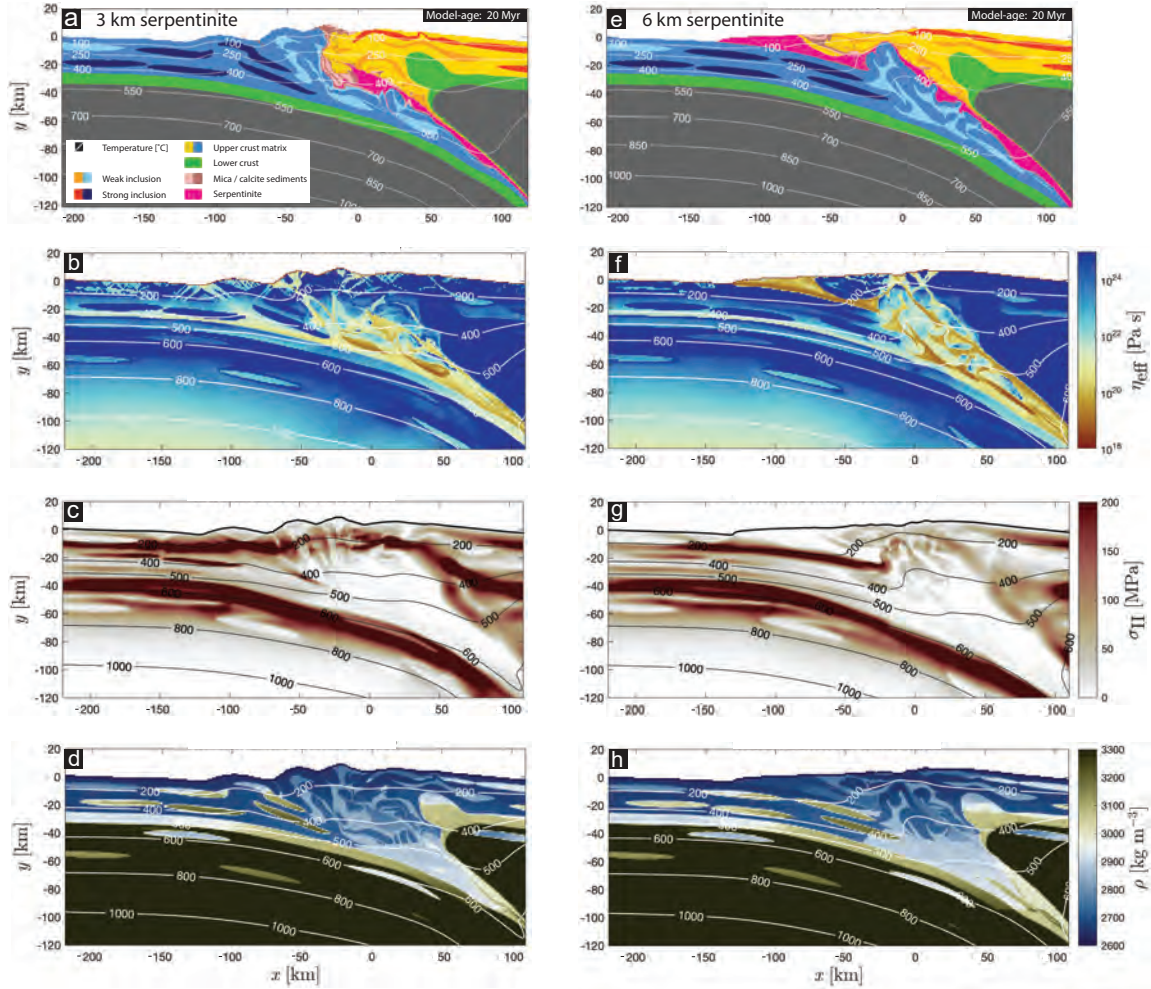
Figure 5.4: Nature of subduction interface during continental collision (3 km and 6 km serpentinite). (a) and (e) model phases. (b) and (f) effective viscosity (η_{eff}), highlighting the low viscosity plate interface propagating to the surface in the 6 km serpentinite model. (c) and (g) second invariant of deviatoric stress tensor components (σ_{II}), demonstrating the weak subduction interface in the 6 km serpentinite model. (d) and (h) effective density (ρ), note the relatively lower density buoyantly exhuming continental crust. Scientific colour maps used are provided by Crameri (2018).

5.4.2 Subduction and syn-convergent exhumation

Figure 5.4 highlights the characteristics of the subduction plate interface during subduction and orogenic wedge formation. For both models with 3 and 6 km serpentinite, a weak plate interface, having effective viscosity of less than *c.* 10^{20} Pas, develops in depths larger than *c.* 25 km (Figure 5.4b and f). The situation is different for the uppermost 25 km. For the 3 km

serpentinite model, a weak plate interface with low effective viscosity ($< 10^{20}$ Pas) is unable to develop within the uppermost 25 km due to the absence of serpentinite in this region (Figure 5.4a and b). Largest deviatoric stresses are *c.* 200 MPa in the uppermost 25 km (Figure 5.4c). These large deviatoric stresses form a more or less continuous horizontal layer indicating that the entire upper part of the orogen is under compression (Figure 5.4c). In contrast, for the 6 km serpentinite model, a weak plate interface made of serpentinite develops in the uppermost 25 km (Figure 5.4f and g). Deviatoric stresses are smaller in the uppermost 25 km of the orogen centre, compared to the 3 km serpentinite model (Figure 5.4g). The different strength of the plate interface in the upper region of the orogen has a strong impact on the exhumation, as will be discussed below. For both the 3 and 6 km serpentinite models, the overall density structure is similar (Figure 5.4d and h), so that differences in density and buoyancy are most likely not causing differences in exhumation dynamics between the two models.

We use color-coding of markers based on their initial paleogeographic position prior to subduction to study their *P-T* trajectories during subduction, collision and exhumation (Figure 5.5). We focus on the passive margin of the subducting plate. Furthermore, we analyse representative *P-T* pathways of individual markers (Figure 5.5). Numerical simulations with a 3 km serpentinite thickness (Figure 5.5a-c) subduct continental portions of the distal hyper-extended domain to depths of >100 km. However, these high-pressure domains are unable to exhume to depths shallower than 40 km (Figure 5.5c) and are prevented from reaching the surface by the over-riding plate. These subducted units do not retain their coherency and subsequently form a mechanical mixture below the overriding plate (Figure 5.5c). The overriding plate also forms a strong buttress to the more proximal domains towards the foreland, preventing them from being subducted (Figure 5.5a and c). The continental collision subsequently initiates foreland-directed folding and thrusting of continental material at shallow depths, as seen by the deformation of the weak and strong elliptical regions within the subducting continental lithosphere (Figure 5.5c).

Numerical simulations with a 6 km serpentinite thickness (Figure 5.5d-f) also subduct continental portions of the distal hyper-extended domain to depths of >100 km. In contrast to
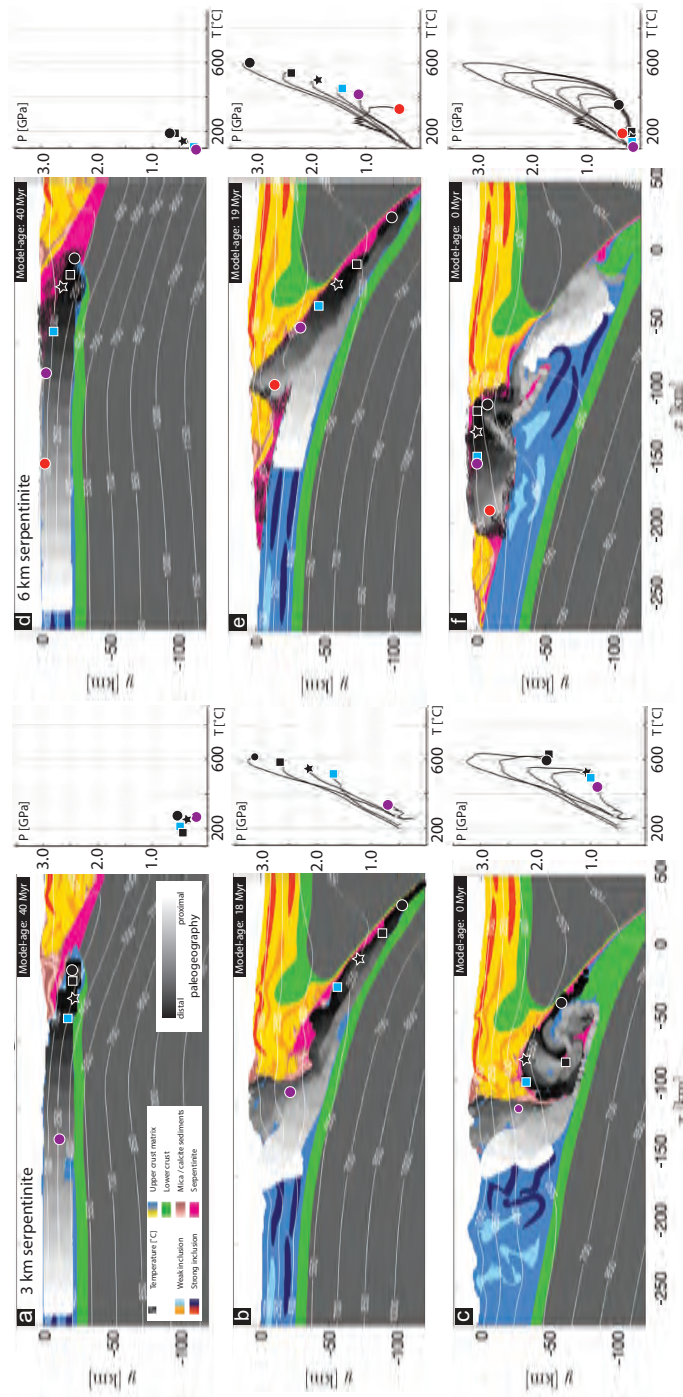
Figure 5.5: Model phase evolution of subduction and exhumation of continental crust. (a)-(c) 3 km serpentinite numerical model where markers are coloured by paleogeographic position at the former hyper-extended margin, as well as representative *P-T* evolution for subducted continental particles. (d)-(f) 6 km serpentinite numerical model where markers are coloured by paleogeographic position at the former hyper-extended margin, as well as representative *P-T* evolution for subducted continental particles.

the simulation with 3 km serpentinite thickness, considerable portions of the subducted rocks are exhumated to < 5 km depth (Figure 5.5f). *P-T* trajectories for representative markers within the subducting crust exhibit a clockwise burial and exhumation pathway (Figure 5.5f). The structural coherency of subducted and exhumed continental portions is maintained. The former paleogeographic transition from distal to proximal can still be observed in the final exhumed configuration, where distal parts are found within the core of the orogeny and proximal portions towards the foreland (Figure 5.5f). During the early stages of decompression, after peak *P* has been attained, buoyant exhumation of continental markers follows a near-isothermal decompression pathway (Figure 5.5f).
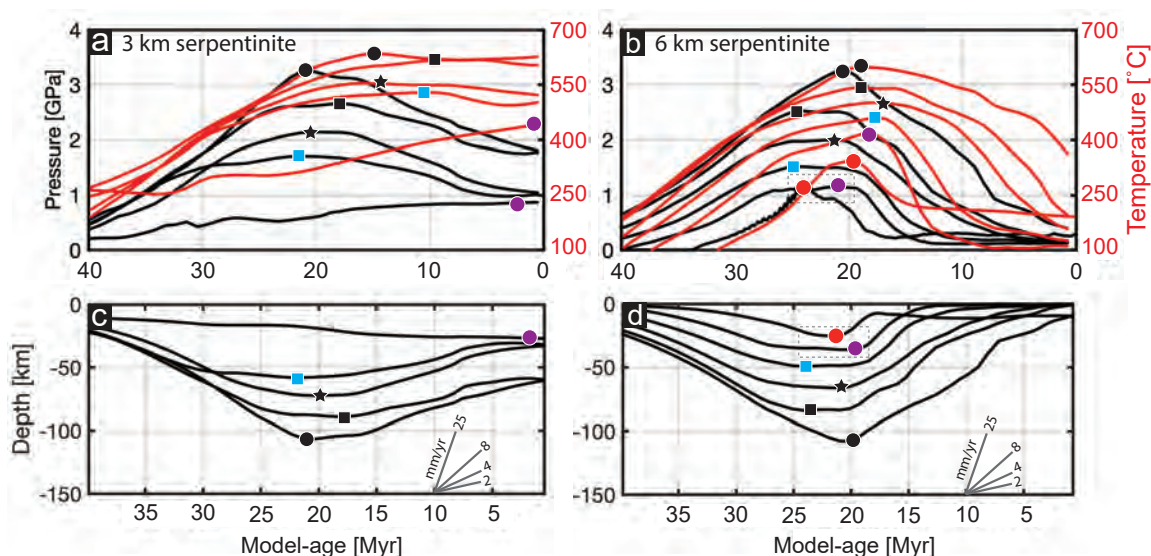
Figure 5.6: Marker evolution of continental particles during subduction, where symbols indicate the conditions of peak metamorphic grade (same as those in Figure 5.5). (a) and (b) *P-T*-time evolution with peak temperature and peak pressure conditions indicated. (c) and (d) depth-time evolution with maximum depth indicated and representative exhumation velocity gradients. Dashed boxes in (b) and (d) highlight the contribution of tectonic pressure for the red circle marker.

Figure 5.6 shows the temporal evolution of pressure, temperature and depth for markers indicated in Figure 5.5 for both 3 km and 6 km serpentinite thicknesses. Due to the lack of exhumation of deeply subducted particles for the 3 km serpentinite model, we do not observe notable cooling after peak conditions are attained (Figure 5.6a). In contrast, for the 6 km serpentinite model we observe cooling during exhumation (Figure 5.6b and d). For both models, we observe that peak values of *P* and *T* do not occur at the same time (Figure 5.6a

and b). Typically, peak T values post-date peak P values with larger discrepancies occurring for models with 3 km serpentinite (Figure 5.6a).

For the 3 and 6 km serpentinite models, the average vertical burial velocities of markers buried deeper than 50 km are $c.$ 4.5 mm/yr (Figure 5.6c and d). The average exhumation velocities for the 3 km serpentinite model do not exceed 3 mm/yr (Figure 5.6c). The exhumation velocities are, hence, slower than the burial velocities. The average exhumation velocities for the 6 km serpentinite model are $c.$ 6.5 mm/yr (Figure 5.6d). However, for short time intervals of few million years, exhumation velocities can exceed 10 mm/yr (e.g. marker indicated by solid black circle between $c.$ 9 and 7 Myr in Figure 5.6d). These exhumation velocities, hence, are larger than subduction-related burial velocities (Figure 5.6d).

For one marker of the simulation with 6 km serpentinite, a significant deviation from the lithostatic pressure is observed (red circle marker, Figure 5.5e and f, 5.6b and S4). This marker is buried to a maximal depth of $c.$ 25 km (Figure 5.6d). The peak P (indicated by the red circle) is similar to the peak P of a neighboring marker (indicated by the purple circle), which has been buried $c.$ 14 km deeper. The two markers are indicated in the dashed boxes in Figure 5.6b and d, to easily compare their similar peak P but different maximal burial depth. For the marker indicated with the red circle (Figure 5.6b and d), the peak P is $c.$ 0.4 GPa higher with respect to the corresponding lithostatic pressure, indicating a so-called tectonic overpressure (see also Figure S4).

5.4.3   Peak metamorphic conditions

Peak metamorphic conditions of continental markers that are subducted during convergence are presented in Figure 5.7. For similar areas within the hyper-extended margin (Figure 5.5a and d), the distribution of peak P and T conditions for models with 3 km and 6 km serpentinite vary considerably (Figure 5.7). The paleogeographic position of markers prior to subduction also varies for the two models. For 3 km serpentinite, the range of peak P-T conditions spans a considerable range of pressures, however, the temperature ranges for the corresponding pressure values are more narrow for max. T values (Figure 5.7a), compared to

max. P values (Figure 5.7b). The paleogeographic position shows that markers showing lower grade conditions originate from the more proximal portions of the hyper-extended margin, whereas markers that record high grade conditions originate from distal regions (Figure 5.7a and b). For the 6 km serpentinite model, the temperature ranges for the corresponding pressure values span a broader temperature range compared to 3 km serpentinite models (Figure 5.7c and d). This temperature range does not vary as considerably between max. T (Figure 5.7c) and max. P (Figure 5.7d) compared to the 3 km serpentinite model. The paleogeographic position correlates stronger with temperature rather than pressure, with more proximal regions reaching higher peak T compared to more distal regions (Figure 5.7c and d).

Considering only the markers that are subducted and subsequently exhumed to <20 km depth (red points Figure 5.7 and Figure 5.8), we observe a significant difference between models with 3 and 6 km serpentinite: markers for the 3 km serpentinite model do not record >1 GPa and >400 (Figure 5.8a and b), compared to markers for the 6 km serpentinite model that record >3.0 GPa and >600 (Figure 5.8c and d). The majority of ages of peak P and T for the 3 km serpentinite model occur late in the model evolution (15–5 Myr before the model stops at 0 Myr) (Figure 5.8a and b). Peak metamorphic ages for the 6 km serpentinite model based on max. T show a trend of older ages (25–5 Myr) compared to the 3 km serpentinite model, where we observe younger ages at higher temperatures and lower pressures (e.g. 0.5 GPa and 400 , Figure 5.8a). Peak metamorphic ages corresponding to max. P values in the 6 km serpentinite model show predominantly older ages (40–5 Myr) compared to max. T values (Figure 5.8c). Ages for max. T and max. P values exhibit a general trend of older ages for peak metamorphism with increasing temperature (Figure 5.8d).

As outlined in section 5.3.3, peak metamorphic facies are mapped within the modelled orogen for continental crust that has been subducted and exhumed. Figure 5.9a and c shows the metamorphic facies distribution for the 3 km serpentinite model based on peak P-T values corresponding to max. T (Figure 5.9a and b) and max. P (Figure 5.9c and d). Overall, the metamorphic facies are distributed in a horizontally layered manner, in cross section view, across the orogen (Figure 5.9a and c). The majority of subducted markers record eclogite
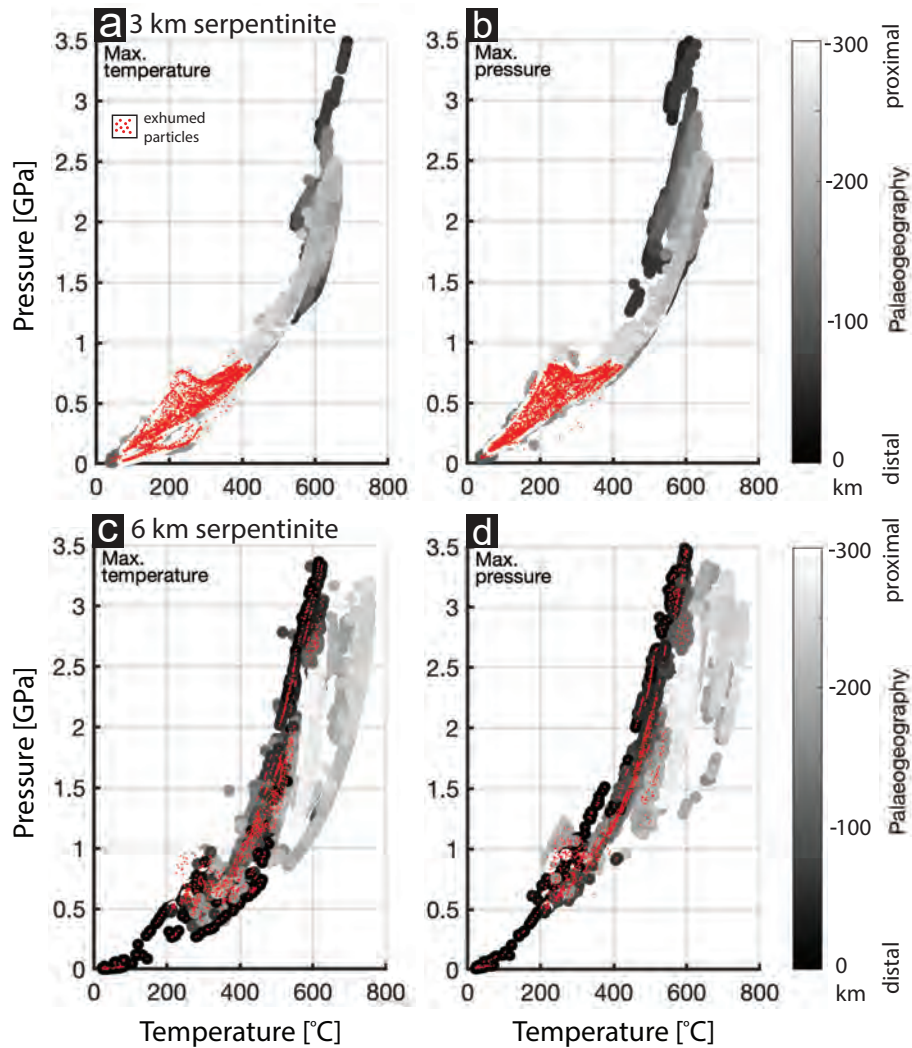
Figure 5.7: Maximum *P-T* conditions attained by subducted particles (indicated in Figure 5.5), coloured as a function of initial paleogeography within the hyper-extended margin prior to subduction, particles exhumed to <20 km depth are indicated in red. Max. temperature corresponds to *P-T* conditions taken using the maximum temperature attained during subduction. Max. pressure corresponds to *P-T* conditions taken using the maximum pressure attained during subduction (see methods section 5.3.2).

facies and are confined to depths larger than *c.* 40 km. Minor volumes of UHP facies are present in the deeper portions of the orogen where substantial tectonic mixing has occurred (*c.* 40 km) (Figure 5.9a and b). Higher volumes of blueschist and UHP facies are present for peak conditions based on max. *P* values (Figure 5.9c and d), than compared to max. *T* (Figure 5.9a and b).
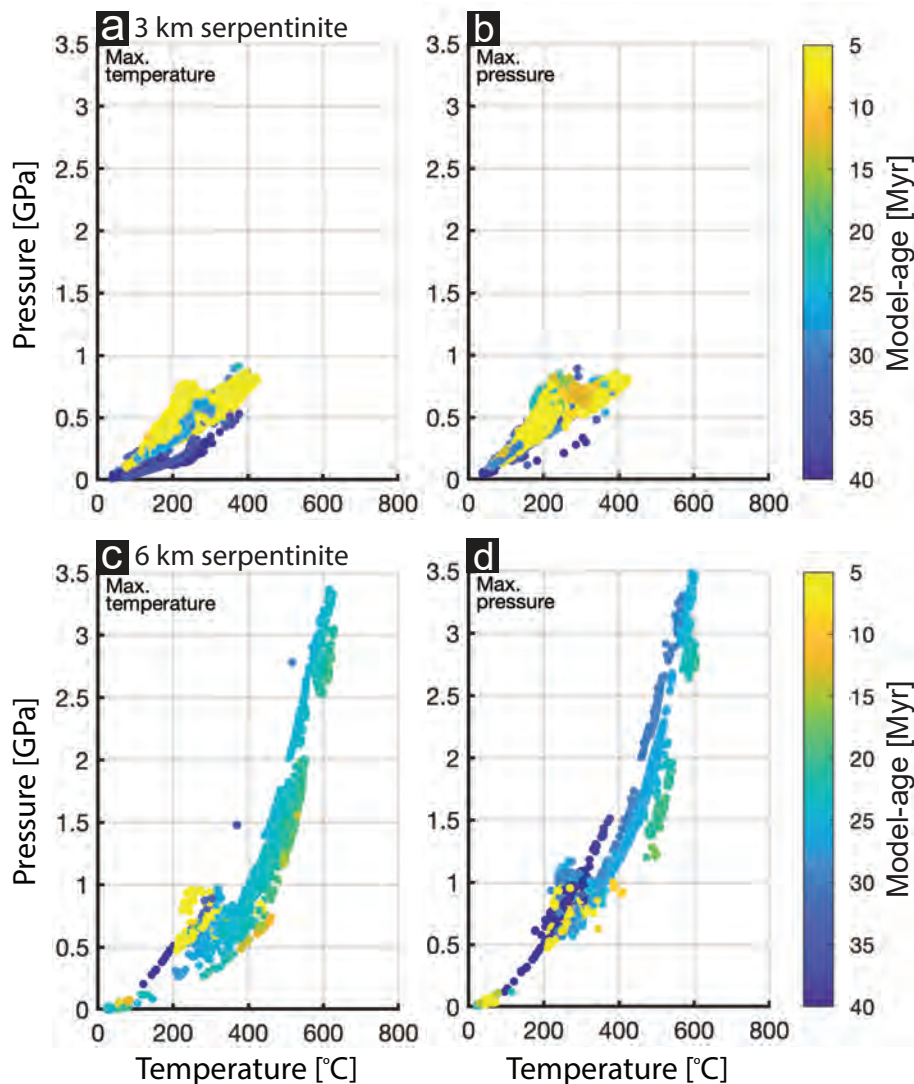
Figure 5.8: Maximum *P-T* conditions attained by particles subducted and exhumed to <20 km depth, coloured as a function of age of peak metamorphic conditions. Max. temperature corresponds to *P-T* conditions taken using the maximum temperature attained during subduction. Max. pressure corresponds to *P-T* conditions taken using the maximum pressure attained during subduction (see methods section 5.3.2).

Figure 5.9e and g shows the metamorphic facies distribution for the 6 km serpentinite model. Overall, metamorphic facies of continental regions exhumed to depths <20 km are distributed laterally across the orogen. The highest grades are observed within the core of the orogen closer to the upper plate and decrease in grade towards the foreland (Figure 5.9e and g). For peak metamorphic values based on max. *T*, metamorphic grades ranging from UHP, eclogite, blueschist, greenschist and zeolite are observed within the uppermost 20 km (Figure 5.9e).

Similar to the 3 km serpentinite model, the 6 km serpentinite model also contains relatively larger volumes of UHP and blueschist facies for peak conditions based on max. P values (Figure 5.9g and d), compared to max. T (Figure 5.9e and f). High temperature amphibolite facies occur in small volumes between 30–40 km depth for max. T based facies models (Figure 5.9e), something that is not observed in max. P based facies models (Figure 5.9g).

5.5 Discussion

5.5.1 Serpentinite thickness and plate interface strength

The variation in thickness of serpentinized exhumed mantle (3 and 6 km), separating the hyper-extended passive margins formed during rifting, has a dramatic effect on the subduction and exhumation style in the modelled orogens. In our models, the weak serpentinite is the main model feature that controls the strength of the emerging subduction interface. Where serpentinite is present and numerically resolvable along the plate interface, there the interface is weak. Where serpentinite is missing, or numerically not resolvable, there the interface is strong (Figure 5.4). In nature, the emerging plate interface strength is likely also controlled by more complex processes such as fluid-induced softening, reaction-induced softening, partial melting, grain size reduction or anisotropy development. These microscale and multi-phase processes are currently not considered in our large-scale lithosphere–upper mantle model. Therefore, the presence and distribution of serpentinite along the emerging plate interface is a proxy for the plate interface strength in our model. In our model, an initial serpentinite thickness of 6 km is required so that a weak plate interface with a layer of sheared serpentinite can develop and be numerically resolved. A 6 km thick serpentinite is larger than typically observed thicknesses of serpentinites above exhumed mantle, such as in the Piemonte-Liguria domain (McCarthy et al., 2020). The main reason for the unrealistic serpentinite thickness in our model is the numerical resolution of 1×1 km. To be able to form a numerically resolvable layer of serpentinite after significant shearing and thinning during subduction, an initial thickness of 6 km is required in our model. Consequently, the applied thickness of serpentinite should not be compared directly with typical natural thicknesses of serpentinite.
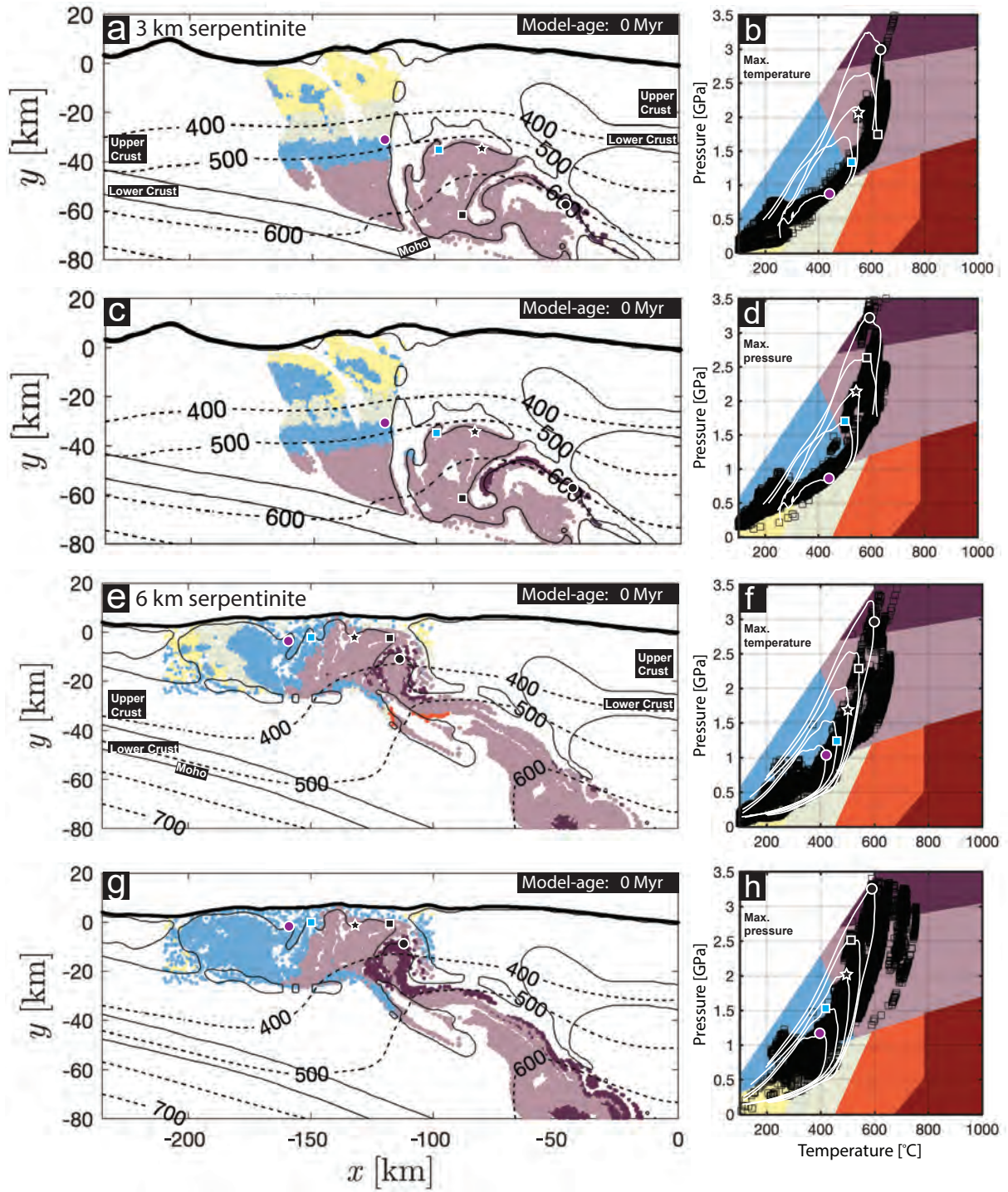
Figure 5.9: Caption on next page.

Figure 5.9: (a) Metamorphic facies distribution of 3 km serpentinite model based on max. temperature. (b) Representative maximum *P-T* conditions over metamorphic facies grid (Philpotts and Ague, 2009, black squares, modified after) and representative *P-T* loops (similar to markers in Figures 5 and 6 where peak conditions are indicated by coloured markers). (c) Metamorphic facies distribution of 3 km serpentinite model based on max. pressure. (d) Representative maximum *P-T* conditions over metamorphic facies grid (black squares) and representative *P-T* loops (similar to markers in Figures 5 and 6 where peak conditions are indicated by coloured markers). (e) Metamorphic facies distribution of 6 km serpentinite model based on max. temperature. (f) Representative maximum *P-T* conditions over metamorphic facies grid (black squares) and representative *P-T* loops (similar to markers in Figures 5 and 6 where peak conditions are indicated by coloured markers). (g) Metamorphic facies distribution of 6 km serpentinite model based on max. pressure. (h) Representative maximum *P-T* conditions over metamorphic facies grid (black squares) and representative *P-T* loops (similar to markers in Figures 5 and 6 where peak conditions are indicated by coloured markers).

5.5.2 Syn-convergent exhumation

Published syn-convergent exhumation models (e.g. Butler et al., 2014) have been criticised because they often require significant erosion which is not observed in several regions exhibiting exhumed (U)HP terranes (e.g. Malusà et al., 2015; Liao et al., 2018). In our syn-convergent exhumation model with a weak plate interface (6 km serpentinite thickness), significant erosion is absent (Figure 5.5 and 5.10). The low viscosity serpentinites form a weak interface in the uppermost 25 km of the emerging orogen (Figure 5.4 and 5.5e). The upper crust of the upper plate can, therefore, easily thrust above the lower plate towards the foreland. The subducted buoyant crust of the lower plate pushes upward and causes the upper plate to neck, or to boudinage, and to ultimately separate (Figure 5.10). This necking and lateral separation indicates local upper plate extension. During this extension, the separated upper plate rocks move towards the foreland, which is possible due to the weak interface below the separated unit. This separation enables the subducted rocks from the lower plate to exhume to the surface (Figure 5.4, 5.5f, 5.10a to c). The separation and local extension is also the reason why erosion is not required in our syn-convergent exhumation model.

Another feature of our syn-convergent exhumation model is a prominent shear zone with a normal shear sense (Figure 5.10). To visualize the shear sense, an initially rectangular box, who's long axis is parallel with the subduction interface, is plotted using four numerical markers that define the corners of the rectangle (Figure 5.10a). During subduction, the box

is progressively sheared with a normal sense of shear as the material below the subduction interface is being exhumed (Figure 5.10b-d). The sides of the initial rectangle parallel to the subduction interface remain at fixed distances during progressive exhumation, attesting to the coherency of the exhuming material (Figure 5.10c and d). The sides of the initial rectangle perpendicular to and across the subduction interface are significantly extended (Figure 5.10d). Using the deformed box as a shear sense indicator, we observe local normal sense (extensional) shear between the overriding plate and the exhuming continental units, during overall convergence.

The model with strong plate interface (3 km serpentinite thickness) does not show significant exhumation. The absence of exhumation is largely due to the behaviour of the overriding plate (Figures 5.4b, c, 5.8a and c). The overriding plate acts like a strong lid and prevents HP units from exhuming to the surface. Local extension of the upper plate is inhibited, due to the lack of a weak plate interface in the uppermost 25 km and the collision of the upper crusts of the two passive margins (Figure 5.4a)

5.5.3   Predictive modelling of metamorphic facies

Our results indicate that using the peak P and T, incurred by markers during their clockwise P-T path, is a good approximation for the distribution of subduction-related metamorphic facies (Figure 5.9). The assumptions made here with regards to "freezing" in time the peak metamorphic grades, expressed in petrology as assemblages (section 5.3.3), do not differ considerably from the assumptions made when applying geo-thermobarometers to natural samples. These assumptions are mainly, 1) equilibrium conditions in pseudo-section calculations, 2) equilibrium due to water presence or water saturated conditions, 3) peak metamorphic conditions can be identified with textural observations, and 4) kinetics can be neglected. Questions arising from the assumption that the relative phases in a peak assemblage equilibrated at a single P-T condition are not evaluated in this study (e.g. Spear, 1989; Spear et al., 2017). Such factors as the kinetics of metamorphic reactions during prograde pathways focus on the scale of the mineral, whereas peak metamorphic conditions applied to the

entire orogeny focus on regional-scale trends (Figure 5.2). Considerable effort has been made to map out such large-scale subduction related metamorphic trends throughout the Western Alps (e.g. Agard et al., 2002; Babist et al., 2006; Beltrando et al., 2010a; Oberhänsli et al., 2004; Bousquet et al., 2008), and these trends primarily focus on peak P and T conditions. Therefore, we find the application of our simplified metamorphic facies model to regional metamorphic facies distributions observed in natural orogens justified.

Differences in the metamorphic architecture of the modelled orogeny arise when using max. P or max. T values for defining the metamorphic facies in P-T space (Figure 5.9 and S4). Although the larger-scale metamorphic structure is consistent, occurrences of blueschist facies and UHP facies P-T conditions are more widespread in both 3 km and 6 km serpentinite models when using max. P (Figure 5.9c and g). This is primarily due to peak P and T values not being consistent (Figure S4), e.g. where a decrease in P occurs during continued heating. Peak T can be between 50–100 hotter than the corresponding T at peak P (e.g. red circle marker, Figure 5.5e, f and Figure 5.6b). The observed increase in blueschist and UHP facies occurrences for max. P values likely reflects the pressure dependent slope of the lower boundaries of metamorphic facies in P-T space (Figure 5.2a). This P dependency is exemplified if we consider what facies are being replaced by blueschist and UHP facies when considering max. P. Typically, blueschist facies replaces greenschist facies, and UHP facies replaces HP facies (Figure 5.9e and g). Therefore, the use of metamorphic facies in our models indicates relative P-T conditions (Ghent, 2020).

5.5.4 Application to the Western Alps

For the model with a strong plate interface (3 km serpentinite thickness; Figure 5.9a and c), the magnitudes of peak metamorphic grades are in agreement with exhumed (U)HP units observed in the Western Alps (Figure 5.9b and d). However, for this model the rocks with (U)HP facies remain at depths of >40 km and do not exhume close to the surface. The absence of significant exhumation is evident in the horizontally-layered metamorphic architecture (Figure 5.9a and c) as well as the absence of closed clockwise P-T loops (Figure 5.9b
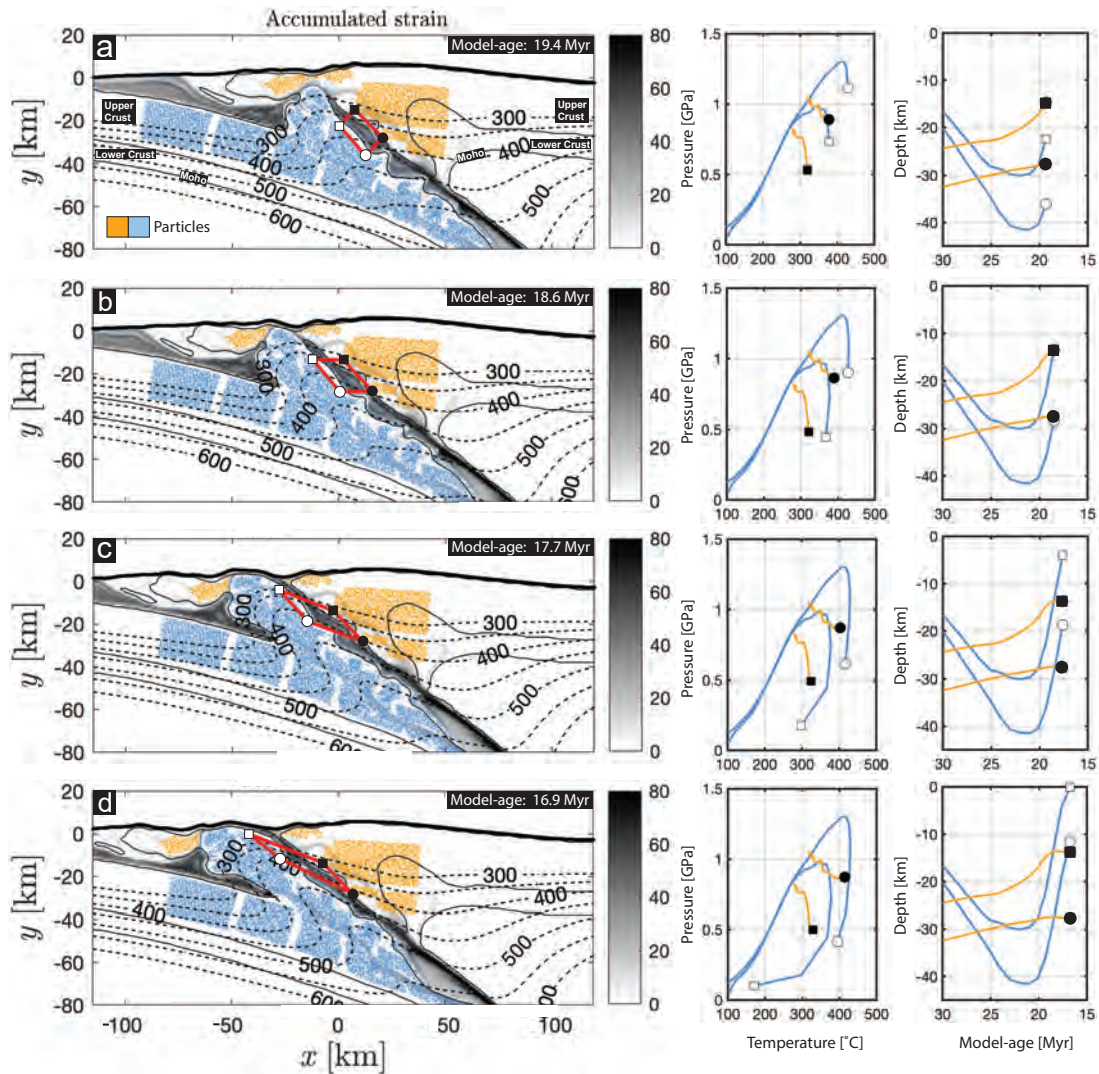
Figure 5.10: 6 km serpentinite model accumulated strain evolution. Particles indicated from overriding plate (yellow) and subducting plate (blue). Red box whose longest sides correspond to the upper plate and exhuming lower plate, indicating syn-convergent extensional shear during exhumation of subducted continental material across the major subduction zone interface. Corresponding *P-T* and Depth-time evolution plots for particles at the corners of the initial red box.

and d). Therefore, the model a with strong plate interface is not applicable to the Western Alps, mainly due to the lack of exhumation of (U)HP units. The resulting metamorphic architecture for the model with weak plate interface and syn-convergent exhumation agrees to first order with the metamorphic facies distribution in the Western Alps (Figure 5.2 and 5.11). In the Western Alps, high-grade internal metamorphic zoning exists showing a decrease in grade

towards the foreland (e.g. Ernst, 1972). The same trend exists in the modelled metamorphic facies distribution (Figure 5.11). However, more external (also lower grade) domains in the Alps (e.g. Aar massif) are observed to have horizontal (or doming) peak metamorphic zoning patterns (e.g. Nibourel et al., 2021). The metamorphic facies gradient from high to low grade also predicts the subduction polarity (Ernst, 1971, 1972), whereby the direction of increasing grade is the direction of lower-plate subduction (Figure 5.11). The metamorphic facies distribution, hence, preserves, or "fossilizes", the subduction related metamorphic architecture. Serpentinites control to some extent this "fossilization" process by aiding exhumation of HP units to the surface via buoyancy and lubrication of a low-viscosity subduction interface. The widespread occurrences of serpentinites associated with HP domains within the Western Alps, e.g. the Zermatt-Saas ophiolite (e.g. Forster et al., 2004), indicate their involvement in exhumation processes (Schwartz et al., 2001; Yang et al., 2020; Agard et al., 2018; Ruh et al., 2015; Guillot et al., 2015; Chang et al., 2009).

The differences between the two models (strong and weak interface) in the modelled metamorphic architecture arise due to two contrasting styles of orogeny: 1) pure wedge-like thrusting associated with horizontally layered metamorphic zoning for a strong interface (Figure 5.9a), and 2) wedge formation involving syn-convergent exhumation associated with vertically layered metamorphic zoning for a weak interface (Figure 5.9e). The two numerical models presented here are endmember representations of metamorphic facies development, whereas in nature, and specifically the Alps, a combination of these endmembers likely generated observed orogens.

Inherited structural complexity deriving from extensional tectonics within the former passive margin (Figure 5.1a) may also contribute to the structurally complex and minor volumes of exhumed coherent UHP units observed throughout the Western Alps, e.g. Brossasco-Isasca unit (BIU) within the Dora Maira massif (Figure 5.2) (e.g. Rubatto and Hermann, 2001; Groppo et al., 2019). In our models with a weak interface there are subducted and exhumed units which have peak P-T values similar to the ones of most units of the Dora Maira massif (2–2.4 GPa and 500–540 : Groppo et al., 2019). However, the UHP and high-T markers similar to values for the BIU are not exhumed (Figure 5.11d). The BIU is a very small

tectonic slice (*c.* 1 km thickness) and our model cannot resolve such small units and shear zones around such small units due to the numerical resolution of 1×1 km. In nature, the BIU unit might have been exhumed as a small individual slice, but the exhumation mechanism remains disputed. Simple numerical models have shown that significant strain localization around the BIU might have enabled diapiric exhumation of the BIU as an individual slice along the subduction interface after its detachment from the subducting European plate (Schmalholz and Schenker, 2016).

Progressive exhumation of HP footwall material along a major normal sense shear zone has been suggested for several regions throughout the Alps (Beltrando et al., 2010b; Bucher et al., 2003; Campani et al., 2010a,b; Cawood and Platt, 2020; Reddy et al., 1999, 2003; Wheeler et al., 2001; Ring and Merle, 1992; Mancktelow, 1985; Manzotti et al., 2014b). Although shear sense indicators are documented, the actual mechanism for generating such normal sense structural features is still unclear (e.g. Bucher et al., 2003). Two scenarios are possible: 1) periods of intermittent far-field plate divergence between periods of convergence (e.g. Beltrando et al., 2010b; Reddy et al., 1999), or 2) extrusion of subducted material during continuous plate convergence (e.g. Chemenda et al., 1995; Duretz et al., 2012; Froitzheim et al., 2003, 2006; Keller et al., 2005; Butler et al., 2014). Our model results for syn-convergent exhumation agree with shear sense indicators resulting from extrusion of subducted material (e.g. Chemenda et al., 1995; Duretz et al., 2012; Froitzheim et al., 2003, 2006; Keller et al., 2005) (Figure 5.10). This model also shows the separation of the upper plate crust during exhumation (Figure 5.10c and d, yellow particles). Such separation of the Adriatic upper plate could explain the far-travelled Adria-derived units within the external domains of the Western Alps, such as the Gets and Simme nappes, which have been correlated to the Adriatic passive margin (Figure 5.10) (Escher et al., 1997; Gasinski et al., 1997; Ferrando et al., 2004).

Estimated exhumation velocities for some exhumed (U)HP units in the Western Alps indicate that exhumation velocities are approximately equal to or larger than the burial velocities due to subduction (e.g. Rubatto and Hermann, 2001; Manzotti et al., 2018). In our syn-convergent exhumation model, the fastest burial velocities are *c.* 4.5 mm/yr and average

exhumation velocities are 6.5 mm/yr (Figure 5.6d). The fastest exhumation velocities even exceed 10 mm/yr (Figure 5.6d). Our syn-convergent exhumation model, hence, exhibits representative exhumation velocities which are approximately equal to or larger than the associated burial velocities, which agrees with estimated exhumation velocities for the Western Alps (e.g. Rubatto and Hermann, 2001; Manzotti et al., 2018).

In summary, our model of syn-convergent exhumation agrees with the following observations and data for the Western Alps: 1) regional-scale structurally coherent units with the same metamorphic facies (Figures 5.2 and 5.11), 2) a continuous metamorphic facies gradient with highest grade in the internal domain and lowest grade in the external domain (Figures 5.2 and 5.11), 3) modelled P-T-t paths agree with estimated P-T-t paths for representative volumes of major tectonic units, such as the Dora Maira massif (Figure 5.11), 4) exhumation without significant erosion, visible by the essentially constant area of model units (Figure 5.5 and 5.10), 5) normal shear sense observed in the upper regions of some exhumed units (Figure 5.10), 6) remnants of tectonic units originating from the Adriatic margin which are found in the external domain of the Western Alps (e.g. Simme and Gets nappes; Figures 5.1, 5.5 and 5.10), and 5.7) exhumation velocities that are equal to or larger than the subduction velocities (Figure 5.6).

5.5.5 Deviations from lithostatic pressure

The rock pressure cannot be lithostatic, or hydrostatic, everywhere within the crust during orogeny, because plate driving forces, rock deformation and lateral topography variations are caused by differential stresses (e.g. Turcotte and Schubert, 2002; Schmalholz et al., 2019). The magnitude of the deviation of rock pressure from lithostatic pressure during orogeny is disputed. Several studies propose that some observed metamorphic rocks indicate pressures that are significantly larger than the lithostatic pressure, say >0.2 GPa (e.g. Jamtveit et al., 2018; Luisier et al., 2019; Putnis et al., 2021; Vaughan-Hammon et al., 2021). These potential deviations from lithostatic pressure, so-called tectonic pressure (e.g. Petrini and Podladchikov, 2000; Mancktelow, 2008; Moulas et al., 2013; Schmalholz and Podladchikov, 2013; Gerya,

2015), are commonly proposed for smaller units, such as lenses or shear zones, typically having a size of less than 100 m. Our model cannot resolve such smaller scale units, which usually are interpreted to have significantly different strength than the surrounding rocks. However, one numerical marker of the syn-convergent exhumation model (red circle in Figure 5.6) shows a deviation from lithostatic pressure of *c.* 0.4 GPa. Furthermore, some studies propose that deviations from lithostatic pressure can be caused by differential volumetric deformation, e.g. during dehydration reactions (Luisier et al., 2019). Such volumetric changes are not considered in our model assuming incompressible deformation. Therefore, due to the applied numerical resolution of $1{\times}1$ km and the assumption of incompressible deformation, our model results are not suitable to study potential deviations from lithostatic pressure occurring on spatial scales of less than 1 km.
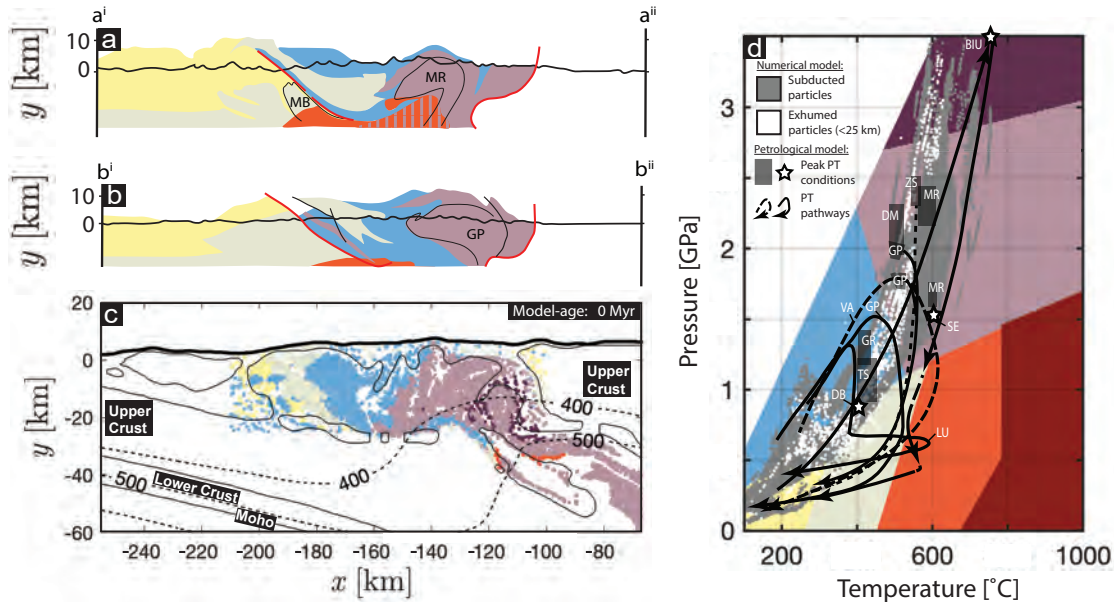
Figure 5.11: Comparison of petrological metamorphic facies section with numerical results. (a) and (b) petrologically-inspired metamorphic facies cross-section of the Western Alps (modified after Oberhänsli et al. (2004) and Bousquet et al. (2008)). (c) numerical results of metamorphic facies distribution for 6 km serpentinite based on maximum temperature. (d) *P-T* metamorphic facies grid (modified after Philpotts and Ague, 2009) comparing peak numerical *P-T* values (for all particles and exhumed particles) with representative *P-T* estimates for Western Alpine units (references within Figure 5.2). The vertical and horizontal scales for the cross sections in panel a) to c) are identical.

5.6   Conclusions

The applied petrological–thermomechanical numerical model calculates the metamorphic facies evolution and distribution during orogenesis with approximately 10'000 markers recording peak temperature and pressure. In our models, the location and orientation of subduction is not prescribed and subduction initiates self-consistently during convergence. A subduction plate interface develops which is either weak or strong depending on the initial serpentinite thickness. For initially thinner serpentinite, here 3 km, the serpentinite is strongly sheared and thinned during subduction so that it does not form a continuous weak layer along the plate interface and, hence, the plate interface is strong. In contrast, for initially thicker serpentinite, here 6 km, enough serpentinite is available, and numerically resolvable, to form a continuous layer along the plate interface and, hence, to form a weak interface. For the weak interface, syn-convergent exhumation occurs. The resulting metamorphic facies distribution shows two main characteristics: (i) exhumed, structurally coherent regions with the same metamorphic facies, which indicate the absence of significant mechanical mixing, or tectonic mélange, and (ii) a facies distribution showing a transition from eclogite to blueschist to greenschist facies when going from the internal to external (towards foreland) domains. Both the modelled structural coherency of major metamorphic units and the facies variation from high- to low-grade when going from internal to external domains agree, to first order, with observations in the Western Alps. In models with a stronger plate interface, the metamorphic facies distribution is different, showing a horizontally layered distribution with higher grade rocks at larger depths. This model also shows only minor exhumation and does not reproduce the main characteristics of the Western Alps.

Tracing 10'000 numerical markers allows for the analysis of the paleogeography and age of peak metamorphism of subducted and exhumed units. The paleogeographic position of subducted and exhumed portions for the model with a weak interface typically derive from the more distal portions of the subducted continental margin. This agrees with paleogeographic reconstructions for the Western Alps where high-grade units such as the middle-Penninic Monte Rosa, Gran Paradiso and Dora Maira massifs derive from distal regions of the European

margin. The age distribution of peak metamorphism for the model with weak interface shows a weak overall trend whereby higher grades of peak metamorphism occur during earlier periods of the model history.

The modelled metamorphic architecture is based on the simple assumption that peak values of pressure and temperature reflect subduction related metamorphism during burial and exhumation of continental rocks. This assumption predicts well the large-scale subduction-related metamorphic structure in the Western Alps. However, differences arise when using peak pressure (*c.* 0.4 GPa tectonic pressure) or temperature (*c.* 50 continued heating during decompression) when defining a metamorphic facies in *P-T* space. Metamorphic facies defined by peak temperature values closely resemble the first-order metamorphic architecture in the Western Alps, whereas peak pressure values over-estimate blueschist volumes. In nature, peak metamorphism may be defined in some areas by a mixture of both peak temperature and peak pressure values.

The presented numerical model predicts syn-convergent exhumation by extrusion. Exhumation is enabled by local upper-plate extension and the formation of a large-scale normal-sense shear zone at the subduction plate interface. Therefore, the exhumation of (U)HP rocks can be supported by local extensional kinematics during continuous plate convergence. However, such exhumation does not require regional-scale plate divergence. The local extension also enables syn-convergent exhumation without significant erosion. Therefore, our model and the newly calculated metamorphic facies distribution show that syn-convergent exhumation could have been the controlling exhumation mechanism during the Western Alpine orogeny.

We propose that future numerical modelling studies of orogeny should also generate metamorphic facies distributions, as we did here, as an additional test for the applicability of the employed model to specific natural orogens, such as the Western Alps.

5.7   Appendix

The supporting information here contains a detailed description of the numerical algorithm used, the modelling approach and the initial model configuration. We present a systematic analysis of numerical parameters. For this, we tested the impact of (i) the continental crustal strength by employing experimentally derived flow law parameters for either a wet anorthite (strong) or a Westerly granite (weak) rheology. Further, we (ii) tested various magnitudes of the serpentinite layer thickness which is used as a proxy for the degree of serpentinisation. Finally, we (iii) tested the importance of the various applied convergence velocity magnitudes on the subduction and exhumation dynamics. A brief justification for the configuration used to numerically map metamorphic facies is also presented here.

A repository of data, post-processing scripts, and visualisation scripts is available on Zenodo via https://zenodo.org/record/5521214#.YUsjJ9MzaLU.

Algorithm description

As common in continuum mechanics, we solve the thermomechanically coupled equations for continuity of material, conservation of momentum and energy expressed w.r.t temperature, T, as

$$\frac{\partial v_i}{\partial x_i} = 0 \tag{5.1}$$

$$\frac{\partial \sigma_{ij}}{\partial x_j} = -\rho \, g_i \tag{5.2}$$

$$\rho \, c_{\mathrm{P}} \frac{\mathrm{D}T}{\mathrm{D}t} = \frac{\partial}{\partial x_i}\left(k \, \frac{\partial T}{\partial x_i} \right) + H_{\mathrm{A}} + H_{\mathrm{D}} + H_{\mathrm{R}} \; , \tag{5.3}$$

where v is velocity, x is the coordinate, i and j indicate the horizontal ($j,j{=}1$) or vertical ($i,j{=}2$) direction, ρ denotes density, $g_i = \left[0; -9.81\right]$ are the components of the gravitational acceleration vector, c_{P} is heat capacity, k is thermal conductivity, $\frac{\mathrm{D}}{\mathrm{D}t}$ is the material time derivative, H_{A}, H_{D} and H_{R} are contributions resulting from adiabatic processes, viscoplastic dissipation and radiogenic heat production, respectively. We here employ the extended Boussinesq approximation, i.e. the slowly flowing fluid is considered to be incompressible, density changes are only taken into account when multiplied with gravitational acceleration and adiabatic processes only impact on temperature (Candioti et al., 2020). The total stress tensor components are defined as

$$\sigma_{ij} = -P\delta_{ij} + 2 \, \eta^{\mathrm{eff}} \, \dot{\varepsilon}_{ij}^{\mathrm{eff}} \; , \tag{5.4}$$

where $\delta_{ij} = 0$ if $i \neq j$, or $\delta_{ij} = 1$ if $i = j$, η^{eff} is the effective viscosity, $\dot{\varepsilon}_{ij}^{\mathrm{eff}}$ are the components of the effective deviatoric strain rate tensor,

$$\dot{\varepsilon}_{ij}^{\mathrm{eff}} = \left(\dot{\varepsilon}_{ij} + \frac{\tau_{ij}^{o}}{2 \, G \Delta t} \right) \; , \tag{5.5}$$

where G is the shear modulus, Δt is the time step and τ_{ij}^{o} are the deviatoric stress tensor components of the preceding time step. We consider visco–elasto–plastic rheologies by additive decomposition (Maxwell model) of the total deviatoric strain rate tensor components

$\dot{\varepsilon}_{ij}$ into contributions from the viscous (dislocation, diffusion and Peierls creep), plastic and elastic deformation as

$$\dot{\varepsilon}_{ij} = \dot{\varepsilon}_{ij}^{\text{ela}} + \dot{\varepsilon}_{ij}^{\text{pla}} + \dot{\varepsilon}_{ij}^{\text{dis}} + \dot{\varepsilon}_{ij}^{\text{dif}} + \dot{\varepsilon}_{ij}^{\text{pei}} \ . \tag{5.6}$$

Furthermore, we perform an iteration cycle locally on each grid cell until Eq. 5.6 is satisfied (e.g. Popov and Sobolev, 2008). The effective viscosity for the dislocation and Peierls creep flow law is a function of the second invariant of the respective strain rate components $\dot{\varepsilon}_{\text{II}}^{\text{dis,pei}} = \tau_{\text{II}}/(2\eta^{\text{dis,pei}})$

$$\eta^{\text{dis}} = \frac{2^{\frac{1-n}{n}}}{3^{\frac{1+n}{2n}}} \ \zeta \ A^{-\frac{1}{n}} \ \left(\dot{\varepsilon}_{\text{II}}^{\text{dis}}\right)^{\frac{1}{n}-1} \ \exp\left(\frac{Q+PV}{nRT}\right) \ \left(f_{\text{H}_2\text{O}}\right)^{-\frac{r}{n}} \ , \tag{5.7}$$

where the ratio in front of the pre-factor ζ is a correction factor (e.g. Schmalholz and Fletcher, 2011). A, n, Q, V, $f_{\text{H}_2\text{O}}$ and r are material parameters determined in laboratory experiments. Diffusion creep is taken into account for the mantle material and its viscosity is defined as

$$\eta^{\text{dif}} = \frac{1}{3} \ A^{-1} \ d^m \ \exp\left(\frac{Q+PV}{RT}\right) \ \left(f_{\text{H}_2\text{O}}\right)^{-r}, \tag{5.8}$$

where d is grain size and m is a grain size exponent. Effective Peierls viscosity is calculated using the experimentally derived flow law by (Goetze and Evans, 1979) in the regularised form (Kameyama et al., 1999) as

$$\eta^{\text{pei}} = \frac{2^{\frac{1-s}{s}}}{3^{\frac{1+s}{2s}}} \ \hat{A} \ \left(\dot{\varepsilon}_{\text{II}}^{\text{pei}}\right)^{\frac{1}{s}-1} \ , \tag{5.9}$$

where s is a stress exponent:

$$s = 2 \ \gamma \ \frac{Q}{RT}(1-\gamma) \ . \tag{5.10}$$

$\hat{A}$ in Eq. (5.9) is

$$\hat{A} = \left[A_{\mathrm{P}} \ \exp \left(- \frac{Q(1-\gamma)^2}{RT} \right) \right]^{-\frac{1}{s}} \gamma \sigma_{\mathrm{P}} \ , \tag{5.11}$$

where A_{P} is a pre-factor, γ is a fitting parameter and σ_{P} is a characteristic stress value. Brittle-plastic failure is included by limiting the stresses by a Drucker-Prager yield function

$$F = \tau_{\mathrm{II}} - P \ \sin \phi - C \ \cos \phi \ , \tag{5.12}$$

where ϕ is the internal angle of friction and C is the cohesion. In case the yield condition is met ($F \geq 0$), the equivalent plastic viscosity is computed as

$$\eta^{\mathrm{pla}} = \frac{P \ \sin \phi + C \ \cos \phi}{2 \dot{\varepsilon}_{\mathrm{II}}^{\mathrm{eff}}} \tag{5.13}$$

and the effective deviatoric strain rate is equal to the plastic contribution of the deviatoric strain rate (Eq. 5.5). At the end of the iteration cycle, the effective viscosity in Eq. 5.4 is either computed as the quasi-harmonic average of the viscoelastic contributions

$$\eta^{\mathrm{eff}} = \begin{cases} \left(\frac{1}{G \Delta t} + \frac{1}{\eta^{\mathrm{dis}}} + \frac{1}{\eta^{\mathrm{dif}}} + \frac{1}{\eta^{\mathrm{pei}}} \right)^{-1} & , \ F < 0 \\ \eta^{\mathrm{pla}} & , \ F \geq 0 \end{cases} \tag{5.14}$$

or is equal to the viscosity η^{pla} calculated at the equivalent plastic stress according to Eq. 5.13. Rigid body rotation is computed analytically at the end of each time step as

$$\tau_{ij} \ = \ \mathbf{R^T} \ \tau_{ij} \ \mathbf{R} \ , \tag{5.15}$$

$$\mathbf{R} \ = \ \begin{bmatrix} \cos \theta & -\sin \theta \\ \sin \theta & \cos \theta \end{bmatrix} \ , \tag{5.16}$$

$$\theta \ = \ \Delta t \ \omega_{ij} \ , \tag{5.17}$$

$$\omega_{ij} \ = \ \frac{1}{2} \left(\frac{\partial v_j}{\partial x_i} - \frac{\partial v_i}{\partial x_j} \right) \ , \tag{5.18}$$

$$\tag{5.19}$$

where $\mathbf{R}$ is the rotation matrix, $^{\mathbf{T}}$ is the transpose operator, θ is the rotation angle and ω_{ij} are components of the vorticity tensor.

Systematic parameter analysis

To identify end-member models for exhumation dynamics, we tested different values for the initial thickness of the serpentinite layer (3, 5 and 6 km) as a proxy for the degree of serpentinisation as well as different experimentally derived flow law parameters for the continental crustal matrix (wet anorthite and Westerly granite, see Table S1). Candioti et al. (2021) showed that the strength of serpentinites lubricating the subduction interface and the strength of the continental crust significantly alters the subduction and exhumation dynamics within growing collision orogens. In addition to those parameters, we test the impact of various applied convergence velocity magnitudes (0.5, 1.0 and 1.5 cm/yr) after basin closure (140 Myr) on the subduction and exhumation dynamics. During the Alpine orogeny, the collision of Europe and Adria at ca. 35-30 Ma lead to a reduction of the far-field convergence velocity (e.g. Handy et al., 2015) and, therefore, likely changed the dynamics within the collisional stage of the orogeny. The models presented in the main article are shown in Figure S2d (6 km serpentinite thickness) and Figure S2f (3 km serpentinite thickness). We chose these two models because they predict end-member type dynamics that are often used to explain the exhumation of (ultra)high-pressure rocks during the formation of the European Western Alps (e.g. Platt, 1986; Butler et al., 2014; Dal Zilio et al., 2020).

Figure S2 shows end-member models of varied convergence velocities and varied serpentinite layer thickness. These models employ a Westerly granite (weak) rheology for the continental crustal matrix. For low serpentinite layer thickness (3 km, Figure S2c,f,i) imbricated thrusting occurs during the growth of the orogenic wedge for all tested convergence velocities (see also Candioti et al., 2021). Deep subduction and subsequent exhumation of continental crustal units close to the surface is not observed in this kind of models. For a serpentinite layer thickness ≥ 5 km and all convergence velocity magnitudes tested, the continental crustal material is exhumed close to the surface along the serpentinized subduction interface (Figure S2a,b,d,e,g,h).

Figure S3 shows end-member models of varied convergence velocity and serpentinite layer thickness that employ a wet anorthite (strong) rheology for the continental crustal matrix.

A combination of a thin serpentinite layer (3 km) and an intermediate convergence velocity (1.0 cm/yr, Figure S3f) as well as any combinations of serpentinite layer thickness and a fast convergence velocity (1.5 cm/yr, Figure S3g-i) yields to deep subduction of continental crustal units. However, these units are not exhumed along the subduction interface, but relaminate below the overriding plate. Only for a slow convergence velocity (0.5 cm/yr, Figure S3a-c), or an intermediate convergence velocity in combination with a serpentinite layer thickness ≥ 5 km (Figure S3d,e) the subducted continental crustal units are exhumed close to the surface.

Defining numerical metamorphic facies

Figure S4 highlights the differences in metamorphic facies resulting from the numerical approach. Defining a facies in P-T space in this study involves using max. P or max. T values (Figure S4c). Areas within the model with significantly higher mean stress values (P) compared to the corresponding hydrostatic P (or low stressed neighbouring markers), can exhibit different metamorphic facies, e.g. blueschist instead of greenschist for max. T (Figure S4c).
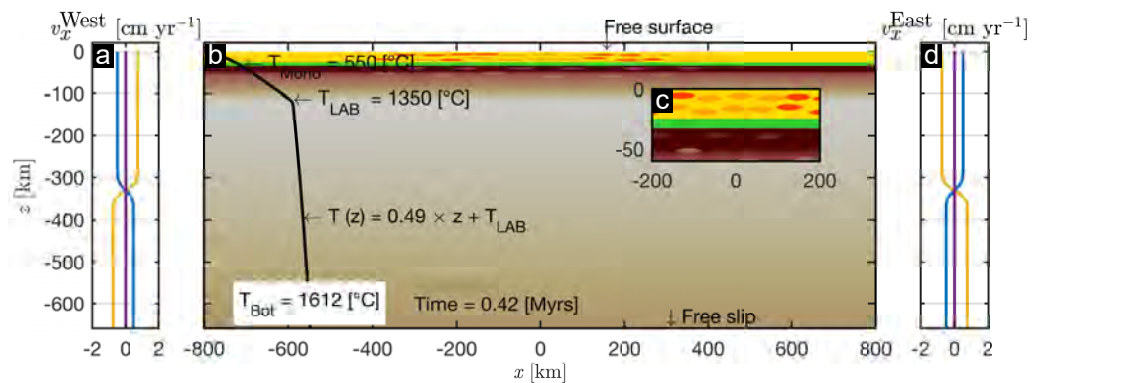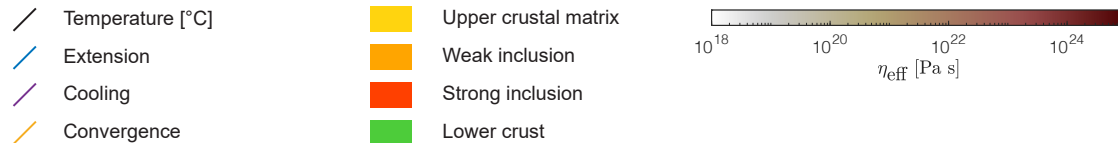
Figure S1: a & **d** Velocity boundary condition values defined at the western and eastern boundary. Duration of deformation periods as follows: extension = 50 Myr, no deformation = 60 Myr, convergence = 30 Myr with 1.5 cm yr^{-1} and 1.0 cm yr^{-1} until the end of the simulation. **b** Entire model domain, initial thermal profile and mechanical boundary conditions at the top and bottom boundary. White to red colour is the viscosity field in the mantle calculated by the numerical algorithm and yellow to orange and green colours are the upper and lower crust, respectively. Rheological parameters used for crustal matrix = Wet Anorthite with weakening prefactor 0.3 during extension and cooling, Westerly Granite during convergence; lithosphere and upper mantle = Strong mantle, elliptical inclusions in the lithosphere = Weak mantle. Material parameters for all phases as indicated in Table S1. **c** Enlargement of the domain centre. Colouring in all subplots as indicated in the figure legend.
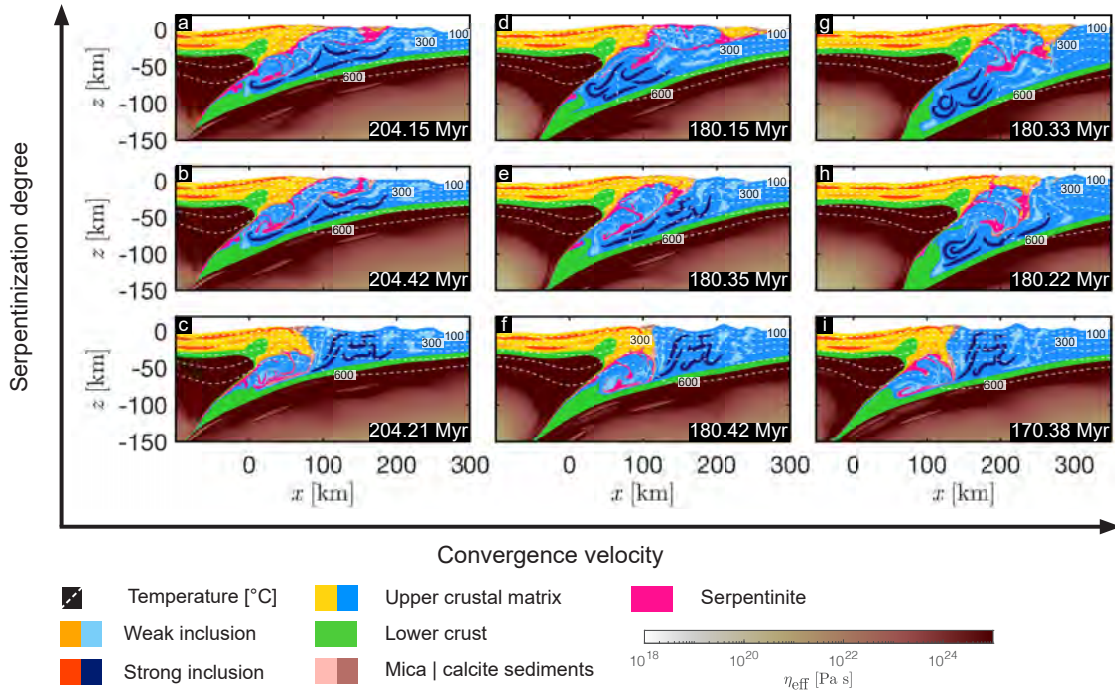
Figure S2: For all panels: yellow to orange and light to dark blue indicate the upper crust, green is the lower crust, magenta is the serpentinite and white to red is the viscosity field in the mantle calculated by the numerical algorithm. Columns show models with increasing convergence velocity after basin closure (140 Myr): left column = 0.5 cm/yr, middle column = 1.0 cm/yr and right column = 1.5 cm/yr. Rows show models with increasing serpentinite layer thickness: bottom row = 3 km, middle row = 5 km and top row = 6 km. With increasing convergence velocity advection dominates the dynamics. Although the general deformation style is very similar, magnitudes of temperature are slightly lower at faster convergence rates (compare depth of 600 °C isotherm in **c**,**f** & **i**). With increasing serpentinite layer thickness the deformation style changes significantly. **d-f** Upper crustal imbricated thrusting inhibits deep subduction of continental crust when the serpentinite layer is relatively thin. For serpentinite layer thicknesses ≥5 km, continental crust is subducted deep into the mantle and exhumed back to the surface as shown in the reference model (panel **d**, described in main section).
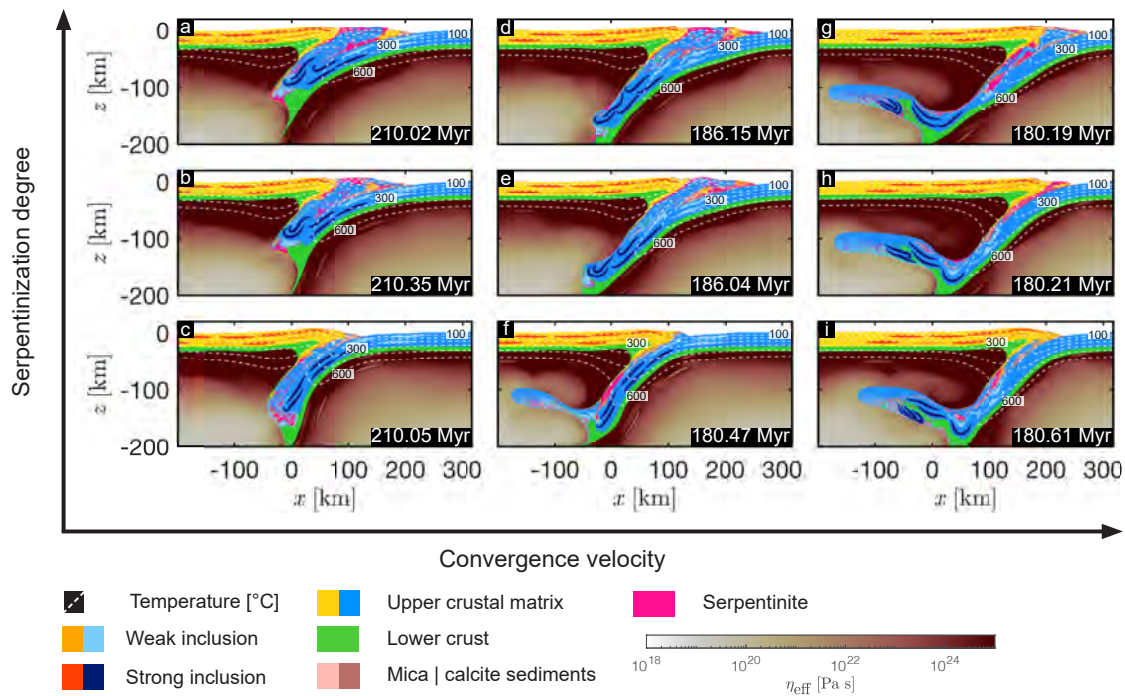
Figure S3: For all panels: yellow to orange and light to dark blue indicate the upper crust, green is the lower crust, magenta is the serpentinite and white to red is the viscosity field in the mantle calculated by the numerical algorithm. Columns show models with increasing convergence velocity after basin closure (140 Myr): left column = 0.5 cm/yr, middle column = 1.0 cm/yr and right column = 1.5 cm/yr. Rows show models with increasing serpentinite layer thickness: bottom row = 3 km, middle row = 5 km and top row = 6 km. With increasing convergence velocity, the deeply subducted crustal units cannot be exhumed back to the surface (**g-i**). For reduced convergence rates and increased serpentinite layer thickness (**d** & **e**) exhumation of deeply subducted crustal units along the subduction interface is still feasible.
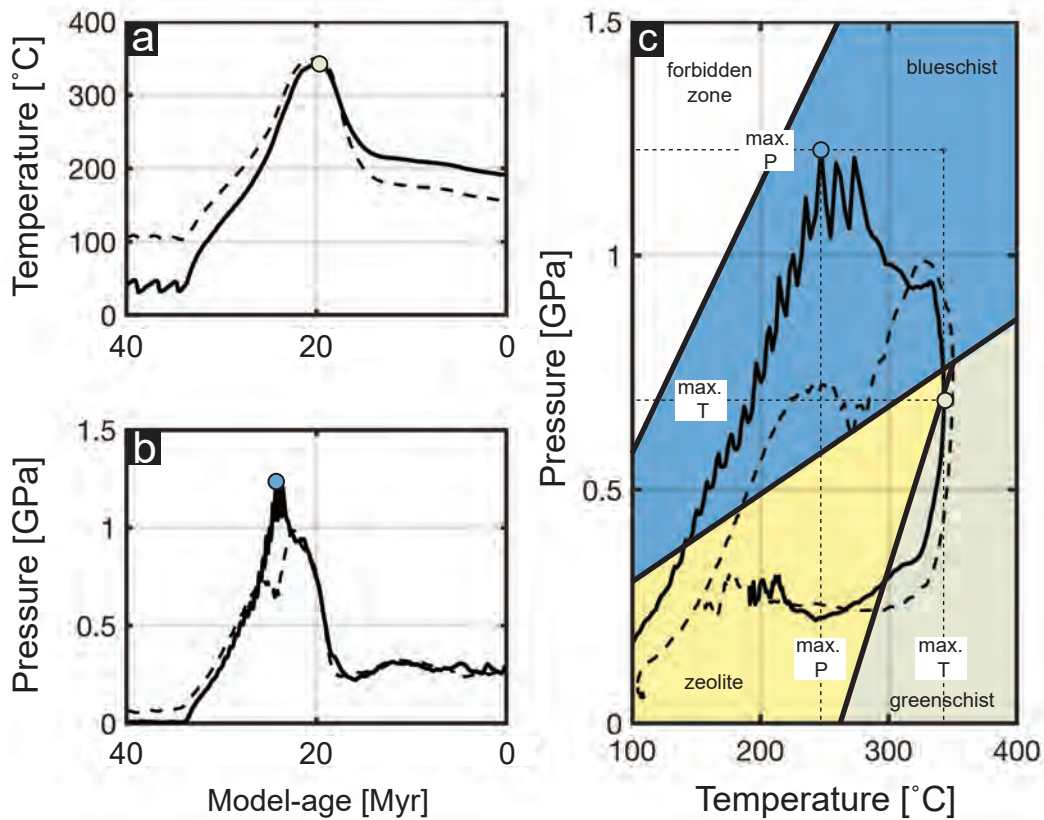
Figure S4: Numerical metamorphic facies variability using maximum pressure or maximum temperature. Pressure-temperature evolution of numerical marker with tectonic pressure (solid black line) compared to a marker in close proximity (≤ 2 km), without significant tectonic pressure (dashed black line). **a** Temperature evolution through time. **b** Pressure evolution through time. **c** Pressure-temperature evolution overlaying metamorphic facies grid (adapted from Philpotts and Ague, 2009) indicating disparity of predicted metamorphic facies for solid black line marker, using maximum pressure (blueschist) or maximum temperature (greenschist).

Table S1: Physical parameters used in the numerical simulations.

Model unit	Rheology (Reference)	k [W m^{-1} K^{-1}]	H_R [W m^{-3}]	C [Pa]	ϕ [°]
Crustal matrix 1[*,a]	Wet Anorthite (Rybacki and Dresen, 2004)	2.25	1.0200×10^{-6}	1×10^7	30
Crustal matrix 2[*,a]	Westerly Granite (Hansen and Carter, 1983)	2.25	1.0200×10^{-6}	1×10^7	30
Weak inclusion[*,a]	Wet Quartzite (Ranalli, 1995)	2.25	1.0200×10^{-6}	1×10^6	5
Strong inclusion[*,a]	Maryland Diabase (Mackwell et al., 1998)	2.25	1.0200×10^{-6}	1×10^7	30
Calcite[*,a]	Calcite (Schmid et al., 1977)	2.37	0.5600×10^{-6}	1×10^7	30
Mica[*,a]	Mica (Kronenberg et al., 1990)	2.55	2.9000×10^{-6}	1×10^7	15
Lower crust[*,b]	Wet Anorthite (Rybacki and Dresen, 2004)	2.25	0.2600×10^{-6}	1×10^7	30
Strong mantle[*,c]	Dry Olivine (Hirth and Kohlstedt, 2003)	2.75	2.1139×10^{-8}	1×10^7	30
Weak mantle[*,c]	Wet Olivine (Hirth and Kohlstedt, 2003)	2.75	2.1139×10^{-8}	1×10^7	30
Serpentinite[*,d]	Antigorite (Hilairet et al., 2007)	2.75	2.1139×10^{-8}	1×10^7	25

Dislocation creep	A [Pa^{-n-r} s^{-1}]	ζ [ ]	n [ ]	Q [J mol^{-1}]	V [m^3 mol^{-1}]	r [ ]
Crustal matrix 1	3.9811×10^{-16}	0.3^e, 1.0	3.0	356×10^3	0.00×10^{-6}	0.0
Crustal matrix 2	3.1623×10^{-26}	1.0	3.3	186.5×10^3	0.00×10^{-6}	0.0
Weak inclusion	5.0717×10^{-18}	1.0	2.3	154×10^3	0.00×10^{-6}	0.0
Strong inclusion	5.0477×10^{-28}	1.0	4.7	485×10^3	0.00×10^{-6}	0.0
Calcite	1.5849×10^{-25}	1.0	4.7	297×10^3	0.00×10^{-6}	0.0
Mica	1.0000×10^{-138}	1.0	18.0	51.0×10^3	0.00×10^{-6}	0.0
Lower crust	3.9811×10^{-16}	1.0	3.0	356×10^3	0.00×10^{-6}	0.0
Strong mantle	1.1000×10^{-16}	1.0	3.5	530×10^3	14.0×10^{-6}	0.0
Weak mantle[1]	5.6786×10^{-27}	1.0	3.5	480×10^3	11.0×10^{-6}	1.2
Serpentinite	4.4738×10^{-38}	1.0	3.8	8.90×10^3	3.20×10^{-6}	0.0

Diffusion creep[2]	A [Pa^{-n-r} m^m s^{-1}]	m [ ]	n [ ]	Q [J mol^{-1}]	V [m^3 mol^{-1}]	r [ ]
Strong mantle	1.5000×10^{-15}	3.0	1.0	370×10^3	7.5×10^{-6}	0.0
Weak mantle[1]	2.5000×10^{-23}	3.0	1.0	375×10^3	9.0×10^{-6}	1.0

Peierls creep	A_P [s^{-1}]	Q [J mol^{-1}]	V [m^3 mol^{-1}]	σ_P [Pa]	γ [ ]
Mantle3	5.7000×10^{11}	540×10^3	0.0×10^{-6}	8.5×10^9	0.1

$^*c_P = 1050$ [J kg^{-1} K^{-1}] $^a G = 2\times10^{10}$ [Pa], $\rho_0 = 2800$ [kg m^{-3}], $\alpha = 3.5 \times 10^{-5}$ [K^{-1}], $\beta = 1\times10^{-11}$ [Pa^{-1}] $^b G = 2\times10^{10}$ [Pa], $\rho_0 = 2900$ [kg m^{-3}], $\alpha = 3.5\times10^{-5}$ [K^{-1}], $\beta = 1\times10^{-11}$ [Pa^{-1}] $^c G = 2\times10^{10}$ [Pa] $^d G = 1.81\times10^{10}$ [Pa], $\rho_0 = 2585$ [kg m^{-3}], $\alpha = 4.7 \times 10^{-5}$ [K^{-1}], $\beta = 1 \times 10^{-11}$ [Pa^{-1}] ^{e}Weakening prefactor employed during extension and cooling. [1]A water fugacity $f_{H_2O} = 1.0\times10^9$ [Pa] is used. For all other phases $f_{H_2O}= 0.0$ [Pa]. [2]A constant grain size $d = 1\times10^{-3}$ [m] is used. [3]Reference: Goetze and Evans (1979) regularized by Kameyama et al. (1999).

Table S2: Bulk rock composition for phase equilibrium calculations.

Oxides [wt%]	Pelite (avg.)[1,4]	Rhyolite[1,4]	Andesite[1,4]	MORB[1,4]	Hydr. Peridotite[1,4]	Serpentinite[2,4]	Bulk DMM[3,5]
SiO_2	61.500	72.800	57.900	49.200	44.710	44.210	44.710
Al_2O_3	18.600	13.300	17.000	16.100	4.160	3.130	3.980
FeO	10.000	2.440	6.980	10.220	8.070	8.898	8.180
MgO	3.810	0.390	3.330	6.440	39.200	39.240	38.730
CaO	-	-	6.790	10.500	2.420	3.060	3.170
Na_2O	1.460	3.550	3.480	3.010	0.220	-	0.130
K_2O	3.020	4.300	1.620	1.100	-	-	-
H_2O	sat	sat	sat	sat	sat	sat	-
CO_2	sat	sat	sat	sat	-	-	-
Solution models							
Opx(HP)	+	+	+	+	+	+	-
Gt(GCT)	+	+	+	+	+	+	-
feldspar	+	+	+	+	+	+	-
Chl(HP)	+	+	+	+	+	+	-
Sp(HP)	+	+	+	+	+	+	-
O(HP)	+	+	+	+	+	+	-
Stlp(M)	+	+	+	+	-	-	-
Carp	+	+	+	+	-	-	-
Sud	+	+	+	+	-	-	-
Bio(TCC)	+	+	+	+	-	-	-
St(HP)	+	+	+	+	-	-	-
Ctd(HP)	+	+	+	+	-	-	-
Pheng(HP)	+	+	+	+	-	-	-
hCrd	+	+	+	+	+	+	-
Omph	-	-	+	+	+	+	-
GlTrTsPg	-	-	+	+	+	+	-
Pu(M)	-	-	+	+	+	-	-
Act(M)	-	-	+	+	+	+	-
T	-	-	+	-	+	+	-
A-phase	-	-	-	-	+	+	-
Chum	-	-	-	-	+	+	-
B	-	-	-	-	+	+	-
Wus	-	-	-	-	+	+	-
Fperh	-	-	-	-	+	+	-
Atg(PN)	-	-	-	-	+	+	-
Bulk DMM							
C2/c	-	-	-	-	-	-	+
Wus	-	-	-	-	-	-	+
Pv	-	-	-	-	-	-	+
Pl	-	-	-	-	-	-	+
Sp	-	-	-	-	-	-	+
O	-	-	-	-	-	-	+
Wad	-	-	-	-	-	-	+
Ring	-	-	-	-	-	-	+
Opx	-	-	-	-	-	-	+
Cpx	-	-	-	-	-	-	+
Aki	-	-	-	-	-	-	+
Gt_maj	-	-	-	-	-	-	+
Ppv	-	-	-	-	-	-	+
CF	-	-	-	-	-	-	+

Table S2

[1]Bulk rock modified after Winter (2013) [2]Bulk rock modified after Pelletier et al. (2008) [3]Bulk rock modified after Workman and Hart (2005). We assume water saturation in all calculations. Crosses denote solution models used for given lithologies. [4]Thermodynamic database: Holland and Powell (1998) updated in 2002 [5]Thermodynamic database: Stixrude and Lithgow-Bertelloni (2011) for depleted MORB mantle (DMM). Note that only the relative abundance of elements is important for our phase diagram calculations. Details on the solution models can be found in the solution_model.dat data file in Perple_X.

Bibliography

Agard, P., Monié, P., Jolivet, L., Goffé, B., 2002. Exhumation of the schistes lustrés complex: in situ laser probe 40ar/39ar constraints and implications for the western alps. Journal of metamorphic Geology 20 (6), 599–618.

Agard, P., Plunder, A., Angiboust, S., Bonnet, G., Ruh, J., 2018. The subduction plate interface: rock record and mechanical coupling (from long to short timescales). Lithos 320, 537–566.

Amiguet, E., Van De Moortèle, B., Cordier, P., Hilairet, N., Reynard, B., 2014. Deformation mechanisms and rheology of serpentines in experiments and in nature. Journal of Geophysical Research: Solid Earth 119 (6), 4640–4655.

Angiboust, S., Agard, P., Jolivet, L., Beyssac, O., 2009. The zermatt-saas ophiolite: the largest (60-km wide) and deepest (c. 70–80 km) continuous slice of oceanic lithosphere detached from a subduction zone? Terra Nova 21 (3), 171–180.

Babist, J., Handy, M., Konrad-Schmolke, M., Hammerschmidt, K., 2006. Precollisional, multistage exhumation of subducted continental crust: The sesia zone, western alps. Tectonics 25 (6).

Barnicoat, A., Rex, D., Guise, P., Cliff, R., 1995. The timing of and nature of greenschist facies deformation and metamorphism in the upper pennine alps. Tectonics 14 (2), 279–293.

Barrow, G., 1893. On an intrusion of muscovite-biotite gneiss in the south-eastern highlands of scotland, and its accompanying metamorphism. Quarterly Journal of the Geological Society 49 (1-4).

Beaussier, S. J., Gerya, T. V., Burg, J.-P., 2019. 3d numerical modelling of the wilson cycle: structural inheritance of alternating subduction polarity. Geological Society, London, Special Publications 470 (1), 439–461.

Beltrando, M., Compagnoni, R., Lombardo, B., 2010a. (ultra-) high-pressure metamorphism and orogenesis: an alpine perspective. Gondwana Research 18 (1), 147–166.

Beltrando, M., Lister, G. S., Rosenbaum, G., Richards, S., Forster, M. A., 2010b. Recognizing episodic lithospheric thinning along a convergent plate margin: The example of the early oligocene alps. Earth-Science Reviews 103 (3-4), 81–98.

Berger, A., Schmid, S. M., Engi, M., Bousquet, R., Wiederkehr, M., 2011. Mechanisms of mass and heat transport during barrovian metamorphism: A discussion based on field evidence from the central alps (switzerland/northern italy). Tectonics 30 (1).

Bousquet, R., Goffé, B., Vidal, O., Oberhänsli, R., Patriat, M., 2002. The tectono-metamorphic history of the valaisan domain from the western to the central alps: New constraints on the evolution of the alps. Geological Society of America Bulletin 114 (2), 207–225.

Bousquet, R., Oberhänsli, R., Goffé, B., Wiederkehr, M., Koller, F., Schmid, S. M., Schuster, R., Engi, M., Berger, A., Martinotti, G., 2008. Metamorphism of metasediments at the scale of an orogen: a key to the tertiary geodynamic evolution of the alps. Geological Society, London, Special Publications 298 (1), 393–411.

Bucher, S., Schmid, S. M., Bousquet, R., Fügenschuh, B., 2003. Late-stage deformation in a collisional orogen (western alps): nappe refolding, back-thrusting or normal faulting? Terra Nova 15 (2), 109–117.

Burg, J., Gerya, T., 2005. The role of viscous heating in barrovian metamorphism of collisional orogens: thermomechanical models and application to the lepontine dome in the central alps. Journal of Metamorphic Geology 23 (2), 75–95.

Burov, E., Jolivet, L., Le Pourhiet, L., Poliakov, A., 2001. A thermomechanical model of exhumation of high pressure (hp) and ultra-high pressure (uhp) metamorphic rocks in alpine-type collision belts. Tectonophysics 342 (1-2), 113–136.

Butler, J. P., Beaumont, C., Jamieson, R. A., 2014. The alps 2: Controls on crustal subduction and (ultra) high-pressure rock exhumation in alpine-type orogens. Journal of Geophysical Research: Solid Earth 119 (7), 5987–6022.

Campani, M., Herman, F., Mancktelow, N., 2010a. Two-and three-dimensional thermal modeling of a low-angle detachment: Exhumation history of the simplon fault zone, central alps. Journal of Geophysical Research: Solid Earth 115 (B10).

Campani, M., Mancktelow, N., Seward, D., Rolland, Y., Müller, W., Guerra, I., 2010b. Geochronological evidence for continuous exhumation through the ductile-brittle transition along a crustal-scale low-angle normal fault: Simplon fault zone, central alps. Tectonics 29 (3).

Candioti, L. G., Moulas, E., Duretz, T., Schmalholz, S. M., 2021. Buoyancy versus shear forces in building orogenic wedges. Solid Earth 12, 1749–1775.

Candioti, L. G., Schmalholz, S. M., Duretz, T., 2020. Impact of upper mantle convection on lithosphere hyperextension and subsequent horizontally forced subduction initiation. Solid Earth 11 (6), 2327–2357.

Cawood, T. K., Platt, J. P., 2020. Variations in the ptt of deformation in a crustal-scale shear zone in metagranite. Earth and Space Science Open Archive ESSOAr.

Challandes, N., Marquer, D., Villa, I. M., 2003. Dating the evolution of c–s microstructures: a combined 40ar/39ar step-heating and uv laserprobe analysis of the alpine roffna shear zone. Chemical Geology 197 (1-4), 3–19.

Chang, C.-P., Angelier, J., Huang, C.-Y., 2009. Evolution of subductions indicated by mélanges in Taiwan. Springer, pp. 207–225.

Chemenda, A. I., Mattauer, M., Malavieille, J., Bokun, A. N., 1995. A mechanism for syn-collisional rock exhumation and associated normal faulting: Results from physical modelling. Earth and Planetary Science Letters 132 (1-4), 225–232.

Chenin, P., Picazo, S., Jammes, S., Manatschal, G., Müntener, O., Karner, G., 2019. Potential role of lithospheric mantle composition in the wilson cycle: a north atlantic perspective. Geological Society, London, Special Publications 470 (1), 157–172.

Chopin, C., 1984. Coesite and pure pyrope in high-grade blueschists of the western alps: a first record and some consequences. Contributions to Mineralogy and Petrology 86 (2), 107–118.

Chopin, C., 1987. Very-high-pressure metamorphism in the western alps: implications for subduction of continental crust. Philosophical Transactions of the Royal Society of London. Series A, Mathematical and Physical Sciences 321 (1557), 183–197.

Connolly, J., Petrini, K., 2002. An automated strategy for calculation of phase diagram sections and retrieval of rock properties as a function of physical conditions. Journal of Metamorphic Geology 20 (7), 697–708.

Cortiana, G., Dal Piaz, G., Del Moro, A., Hunziker, J., Martin, S., 1998. 40ar-39ar and rb-sr dating of the pillonet klippe and sesia-lanzo basal slice in the ayas valley and evolution of the austroalpine-piedmont nappe stack. Memorie di Scienze Geologiche 50, 177–194.

Crameri, F., 2018. Geodynamic diagnostics, scientific visualisation and staglab 3.0. Geoscientific Model Development 11 (6), 2541–2562.

Dal Piaz, G., Cortiana, G., Del Moro, A., Martin, S., Pennacchioni, G., Tartarotti, P., 2001. Tertiary age and paleostructural inferences of the eclogitic imprint in the austroalpine outliers and zermatt–saas ophiolite, western alps. International Journal of Earth Sciences 90 (3), 668–684.

Dal Zilio, L., Ruh, J., Avouac, J.-P., 2020. Structural evolution of orogenic wedges: interplay between erosion and weak décollements. Tectonics, e2020TC006210.

De Graciansky, P.-C., Roberts, D. G., Tricart, P., 2011. The Birth of the Western and Central Alps: Subduction, Obduction, Collision. Vol. 14. Elsevier, pp. 289–315.

Dewey, J., Helman, M., Knott, S., Turco, E., Hutton, D., 1989. Kinematics of the western mediterranean. Geological Society, London, Special Publications 45 (1), 265–283.

Dewey, J. F., Burke, K., 1974. Hot spots and continental break-up: implications for collisional orogeny. Geology 2 (2), 57–60.

Di Vincenzo, G., Tonarini, S., Lombardo, B., Castelli, D., Ottolini, L., 2006. Comparison of 40ar–39ar and rb–sr data on phengites from the uhp brossasco–isasca unit (dora maira massif, italy): implications for dating white mica. Journal of Petrology 47 (7), 1439–1465.

Duchêne, S., Blichert-Toft, J., Luais, B., Télouk, P., Lardeaux, J.-M., Albarede, F., 1997. The lu–hf dating of garnets and the ages of the alpine high-pressure metamorphism. Nature 387 (6633), 586–589.

Duretz, T., Gerya, T., Kaus, B., Andersen, T., 2012. Thermomechanical modeling of slab eduction. Journal of Geophysical Research: Solid Earth 117 (B8).

Duretz, T., Petri, B., Mohn, G., Schmalholz, S., Schenker, F., Müntener, O., 2016. The importance of structural softening for the evolution and architecture of passive margins. Scientific reports 6 (1), 1–7.

Engi, M., Regis, D., Darling, J., Rubatto, D., Cenki Tok, B., Zucali, M., Compagnoni, R., 2011. Dynamics in the sesia hp terrane: Combined petrochronological and structural analysis. In: Nature of the plate interface in subduction zones.

Engi, M., Todd, C., Schmatz, D., 1995. Tertiary metamorphic conditions in the eastern lepontine alps. Schweizerische Mineralogische und Petrographische Mitteilungen 75 (3), 347–369.

Erdős, Z., Huismans, R. S., Beek, P. v. d., 2019. Control of increased sedimentation on orogenic fold-and-thrust belt structure–insights into the evolution of the western alps. Solid Earth 10 (2), 391–404.

Ernst, W., 1971. Metamorphic zonations on presumably subducted lithospheric plates from japan, california and the alps. Contributions to Mineralogy and Petrology 34 (1), 43–59.

Ernst, W., 1972. Occurrence and mineralogic evolution of blueschist belts with time. American Journal of Science 272 (7), 657–668.

Escher, A., Beaumont, C., 1997. Formation, burial and exhumation of basement nappes at crustal scale: a geometric model based on the western swiss-italian alps. Journal of Structural Geology 19 (7), 955–974.

Escher, A., Hunziker, J., Marthaler, M., Masson, H., Sartori, M., Steck, A., 1997. Geological framework and structural evolution of the western swiss-italian alps. Deep Structure of the Swiss Alps: Results of the National Research Program 20 (NRP 20), 205–222.

Escher, A., Masson, H., Steck, A., 1993. Nappe geometry in the western swiss alps. Journal of structural Geology 15 (3-5), 501–509.

Eskola, P., 1915. On the relations between the chemical and mineralogical composition in the metamorphic rocks of orijarvi region. Bull. comm. géol. Finlande 44.

Ferrando, S., Bernoulli, D., Compagnoni, R., 2004. The canavese zone (internal western alps): a distal margin of adria. Schweizerische Mineralogische und Petrographische Mitteilungen 84 (1-20).

Forster, M., Lister, G., Compagnoni, R., Giles, D., Hills, Q., Betts, P., Beltrando, M., Tamagno, E., 2004. Mapping of oceanic crust with" HP" to" UHP" metamorphism: The Lago di Cignana Unit,(Western Alps). Geological Society of London.

Frey, M., Desmons, J., Neubauer, F., 1999. Metamorphic maps of the alps. an enclosure to. Schweiz. Mineral. Petrogr. Mitt 79 (1).

Froitzheim, N., Pleuger, J., Nagel, T. J., 2006. Extraction faults. Journal of Structural Geology 28 (8), 1388–1395.

Froitzheim, N., Pleuger, J., Roller, S., Nagel, T., 2003. Exhumation of high-and ultrahigh-pressure metamorphic rocks by slab extraction. Geology 31 (10), 925–928.

Gasinski, A., Slaczka, A., Winkler, W., 1997. Tectono-sedimentary evolution of the upper prealpine nappe (switzerland and france): nappe formation by late cretaceous-paleogene accretion. Geodinamica Acta 10 (4), 137–157.

Gebauer, D., Schertl, H.-P., Brix, M., Schreyer, W., 1997. 35 ma old ultrahigh-pressure metamorphism and evidence for very rapid exhumation in the dora maira massif, western alps. Lithos 41 (1-3), 5–24.

Gerya, T., 2015. Tectonic overpressure and underpressure in lithospheric tectonics and metamorphism. Journal of Metamorphic Geology 33 (8), 785–800.

Gerya, T. V., Stöckhert, B., Perchuk, A. L., 2002. Exhumation of high-pressure metamorphic rocks in a subduction channel: A numerical simulation. Tectonics 21 (6), 6–1–6–19.

Gerya, T. V., Yuen, D. A., 2003. Characteristics-based marker-in-cell method with conservative finite-differences schemes for modeling geological flows with strongly variable transport properties. Physics of the Earth and Planetary Interiors 140 (4), 293–318.

Ghent, E., 2020. Metamorphic facies: A review and some suggestions for changes. The Canadian Mineralogist 58 (4), 437–444.

Gianola, O., Schmidt, M. W., von Quadt, A., Peytcheva, I., Luraschi, P., Reusser, E., 2014. Continuity in geochemistry and time of the tertiary bergell intrusion (central alps). Swiss Journal of Geosciences 107 (2), 197–222.

Goetze, C., Evans, B., 1979. Stress and temperature in the bending lithosphere as constrained by experimental rock mechanics. Geophysical Journal International 59 (3), 463–478.

Goffé, B., Bousquet, R., 1997. Ferrocarpholite, chloritoid and lawsonite in metapelites of the versoyen and petit st bernard units (valais zone, western alps). Schweizerische Mineralogische und Petrographische Mitteilungen 77 (2), 137–147.

Gregory, C. J., McFarlane, C. R., Hermann, J., Rubatto, D., 2009. Tracing the evolution of calc-alkaline magmas: in-situ sm–nd isotope studies of accessory minerals in the bergell igneous complex, italy. Chemical Geology 260 (1-2), 73–86.

Groppo, C., Ferrando, S., Gilio, M., Botta, S., Nosenzo, F., Balestro, G., Festa, A., Rolfo, F., 2019. What's in the sandwich? new p–t constraints for the (u) hp nappe stack of southern dora-maira massif (western alps). European Journal of Mineralogy 31 (4), 665–683.

Guillot, S., Hattori, K., 2013. Serpentinites: essential roles in geodynamics, arc volcanism, sustainable development, and the origin of life. Elements 9 (2), 95–98.

Guillot, S., Schwartz, S., Reynard, B., Agard, P., Prigent, C., 2015. Tectonic significance of serpentinites. Tectonophysics 646, 1–19.

Hacker, B. R., Gerya, T. V., 2013. Paradigms, new and old, for ultrahigh-pressure tectonism. Tectonophysics 603, 79–88.

Handy, M. R., Ustaszewski, K., Kissling, E., 2015. Reconstructing the alps–carpathians–dinarides as a key to understanding switches in subduction polarity, slab gaps and surface motion. International Journal of Earth Sciences 104 (1), 1–26.

Hansen, F., Carter, N., 1983. Semibrittle creep of dry and wet westerly granite at 1000 mpa. In: The 24th US Symposium on Rock Mechanics (USRMS). American Rock Mechanics Association.

Hess, H., 1955. Serpentines, orogeny, and epeirogeny. Geol. Soc. Am. Spec. Paper 62, 391–407.

Hilairet, N., Reynard, B., Wang, Y., Daniel, I., Merkel, S., Nishiyama, N., Petitgirard, S., 2007. High-pressure creep of serpentine, interseismic deformation, and initiation of subduction. Science 318 (5858), 1910–1913.

Hirth, G., Kohlstedt, D., 2003. Rheology of the upper mantle and the mantle wedge: A view from the experimentalists. Geophysical Monograph-American Geophysical Union 138, 83–106.

Holland, T., Powell, R., 1998. An internally consistent thermodynamic data set for phases of petrological interest. Journal of metamorphic Geology 16 (3), 309–343.

Inger, S., Ramsbotham, W., Cliff, R., Rex, D., 1996. Metamorphic evolution of the sesia-lanzo zone, western alps: time constraints from multi-system geochronology. Contributions to Mineralogy and Petrology 126 (1-2), 152–168.

Isacks, B., Oliver, J., Sykes, L. R., 1968. Seismology and the new global tectonics. Journal of Geophysical Research 73 (18), 5855–5899.

Jamieson, R. A., Beaumont, C., Fullsack, P., Lee, B., 1998. Barrovian regional metamorphism: Where's the heat? Geological Society, London, Special Publications 138 (1), 23–51.

Jamtveit, B., Moulas, E., Andersen, T. B., Austrheim, H., Corfu, F., Petley-Ragan, A., Schmalholz, S. M., 2018. High pressure metamorphism caused by fluid induced weakening of deep continental crust. Scientific Reports 8 (1), 1–8.

Kameyama, M., Yuen, D. A., Karato, S.-I., 1999. Thermal-mechanical effects of low-temperature plasticity (the peierls mechanism) on the deformation of a viscoelastic shear zone. Earth and Planetary Science Letters 168 (1-2), 159–172.

Keller, L. M., Hess, M., Fügenschuh, B., Schmid, S. M., 2005. Structural and metamorphic evolution of the camughera–moncucco, antrona and monte rosa units southwest of the simplon line, western alps. Eclogae Geologicae Helvetiae 98 (1), 19–49.

Kiss, D., Candioti, L. G., Duretz, T., Schmalholz, S. M., 2020. Thermal softening induced subduction initiation at a passive margin. Geophysical Journal International 220 (3), 2068–2073.

Kiss, D., Podladchikov, Y., Duretz, T., Schmalholz, S. M., 2019. Spontaneous generation of ductile shear zones by thermal softening: Localization criterion, 1d to 3d modelling and application to the lithosphere. Earth and Planetary Science Letters 519, 284–296.

Kronenberg, A. K., Kirby, S. H., Pinkston, J., 1990. Basal slip and mechanical anisotropy of biotite. Journal of Geophysical Research: Solid Earth 95 (B12), 19257–19278.

Kurz, W., Froitzheim, N., 2002. The exhumation of eclogite-facies metamorphic rocks—a review of models confronted with examples from the alps. International Geology Review 44 (8), 702–743.

Lardeaux, J.-M., 2014. Deciphering orogeny: a metamorphic perspective. examples from european alpine and variscan belts: Part i: Alpine metamorphism in the western alps. a review. Bulletin de la Société Géologique de France 185 (2), 93–114.

Lardeaux, J.-M., JM, L., 1982. Relations entre le metamorphisme et la deformation dans la zone sesia-lanzo (alpes occidentales) et le probleme de l'eclogitisation de la croute continentale.

Le Breton, E., Brune, S., Ustaszewski, K., Zahirovic, S., Seton, M., Müller, R. D., 2021. Kinematics and extent of the piemont–liguria basin–implications for subduction processes in the alps. Solid Earth 12 (4), 885–913.

Le Pichon, X., 1968. Sea-floor spreading and continental drift. Journal of Geophysical Research 73 (12), 3661–3697.

Lemoine, M., Bas, T., Arnaud-Vanneau, A., Arnaud, H., Dumont, T., Gidon, M., Bourbon, M., de Graciansky, P.-C., Rudkiewicz, J.-L., Megard-Galli, J., 1986. The continental margin of the mesozoic tethys in the western alps. Marine and petroleum geology 3 (3), 179–199.

Liao, J., Malusà, M. G., Zhao, L., Baldwin, S. L., Fitzgerald, P. G., Gerya, T., 2018. Divergent plate motion drives rapid exhumation of (ultra) high pressure rocks. Earth and Planetary Science Letters 491, 67–80.

Liati, A., Gebauer, D., Fanning, C. M., 2009. Geochronological evolution of hp metamorphic rocks of the adula nappe, central alps, in pre-alpine and alpine subduction cycles. Journal of the Geological Society 166 (4), 797–810.

Luisier, C., Baumgartner, L., Schmalholz, S. M., Siron, G., Vennemann, T., 2019. Metamorphic pressure variation in a coherent alpine nappe challenges lithostatic pressure paradigm. Nature communications 10 (1), 1–11.

Mackwell, S., Zimmerman, M., Kohlstedt, D., 1998. High-temperature deformation of dry diabase with application to tectonics on venus. Journal of Geophysical Research: Solid Earth 103 (B1), 975–984.

Malusà, M. G., Faccenna, C., Baldwin, S. L., Fitzgerald, P. G., Rossetti, F., Balestrieri, M. L., Danišík, M., Ellero, A., Ottria, G., Piromallo, C., 2015. Contrasting styles of (u) hp rock exhumation along the cenozoic adria-europe plate boundary (western alps, calabria, corsica). Geochemistry, Geophysics, Geosystems 16 (6), 1786–1824.

Malusà, M. G., Guillot, S., Zhao, L., Paul, A., Solarino, S., Dumont, T., Schwartz, S., Aubert, C., Baccheschi, P., Eva, E., 2021. The deep structure of the alps based on the cifalps seismic experiment: A synthesis. Geochemistry, Geophysics, Geosystems 22 (3), e2020GC009466.

Mancktelow, N., 1985. The simplon line: a major displacement zone in the western lepontine alps. Eclogae Geologicae Helvetiae 78 (1), 73–96.

Mancktelow, N. S., 2008. Tectonic pressure: Theoretical concepts and modelled examples. Lithos 103 (1-2), 149–177.

Manzotti, P., Ballevre, M., Zucali, M., Robyr, M., Engi, M., 2014a. The tectonometamorphic evolution of the sesia–dent blanche nappes (internal western alps): review and synthesis. Swiss Journal of Geosciences 107 (2), 309–336.

Manzotti, P., Bosse, V., Pitra, P., Robyr, M., Schiavi, F., Ballevre, M., 2018. Exhumation rates in the gran paradiso massif (western alps) constrained by in situ u–th–pb dating of accessory phases (monazite, allanite and xenotime). Contributions to Mineralogy and Petrology 173 (3), 24.

Manzotti, P., Zucali, M., Ballevre, M., Robyr, M., Engi, M., 2014b. Geometry and kinematics of the roisan-cignana shear zone, and the orogenic evolution of the dent blanche tectonic system (western alps). Swiss Journal of Geosciences 107 (1), 23–47.

McCarthy, A., Tugend, J., Mohn, G., Candioti, L., Chelle-Michou, C., Arculus, R., Schmalholz, S. M., Müntener, O., 2020. A case of ampferer-type subduction and consequences for the alps and the pyrenees. American Journal of Science 320 (4), 313–372.

Miyashiro, A., 2012. Metamorphism and metamorphic belts. Springer Science & Business Media.

Mohn, G., Manatschal, G., Müntener, O., Beltrando, M., Masini, E., 2010. Unravelling the interaction between tectonic and sedimentary processes during lithospheric thinning in the alpine tethys margins. International Journal of Earth Sciences 99 (1), 75–101.

Morgan, W. J., 1968. Rises, trenches, great faults, and crustal blocks. Journal of Geophysical Research 73 (6), 1959–1982.

Moulas, E., Podladchikov, Y. Y., Aranovich, L. Y., Kostopoulos, D., 2013. The problem of depth in geology: When pressure does not translate into depth. Petrology 21 (6), 527–538.

Nibourel, L., Berger, A., Egli, D., Heuberger, S., Herwegh, M., 2021. Structural and thermal evolution of the eastern aar massif: insights from structural field work and raman thermometry. Swiss journal of geosciences 114 (1), 1–43.

Oberhänsli, R., Bousquet, R., Engi, M., Goffé, B., Gosso, G., Handy, M., Höck, V., Koller, F., Lardeaux, J., Polino, R., 2004. Metamorphic structure of the alps. CCGM (Commission of the Geological Maps of the World), Paris.

Oberli, F., Meier, M., Berger, A., Rosenberg, C. L., GierÉ, R., 2004. U-th-pb and 230th/238u disequilibrium isotope systematics: Precise accessory mineral chronology and melt evolution tracing in the alpine bergell intrusion. Geochimica et Cosmochimica Acta 68 (11), 2543–2560.

Pelletier, L., Müntener, O., Kalt, A., Vennemann, T. W., Belgya, T., 2008. Emplacement of ultramafic rocks into the continental crust monitored by light and other trace elements: An example from the geisspfad body (swiss-italian alps). Chemical Geology 255 (1-2), 143–159.

Petri, B., Duretz, T., Mohn, G., Schmalholz, S. M., Karner, G. D., Müntener, O., 2019. Thinning mechanisms of heterogeneous continental lithosphere. Earth and Planetary Science Letters 512, 147–162.

Petrini, K., Podladchikov, Y., 2000. Lithospheric pressure-depth relationship in compressive regions of thickened crust. Journal of metamorphic Geology 18 (1), 67–77.

Philpotts, A., Ague, J., 2009. Principles of igneous and metamorphic petrology. Cambridge University Press.

Platt, J., 1986. Dynamics of orogenic wedges and the uplift of high-pressure metamorphic rocks. Geological society of America bulletin 97 (9), 1037–1053.

Popov, A., Sobolev, S. V., 2008. Slim3d: A tool for three-dimensional thermomechanical modeling of lithospheric deformation with elasto-visco-plastic rheology. Physics of the earth and planetary interiors 171 (1-4), 55–75.

Putnis, A., Moore, J., Prent, A. M., Beinlich, A., Austrheim, H., 2021. Preservation of granulite in a partially eclogitized terrane: Metastable phenomena or local pressure variations? Lithos 400, 106413.

Ranalli, G., 1995. Rheology of the Earth. Springer Science & Business Media.

Reddy, S., Wheeler, J., Cliff, R., 1999. The geometry and timing of orogenic extension: an example from the western italian alps. Journal of Metamorphic Geology 17, 573–590.

Reddy, S. M., Wheeler, J., Butler, R. W. H., Cliff, R. A., Freeman, S., Inger, S., Pickles, C., Kelley, S. P., 2003. Kinematic reworking and exhumation within the convergent alpine orogen. Tectonophysics 365 (1-4), 77–102.

Ring, U., Merle, O., 1992. Forethrusting, backfolding, and lateral gravitational escape in the northern part of the western alps (monte rosa region). Geological Society of America Bulletin 104 (7), 901–914.

Rubatto, D., Gebauer, D., Compagnoni, R., 1999. Dating of eclogite-facies zircons: the age of alpine metamorphism in the sesia–lanzo zone (western alps). Earth and Planetary Science Letters 167 (3-4), 141–158.

Rubatto, D., Hermann, J., 2001. Exhumation as fast as subduction? Geology 29 (1), 3–6.

Rubatto, D., Hermann, J., Berger, A., Engi, M., 2009. Protracted fluid-induced melting during barrovian metamorphism in the central alps. Contributions to Mineralogy and Petrology 158 (6), 703–722.

Ruh, J. B., Le Pourhiet, L., Agard, P., Burov, E., Gerya, T., 2015. Tectonic slicing of subducting oceanic crust along plate interfaces: Numerical modeling. Geochemistry, Geophysics, Geosystems 16 (10), 3505–3531.

Ryan, P. D., Dewey, J. F., 2019. The sources of metamorphic heat during collisional orogeny: The barrovian enigma. Canadian Journal of Earth Sciences 56 (12), 1309–1317.

Rybacki, E., Dresen, G., 2004. Deformation mechanism maps for feldspar rocks. Tectonophysics 382 (3-4), 173–187.

Saliot, P., 1973. Principal zones of metamorphism in french-alps-distribution and significance. COMPTES RENDUS HEBDOMADAIRES DES SEANCES DE L ACADEMIE DES SCIENCES SERIE D 276 (24), 3081–&.

Schenker, F. L., Schmalholz, S. M., Moulas, E., Pleuger, J., Baumgartner, L. P., Podladchikov, Y., Vrijmoed, J., Buchs, N., Müntener, O., 2015. Current challenges for explaining (ultra) high-pressure tectonism in the pennine domain of the central and western alps. Journal of Metamorphic Geology 33 (8), 869–886.

Schlunegger, F., Willett, S., 1999. Spatial and temporal variations in exhumation of the central swiss alps and implications for exhumation mechanisms. Geological Society, London, Special Publications 154 (1), 157–179.

Schmalholz, S. M., Duretz, T., Hetényi, G., Medvedev, S., 2019. Distribution and magnitude of stress due to lateral variation of gravitational potential energy between indian lowland and tibetan plateau. Geophysical Journal International 216 (2), 1313–1333.

Schmalholz, S. M., Fletcher, R. C., 2011. The exponential flow law applied to necking and folding of a ductile layer. Geophysical Journal International 184 (1), 83–89.

Schmalholz, S. M., Podladchikov, Y. Y., 2013. Tectonic overpressure in weak crustal-scale shear zones and implications for the exhumation of high-pressure rocks. Geophysical Research Letters 40 (10), 1984–1988.

Schmalholz, S. M., Schenker, F. L., 2016. Exhumation of the dora maira ultrahigh-pressure unit by buoyant uprise within a low-viscosity mantle oblique-slip shear zone. Terra Nova 28 (5), 348–355.

Schmid, S., Boland, J., Paterson, M., 1977. Superplastic flow in finegrained limestone. Tectonophysics 43 (3-4), 257–291.

Schmid, S., Kissling, E., 2000. The arc of the western alps in the light of geophysical data on deep crustal structure. Tectonics 19 (1), 62–85.

Schmid, S. M., Fügenschuh, B., Kissling, E., Schuster, R., 2004. Tectonic map and overall architecture of the alpine orogen. Eclogae Geologicae Helvetiae 97 (1), 93–117.

Schmid, S. M., Kissling, E., Diehl, T., van Hinsbergen, D. J., Molli, G., 2017. Ivrea mantle wedge, arc of the western alps, and kinematic evolution of the alps–apennines orogenic system. Swiss Journal of Geosciences 110 (2), 581–612.

Schmid, S. M., Pfiffner, O.-A., Froitzheim, N., Schönborn, G., Kissling, E., 1996. Geophysical-geological transect and tectonic evolution of the swiss-italian alps. Tectonics 15 (5), 1036–1064.

Schwartz, S., Allemand, P., Guillot, S., 2001. Numerical model of the effect of serpentinites on the exhumation of eclogitic rocks: insights from the monviso ophiolitic massif (western alps). Tectonophysics 342 (1-2), 193–206.

Spear, F. S., 1989. Petrologic determination of metamorphic pressure-temperature-time paths. Metamorphic Pressure-Temperature-Time Paths 7, 1–55.

Spear, F. S., Pattison, D. R., Cheney, J. T., 2017. The metamorphosis of metamorphic petrology. The Web of Geological Sciences: Advances, Impacts, and Interactions II, Geol. Soc. Am 523, 31–73.

Steck, A., Hunziker, J., 1994. The tertiary structural and thermal evolution of the central alps—compressional and extensional structures in an orogenic belt. Tectonophysics 238 (1-4), 229–254.

Steck, A., Masson, H., Robyr, M., 2015. Tectonics of the monte rosa and surrounding nappes (switzerland and italy): Tertiary phases of subduction, thrusting and folding in the pennine alps. Swiss Journal of Geosciences 108 (1), 3–34.

Stixrude, L., Lithgow-Bertelloni, C., 2011. Thermodynamics of mantle minerals-ii. phase equilibria. Geophysical Journal International 184 (3), 1180–1213.

Stöckhert, B., Gerya, T. V., 2005. Pre-collisional high pressure metamorphism and nappe tectonics at active continental margins: A numerical simulation. Terra Nova 17 (2), 102–110.

Stüwe, K., 1998. Heat sources of cretaceous metamorphism in the eastern alps—a discussion. Tectonophysics 287 (1-4), 251–269.

Tilton, G., Schreyer, W., Schertl, H.-P., 1989. Pb-sr-nd isotopic behavior of deeply subducted crustal rocks from the dora maira massif, western alps, italy. Geochimica et Cosmochimica Acta 53 (6), 1391–1400.

Trümpy, R., 1975. Penninic-austroalpine boundary in the swiss alps: a presumed former continental margin and its problems. American Journal of Science 275 (A), 209–238.

Turcotte, D. L., Schubert, G., 2002. Geodynamics. Cambridge university press.

Vaughan-Hammon, J. D., Luisier, C., Baumgartner, L. P., Schmalholz, S. M., 2021. Peak alpine metamorphic conditions from staurolite bearing metapelites in the monte rosa nappe (central european alps) and geodynamic implications. Journal of Metamorphic Geology.

von Blackenburg, F., 1992. Combined high-precision chronometry and geochemical tracing using accessory minerals: applied to the central-alpine bergell intrusion (central europe). Chemical Geology 100 (1-2), 19–40.

Vuichard, J., Ballevre, M., 1988. Garnet–chloritoid equilibria in eclogitic pelitic rocks from the sesia zone (western alps): their bearing on phase relations in high pressure metapelites. Journal of metamorphic Geology 6 (2), 135–157.

Warren, C., 2013. Exhumation of (ultra-) high-pressure terranes: concepts and mechanisms. Solid Earth 4 (1), 75–92.

Warren, C., Beaumont, C., Jamieson, R. A., 2008. Modelling tectonic styles and ultra-high pressure (uhp) rock exhumation during the transition from oceanic subduction to continental collision. Earth and Planetary Science Letters 267 (1-2), 129–145.

Wegener, A., 1915. Die entstehung der kontinente und ozeane: Brunswick. Friedrich Vieweg Sohn.

Wheeler, J., Reddy, S., Cliff, R., 2001. Kinematic linkage between internal zone extension and shortening in more external units in the nw alps. Journal of the Geological Society 158 (3), 439–443.

Wiederkehr, M., Bousquet, R., Schmid, S. M., Berger, A., 2008. From subduction to collision: thermal overprint of hp/lt meta-sediments in the north-eastern lepontine dome (swiss alps) and consequences regarding the tectono-metamorphic evolution of the alpine orogenic wedge. Swiss Journal of Geosciences 101 (1), 127–155.

Wiederkehr, M., Bousquet, R., Ziemann, M., Schmid, S., Berger, A., 2007. Thermal structure of the valaisan and ultra-helvetic sedimentary units of the northern lepontine dome—consequences regarding the tectono-metamorphic evolution. EGU, Wien.

Wilson, J. T., 1966. Did the atlantic close and then re-open?

Winter, J. D., 2013. Principles of igneous and metamorphic petrology. Pearson education.

Workman, R. K., Hart, S. R., 2005. Major and trace element composition of the depleted morb mantle (dmm). Earth and Planetary Science Letters 231 (1-2), 53–72.

Yamato, P., Agard, P., Burov, E., Le Pourhiet, L., Jolivet, L., Tiberi, C., 2007. Burial and exhumation in a subduction wedge: Mutual constraints from thermomechanical modeling and natural p-t-t data (schistes lustrés, western alps). Journal of Geophysical Research: Solid Earth 112 (B7).

Yamato, P., Burov, E., Agard, P., Le Pourhiet, L., Jolivet, L., 2008. Hp-uhp exhumation during slow continental subduction: Self-consistent thermodynamically and thermomechanically coupled model with application to the western alps. Earth and Planetary Science Letters 271 (1-4), 63–74.

Yang, J., Lu, G., Liu, T., Li, Y., Wang, K., Wang, X., Sun, B., Faccenda, M., Zhao, L., 2020. Amagmatic subduction produced by mantle serpentinization and oceanic crust delamination. Geophysical Research Letters 47 (9), e2019GL086257.

CHAPTER 6

General Conclusion

The aims of this thesis were to examine further the apparent discrepancies in peak pressure incurred by the Monte Rosa nappe during peak Alpine metamorphism. Five general explanations have been proposed to explain these P variations: (1) tectonic mélange, (2) differences in thermodynamic databases used in different studies, (3) lower P lithologies (e.g. metagranite) do not exhibit a high-P imprint due to sluggish kinetics, (4) lower P lithologies (e.g. metagranite) did experience high-P conditions but were later retrogressed, and (5) mechanical pressure variations (tectonic, or dynamic, pressure). These hypothesise have been addressed throughout this thesis through detailed geological analysis of portions in the Monte Rosa nappe that contain abundant high pressure whiteschists, including petrological investigations of newly discovered high pressure lithologies (whiteschist occurrences, basement metapelites containing staurolite, and unique chloritoid + zoisite bearing assemblages), as well as orogenic scale petrological-thermomechanical modelling of Alpine subduction and exhumation applied directly to the Western Alps. In this section I will briefly summarise these results within the context of the 5 possible explanations into different pressures recorded, as well as the limitations of the techniques, and the future work that should be addressed not only with respects to the Alpine evolution of the Monte Rosa or the Western Alps, but also within high-pressure metamorphic geology in general.

6.1   Summary and discussion of results

A comprehensive geological study of the Monte Rosa nappe and overlying Zermatt-Saas exposed at the cirque du Véraz, val d'Ayas, Italy, has been made. The area is significant in that it contains the largest concentration of high-P whiteschists compared to anywhere else in the Monte Rosa nappe. Particular focus has been made on the Alpine characteristics of the Monte Rosa's geological evolution. An important aspect of these investigations has been to identify any structures that indicate major tectonic reworking during peak Alpine metamorphism, more specifically, the presence of a tectonic mélange that could juxtapose high-P whiteschists next to lower P lithologies. Detailed investigations in these portions of the nappe indicate that no structures related to tectonic mélange are present. Portions of

the Monte Rosa nappe that are exposed at Véraz represent a coherent unit, not only between whiteschist and metagranite bodies (indicating whiteschists are a metasomatic equivalent to metagranites), but also between metagranite and metapelite lithologies, where pre-Alpine igneous structures such as cross-cutting dykes and contact metamorphic mineral indicators are preserved.

Within the nappe, major Alpine movements largely agree with previously studies that indicate top-N shearing associated with subduction of the European margin below Adria and nappe emplacement, and top-S shearing and folding associated with late Alpine backfolding. Alpine movements exposed at Véraz, are not synonymous with peak Alpine metamorphic conditions. This lack of deformation has many implications when reconstructing the subduction environment of the Monte Rosa. The lack of peak Alpine deformation could indicate: (1) deformation did occur but was later retrogressed, (2) there were insignificant differential stresses, or (3) the Monte Rosa complex had significant strength. Petrological examinations of newly discovered outcrops of whiteschists do not indicate syn-deformation equilibration at peak metamorphic conditions, but are actively deformed closely after peak metamorphic equilibration. Equally, deformation fabrics have not been overprinted by low grade minerals, therefore retrogression is not the only viable option. A period of low differential stresses during peak metamorphism may be a possibility in some areas, however, the lack of strain indicators does not necessarily indicate low differential stresses. The lack of high-P fabrics could be indicative of the Monte Rosa having significant strength during this time, especially considering the preservation of pre-Alpine igneous features throughout the nappe, and the large volumes of intrusive felspar dominated metagranite. The large strength of the Monte Rosa granite is exemplified when looking at deformation structures throughout the nappe. Typically, high strain features are confined to areas within the surrounding basement rocks, that cover a large area, and are demonstrated to envelope the strong granite (see maps and cross-sections). Whereas, within the granite, high strain features are scarce, and typically occur along thin shear zones with metre-scale offset, or close the basement contact. This contrast in rheology is best observed when tracing aplitic dykes that are undeformed within the granite, and that become increasing deformed when entering the surrounding basement.

Equally, not all of the basement is deformed, many areas within the basement also preserve pre-Alpine features (contact metamorphic aureole) and even preserve pre-intrusive features such as high-T garnets relates to Variscan orogenesis. This strain shadowing could be linked to geometrical effects of nearby intrusive granitoid bodies. Large rheological strength contrasts favour disparities in P originating from mechanical pressure variations (Luisier et al., 2019), i.e. between the strong metagranite and weak whiteschist. The heterogeneity of deformation throughout the Monte Rosa nappe, and the complete lack of deformation associated with peak Alpine metamorphism could be a good indicator of an ideal environment for tectonic pressure to have occurred. However, the lack of deformation, as discussed earlier, could indicate both low differential stresses or high strength.

Detailed petrological investigations of a newly discovered body of whiteschist shows striking similarities to previously reported occurrences (Luisier et al., 2019; Chopin and Monié, 1984). Both fine grained and coarse grained whiteschists within a single outcrop continue to indicate metamorphic formation conditions (c. 2.2 GPa) that deviate from lower P metagranites (c. 1.6 GPa). However, the new outcrop is not fully embedded within the granite and therefore the provenance is not fully constrained. Detailed petrological examinations and comparisons with former studies suggests that the chemistry is indicative of a similar metasomatic origin prior to peak Alpine metamorphism. Mg enrichment during metasomatism has been demonstrated in former studies, and this is supported in new whiteschist outcrops with the occurrences of Mg-rich phases such as talc and chloritoid. Mg zoning in natural samples of chloritoid within whiteschists was used to constrain modelled P-T pathways for the whiteschist prograde evolution during fractional crystallisation, predicted by pseudo-section modelling of chloritoid. One end-member P-T pathway is characterised by an isothermal P increase from 1.6 GPa to 2.2 GPa, which would presumably represent a dramatic isothermal tectonic pressure event. However, the resulting predicted zoning patterns of Mg in chloritoid do not agree with natural zoning. What is more realistic is a situation where a deviation in P coincided with continued heating during subduction. It is also difficult to justify a short-lived period of tectonically induced overpressure, due to the location of the whiteschist at the contact, i.e. not fully enclosed in granite. This along with the preliminary P-T modelling suggests that isothermal

P increases are not fully supported, and perhaps reaction-induced P increases may also be at play. Analysis between natural and modelled Mg zoning in chloritoid should also be taken with caution. A number of caveats are associated with this method. A large amount of studies apply this method to garnet growth zoning (e.g. Gaidies et al., 2008; Robyr et al., 2014), and this is reasonable, since garnet is an almost spherical mineral with more or less isotropic characteristics. Chloritoid, however, provides more head-aches, considering its non-spherical crystal shape as well as observed sector zoning that may indicate variable growth rates, and linked to this, the likelihood that certain mineralogical properties are anisotropic. Another caveat of this method is the assumed closed chemical system, that define a fixed bulk rock chemistry during prograde needed for assemblage diagram calculations. The influx or removal of fluids may have played a role during whiteschist formation. Certainly this is something to consider, but a closed system may also be a good assumption during a reaction-induced pressure increase, due to a fixed volume needed. Comparisons of three-dimensional growth zoning element profiles should be extended to more minerals, not only garnet, and more constraints for chloritoid growth would be of value when attempting to constrain the P-T history of whiteschists in the Monte Rosa nappe. A more thorough and statistical examination of textures, zoning profiles, phase relationships etc. in natural whiteschist samples would be of value, and provide further insight and constraints into the metamorphic prograde history of whiteschists.

Another important result of new occurrences of whiteschists explored in this thesis, are the sensitivity of thermodynamic databases used and the assumptions included within them (i.e. water activity). Comparisons of geochemical data from new whiteschist outcrops with that of whiteschists from the same area with unknown provinces show strong similarities (Chopin and Monié, 1984). However, the differences in P calculated for the same chemistry differ for a water activity of 1 at 2.2 GPa (this study), and a water activity of 0.6 at 1.6 GPa (Chopin and Monié, 1984). Therefore, some disparities in P may be a result of different thermodynamic assumptions, which should be carefully considered in petrological examinations and should be investigated more (Luisier et al., 2018, PhD thesis).

Investigations into newly discovered staurolite-bearing metapelitic assemblages in close proximity to, and structurally coherent with, whiteschist and metagranite lithologies was undertaken. Detailed petrological and pseudo-section analysis indicate a peak Alpine metamorphic imprint of 1.6 ± 0.2 GPa and 585 ± 20 °C, for previously unreported staurolite bearing metapelites in the Oberbau portions of the Monte Rosa nappe. These results continue to highlight that whiteschist lithologies show higher pressures (0.6 ± 0.2 GPa) compared to other lithologies within the nappe. The same thermodynamic database as Luisier et al. (2019) was used, demonstrating that P differences are not solely due to different thermodynamic assumptions, mixing models etc. Estimates continue to highlight the disparities in peak P even with considerations of Zn in staurolite. However, more experimental works needs to be done for Zn-staurolite end-members in order to accurately quantify P and T of stable staurolite assemblages.

Staurolite bearing assemblages have been demonstrated to occur within centimetre size pseudomorphs after andalusite, that were likely former contact metamorphic minerals associated with the thermal peak during Permian-aged intrusion of granites. This observation highlights that large areas of the nappe are free from Alpine reworking, and that portions of the nappe perhaps had reasonable strength. Preservation of pre-Alpine contact metamorphism textures also likely indicate that retrogression of higher grade metamorphic minerals did not occur before $c.$ 1.6 GPa. The occurrence of such mineral assemblages highlights the importance of detailed petrological analysis needed to identify small-scale, local equilibria in metamorphic rocks. Staurolite was most likely the only Zn bearing phase and thus its formation was heavily influences by the protolith chemistry and metasomatic history. Since the outcrop is free from late Alpine reworking the importance of deformation during retrogression that may erase high pressure fabrics may also be a factor. Metapelite lithologies also make it difficult to argue for P variations based on kinetics, as pelitic rocks typically have a high water content. A more detailed textural analysis of pseudomorphs after andalusite containing staurolite $+$ chloritoid may be of some value. Constraining the stoichiometric exchanges needed to form the assemblage after andalusite could give good insight into the local pre-Alpine metasomatic history.

Locating a potential whiteschist described by Peter Bearth near the Jägerhorn peak was undertaken. However, preliminary petrological analysis of samples indicates that the outcrop in question is most likely not a whiteschist. A unique assemblage of chloritoid + zoisite was identified. Preliminary pseudo-section calculations indicate a peak Alpine P of 1.6 GPa, which again highlights the higher P of 2.2 GPa for whiteschists throughout the Monte Rosa. Opportunities to find whiteschists within the Monte Rosa nappe that are free from Alpine metamorphic imprints are scarce, if not impossible. This likely highlights an important aspect of the whiteschist propensity to re-equilibrate during peak Alpine metamorphism, potentially owing to significant fluid contents.

State-of-the-art numerical modelling of subduction zones, that use c. 10,000 numerical markers, has to the first order predicted the large-scale metamorphic architecture of the western Alps. The presented numerical model uses a simple assumption that peak T (sometimes synonymous with peak P) will record the subduction related metamorphic imprint. Maximum P and T do not always correspond to a single point in P-T space, and therefore the maximum temperature may not always be the maximum depth of burial. However, what is significant to highlight is that proportionally, only a few markers show deviations from lithostatic P. This is a significant point in two regards: (1) it demonstrates that P dominated metamorphism is an exception to a larger temperature dominated and close to lithostatic environment, and (2) that a general model based on fundamental laws of physics predicts significant tectonic pressure (c. 0.4 GPa), albeit confined to only a few small regions within the model. The models also highlight the importance of serpentinites for exhumation, whereby a low proportion of serpentinite will provide an insufficiently weak subduction interface needed to exhume deeply buried continental crust. The importance of serpentinite during subduction and exhumation is further poignant, by the presence of ophiolitic sequences (containing significant amounts of serpentinite) enveloping the Monte Rosa nappe (Zermatt-Saas and Antrona). Within the nappe itself, it is difficult to locate shear zones that accommodate large displacements needed for exhumation. However, considering that the Monte Rosa was (passively) subducted as part of the down-going slab, it could be reasonable to assume that a lot of strain was accommodated at the nappe boundaries, i.e. between the Monte Rosa and Zermatt-Saas, or

reactivated inherited structures e.g. paleogeographic topography and low-angle extensional sear zones. Large amounts of serpentinite likely accommodated the majority of this strain, governing the style of exhumation for nappes such as the Monte Rosa, large-scale orogenic architecture, and metamorphic facies distribution.

Syn-convergent exhumation was predicted for models demonstrating a metamorphic architecture similar to that of the Western Alps. This style of exhumation has been proposed within the Alps, especially for the Monte Rosa nappe where major extensional shear indicators have been observed to operate at deep metamorphic grades (Reddy et al., 1999, 2003). This extrusion style of exhumation highlights that regional scale plate divergence is not required to form extensional type shear indicators. The significance of this exhumation style should be further investigated in the field.

What is still missing in numerical models, is the widespread, late orogenic backfolding, that can be observed at many scales from local asymmetrical crenulations to the nappe-scale influencing the present-day geometry. In the field, there are clear distinctions between planar nappe forming shear zones with little folding and large displacements, and deformation associated with late-stage folding. This could be due to many factors including the stress-state during an evolving orogen, rheology and geometry of subducting material, deformation mechanism regime etc. Field observations highlight a nappe refolding geometry, where the limbs of the fold are moving with opposite shear directions and the hinges of the folds exhibit relatively low strain (e.g. preservation of contact metamorphic textures). This deformation is characteristic of a buckling instability, and the presented numerical models indicate that buckling can trigger exhumation of deeply subducted units (Candioti et al., 2021, textitunder review). Numerical models also indicate that buckle instabilities can generate significant dynamic pressure (0.4 GPa) at the fold hinge. This could be applicable to the Monte Rosa nappe exposed at val d'Ayas, considering it contains the highest concentrations of high-P whiteschists, and the area is located at the true axial fold hinge of the Monte Rosa nappe. Periods of high differential stress may have been active prior to backfolding of the Monte Rosa nappe, and rheologically weak heterogeneities (whiteschist fingers) may have significantly de-

viated from lithostatic pressure during this time. This may also explain why no deformation fabrics active during the over-pressued period have been observed.
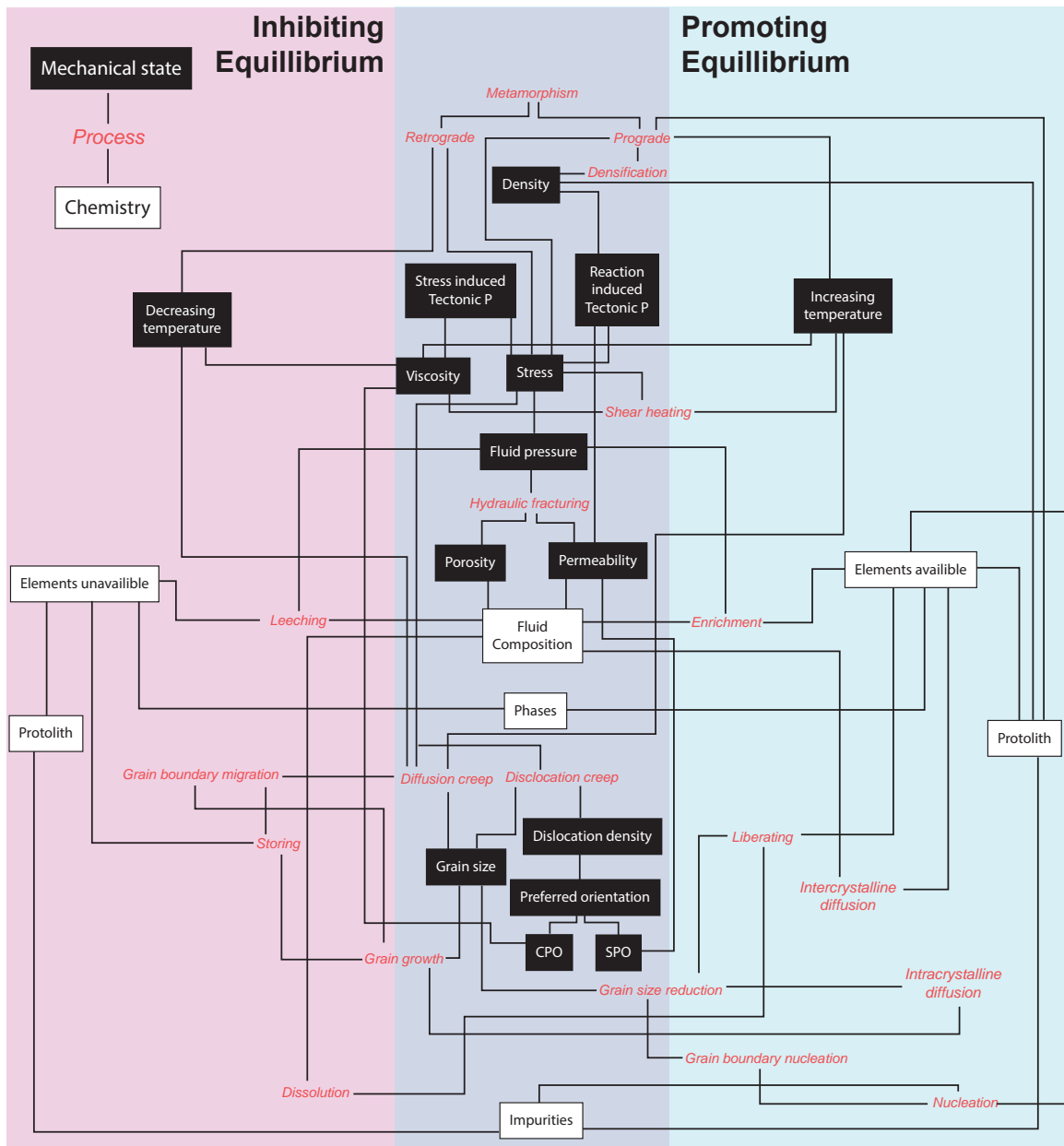
Figure S1: Extremely schematic diagram demonstrating the interplay between mechanics and chemistry and the possible resulting equilibrium state in a metamorphically evolving rock (initially inspired from conversations with J. Wheeler). CPO = crystallographic preferred orientation, SPO = shape preferred orientation.

Volumetrically low proportions of high-P whitseschists ($< 1\%$) throughout the Monte Rosa nappe indicate that mechanical pressure variations are exceptions to an environment where

lithostatic pressure provides us with a reasonable estimate for a rocks burial history. The question of the presence of tectonic pressure throughout the Earth is one that does not need to be addressed here, as it is a fundamental result of force balance. A more pressing question to ask is the relative magnitude of such a process. Three important scales are important to address: (1) the actual magnitude of tectonic pressure (within error i.e. 0.05 GPa, or considerable at > 0.2 GPa), (2) the spatial scale? Is it isolated to small areas, or could it be applicable to the size of the orogen, and (3) the temporal scale, i.e. are the timescales of tectonic pressure sufficiently long-lived for kinetic barriers to be overcome and thus equilibration of higher P phases? This thesis highlights that (1) magnitudes of 0.6 $\pm$ 0.2 GPa are feasible from petrological studies and numerical modelling, (2) low volume proportions of the nappe (< 1 % representing whiteschist volumes) are affected by deviations from lithostatic, and (3) significant periods of tectonic pressure are likely short-lived.

I will conclude this thesis by presenting Figure S1, that demonstrates the complexity of coupling mechanical processes with chemical processes. Metamorphic petrology and rock mechanics deal with unimaginably complex natural materials. Metamorphic equilibrium assemblages that are part of an evolving temperature, pressure and chemical environment, as well as the influence of deformation remains a large field of research to be further explored. The relative importance and magnitude of these processes is a worthwhile pursuit. For the Monte Rosa, it is becoming increasingly apparent that tectonic pressure is a feasible, metamorphically significant but rare geological phenomena; rather than a widespread and common occurrence, or even an impossibility.

6.2 Outlook

The work presented here, has provided further understanding into the geological evolution of the Monte Rosa nappe. Particular attention has been made for the Alpine orogenic event. In order to have a more complete understanding of this evolution, several areas of field research should be addressed within the massif:

- Investigations into high altitude areas of the Monte Rosa massif, e.g. surrounding the Durfourspitz. A considerable amount of whiteschists have been located west of the Stellihorn shear zone in the Oberbau regions, detailed investigations (as well as significantly retreating glaciers) may uncover more.

- Investigate areas throughout the Monte Rosa nappe that accommodated large amounts of strain related to Alpine orogenesis. Such studies could provide more insight into subduction/exhumation mechanisms at the nappe boundaries, or internally e.g. the Stellihorn shear zone.

- Location and analysis of Alpine-aged eclogitic mafic boudins within the Monte Rosa nappe, in order to characterise a peak metamorphic imprint, as well as provenance and tectonic history.

- Characterise all scales of backfolding, traversing from the upper portions of the nappe (e.g. Zermatt-Saas contact at val d'Ayas, Italy) to the lower portions of the nappe (Vanzone, Italy). Analysis from the upper portions of the large-scale backfold hinge, to the core of the backfold will provide a clearer framework when deciphering the mechanisms of backfolding.

Numerical models that simulate an entire geodynamic cycle have provided insights into the metamorphic evolution of the Western Alps. However, numerical models applied to the Western Alps have not been successful in capturing other large-scale, first order features including:

- Late Alpine backfolding. Numerical investigation into the geometrical relationships required to switch from subduction/nappe emplacement to backfolding kinematics may illuminate backfolding mechanisms.

- Late-stage Barrovian thermal event, i.e. the Lepontine Dome. Numerical models still do not have temperatures sufficiently high enough that match petrologically inspired late orogenic thermal isograds throughout the Alps.

Investigations into metamorphically recorded pressure variations within the Monte Rosa nappe, continue to highlight small volumes where contributions of tectonic pressure may play an important role, and that, on the scale of the orogen, tectonic pressure likely does not play a significant role. Research into the interplay between tectonics and metamorphism should continue to address the following questions:

- Scale of tectonic pressure? Grainscale, outcrop and nappe scale? Temporal scales?

- Kinetic factors during prograde P-T modelling? Extension of metamorphic assemblage diagrams that consider rate dependant parameters e.g. chemical affinity.

- Numerical modelling of coupled chemical and mechanical systems. Coupled two phase chemical-thermomechanical modelling of simple chemical systems (e.g. whiteschist genesis) could illuminate mechanisms such as chemically induced dynamic pressure. Investigations into the interplay between tectonic pressure generated via phase changes or by applied differential stresses.

- What other metamorphic terranes throughout the Earth could provide evidence for local tectonic pressure?

Bibliography

Chopin, C., Monié, P., 1984. A unique magnesiochloritoid-bearing, high-pressure assemblage from the monte rosa, western alps: petrologic and 40 ar-39 ar radiometric study. Contributions to Mineralogy and Petrology 87 (4), 388–398.

Gaidies, F., De Capitani, C., Abart, R., 2008. Theria_g: a software program to numerically model prograde garnet growth. Contributions to Mineralogy and Petrology 155 (5), 657–671.

Luisier, C., Baumgartner, L., Schmalholz, S. M., Siron, G., Vennemann, T., 2019. Metamorphic pressure variation in a coherent alpine nappe challenges lithostatic pressure paradigm. Nature communications 10 (1), 1–11.

Reddy, S., Wheeler, J., Cliff, R., 1999. The geometry and timing of orogenic extension: an example from the western italian alps. Journal of Metamorphic Geology 17, 573–590.

Reddy, S. M., Wheeler, J., Butler, R. W. H., Cliff, R. A., Freeman, S., Inger, S., Pickles, C., Kelley, S. P., 2003. Kinematic reworking and exhumation within the convergent alpine orogen. Tectonophysics 365 (1-4), 77–102.

Robyr, M., Darbellay, B., Baumgartner, L., 2014. Matrix-dependent garnet growth in polymetamorphic rocks of the sesia zone, italian alps. Journal of metamorphic geology 32 (1), 3–24.

Appendix: On backflow associated with oceanic and continental subduction

Evangelos Moulas[1], Mark T. Brandon[2], Joshua D. Vaughan-Hammon[3], Stefan M. Schmalholz[3]

[1]Institute of Geosciences Mainz Institute of Multiscale Modeling, Johannes-Gutenberg University, 55128 Mainz, Germany.

[2]Department of Earth and Planetary Sciences, Yale University, New Haven, CT 06511, USA.

[3]Institut des Sciences de la Terre, University of Lausanne, Lausanne, Switzerland.

On backflow associated with oceanic and continental subduction

Evangelos Moulas [1], Mark T. Brandon,[2] Joshua D. Vaughan Hammon [3] and
Stefan M. Schmalholz [3]

[1]*Institute of Geosciences & Mainz Institute of Multiscale Modeling (M³ODEL), Johannes-Gutenberg University,* 55128 *Mainz, Germany.*
E-mail: *evmoulas@uni-mainz.de*
[2]*Department of Earth and Planetary Sciences, Yale University, New Haven, CT* 06511, *USA*
[3]*Institut des sciences de la Terre, University of Lausanne,* 1015 *Lausanne, Switzerland*

SUMMARY

A popular idea is that accretion of sediment at a subduction zone commonly leads to the formation of a *subduction channel*, which is envisioned as a narrow zone located above a subducting plate and filled with vigorously circulating accreted sediment and exotic blocks. The circulation can be viewed as a forced convection, with downward flow in the lower part of the channel due to entrainment by the subducting plate, and a 'backflow' in the upper part of the channel. The backflow is often cited as an explanation for the exhumation of high-pressure/low-temperature metamorphic rocks from depths of 30 to 50 km. Previous analyses of this problem have mainly focused on the restricted case where the walls bounding the flow are artificially held fixed and rigid. A key question is if this configuration can be sustained on a geologically relevant timescale. We address this question using a coupled pair of corner flows. The *pro-corner* accounts for accretion and deformation directly above the subducting plate, and the *retro-corner* corresponds to a deformable region in the overlying plate. The two corners share a *medial boundary*, which is fully coupled but is otherwise free to rotate and deform. Our results indicate that the maintenance of a stable circulating flow in a narrow pro-corner ($<15°$) requires an unusually large viscosity ratio, $\mu_{\mathrm{retro}}/\mu_{\mathrm{pro}} > 10^3$. For lower viscosity ratios, the medial boundary would rotate rearwards, converting the initially narrow pro-corner into an obtuse geometry. For a stable narrow corner, we show that the backflow within the corner is caused by downward convergence of the incoming flow and an associated downward increase in dynamic pressure, which reaches a maximum at the corner point. The total pressure is thus expected to be much greater than predicted using a lithostatic gradient, which means that estimates of depth from metamorphic pressure would have to be adjusted accordingly. In addition, we show that the velocity fields associated with a forced corner flow and a buoyancy-assisted channel flow are nearly identical. As such, structural geology studies are not sufficient to distinguish between these two processes.

Key words: Numerical approximations and analysis; Numerical modelling; Continental margins: convergent; Dynamics of lithosphere and mantle; Subduction zone processes.

1 INTRODUCTION

1.1 Subduction, mélanges and channel flow

The modern Earth has about 92 000 km of convergent-plate boundaries (Bird 2003). About 56 per cent of that length involves subduction of oceanic lithosphere and about 25 per cent of that length involves subduction of continental lithosphere. Continental subduction was first proposed by Ampferer & Hammer (1911) and Argand (1916, 1924) for the Alps and the Himalaya. The idea was greatly expanded during the middle 1900s with the discovery of

Wadati–Benioff zones, indicating large-scale subduction of oceanic lithosphere. We start with this history because we find it useful to use the term *subduction zone* in a generic sense to indicate a lithosphere-scale boundary where one plate is carried beneath another, regardless of the composition of the subducting plate.

A subduction zone must start with the formation of a sharp fault boundary. The subducting plate commonly includes a sedimentary cover, which can have a thickness ranging from 0 to 10 km. If present, part or all of the sedimentary cover can be carried deep into the subduction boundary. There has been much research, speculation, and debate about the deformation that occurs within this

boundary zone. Some authors favor a view that the deformation occurs mainly by thrust imbrication, and others argue for a more mobile and chaotic style of deformation, as represented by the term *mélange* (e.g. Ring & Brandon 1999; Krohe 2017). We expand on this topic because the idea of tectonic mixing has long been a motivating factor for the idea of a channel flow associated with subduction.

A mélange is a regional-scale mappable body, characterized by a chaotic block-and-matrix structure (Cowan 1985). In some cases, the blocks can be shown to be 'exotic', in that they were introduced into the matrix during the formation of the mélange. The classic example is the mudstone-matrix mélanges of the Franciscan Complex, which locally contain blueschists and eclogites with metamorphic pressure up to ∼1.5 GPa (Wakabayashi 2015).

There has been a long debate about the origin of this deformational style. Starting in the 1970s, many geologists considered mélanges to be a distinctive and diagnostic feature of deformation within an active subduction zone. Many mélanges display a scaly foliation, which has been taken as evidence that the mixing process was associated with shearing. High pore-fluid pressures are commonly invoked as well to account for the pervasive and fluid-like mixing observed in most mélanges. It is useful to note that scientific drilling at modern subduction zones has yet to find an actively forming tectonic mélange (Lundberg & Moore 1986). Perhaps this discovery will require drilling to much greater depths than is currently possible.

An alternative interpretation is that the chaotic and highly mixed structure observed in mélanges was formed by mass wasting in the surface environment, rather than by tectonic processes at depth. Improvements in seafloor imaging over the last several decades have lead to the recognition that mass wasting is common at subduction zones, due to the tectonically oversteepened topography above the subduction thrust (e.g. Claussmann *et al.* 2021). Mass-wasting deposits are known to commonly accumulate in trench basins and thus should be expected to be part of the sedimentary cover that is carried into the subduction zone. Relevant near-modern examples of subducted mass-wasting deposits include the Lichi mélange of Taiwan (Page & Suppe 1981; Chang *et al.* 2001) and the Argille Scagliose of the northern Apennines in Italy (Camerlengi & Pini 2009).

We introduce here a modified corner-flow solution, which provides a generalized framework for assessing the mechanics and evolution of a narrow shear zone filled with a weak material. However, we make no assumptions about the possibility of chaotic mixing within the zone.

1.2 Corner flow

Our study is motivated by the original corner flow model of Cloos (1982, 1984), which was proposed as an explanation for the co-occurrence of mélange and exotic high-pressure/low-temperature (HP/LT) blocks in the Franciscan Complex of California. Cloos envisioned that much of the Franciscan was 'processed' by flow within a narrow angular region, with an opening angle of about 15°, which tapers down to a corner point located at a depth of about 40 km (Fig. 1a). In his original work, Cloos (1982) coined the term 'flow mélange' to emphasize the mixing that might occur within a narrow corner flow. In that original model, the upper boundary of the proposed corner region is held fixed, and the lower boundary is assigned a downward velocity oriented parallel to the boundary and equal to the velocity of the subducting plate.

Our focus here is to investigate the mechanical conditions and the long-term stability of flow in corner regions. The *corner flow* problem is one of the few cases in fluid dynamics where the flow field can be fully specified in analytical form, in terms of velocity, stress, and pressure. Fig. 1 illustrates tectonic settings that are amenable to analysis using the corner flow solution. Many applications have emphasized the velocity field but we show the significance of the pressure and stress field as well. Given Cloos' boundary conditions (1982; see also Fig. 1a), the material in the lower part of the corner is entrained downward with the subducting plate, but the convergence of flow within the narrow corner causes the flow to reverse and ascend within the upper part of the corner. Cloos (1982, 1984) argued that this *backflow* was responsible for carrying HP/LT metamorphic blocks of the Franciscan Complex back to the surface. As a result, Cloos (1982, 1984) viewed Franciscan mélanges to be diagnostic of the mixing associated with corner flow.

England & Holland (1979) had already proposed a similar model for the exhumation of HP/LT metamorphic rocks in the Austrian Alps. Their model involved a channel parallel to the subducting plate and extending to depths of ∼50 km, where the Austrian eclogites were thought to have originated. The low-density materials inside the channel are entrained downward with the subducting plate, which results in backflow within the upper part of the channel caused by positive buoyancy relative to the surrounding crust and mantle. In contrast, the backflow associated with the classic corner flow model is entirely driven by boundary velocities and buoyancy effects are notably ignored.

Shreve & Cloos (1986) and Cloos & Shreve (1988a,b) modified the original corner flow idea to account for a more arbitrary channel/corner geometry, and to include buoyancy forces as well. The term *subduction channel* was coined by Cloos & Shreve (1988a,b), and that term is now widely used in the literature. More recent studies have considered the effects of inclined and/or deformable walls (Mancktelow 1995; Raimbourg & Kimura 2008). Our analysis includes these possibilities.

The concept of a subduction channel was further advanced by numerical modeling. In particular, Gerya *et al.* (2002) created a detailed simulation of a narrow channel with a circulating flow, extending to depths of ∼50 km and in some cases even 100 km. The internal geometry and rheologies used in their study were selected to match a 'consensus view' of what a subduction zone might look like. The two-way flow was once again envisioned as a possible mechanism for returning HP/LT metamorphic rocks back to the surface. Their simulations included cases where the flow field developed local vortices, but this result was not an emergent feature of the simulation, but instead was imposed by placement of a large re-entrant into the upper boundary of the channel.

As highlighted by Mancktelow (1995), the subduction-channel model can be viewed as a corner flow with a very narrow opening angle. At the other extreme, the wedge models of Cowan & Silling (1978), Willett *et al.* (1993), Beaumont & Quinlan (1994) and Jamieson & Beaumont (2013) can be viewed as corner flows with very large opening angles. Cowan & Silling (1978) demonstrated this point by showing the similarity of the velocity field observed in their scaled analogue model of a wedge with a 90° corner geometry, and that for a corner flow with the same velocity boundaries and a 90° geometry.

We consider the corner-flow solution as providing a general mechanical representation of a wide range of models, from channels, narrow corners and wide wedges. Our analysis here is based on two-corner flows that are coupled across a common medial boundary

(a) Narrow Subduction-Corner Flow

20 km

(b) Wide Subduction-Corner Flow

20 km

(c) Mantle Corner Flows

100 km

(d) Mid-Ocean Ridge Corner Flows

20 km
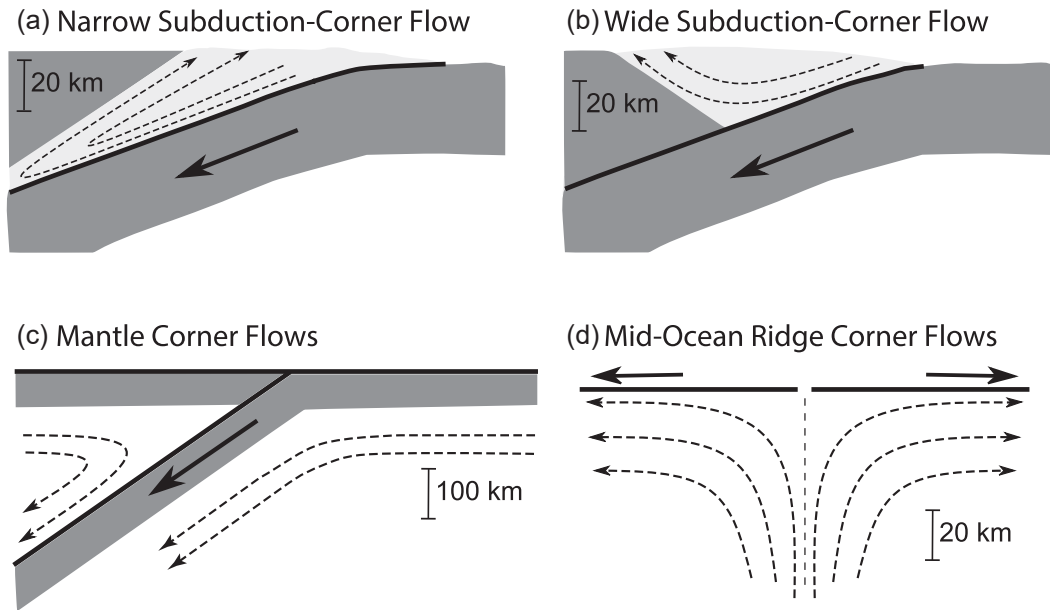
Figure 1. Schematic geometries that illustrate the essential parts of various corner-flow models (modified after Tovish *et al.* 1978; Cloos 1982; Spiegelman & McKenzie 1987; Willett *et al.* 1993). The dark grey regions depict rigid plates. The dashed arrows indicate flow lines. The scales are approximate and the sections have no vertical exaggeration.

(Fig. 2). The *pro-corner* is equivalent to the channel/corner discussed above. The *retro-corner* lies rearward of the pro-corner, and corresponds to what many authors would call the 'upper plate'. Note however that the introduction of a retro-corner allows this 'upper plate' region to deform if the loads become large enough. The pro- and retro-corners have different viscosities, as represented by μ_1 and μ_2, respectively. Following the notation as shown in Fig. 2, the corner point is designated by an 'S', which highlights the fact that the boundary conditions are the same as the S-point boundary condition introduced by Willett *et al.* (1993), and Beaumont & Quinlan (1994). Following their convention, the retro-boundary is assigned to the Moho in the overriding plate. This decision accounts for the fact that the upper-plate mantle that underlies this boundary should be much stronger (higher viscosity) than the overlying crust. Thus θ_2 is set to 150°, which implies that the subducting plate dips at 30° relative to a horizontal upper-plate Moho. The pro- and retro-boundaries are held fixed in space, and are assigned uniform velocities $\vec{V}_0$ and $\vec{V}_2$ (Fig. 2). For the analysis here, the retro-boundary is assigned a zero velocity ($\vec{V}_2 = \vec{0}$, i.e. no slip on the boundary), but the retro-corner is otherwise free to deform internally. The velocities are all specified relative to a fixed corner (S-point fixed reference frame). The velocity on the pro-boundary accounts for entrainment and basal accretion, as represented by the radial and circumferential components of $\vec{V}_0$ relative to the pro-boundary. For simplicity, we focus exclusively on the case of entrainment, which means that $\vec{V}_0$ is parallel to the pro-boundary and $|\vec{V}_0| = -U$.

In previous corner-flow models, the parameter U was often assumed to be equal to the velocity of the subducting plate, but this assumption overlooks the fact that discrete slip on the subduction thrust accounts for much of the subduction velocity. For the Cascadia subduction zone, Pazzaglia & Brandon (2001) showed that the long-term velocities at the base of the Cascadia wedge in Washington State are about an order of magnitude smaller than the subduction velocity. Thus, for a typical subduction velocity of ~50 mm a^{-1}, we might expect an entrainment velocity $U \approx 5$ mm a^{-1}. Note that

if the pro-boundary were fully decoupled from the subducting plate, then $U = 0$ and there would be no flow within the pro-corner.

1.3 Organization of the paper

The paper is organized into three parts. The first part reviews solutions for a single corner (Section 2.1) and shows the derivation of an analytical solution for coupled corner flows (Section 2.2). In addition, we describe a numerical method that we use for comparison with the analytical approach (Section 2.3). In the second part (Sections 3.1 and 3.2), we present results from the analytical two-corner solution to assess the conditions necessary for maintenance of a stable corner geometry. We focus on the backflow, as this part of the flow field is thought to be important for exhumation of HP/LT rocks. Our results show that, for narrow corners where the backflow is strongest, the dynamic pressure within the corner is typically of the same order as the lithostatic pressure. The third part uses numerical results (Section 3.3) to understand the rate at which the pro-corner evolves towards a stable geometry. We finish with a discussion regarding the implications of our results for structural and metamorphic studies of subduction zones.

2 METHODS

2.1 Analytical solutions for corner flow in geodynamics

Analytical models provide a way to reduce a problem to a simpler form and a smaller set of controlling variables (e.g. Fletcher 1977; Emerman & Turcotte 1983; Medvedev 2002; Schmalholz 2011; Ribe & Xu 2020). Corner-flow solutions have been widely used in geodynamics, with applications to orogenic wedges (Figs 1a and b; Cowan & Silling 1978; Cloos 1982), and for the study of mantle flow associated with subduction (Fig. 1c; Stevenson & Turner 1977; Tovish *et al.* 1978), spreading centers (Fig. 1d; McKenzie 1969; Spiegelman & McKenzie 1987), and backarc spreading (Ribe 1989).
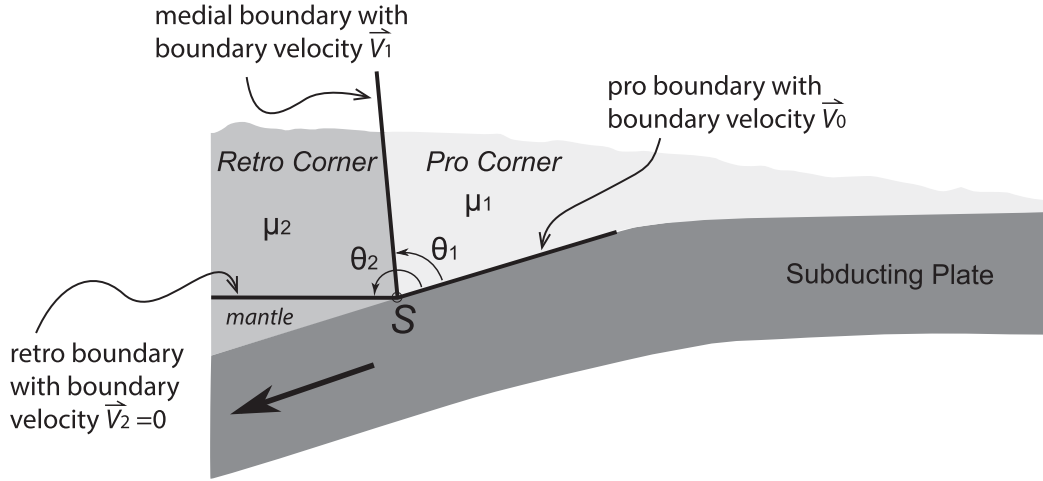
Figure 2. Schematic illustration of two coupled corner flows. The pro-corner is equivalent to the 'subduction corner' or 'subduction channel' considered in previous models. The retro-corner represents a deformable region within the overriding plate. This configuration allows us to test the long-term stability of the pro-corner. The pro-and retro-corners are assigned different viscosities μ_1 and μ_2, respectively, where $\mu_2 > \mu_1$.

In our opinion, Batchelor (1967), Dean & Montagnon (1949), McKenzie (1969) and Moffatt (1964) provide good introductions to this topic. These papers generally focus on the simple case where the material in the corner has a uniform viscosity, and one of the boundaries has uniform cirumferential velocity and the other boundary is stationary. However, the corner-flow problem has been extended to include more complex boundary conditions (Moffatt 1964; Sprittles & Shikhmurzaev 2011), more complex configurations (coupled corner flows: Anderson & Davis 1993; leaky corner: Rieder & Schneider 1983) and nonlinear rheologies (Tovish *et al.* 1978; Riedler & Schneider 1983; Henriksen & Hassager 1989; Ribe 2015, 2018). This last development is important because it has shown that the kinematics of a corner flow are relatively insensitive to the specifics of the rheology. In fact, the assumption of constant viscosity is common invoked in studies of subduction zones, shear zones, wedges, glaciers, and mantle convection (e.g. McKenzie 1969; Spiegelman & McKenzie 1987; England & Wilkins 2004; Pollard & Fletcher 2005; Moulas *et al.* 2014). Based on this background, we too have decided that constant viscosity is an appropriate approximation for a first-order analysis of corner flow. Of course, numerical methods allow the use of more realistic rheologies, and this capability may be useful for situations where simulations can be directly compared with observations.

2.2 Analytical solution for the two-corner region

Herein, we develop a two-corner solution for our analysis of corner flow in subduction zones. Anderson & Davis (1993) provide a general development of two-corner solutions as relevant to fluid dynamics.

The stream function ψ provides a method for setting up a general solution for a slow incompressible viscous flow (i.e. Stokes flow) in a single corner. The stream function can be written in polar coordinates as

$$\psi\,(r,\theta) = r\,f\,(\theta),\tag{1}$$

where r is the radial coordinate and θ is the angular coordinate relative to the corner point. The function $f(\theta)$ is selected so that the stream function satisfies the biharmonic equation, $\nabla^4\psi\,(r,\theta) = 0$, which ensures a full solution for velocities and stresses inside the corner region and extending to $r = +\infty$. For the classic corner-flow

solution with kinematic boupdary conditions, the angular function in eq. (1) has the general form

$$f\,(\theta) = A\cos{(\theta)} + B\sin{(\theta)} + C\theta\cos{(\theta)} + D\theta\sin{(\theta)}.\tag{2}$$

The constants A, B, C, D are determined by setting constant velocities on each of the two boundaries of the corner, located at θ_0 and θ_1. The two velocity components for each of the two boundaries means that there are four boundary equations, which are solved to get the four unknown constants A, B, C, D. Velocities and stress components for the flow field inside the corner are obtained by differentiation of the stream function (c.f., McKenzie 1969, p. 15–16). The radial V_r and circumferential V_θ components of the velocities are given by

$$V_r = \frac{1}{r}\frac{\partial\psi}{\partial\theta},\ V_\theta = -\frac{\partial\psi}{\partial r},\tag{3}$$

where a positive radial velocity indicates motion outward from the corner, and a positive circumferential velocity indicates a counterclockwise motion.

The components of the deviatoric stress tensor τ_{ij} in polar coordinates are given by

$$\tau_{rr} = 2\mu_k\frac{\partial V_r}{\partial r},\tag{4a}$$

$$\tau_{\theta\theta} = 2\mu_k\left(\frac{1}{r}\frac{\partial V_\theta}{\partial\theta} + \frac{V_r}{r}\right),\tag{4b}$$

and

$$\tau_{r\theta} = \mu_k\left(\frac{1}{r}\frac{\partial V_r}{\partial\theta} + \frac{\partial V_\theta}{\partial r} - \frac{V_\theta}{r}\right),\tag{4c}$$

where μ_k is the dynamic viscosity and the subscript k is used to designate between two corners. For the single corner case discussed here, $k = 1$.

The radial symmetry of the corner flow indicates that normal deviatoric stresses, τ_{rr} and $\tau_{\theta\theta}$, are identically zero, which means that $\tau_{r\theta}$ is the only non-zero component of the deviatoric stress tensor (McKenzie 1969, p. 15; Tovish *et al.* 1978). The total stress tensor σ_{ij} is related to the deviatoric stress tensor τ_{ij} by

$$\sigma_{ij} = -P\delta_{ij} + \tau_{ij},\tag{5}$$

which indicates that the total pressure P is equal to the negative mean stress (δ_{ij} is the Kronecker delta). The total pressure P is the
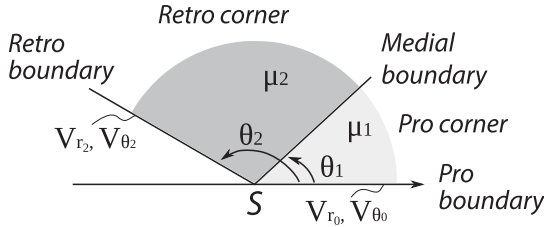
Figure 3. Convention used the for two-corner flow problem. The corner regions require specification of uniform velocity components (V_r, V_θ) in the radial and circumferential directions for each boundary.

sum of the static pressure P_s, which is defined as the pressure in the static state (i.e. zero flow), and the dynamic pressure P_d, which is associated with an active flow. In geodynamics, $P_s = \rho g z$ where ρ is the density, g is the gravitational acceleration, and z is depth relative to the Earth's surface. Small corrections to this formula apply in the case where the material is compressible and where the pressure at the surface is not exactly zero (e.g. Moulas *et al.* 2019). Note that the corner-flow solution is dependent on P_d, but is entirely independent on P_s. The dynamic pressure P_d is determined by integrating the following stress-equilibrium equation,

$$-\frac{\partial P_d}{\partial r} + \frac{1}{r}\frac{\partial \tau_{r\theta}}{\partial \theta} = 0, \tag{6}$$

in the radial direction (e.g. Tovish *et al.* 1978).

Our discussion of results is assisted by normalizing (or 'non-dimensionalizing') field variables relative to characteristic values for the subduction problem. Velocities are normalized by the entrainment velocity at the base of a typical accreting subduction wedge, which we estimate to be $U_c \approx 5$ mm a^{-1}. Note that the radial velocity component, V_{r_0}, at the base of the pro-corner becomes $V_{r_0}/U_c = -1$ when converted into a non-dimensional form. The negative indicates that entrainment draws material downwards to the corner point. Given the radial geometry of the corner-flow problem, there is no characteristic length-scale. Thus, we select a length-scale, $L_c = 10$ km, that is representative of the region of interest adjacent to the corner point. A characteristic timescale for flow in the vicinity of the corner point is given by $t_c = L_c/U_c = 2$ Ma. The characteristic viscosity is set to $\mu_c = 10^{19}$ Pa s, which is about 100 time less than the viscosity of the upper mantle ($\sim 10^{21}$ Pa s). All stresses and pressure are normalized by the characteristic viscous shear stress, which is defined by $\tau_c = \mu_c U_c/L_c \approx 0.16$ MPa. Note that the solution for the velocity field in a corner flow problem does not require specification of a viscosity. Viscosity is only needed when calculating stresses and pressure. In addition, the non-dimensional approach ensures that our stress and pressures are only sensitive to the relative variation in viscosity, not the absolute values.

The two-corner problem (Fig. 3) is solved using two coupled stream functions,

$$\psi_k (r, \theta) = r (A_k \cos(\theta) + B_k \sin(\theta) + C_k \theta \cos(\theta) + D_k \theta \cos(\theta)), \tag{7}$$

where the subscript $k = 1, 2$, representing the pro- and retro-corners, respectively. The paired stream functions now contain eight unknown constants, A_k, B_k, C_k, D_k with k accounting for the two corners. The boundary conditions provide eight equations, which are used to solve for these constants. Four of these equations are:

$$V_r (r, \theta_0) = V_{r_0}, \tag{8a}$$

$$V_\theta (r, \theta_0) = V_{\theta_0}, \tag{8b}$$

$$V_r (r, \theta_2) = V_{r_2}, \tag{8c}$$

and

$$V_\theta (r, \theta_2) = V_{\theta_2}. \tag{8d}$$

For the remaining four equations, we consider the continuity of velocity and traction along the medial boundary, $\theta = \theta_1$. However, since $\tau_{rr} = \tau_{\theta\theta} = 0$, the total stress components normal to the medial boundary are equal to P_d. Therefore, the continuity of velocity and the stress balance at the medial boundary provides the remaining four equations, and they reduce to

$$V_r(r, \theta_1)^{\text{retro}} = V_r(r, \theta_1)^{\text{pro}}, \tag{9a}$$

$$V_\theta(r, \theta_1)^{\text{retro}} = V_\theta(r, \theta_1)^{\text{pro}}, \tag{9b}$$

$$P_d(r, \theta_1)^{\text{retro}} = P_d(r, \theta_1)^{\text{pro}}, \tag{9c}$$

and

$$\tau_{r\theta}(r, \theta_1)^{\text{retro}} = \tau_{r\theta}(r, \theta_1)^{\text{pro}}. \tag{9d}$$

The medial boundary is marked by a discontinuity in viscosity, and typically this would cause a discontinuity in the P_d field. However, the derivation above shows that the two-corner problem is special in that the P_d field is continuous across the medial boundary, as concluded by eq. (9c).

The polar velocity coordinates can be converted into Cartesian coordinates using the following transformation:

$$V_x = V_r \cos(\theta) - V_\theta \sin(\theta), \tag{10a}$$

and

$$V_y = V_r \sin(\theta) + V_\theta \cos(\theta), \tag{10b}$$

where x and y are oriented at $\theta = 0°$ and $90°$, respectively.

The electronic supplement contains a computer-algebra (wxMaxima) script that was used to find the analytical solution for the eight unknown constants, and two MATLAB programs that were used to calculate and visualize the full analytical solution.

2.3 Numerical calculations

We compare our analytical two-corner solution with numerical solutions produced by the open-source finite-difference code M2Di (Räss *et al.* 2017), which solves the incompressible Stokes equations using finite difference on a staggered grid. M2Di has been extensively benchmarked and tested for problems that involve viscosity discontinuities, folding/necking instabilities, and general geodynamic calculations (Schmid & Podladchikov 2003; Adamuszek *et al.* 2016).

One common problem with numerical modeling is the inability of the mesh to remain conformal with material interfaces, which causes discretization errors. This problem can be treated by increasing the grid resolution as shown in Fig. 4(a). In addition, we have added a semi-Lagrangian, backward-characteristic method (*cf.* Beuchert & Podladchikov 2010) to M2Di to ensure better performance with advection of material. This approach has been tested in cases of folding in the presence of heterogeneities for large strains (Moulas & Schmalholz 2020).

The numerical solutions were run with the two-corner problem set to $\theta_2 = 180°$, which provides an easier geometry for implementing the boundary conditions. Fig. 4 shows benchmark comparisons of the numerical solutions. For these cases, we used a square domain and applied boundary velocities determined from the analytical solution. Figs 4(b) and (c) shows that the P_d field calculated by the
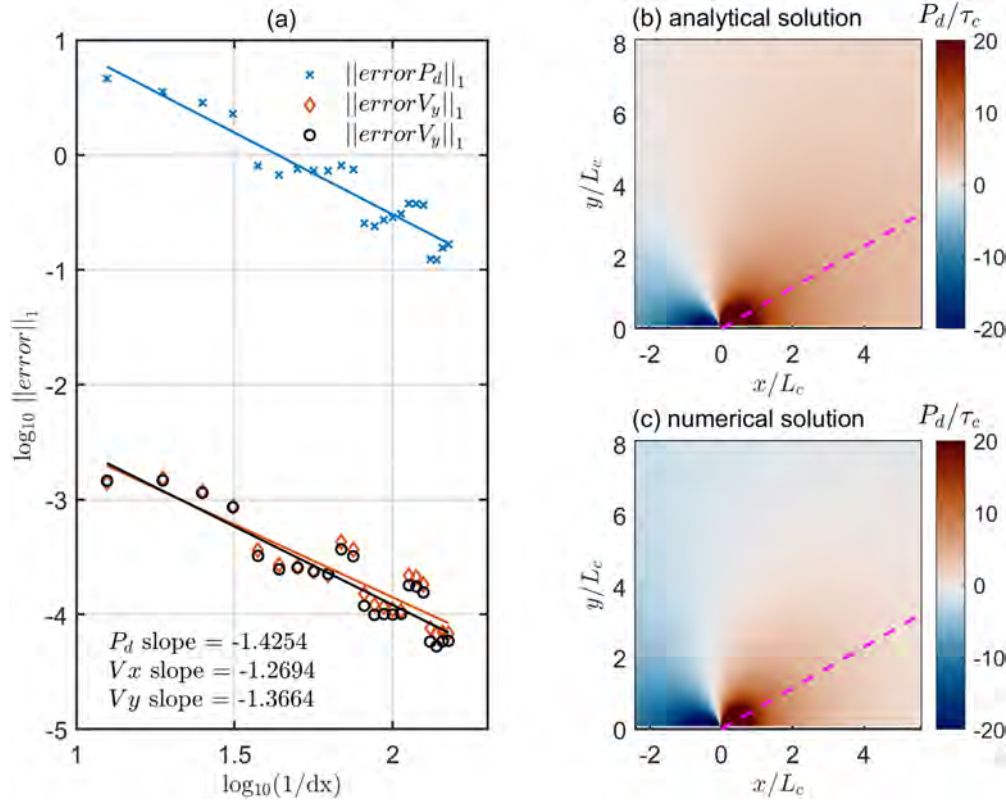
Figure 4. Comparison of analytical and numerical solutions for a pro-corner with opening angle of 30° and $\frac{\mu_2}{\mu_1} = 10^3$. The remaining parameters are $\theta_0 = 0$, $\theta_2 = 180°$, $V_{r_0} = -1$, $V_{\theta_0} = 0$, $V_{r_2} = 0$, $V_{\theta_2} = 0$. (a) Error for dynamic pressure P_d, and the horizontal V_x and the vertical V_y velocity components plotted as a function of the uniform grid increment $(1/dx)$. The solid lines indicate linear fits to the actual numerical results (indicated by symbols) and they show that the results are ~1 order of magnitude more precise for an order of magnitude greater spatial resolution. The error is the average of the absolute difference between the analytical and the numerical solutions for the square domain shown in the right panels. See Duretz *et al.* (2011) and Räss *et al.* (2017) for more details about error analysis. Comparison of (b) analytical and (c) numerical solutions show that the P_d fields around the corner are match closely and are continuous across the medial boundary, which is indicated by the magenta dashed line.

numerical method is very similar to that given by the analytical solution. Other observations that support the success of the numerical method are that the P_d field is continuous across the medial boundary, as required by eq. (9c), and varies smoothly around the corner point, which is a singularity and thus a potential source of numerical instability.

Later in the paper, we use the numerical method to evaluate the time evolution of the medial boundary. For those cases, the numerical domain is rectangular, with free-slip conditions for all sides except for the bottom side ($y = 0$) where a Dirichlet condition is used, with a constant horizontal velocity used for $x > 0$ and zero horizontal velocity for $x \leq 0$, and zero vertical velocity for all x.

3 RESULTS

3.1 Flow patterns as a function of geometry and viscosity ratio

The predicted flow pattern is fully defined by the location of the pro, medial and retro boundaries at θ_0, θ_1, θ_2; the boundary velocity components V_{r_0}, V_{θ_0}, V_{r_2}, V_{θ_2}; and the viscosity ratio between the two regions μ_2/μ_1. For the subduction problem, all of the boundary velocity components are set to zero, except for $V_{r_0} = -U$, which accounts for entrainment above the subduction thrust (Fig. 2). The geometry of the subduction zone relative to the upper-plate Moho

is set to $\theta_2 = 150°$ (i.e. a subduction zone with a 30° dip passing beneath a flat upper-plate Moho). We now consider how the velocity field changes as a function of the orientation of the medial boundary, and the viscosity ratio, over the range $\mu_2/\mu_1 = 1$ to 10^3 (Figs 5–7).

We start with the case where the pro-corner has an acute opening angle ($\theta_1 = 30°$) with μ_2/μ_1 increasing from 1 to 10^3. (Note that $\mu_2/\mu_1 = 1$ is equivalent to a solution for a single corner, given that $\mu_2 = \mu_1$.) The resulting velocity fields show a gradual transition from a single obtuse corner flow when $\mu_2/\mu_1 = 1$ (Fig. 5a) to a single acute corner flow as $\mu_2/\mu_1 \rightarrow \infty$ (Fig. 5d). However, when μ_2/μ_1 is small, the velocity vectors adjacent to the medial boundary are generally oblique to that boundary, which means that the boundary will migrate rearward with time. In turn, Fig. 5(d) shows that when μ_2/μ_1 is sufficient large, the medial boundary becomes approximately stable, in that the flow no longer crosses the medial boundary. This simple observation leads to one of our main conclusions, that an acute pro-corner can only be sustained when there is a very large viscosity ratio, such as $\mu_2/\mu_1 > 1000$. For comparison, consider that the viscosity ratio for a subducting slab relative to the upper mantle is estimated to be less than 1000, and most likely in the range of 100–300 (Schellart 2008).

We now consider the case (Fig. 6) where the pro-corner has an obtuse opening angle ($\theta_1 = 130°$). The examples show the same range in μ_2/μ_1, from 1 to 10^3. Note that for the smallest viscosity ratio (Fig. 6a), the velocities decrease to very small values
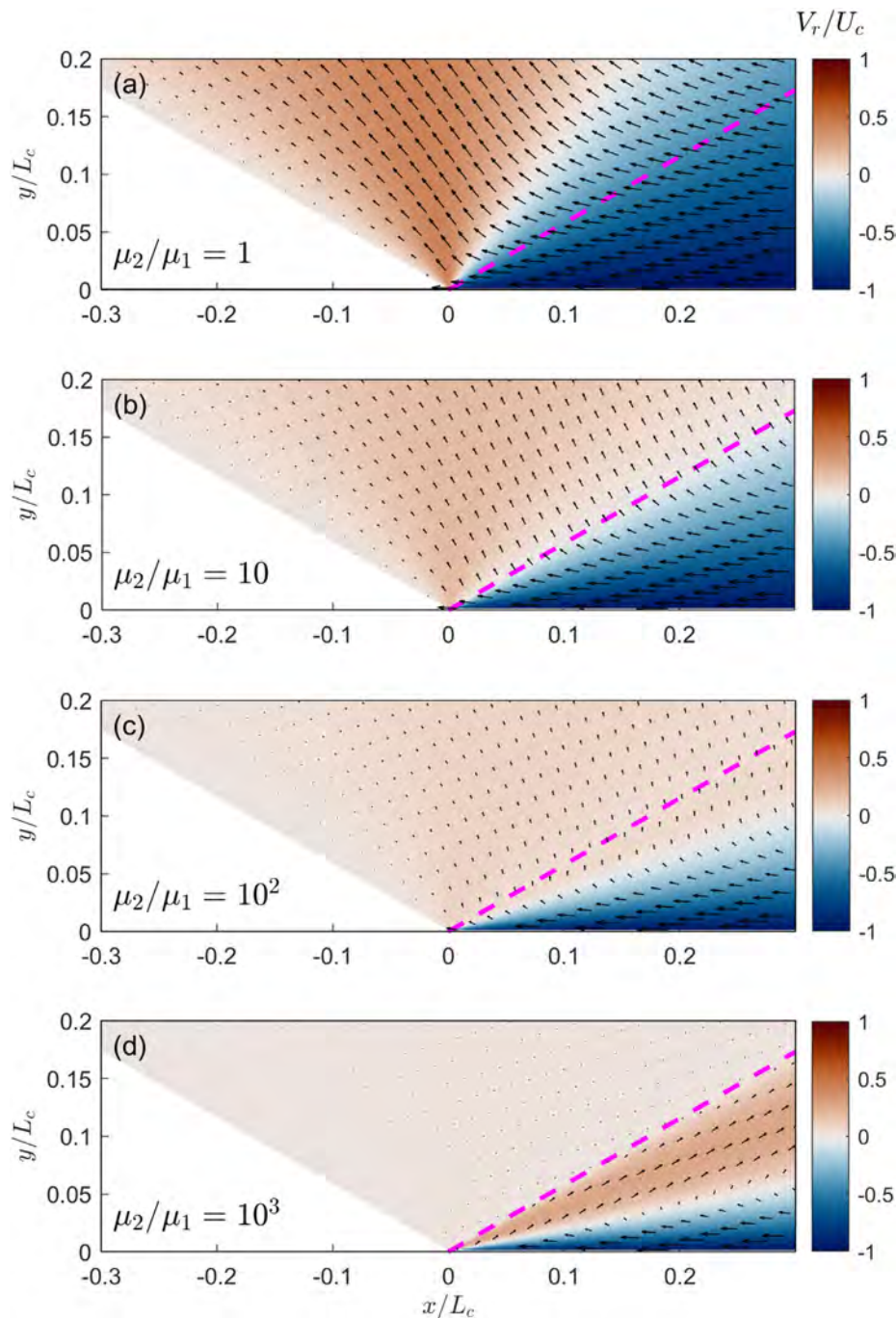
Figure 5. Velocity fields for a two-corner flow with $\theta_1 = 30°$ and $\theta_2 = 150°$, and with different viscosity ratios μ_2/μ_1, ranging from 1 to 10^3. The medial boundary is marked by a magenta dashed line. The grid of arrows shows the velocity field, and the colour map shows the magnitude of the radial velocity component, with positive values indicating flow away from the corner.

adjacent to the retro-boundary, but they are sufficient to cause the medial boundary to slowly migrate rearward with time. For all of the remaining examples, the velocity vectors adjacent to the medial boundary are zero or subparallel to that boundary, so the boundary is stable.

Fig. 7 shows examples for a very narrow pro-corner, where $\theta_1 = 10°$. The first example (Fig. 7a) shows that pro-corner is unstable even with a very large viscosity ratio $\mu_2/\mu_1 = 10^3$. Also note that there is no backflow in this example. Instead, the high dynamic pressure inside the corner causes the medial boundary to migrate rearward. Fig. 7(b) shows that a viscosity ratio of $\mu_2/\mu_1 > 10^4$ is

able to maintain a stable pro-corner for this case. Thus, our overall conclusions from these examples are: 1) a stable pro-corner requires either a large viscosity ratio or an obtuse opening angle, and 2) backflow only occurs in a pro-corner with an acute opening angle and a very strong retro corner.

3.2 Dynamic pressure

One of the features of the analytical solution for the corner flow is the prediction of large dynamic pressure in the vicinity of the corner point. The dynamic pressure for the two-corner problem is given
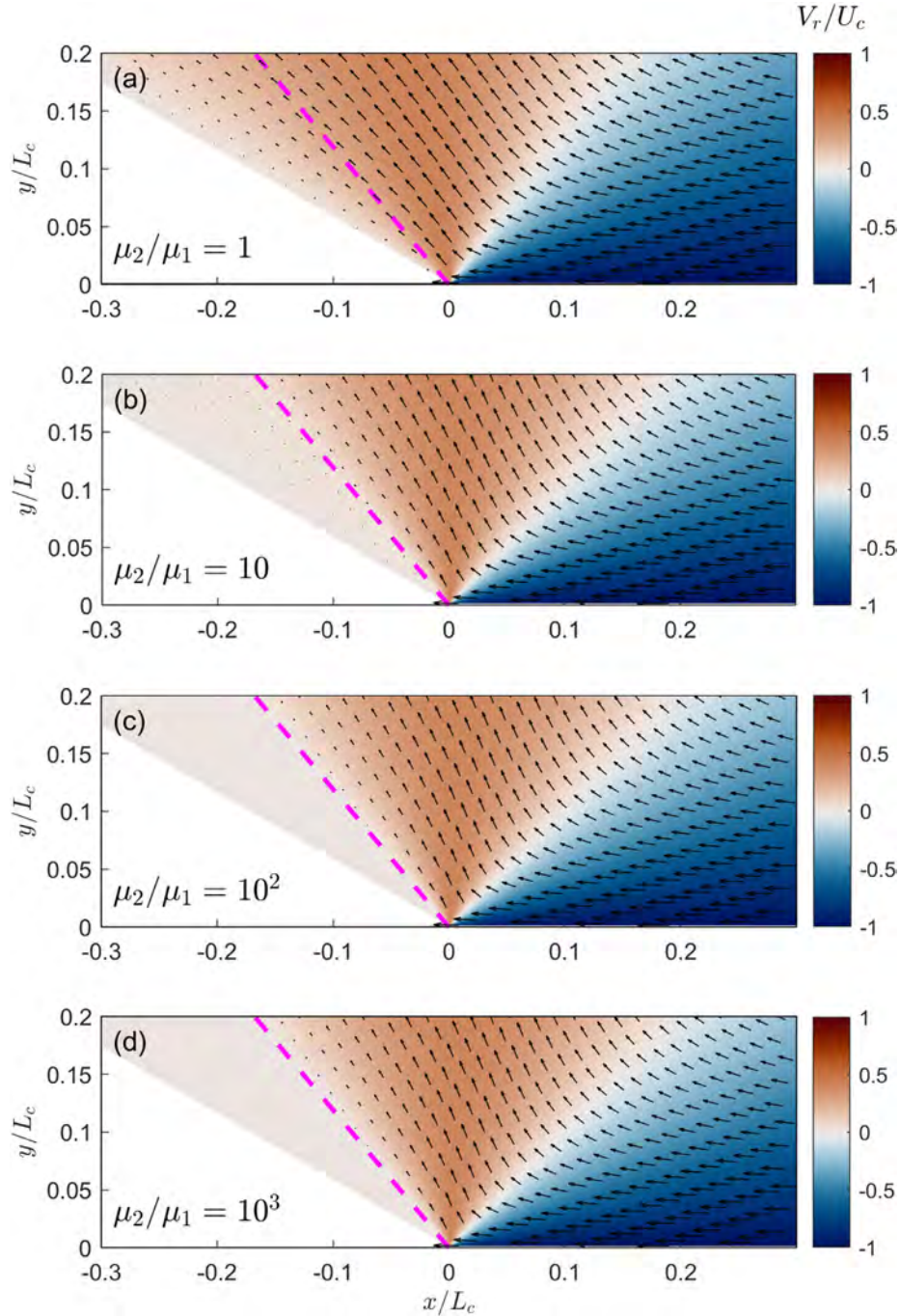
Figure 6. Velocity fields for a two-corner flow with $\theta_1 = 130°$ and $\theta_2 = 150°$. See Fig. 5 for further details.

by

$$P_d^k / \tau_c = 2 \left(\frac{\mu_k}{\mu_1} \right) \frac{C_k \cos(\theta) + D_k \sin(\theta)}{r/L_c}, \qquad (11)$$

where k indicates the corner domain. Fig. 8 shows P_d fields for an acute pro-corner, with μ_2/μ_1 varying from 1 to 10^3. Note that P_d is continuous across the medial boundary, as required by eq. 9c. Numerical simulations by van Keken *et al.* (2008) indicate that for a single narrow corner with rigid walls, the high in P_d is centered on the corner, and can reach values of 100 MPa. For our two-corner solutions, we find that the P_d high is influenced by the viscosity ratio. In all examples, the P_d high is offset rearward relative to the symmetric arrangement reported by van Keken *et al.* (2008).

The largest offset is found for the first example (Fig. 8a), which is equivalent to a single obtuse corner given that $\mu_2/\mu_1 = 1$, and the offset decreases with increasing μ_2/μ_1. We speculate that it would become increasingly symmetric within an acute pro-corner as $\mu_2/\mu_1 \to \infty$, which approximates the case considered by van Keken *et al.* (2008).

Fig. 9(a) shows P_d in the pro-corner as a function of the radial distance along a section that follows the bisector of the pro-corner. Fig. 9(b) shows P_d at a fixed radial distance, $r/L_c = 1$ along the medial boundary, and as a function of varying pro-corner angles, θ_1. These plots show that within a specific two-corner problem, P_d increases with decreasing r/L_c, and reaches a maximum at the corner point. And when considered as a function of configuration,
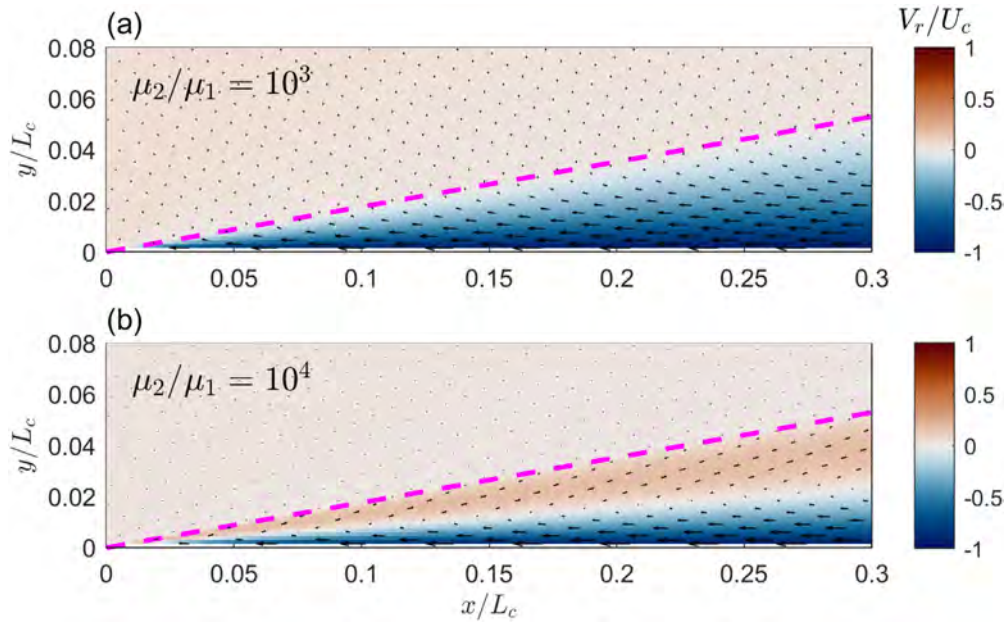
Figure 7. Velocity fields for a two-corner flow with $\theta_1 = 10°$ and $\theta_2 = 150°$ for viscosity ratios μ_2/μ_1 equal to 10^3 (a) and 10^4 (b). See Fig. 5 for further details.
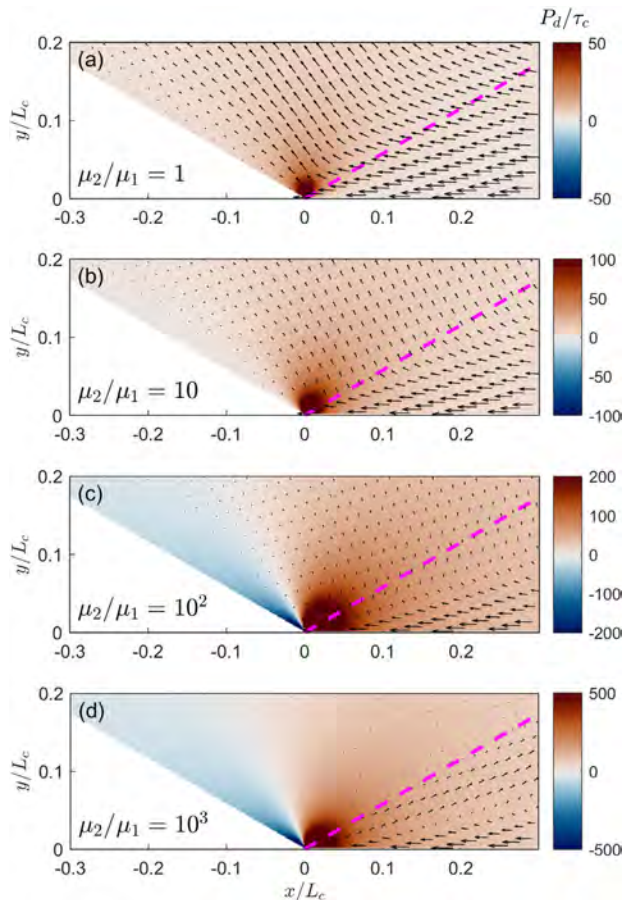
Figure 8. Dynamic pressure P_d field for a two-corner flow. The value of dynamic pressure has been normalized to the characteristic stress (τ_c). See Fig. 5 for further details.

the overall magnitude of P_d increases with increasing μ_2/μ_1 or with decreasing θ_1.

3.3 Maintaining the corner geometry

A consequence of the analytical solution of the two-corner region (eqs 1–3) is that the circumferential velocity V_θ (i.e. normal to the radial direction) only depends on θ and otherwise remains constant as a function of r. This situation means that the motion of material points along a specified direction, θ, will include a rotation around the corner point that decreases in rate with increasing r (i.e. $\omega = V_\theta/r$ where $V_\theta(\theta) = $ constant).

This feature of the analytical solution indicates that there will always be some circumferential shearing of the medial boundary. More specifically, V_θ at the medial boundary will increase with decreasing μ_2/μ_1 or decreasing θ_1. As V_θ increases, so does the rearward migration and distortion of the medial boundary. In other words, increasing values of V_θ for the medial boundary indicate increasing instability for the pro-corner.

This conclusion is supported by numerical simulations in Fig. 10, which show the effect of this circumferential shearing after about $2t_c \approx 4$ Ma of flow (assuming characteristic values for U_c and L_c). The left and right set of examples are for acute pro-corners that start with opening angles $\theta_1 = 30°$ and $10°$, respectively. All of the examples show various developments of a large rearward-directed bulge in the medial boundary near the corner point. The examples show that pro-corner becomes more stable with an increasing viscosity ratio or an increasing opening angle.

Fig. 11 shows the normalized circumferential velocity, V_θ/U_c, as a function of θ_1 and μ_2/μ_1, as determined from our two-corner analytical solution. The plot summarizes the conditions required to maintain a stable pro-corner. The white dashed line corresponds to $V_\theta/U_c = 2$ per cent, which we use to distinguish between stable and unstable corners.

3.4 Comparison to the England and Holland channel-flow model

An important aspect of the channel-flow models of England & Holland (1979) and Shreve & Cloos (1986) is that they account for
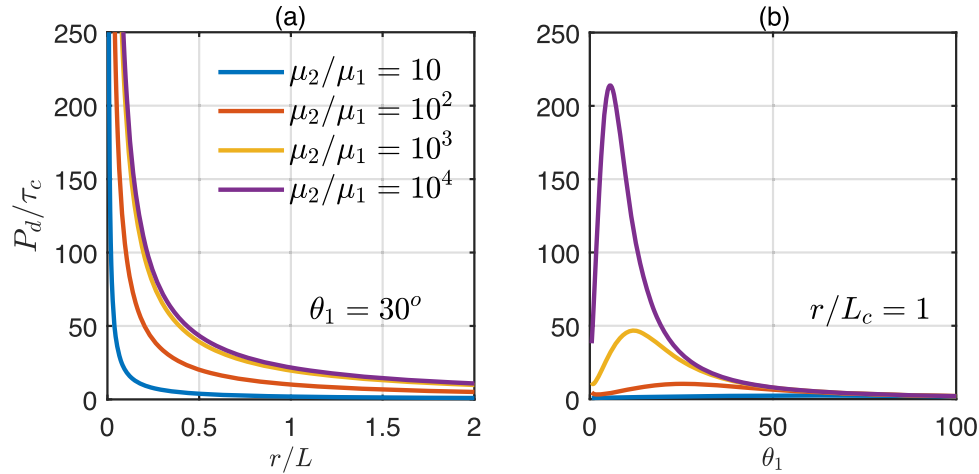
Figure 9. (a) Non-dimensional dynamic pressure P_d versus r for a pro-corner with an opening angle $\theta_1 = 30°$. The values are for a transect along the centre of the pro-corner ($\theta = \theta_1/2$). (b) Non-dimensional dynamic pressure P_d at $r/L_c = 1$ on the medial boundary and as a function of difference opening angles, θ_1, for the pro-corner.

buoyancy, an effect that is otherwise ignored in the corner-flow solutions considered above. Buoyancy becomes important when there is a significant contrast between the density of the material in the channel, and that of the adjacent walls ($\Delta\rho = \rho_c - \rho_w$). A positive density contrast would enhance downward flow within the channel, and a negative density contrast might activate a backflow in the upper part of the channel. We have seen above that backflow in forced corner flows is limited to the case of a stable narrow corner, and the driving force is a large dynamic pressure gradient created by the downward convergence of the flow. We show here that it is difficult to use the velocity fields associated with backflow to distinguish the driving force, whether buoyancy or dynamic pressure.

Here, we develop an approximation for a channel that has both (1) a dynamic pressure gradient parallel to the channel, as present in a narrow corner, and (2) a buoyancy gradient parallel to the channel, as is present in a buoyancy-driven channel flow. The layout for the comparison is shown in Figs 12(a) and (b). Two narrow corner geometries are considered, with opening angles of 5° and 15°.

The approximate relationship for the channel-parallel velocity V_x is developed in the Appendix. The final equation is

$$V_x = \frac{1}{2\mu}\left[\frac{dP_d}{dx} + \Delta\rho g_x\right](y^2 - Hy) + U\left(\frac{y}{H} - 1\right), \quad (12)$$

where μ is the viscosity of the material in the channel, H is the thickness of the channel, x is distance upward along the channel, and U is the entrainment velocity at the lower boundary of the flow. The gravitational acceleration vector is downward and oblique to the lower boundary (as expected for a dipping subduction zone). The constant g_x is the component of the gravitational acceleration parallel to the channel.

The similarity of the corner and channel velocity fields is indicated by the arrangement of the two terms in the square bracket of eq. (12). The first term, dP_d/dx, is the dynamic pressure gradient parallel to the channel. The second term, $\Delta\rho g_x$, is the buoyancy-related pressure gradient parallel to the channel. Eq. (12) shows that these two gradient terms have a similar influence on the V_x field.

This conclusion is illustrated by the results in Figs 12(c) and (d), which shows V_x/U_c across the channel for the two examples. The solid lines show the corner-flow solutions for V_x/U_c for the corner geometries in Figs 12(a) and (b). The plus and diamond symbols

show results for the channel-flow approximation (eq. 12) for V_x/U_c using a dynamic-pressure gradient and a buoyancy gradient, both oriented parallel to the channel. These examples demonstrate that the velocity fields alone are not sufficient to distinguish between a backflow driven by a dynamic pressure gradient or a buoyancy gradient, or a combination of the two.

4 DISCUSSION

An essential feature of the classic corner-flow model is the occurrence of backflow in acute corners (Fig. 1a). The backflow provides an interesting way in which HP/LT metamorphic rocks might be returned to the surface in subduction-zone settings. In the corner-flow model, the backflow is caused by convergence of the incoming flow. Our two-corner solution reveals that the maintenance of a stable pro-corner requires a large viscosity ratio ($\mu_2/\mu_1 \geq 10^3$, Fig. 5), and/or a relatively large opening angle ($\theta_1 > 90°$, Figs 10 and 11). Conversely, a pro-corner with a narrow opening angle ($\theta_1 < 30°$) and a viscosity ratio $\mu_2/\mu_1 < 10^2$ will evolve towards a larger opening angle, and the medial boundary will likely become distorted during this evolution. Nonetheless, we envision that as the pro-corner evolves towards this wider geometry, flow will cause material to move across the corner point, in a fashion similar to that shown for S-point models for wide wedges (Willett *et al.* 1993; Buck & Sokoutis 1994; Allemand & Lardeaux 1997; Medvedev 2002).

These observations suggest the following idea for evolution of subduction zones. When a subduction zone is first initiated, the resulting shear zone can be approximated by a pro-corner that has, by definition, a zero-opening angle, given that there has been no time to fill the corner with subducted sediment. We infer that most subduction zones lack the viscosity contrast required to sustain a narrow corner. Thus, the initially narrow pro-corner will evolve towards an opening angle that is in balance with the viscosity ratio μ_2/μ_1 for the subduction zone. More complex geodynamic models have also illustrated this behavior when an initial narrow subduction channel evolves into an orogenic wedge (Pfiffner *et al.* 2000). If our argument is correct, then the opening angle of the pro-corner at a mature subduction zone could be used to estimate an effective viscosity ratio, μ_2/μ_1, for a real subduction zone.
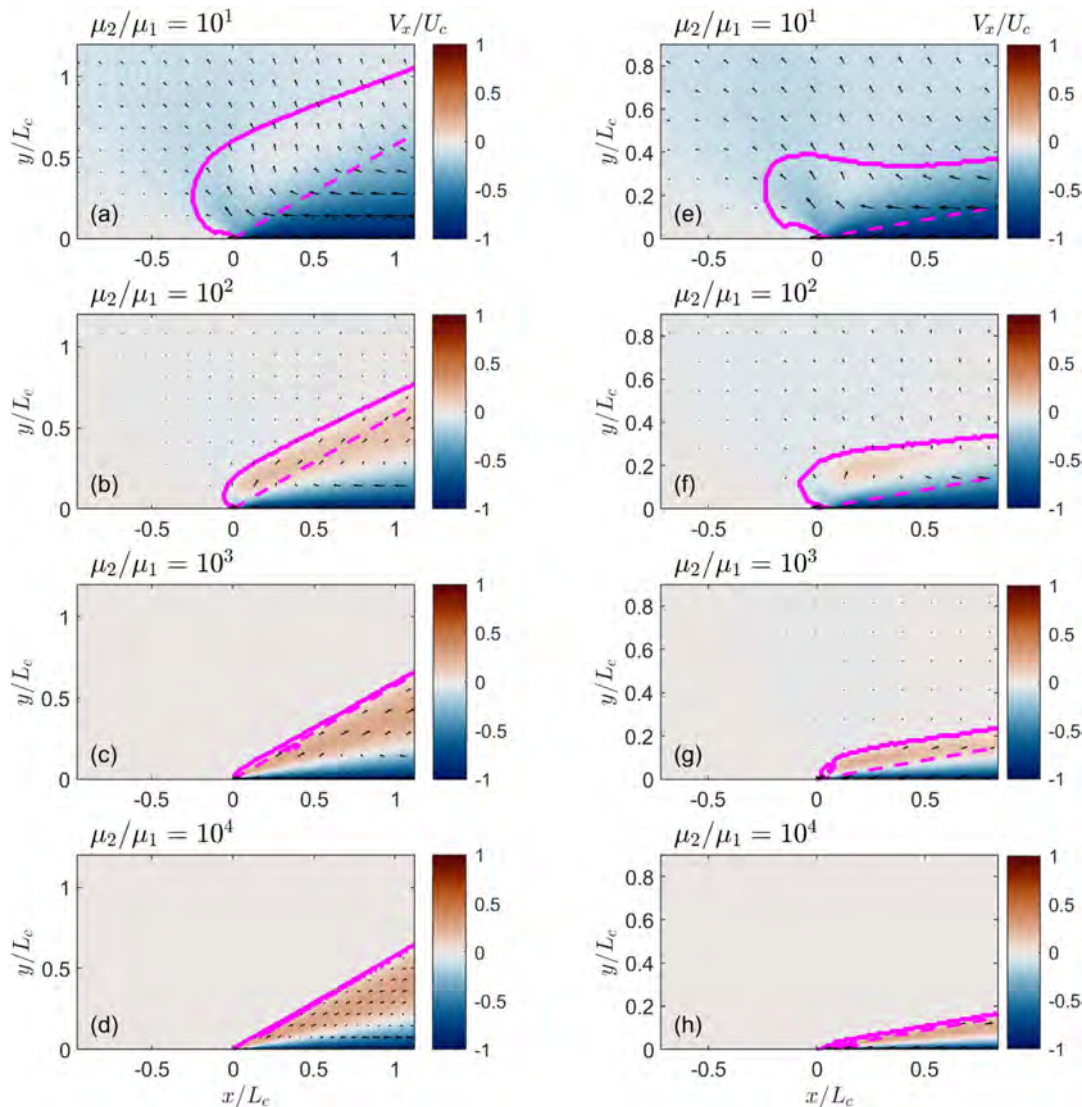
Figure 10. Numerical solutions showing the deformation of the medial boundary after a time interval of about $2t_c \approx 4$ Ma. The initial and final locations of the medial boundary are marked by dashed and solid magenta lines, respectively. Plots (a)–(d) focus on a pro-corner that starts with an acute geometry ($\theta_1 = 30°$), and plots (e)–(h) focus on a pro-corner that starts with very narrow geometry ($\theta_1 = 10°$). The colour map shows the non-dimensional horizontal component of velocity; positive values (brown colour) indicate backflow in the pro-corner. The calculations were done using the M2Di program (see details in Section 2.3).

Another interesting conclusion is that flow in a narrow channel or corner must be accompanied by a significant dynamic pressure high. This is an important issue in that metamorphic pressure is no longer a simple function of depth (Petrini & Podladchikov 2000; Moulas *et al.* 2013; Schmalholz & Podladchikov 2013; Bauville & Yamato 2021). A possible counter argument is that this dynamic pressure high might be reduced if the material inside the pro-corner were very weak. However, our analysis shows that an increase in the viscosity ratio (which is equivalent to 'weakening' the pro-corner materials) will cause an increase, not decrease, in the dynamic pressure high (Fig. 8). Thus, if the HP/LT blocks found in paleo-subduction settings like the Franciscan Complex were in fact exhumed within a narrow subduction channel, then the total pressure, P, must have been significantly greater than the lithostatic pressure, P_s. A rough estimate is that that P_d can reach values similar to P_s, which means that P would be about twice that of the

lithostatic pressure, P_s. As noted above, the blueschists and eclogites found in the Franciscan Complex have metamorphic pressures that range up to ∼1.5 GPa (Wakabayashi 2015). If the dynamic pressure effect were zero, then these pressures would indicate maximum depths of 55 km (average density is taken as 2800 kg m^{-3}). If the dynamic pressure P_d achieves values comparable to the static pressure, P_s, then this maximum depth would be reduced by half, to ∼27 km.

Another interesting feature of our corner flow solutions is that the dynamic pressure high extends across both the pro- and retro-corners. This result counters a common inference that HP/LT metamorphism is somehow related to strong shearing within the subduction zone. There are many examples, however, of HP/LT metamorphic rocks that show little to no deformation. To highlight this, we point to an eclogite sequence in the Zermatt-Sass-Fee zone of the Swiss Alps made famous by Bearth (1959). He discovered
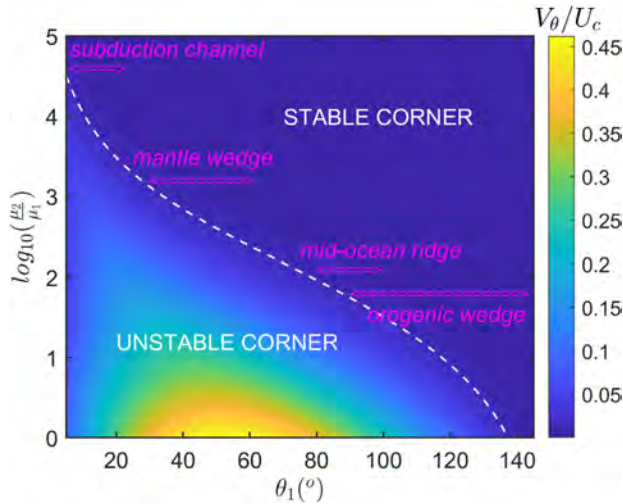
Figure 11. Non-dimensional circumferential velocity, V_θ/U_c, of the medial boundary as a function of the opening of the corner, θ_1, and the logarithm of the viscosity ratio, μ_2/μ_1. The white dashed line corresponds to a contour, where $V_\theta/U_c = 1/50$, and is used to distinguish stable and unstable pro-corners. The magenta labels show the viscosity ratio needed to sustain a stable corner for some representative tectonic settings on the Earth.

that this unit preserved the outlines of pillow basalts, and, in many places, the outlines were essentially undeformed (see fig. 1 in Ernst 2010, for a picture from this unit).

Our analysis overlooks the actual processes associated with accretion. This point is made clear by the fact that the accreted sediments of the pro-corner are already located above the subduction thrust. Accretion marks the transfer of material across the subduction thrust, and it is known to occur adjacent to the trench, as indicated by the term *offscrapping* (or frontal accretion) and also by more deep-seated accretion, which called *underplating* (or basal accretion) (Sample & Fisher 1986). For our analysis, we have set $V_{\theta_0} = 0$ on the pro-boundary, which indicates that we have assumed that underplating is not a significant issue. However, our analysis can be easily extended to include underplating simply by adjusting V_{θ_0} to a positive value consistent with the rate of mass transfer into the pro-corner by this accretionary process. We infer that, with all other factors equal, the addition of an accretionary flux by underplating would further destabilize a narrow pro-corner, and it would probably affect the dynamic pressure as well. However, more work is needed to properly test these inferences.

Another result of this study is relevant for the case where the acute corner is approximated by a typical channel-flow geometry. The results provided by the two solutions (forced vs buoyant channel in Fig. 12) are indistinguishable and both solutions would predict the same velocity for a reasonable set of parameters. The similarity of the two solutions shows, in fact, that structural observations alone are probably not sufficient to distinguish between a buoyancy-driven backflow or a pressure-driven backflow.

At this point, we would like to emphasize that the most important factor for the maintenance of the corner geometry and the generation of backflow is the viscosity ratio between the pro-corner and the overriding plate. Large viscosity ratios can be expected in nature as a consequence of the different lithologies and the variety of physical conditions (temperature, fugacity of volatiles, lithology, etc.). However, there are two competing phenomena that occur in association with metamorphism during subduction. On the one hand, the subduction of material, and the associated pressure and temperature

increase leads to devolatilization and densification within the pro-corner. On the other hand, this devolatilization might also lead to the hydration and weakening of the overriding plate. For both cases, the viscosity ratio decreases and the pro-corner would become less stable and more transient.

Finally, we end with a comment about mélanges. In Cloos' (1982) view, mélange formation is intrinsically related to corner flow, as emphasized by his term 'flow mélange'. However, Cloos (1982) also recognized that the mixing observed in mélanges cannot be directly related to corner flow since the velocity field is laminar (low Reynolds number), and not turbulent. Therefore, he proposed that the mixing was caused by plucking of dense HP/LT blocks from the hanging wall, which then settled at variable rates through the actively flowing material in the pro-corner. The idea of blocks dispersing by 'Stokes settling' within an active corner flow is entirely plausible. However, our analysis indicates that the maintenance of active flow in a narrow corner requires that the material in the pro-corner is exceptionally weak, or the upper plate (i.e. the retro-corner) is exceptionally strong. This requirement provides an approach to test the viability of the subduction channel idea.

5 CONCLUSIONS

A new analytical solution for the study of viscous incompressible flow in corner regions has been developed. The analytical solution shows that the activation of a strong backflow requires a narrow corner, which is the expected situation shortly after initiation of a subduction zone. The convergence of accreted materials into a narrow pro-corner creates a large dynamic pressure. As such, HP/LT metamorphism can occur in such settings at depths much shallower, by as much as a factor of two, than that predicted by the common assumption that the total pressure is equal static pressure. Our inference is that the overlying retro-corner is generally not strong enough to sustain a narrow pro-corner, which means that the medial boundary above the pro-corner will migrate rearward into the overriding plate. Thus, with time, an initially narrow pro-corner will evolve to an obtuse geometry. This wider configuration is consistent with the observation of widespread uplift and deformation across the forearc high at most actively accreting subduction zones.

Much of the discussion about accretion, HP/LT metamorphism, and exhumation at subduction zones is framed by the idea of a confined flow inside a narrow corner or a thin channel. The basic forcing for the flow is thought to be entrainment of accreted materials that overlies the subducting plate. The corner-flow problem is based solely on this kinematic forcing. The channel flow problem includes both kinematic and buoyancy forcing. Some authors have argued that structures in the field may be able to distinguish between these two kinds of forcings. We show that, in fact, the velocity fields associated with kinematic and buoyancy forcings are remarkably similar, and thus would be difficult to diagnosis by structural observations alone.

ACKNOWLEDGEMENTS
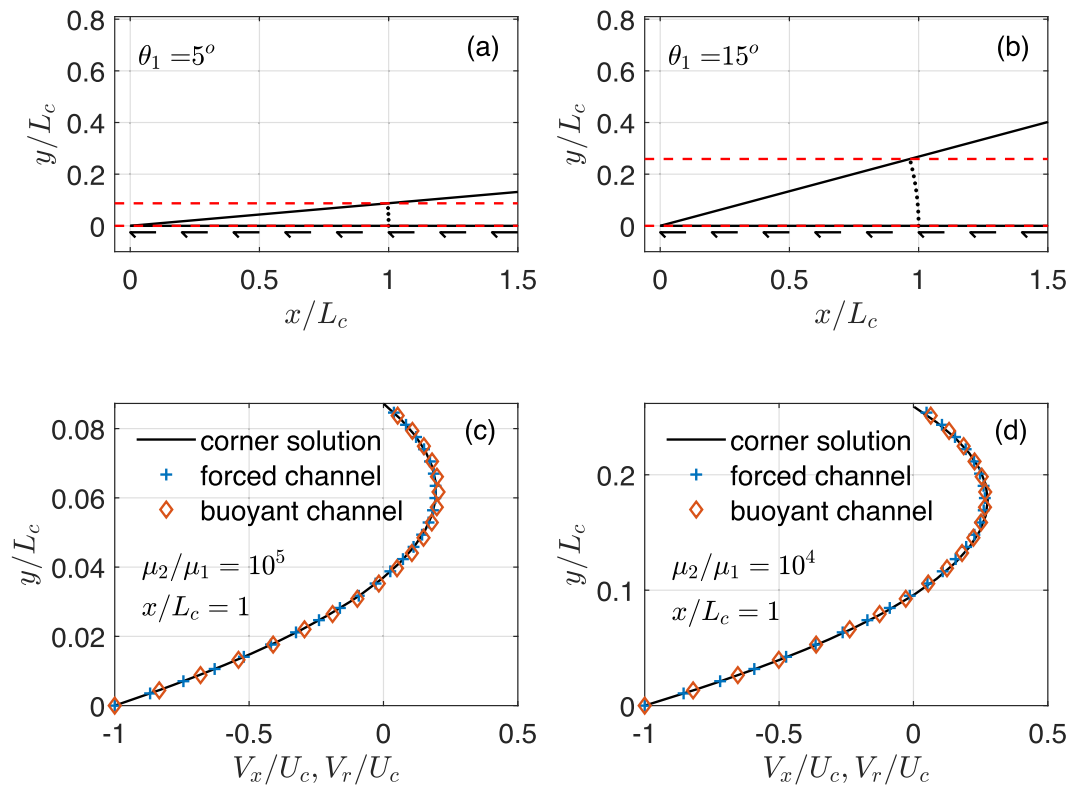
Figure 12. Comparisons of narrow corner flows with forced flows and buoyant flows in channels with similar equivalent thicknesses. Panels (a) and (c) show results for a very narrow case ($\theta_1 = 5°$), and panels (b) and (d) show results for a narrow case ($\theta_1 = 15°$). The viscosity ratios are adjusted to ensure a stable corner. Panels (a) and (b) show the layout for the corner and the equivalent channel for each example. The lower boundary corresponds to the top of the subducting plate, and the barbed arrows indicate the direction for entrainment at the base of the flow field. Panels (c) and (d) show various estimates for V_x/U_c, as measured across the corner or channel at $x/L_c = 1$. The solid lines show the V_x/U_c profiles for the corner-flow solutions, and the symbols show the V_x/U_c profiles as estimated by eq. (12) for specified along-channel gradients in pressure (plus symbols) and buoyancy (diamond symbols). The rest of the model parameters are: the density difference is -300 kg m^{-3}, velocity is 5 cm a^{-1}, and the channel viscosities are ~1.5 × 10^{17} and 1.2 × 10^{18} Pa s for (a) and (b), respectively.

visiting MTB at Yale University. Susan Monsen is acknowledged for her hospitality and patience during our long discussions. MTB thanks Kurt Stüwe for a 2019 field trip introduction to the Austria eclogites. Thibault Duretz and Ludovic Räss are acknowledged for help related to the adaptation of the M2Di solver for the corner geometry.

DATA AVAILABILITY

wxMaxima and MATLAB scripts are provided in the Supporting Information. These files can be used for the calculation and visualization of the analytical solution presented in this work.

REFERENCES

Adamuszek, M., Dabrowski, M. & Schmid, D.W., 2016. Folder: a numerical tool to simulate the development of structures in layered media, *J. Struct. Geol.,* **84,** 85–101.

Allemand, P. & Lardeaux, J.-M., 1997. Strain partitioning and metamorphism in a deformable orogenic wedge: application to the Alpine belt, *Tectonophysics,* **280,** 157–169.

Ampferer, O. & Hammer, W., 1911. *Geologischer Querschnitt durch die Ostalpen vom Allgäu zum Gardasee,* Jahrbuch der Kaiserlich-Königlichen Geologischen Reichsanstalt, Vol. 61, pp. 532–710, Geologischen Reichsanstalt.

Anderson, D.M. & Davis, S.H., 1993. Two-fluid viscous flow in a corner, *J. Fluid Mech.,* **257,** 1–31.

Argand, E., 1916. Sur l'arc des Alpes Occidentales, *Eclogae Geol. Helvetiae,* **14,** 145–191.

Argand, E., 1924. Des Alpes et de l'Afrique, *Bull. Soc. Vaudoise Sci. Nat.,* **55,** 233–236.

Batchelor, G.K., 1967. *An Introduction to Fluid Dynamics,* Cambridge Univ. Press.

Bauville, A. & Yamato, P., 2021. Pressure-to-depth conversion models for metamorphic rocks: derivation and applications, *Geochem. Geophys. Geosyst.,* **22,** e2020GC009280.

Bearth, P., 1959. Über Eklogite, Glaukophanschiefer und metamorphe Pillowlaven, *Schweiz. Mineral. Petrogr. Mitteilungen,* **39,** 267–286.

Beaumont, C. & Quinlan, G., 1994. A geodynamic framework for interpreting crustal-scale seismic-reflectivity patterns in compressional orogens, *Geophys. J. Int.,* **116,** 754–783.

Beuchert, M.J. & Podladchikov, Y.Y., 2010. Viscoelastic mantle convection and lithospheric stresses, *Geophys. J. Int.,* **183,** 35–63.

Bird, P., 2003. An updated digital model of plate boundaries, *Geochem. Geophys. Geosyst.,* **4** , doi:10.1029/2001GC000252.

Buck, W.R. & Sokoutis, D., 1994. Analogue model of gravitational collapse and surface extension during continental convergence, *Nature,* **369,** 737–740.

Camerlengi, A. & Pini, G.A., 2009. Mud volcanoes, olistostromes and Argille scagliose in the Mediterranean region, *Sedimentology,* **56,** 319–365.

Chang, C.P., Angelier, J., Huang, C.Y. & Liu, C.S., 2001. Structural evolution and significance of a mélange in a collision belt: the Lichi Mélange and the Taiwan arc–continent collision, *Geol. Mag.,* **138,** 633–651.

Claussmann, B. *et al.*, 2021. Shelf-derived mass-transport deposits: origin and significance in the stratigraphic development of trench-slope basins, *N.Z. J. Geol. Geophys.,* 1–36, doi:10.1080/00288306.2021.1918729.

Cloos, M., 1982. Flow melanges: numerical modeling and geologic constraints on their origin in the Franciscan subduction complex, California, *Bull. geol. Soc. Am.,* **93,** 330–345.

Cloos, M., 1984. Flow melanges and the structural evolution of accretionary wedges, in *Melanges: Their Nature, Origin, and Significance,* Vol. 198, ed. Raymond, L.A., Geological Society of America.

Cloos, M. & Shreve, R.L., 1988a. Subduction-channel model of prism accretion, melange formation, sediment subduction, and subduction erosion at convergent plate margins: 2. Implications and discussion, *Pure appl. Geophys.,* **128,** 501–545.

Cloos, M. & Shreve, R.L., 1988b. Subduction-channel model of prism accretion, melange formation, sediment subduction, and subduction erosion at convergent plate margins: 1. Background and description, *Pure appl. Geophys.,* **128,** 455–500.

Cowan, D.S., 1985. Structural styles in Mesozoic and Cenozoic mélanges in the western Cordillera of North America, *Bull. geol. Soc. Am.,* **96,** 451–462.

Cowan, D.S. & Silling, R.M., 1978. A dynamic, scaled model of accretion at trenches and its implications for the tectonic evolution of subduction complexes, *J. geophys. Res.,* **83,** 5389–5396.

Dean, W.R. & Montagnon, P.E., 1949. On the steady motion of viscous liquid in a corner, *Math. Proc. Camb. Phil. Soc.,* **45,** 389–394.

Duretz, T., May, D.A., Gerya, T.V. & Tackley, P.J., 2011. Discretization errors and free surface stabilization in the finite difference and marker-in-cell method for applied geodynamics: a numerical study, *Geochem. Geophys. Geosyst.,* **12,** doi:10.1029/2011GC003567.

Emerman, S.H. & Turcotte, D.L., 1983. A fluid model for the shape of accretionary wedges, *Earth planet. Sci. Lett.,* **63,** 379–384.

England, P. & Wilkins, C., 2004. A simple analytical approximation to the temperature structure in subduction zones, *Geophys. J. Int.,* **159,** 1138–1154.

England, P.C. & Holland, T.J.B., 1979. Archimedes and the Tauern eclogites: the role of buoyancy in the preservation of exotic eclogite blocks, *Earth planet. Sci. Lett.,* **44,** 287–294.

Ernst, W.G., 2010. Subduction zone metamorphism—pioneering contributions from the Alps, *Int. Geol. Rev.,* **52,** 1021–1039.

Fletcher, R.C., 1977. Folding of a single viscous layer: exact infinitesimal-amplitude solution, *Tectonophysics,* **39,** 593–606.

Gerya, T.V., Stöckhert, B. & Perchuk, A.L., 2002. Exhumation of high-pressure metamorphic rocks in a subduction channel: a numerical simulation, *Tectonics,* **21,** 6-1-6-19.

Henriksen, P. & Hassager, O., 1989. Corner flow of power law fluids, *J. Rheol.,* **33,** 865–879.

Jamieson, R.A. & Beaumont, C., 2013. On the origin of orogens, *Bull. geol. Soc. Am.,* **125,** 1671–1702.

Krohe, A., 2017. The Franciscan Complex (California, USA)—the model case for return-flow in a subduction channel put to the test, *Gondwana Res.,* **45,** 282–307.

Landau, L.D. & Lifshitz, E.M., 1987. *Course of Theoretical Physics, Vol. 6, Fluid Mechanics,* 2nd edn, Pergamon.

Lundberg, N. & Moore, J.C., 1986. Macroscopic structural features in Deep Sea Drilling Project cores from forearc regions, in *Structural Fabrics in Deep Sea Drilling Project Cores From Forearcs,* Vol. 166, ed. Moore, J.C., Geological Society of America.

Mancktelow, N.S., 1995. Nonlithostatic pressure during sediment subduction and the development and exhumation of high pressure metamorphic rocks, *J. geophys. Res.,* **100,** 571–583.

McKenzie, D.P., 1969. Speculations on the consequences and causes of plate motions, *Geophys. J. R. astr. Soc.,* **18,** 1–32.

Medvedev, S., 2002. Mechanics of viscous wedges: modeling by analytical and numerical approaches, *J. geophys. Res.,* **107,** ETG 9–1-ETG 9-15.

Moffatt, H.K., 1964. Viscous and resistive eddies near a sharp corner, *J. Fluid Mech.,* **18,** 1–18.

Moulas, E., Burg, J.-P. & Podladchikov, Y., 2014. Stress field associated with elliptical inclusions in a deforming matrix: mathematical model and implications for tectonic overpressure in the lithosphere, *Tectonophysics,* **631,** 37–49.

Moulas, E. & Schmalholz, S.M., 2020. The importance of interfacial instability for viscous folding in mechanically heterogeneous layers, *Geol. Soc. Lond. Spec. Publ.*, **487,** 45–58.

Moulas, E., Podladchikov, Y.Y., Aranovich, L.Y. & Kostopoulos, D.K., 2013. The problem of depth in geology: when pressure does not translate into depth, *Petrology,* **21,** 527–538.

Moulas, E., Schmalholz, S.M., Podladchikov, Y., Tajčmanová, L., Kostopoulos, D. & Baumgartner, L., 2019. Relation between mean stress, thermodynamic, and lithostatic pressure, *J. Metamorph. Geol.,* **37,** 1–14.

Page, B.M. & Suppe, J., 1981. The Pliocene Lichi melange of Taiwan; its plate-tectonic and olistostromal origin, *Am. J. Sci.,* **281,** 193–227.

Pazzaglia, F.J. & Brandon, M.T., 2001. A fluvial record of long-term steady-state uplift and erosion across the Cascadia Forearc High, Western Washington State, *Am. J. Sci.,* **301,** 385−431.

Petrini, K. & Podladchikov, Y., 2000. Lithospheric pressure–depth relationship in compressive regions of thickened crust. *J. Metamorph. Geol.,* **18,** 67–77.

Pfiffner, O.A., Ellis, S. & Beaumont, C., 2000. Collision tectonics in the Swiss Alps: insight from geodynamic modeling, *Tectonics,* **19,** 1065–1094.

Pollard, D.D. & Fletcher, R.C., 2005. *Fundamentals of Structural Geology,* Cambridge Univ. Press.

Raimbourg, H. & Kimura, G., 2008. Non-lithostatic pressure in subduction zones, *Earth planet. Sci. Lett.,* **274,** 414–422.

Räss, L., Duretz, T., Podladchikov, Y.Y. & Schmalholz, S.M., 2017. M2Di: concise and efficient MATLAB 2-D Stokes solvers using the finite difference method, *Geochem. Geophys. Geosyst.,* **18,** 755–768.

Ribe, N.M., 1989. Mantle flow induced by back arc spreading. *Geophys. J. Int.,* **98,** 85–91.

Ribe, N.M., 2015. Analytical approaches to mantle dynamics, in *Treatise on Geohpysics,* Vol. 7, pp. 145–196, ed. Bercovici, D., Elsevier.

Ribe, N.M., 2018. *Theoretical Mantle Dynamics,* 1st edn, Cambridge Univ. Press.

Ribe, N.M. & Xu, B., 2020. Subduction of non-Newtonian plates: thin-sheet dynamics of slab necking and break-off, *Geophys. J. Int.,* **220,** 910–927.

Riedler, J. & Schneider, W., 1983. Viscous flow in corner regions with a moving wall and leakage of fluid, *Acta Mech.,* **48,** 95–102.

Ring, U. & Brandon, M.T., 1999. Ductile deformation and mass loss in the Franciscan Subduction Complex: implications for exhumation processes in accretionary wedges, *Geol. Soc. Lond. Spec. Publ.*, **154,** 55, doi:10.1144/GSL.SP.1999.154.01.03.

Sample, J.C. & Fisher, D.M., 1986. Duplex accretion and underplating in an ancient accretionary complex, Kodiak Islands, Alaska, *Geology,* **14,** 160–163.

Schellart, W.P., 2008. Kinematics and flow patterns in deep mantle and upper mantle subduction models: influence of the mantle depth and slab to mantle viscosity ratio, *Geochem. Geophys. Geosyst.,* **9,** doi:10.1029/2007GC001656.

Schmalholz, S.M., 2011. A simple analytical solution for slab detachment, *Earth planet. Sci. Lett.,* **304,** 45–54.

Schmalholz, S.M. & Podladchikov, Y.Y., 2013. Tectonic overpressure in weak crustal-scale shear zones and implications for the exhumation of high-pressure rocks, *Geophys. Res. Lett.,* **40,** 1984–1988.

Schmid, D.W. & Podladchikov, Y.Yu., 2003. Analytical solutions for deformable elliptical inclusions in general shear, *Geophys. J. Int.,* **155,** 269–288.

Shreve, R.L. & Cloos, M., 1986. Dynamics of sediment subduction, melange formation, and prism accretion, *J. geophys. Res.,* **91,** 10 229–10 245.

Spiegelman, M. & McKenzie, D., 1987. Simple 2-D models for melt extraction at mid-ocean ridges and island arcs, *Earth planet. Sci. Lett.,* **83,** 137–152.

Sprittles, J.E. & Shikhmurzaev, Y.D., 2011. Viscous flow in domains with corners: numerical artifacts, their origin and removal, *Comput. Methods Appl. Mech. Eng.,* **200,** 1087–1099.

Stevenson, D.J. & Turner, J.S., 1977. Angle of subduction, *Nature,* **270,** 334–336.

Tovish, A., Schubert, G. & Luyendyk, B.P., 1978. Mantle flow pressure and the angle of subduction: non-Newtonian corner flows, *J. geophys. Res.,* **83,** 5892–5898.

Turcotte, D.L. & Schubert, G., 2014. *Geodynamics,* 3rd edn, Cambridge Univ. Press.

van Keken, P.E. *et al.*, 2008. A community benchmark for subduction zone modeling, *Phys. Earth Planet. Inter.,* **171,** 187–197.

Wakabayashi, J., 2015. Anatomy of a subduction complex: architecture of the Franciscan Complex, California, at multiple length and time scales, *Int. Geol. Rev.,* **57,** 669–746.

Willett, S., Beaumont, C. & Fullsack, P., 1993. Mechanical model for the tectonics of doubly vergent compressional orogens, *Geology,* **21,** 371–374.

SUPPORTING INFORMATION

Supplementary data are available at *GJI* online.

Electronic_Supplementary_Material.zip

Please note: Oxford University Press is not responsible for the content or functionality of any supporting materials supplied by the authors. Any queries (other than missing material) should be directed to the corresponding author for the paper.

APPENDIX: COMPARISON OF CORNER AND CHANNEL FLOW

Here, we derive the equations that are used to compare a channel flow between two parallel walls and a corner flow with a small angle. The channel flow is derived from the equations for slow incompressible viscous flow (Landau & Lifshitz 1987, p. 52; Turcotte & Schubert 2014, p. 270). The coordinates are Cartesian with x is directed upward and parallel to the channel ($\theta = \theta_0$) and y is perpendicular to the channel ($\theta = \theta_0 + 90°$). The governing equation for the total pressure P (equal to the negative mean stress) is

$$\mu \frac{\mathrm{d}^2 V_x}{\mathrm{d}y^2} = \frac{\mathrm{d}P}{\mathrm{d}x} - \rho g_x, \tag{A1}$$

where V_x is the channel-parallel velocity, ρ and μ are the density and viscosity of the material in the channel and g_x is the x-component of gravitational acceleration (parallel to the channel). Eq. (A1) is modified by separating the total pressure P into static P_s and dynamic P_d components, and then simplifying, which give

$$\mu \frac{\mathrm{d}^2 V_x}{\mathrm{d}y^2} = \frac{\mathrm{d}P_d}{\mathrm{d}x} + \Delta \rho g_x, \tag{A2}$$

where $\Delta \rho = \rho_c - \rho_w$ is the density difference between the channel material and the surrounding wall rock. The solution is

$$V_x = \frac{1}{2\mu} \left(\frac{\mathrm{d}P_d}{\mathrm{d}x} + \Delta \rho g_x \right) y^2 + c_1 y + c_2, \tag{A3}$$

where c_1 and c_2 are integration constants determined by the boundary conditions. By setting $V_x = -U$ at $y = 0$ and $V_x = 0$ at $y = H$, we obtain

$$c_1 = \frac{U}{H} - \frac{1}{2\mu} \left(\frac{\mathrm{d}P_d}{\mathrm{d}x} + \Delta \rho g_x \right) H, \tag{A4a}$$

and

$$c_2 = -U. \tag{A4b}$$

We assume that, for the region of interest, the dynamic pressure gradient, $\mathrm{d}P_d/\mathrm{d}x$, is approximately constant and the channel-parallel velocity gradient, $\mathrm{d}V_x/\mathrm{d}x$, is approximately zero. A constant pressure gradient is a reasonable assumption for regions away from the corner ($r/L_c > 1$; see also Fig. 9a).

Eqs (A3) and (A4) can now be used to approximate the radial component in a narrow corner, as shown in Fig. 12. Inspection of eq. (A3) reveals that there are two quadratic terms related to the back-flow component of the velocity field. The first is related to P_d, which is caused by downward convergence associated with the forced flow, and the second is related to the buoyancy forces associated with the density contrast between the channel and surrounding walls. In other words, eq. (A3) is a more general form of the channel-flow solution, and is also similar to the general solutions developed by Shreve & Cloos (1986) and Mancktelow (1995).

The corner-flow solution is represented by setting $\Delta \rho = 0$, which means that buoyancy effects are turned off. Eqs (A3) and (A4) indicate that in the absence of buoyancy forces, the only way to drive a backflow is by a negative gradient in the dynamic pressure $\mathrm{d}P_d/\mathrm{d}x$, as needed to drive the flow upward. We can now consider a narrow corner region (with $\theta_2 = 150°$) at a location $x/L_c = 1$ (x coincides with the radial direction, r, as in Figs 12a and b). The pressure gradient can be approximated at the limit of small angles ($\cos(\theta_1) \approx 1$, $\sin(\theta_1) \approx 0$). Thus, the dynamic pressure gradient within the corner can be approximated from eq. (11) as

$$\frac{\mathrm{d}P_d}{\mathrm{d}r} \approx -2\frac{C_1}{r^2} \tau_c L_c, \tag{A5}$$

where C_1 is an integration constant from the two-corner analytical solution. By inserting the result of eq (A5) into eqs (A3) and (A4), we obtain the solution shown in Figs 12(c) and (d) (forced channel).

Data Availability

All data related to this thesis is stored on the University of Lausanne long term storage platform (DCSR): nasdcsr.unil.ch/RECHERCHE/FAC/FGSE/ISTE/jvaughan/monte_rosa_jvh.

Data for each chapter has been uploaded onto the general-purpose open-access repository Zenodo:

- Chapter 2: https://zenodo.org/record/5519419#.YUnWddMzaLU

- Chapter 3: https://zenodo.org/record/5519374#.YUnSL9MzaLU

- Chapter 4: https://zenodo.org/record/5519475#.YUnc2dMzaLU

- Chapter 5: https://zenodo.org/record/5521214#.YUsjJ9MzaLU

Acknowledgements

Chapter 2 - *Alpine peak pressure and tectono-metamorphic history of the Monte Rosa nappe: cirque du Véraz, upper Ayas valley, Italy*

Chapter 3 - *Peak Alpine metamorphic conditions from staurolite-bearing metapelites in the Monte Rosa nappe (Central European Alps) and geodynamic implications*

Chapter 4 - *In search of Peter Bearth's whiteschist: Jägerhorn peak, Piedmont, Italy*

Chapter 5 - *Metamorphic facies evolution and distribution in the Western Alps predicted by petrological-thermomechanical models*

Curriculum vitae

Joshua D. Vaughan-Hammon

Geologist

Address: 2a Rue des Crêtes
             1018-Lausanne
             Vaud
             Switzerland
Mobile: +41 786953186
E-Mail: joshvh91@gmail.com
Scholar: https://scholar.google.com/citations?user=a2tcL6MAAAAJ&hl=en
LinkedIn: https://www.linkedin.com/in/joshua-vaughan-hammon-83044616a/
ResearchGate: https://www.researchgate.net/profile/Joshua_Vaughan_Hammon
Orcid ID: 0000-0002-0388-146X

- Multidisciplinary geologist with research in: metamorphic petrology, numerical modelling, structural geology, geological mapping and exploration.

EDUCATION

2016 – 2021   **Ph.D. in Earth Science**, University of Lausanne, Switzerland.
Thesis: "Deciphering the tectono-metamorphic evolution of the Monte Rosa nappe: a combined petrological, structural and numerical modelling study"
Supervisors: Stefan Schmalholz and Lukas Baumgartner

2015 – 2016   **MESci. in Earth Sciences with Honours in School of Geology** (1st Class Honors), University of Liverpool, United Kingdom.
Thesis: "The emplacement and evolution of the Alpe Morello peridotite, Ivrea-Verbano Zone, NW Italy: insights from its microstructural and chemical signature"
Supervisor: Elisabetta Mariani

2012 – 2015   **BSc. in Earth Sciences with Honours in School of Geology** (1st Class Honors), University of Liverpool, United Kingdom.
Thesis: "The Geology of Salanfe, Switzerland, within the framework of the Variscan and Alpine orogens"
Supervisor: Elisabetta Mariani

RELEVANT EMPLOYMENT HISTORY

2016 – 2021   **Research assistant**. University of Lausanne, Switzerland.
Stefan Schmalholz and Lukas Baumgartner

2016 – 2021   **Teaching assistant**. University of Lausanne, Switzerland.
Stefan Schmalholz and Lukas Baumgartner

2015 – 2016   **Fieldwork assistant in Italian Alps**. University of Liverpool, United Kingdom.
Elisabetta Mariani and Joseph Aslin

INSTITUTIONAL RESPONSIBILITIES

2021   **Primary teaching assistant**. University of Lausanne, Switzerland.
Tectonics and geodynamics class (2nd year Bachelor)

TEACHING ACTIVITIES

2016 – 2021 **Teaching assistant: Numerical modelling** (3 semesters). University of Lausanne, Switzerland. MATLAB based practical class using differential equations to predict 1D/2D/3D behaviour of ice flow, pollution, erosion, heat diffusion, and wave propagation (1st year Bachelor).

2016 – 2021 **Teaching assistant: Tectonics and Geodynamics** (4 semesters). University of Lausanne, Switzerland. Derivation of analytical solutions and use of MATLAB for fundamental geophysical problems, e.g. stress, strain, folding, rheology (2nd year Bachelor).

2016 – 2021 **Teaching assistant: Quantitative tectonics** (4 semesters). University of Lausanne, Switzerland. Derivation of analytical solutions and use of MATLAB for more complex geophysical problems, e.g. continuum mechanics, shear zones, gravitational potential energy (3rd year Bachelor).

2016 – 2021 **Teaching assistant: Metamorphic field class** (2 excursions). University of Lausanne, Switzerland. Lucomagno, Switzerland. Adamello, Italy. (3rd year Bachelor).

2016 – 2021 **Teaching assistant: Introduction to geological mapping field class** (4 excursions). University of Lausanne, Switzerland. Gemmi Pass, Switzerland. (1st year Bachelor).

ACTIVE MEMBERSHIP IN SCIENTIFIC SOCIETIES

2018 – 2021 Geochemical Society

2016 – 2021 European Geoscience Union

2016 – 2021 Swiss Tectonics Group

2014 – 2016 Petroleum Exploration Society of Great Britain

PRIZES, AWARDS, FELLOWSHIPS

2015 Department PGH Boswell prize: 'Excellence in mapping'. University of Liverpool, United Kingdom.

2014 Petroleum Exploration Society of Great Britain: 'Young professionals scholarship'. University of Liverpool, United Kingdom.

RESEARCH EXPERIENCE

Analytical and laboratory

Optical microscopy, rock preparation, polishing.

Electron probe microanalysis (EPMA): major- and trace-element WDS spot analyses and mapping.

Scanning electron microscopy (SEM): BSE, SE, and cathodoluminescence imaging; energy-dispersive spectrometry mineral chemistry and standardisation; high-angular-resolution electron backscatter diffraction (EBSD).

Programming and mathematics

Programming languages: MATLAB, Julia, Python, Maple, and CUDA.

Thermodynamic phase modelling: Domino/Theriak and Perple_X (+4 years)

Graphical analysis and reduction of geochemical, petrophysical and EBSD data: MATLAB (+5 years) Channel5 (+5 years) XMapTools (+4 years)

Mechanical modelling: (+4 years): 1D, 2D and 3D coupled continuum modelling using finite difference with explicit and implicit solving schemes (MATLAB, Julia).

Coupled 1D two-phase modelling (+2 years) (MATLAB).

Finite element modelling (+2 years) (MATLAB).

Symbolic and numeric computing (+3 years) (Maple).

Parallel computing for multiple GPUs: University of Lausanne supercomputing cluster.

Geographic Information System (ArcGIS, QGIS, GRASS GIS) (+7 years).

Microsoft, Adobe (+15 years).

Fieldwork

Ph.D.	Monte Rosa region, Swiss and Italian Alps: 5 years of field campaign >3000m. Geological mapping of fresh rock exposure due to glacial retreat. Discovery of previously un-reported mineral occurrences.
MESci.	Ivrea-Verbano region, Italian Alps.
BSc.	Thesis area mapping the Morcles Nappe, Switzerland. Spain, Wales, Ireland and Italy.

PERSONAL SKILLS

Full United Kingdom driving license.

French oral and written (5 years living in the French speaking region of Switzerland).

Alpinism (high altitude, glacier environments, multipitch climbing, traditional climbing).

Musical proficiency in guitar, violin, piano, and percussion, as well as sound production.

PUBLISHED ARTICLES:

Vaughan-Hammon, J. D., Luisier, C., Baumgartner, L., Schmalholz, S. M. (2021). Peak Alpine metamorphic conditions from staurolite bearing metapelites in the Monte Rosa nappe (central European Alps) and geodynamic implications. Journal of Metamorphic Geology https://doi.org/10.1111/jmg.12595.

Alpine peak pressure and tectono-metamorphic history of the Monte Rosa nappe: evidence from the cirque du Véraz, upper Ayas valley, Italy. Joshua D. Vaughan-Hammon, Cindy Luisier, Lukas P. Baumgartner, Stefan M. Schmaholz (accepted in the Swiss Journal of Geosciences)

Evangelos Moulas, Mark T. Brandon, Joshua D. Vaughan-Hammon, Stefan M. Schmalholz, On backflow associated with oceanic and continental subduction, Geophysical Journal International, 2021, ggab246, https://doi.org/10.1093/gji/ggab246

ARTICLES SUBMITTED BUT NOT YET ACCEPTED/PUBLISHED:

Metamorphic facies evolution and distribution in the Western Alps predicted by petrological-thermomechanical models. Joshua D. Vaughan-Hammon, Lorenzo G. Candioti, Thibault Duretz and Stefan M. Schmalholz (revisions submitted in the AGU journal G-Cubed)